Modelling the effects of temporal variations of blood flow in tumours

Aleksandra Ardaševa
Corpus Christi College
University of Oxford

Submitted for
Doctor of Philosophy

Trinity 2020

Abstract

Solid tumours have highly irregular vasculatures that are constantly re-modelled, giving rise to spatio-temporal heterogeneity in the level of nutrients, metabolites, and drugs. Such variability requires cells to adapt, and is hypothesised to select for more aggressive cancer phenotypes. Risk spreading through spontaneous phenotypic variations is an ecological concept which is used to explain how species may survive in temporally varying environments. It allows individuals within a species to diversify their phenotypes ensuring that at least some of them can survive in the face of sudden environmental change. In this thesis, we aim to investigate whether cancer cells may adopt this strategy when dealing with rapidly changing levels of nutrient due to temporally-varying blood flow.

Accordingly, we develop and analyse a series of mathematical models of increasing biological complexity in order to investigate, in a systematic way, the impact that temporal variations in the nutrient supply might have on cancer cell populations. First, we present a mathematical model consisting of a system of non-local partial differential equations modelling the evolutionary dynamics of two competing phenotypically-structured populations in the presence of periodically oscillating nutrient levels. The two populations undergo heritable, spontaneous phenotypic variations at different rates. The phenotypic state of each individual is represented by a continuous variable, and the phenotypic landscape of the populations evolves in time due to variations in the nutrient level. We then extend the model by modelling nutrient dynamics explicitly and evaluate the effects of cellular feedback on the environment. Moreover, we develop corresponding individual-based models and study the differences that arise between continuum and discrete approaches at low population sizes.

Exploiting the analytical tractability of our models, coupled with numerical simulations, we identify environmental regimes that select the population with higher rate of spontaneous phenotypic variation. In particular, we expect environmental conditions where cells experience periods of starvation followed by re-oxygenation to promote phenotypic heterogeneity, which is consistent with experimental observations [1]. This allows us to predict how certain interventions, for example, the vascular normalisation strategy that aims at stabilising the blood flow within tumours, could reduce phenotypic heterogeneity and drive the tumour to a treatable phenotype. Furthermore, we apply our discrete model to study adaptive strategies during the metastatic colonisation of distant organs.

Acknowledgements

First of all, I am extremely grateful to my supervisors who made this project possible. Philip and Helen, thank you for your excellent supervision, patience, encouragement and support throughout these few years. Bob and Sandy, I appreciate your endless inspiration and hospitality during my visits at Moffitt Cancer Center, as well as your guidance in the field of mathematical oncology. I would like to thank Tommaso Lorenzi for your guidance and mentorship. It was a pleasure to work with you. I am also grateful to Mehdi Damaghi for the chance to work with experimental data and for valuable discussions.

I would like also to acknowledge people who were around during my time in Oxford and Tampa. Anka, thank you for being a wonderful flatmate over the last three years! Special thanks to SABS 2016 for endless Sporcle entertainment, authentic Italian dinners and chilled evenings together. These years also would not have been as fun and memorable without everyone from WCMB, particularly office S4.08. Moreover, I am very grateful to everyone from IMO at Moffitt Cancer Center for making my stays in Tampa so enjoyable.

Finally, thank you, Jérôme, for being by my side even when being far away.

И напоследок огромное спасибо моим родителям и близким – особенно маме, папе и Тане – за поддержку, предоставленные возможности и мотивацию не сдаваться. Без вас у меня ничего бы не получилось.

Contents

Chapter 1

Introduction

1.1 Overview

Cancer is one of the leading causes of death worldwide, accounting for one in six deaths in 2018 [2]. Originally, cancer was thought to be a disease of genes [3]. However, it is now recognised that tumours are very complex, dynamic, and constantly evolving organ-like ecosystems [4] that consist of various components, including different types of cancer and normal cells, and blood vessels. These different components are related to each other through various non-linear interactions which lead to the very high heterogeneity observed clinically [5]. Variability is observed on multiple levels including genetic, molecular, environmental, and cellular [6]. It is widely acknowledged that the vasculature contributes significantly to the emergence of such heterogeneity [7].

In most biological tissues, the vasculature is the main source of the nutrients that cells require in order to maintain not just growth, but also homeostasis. At the same time, blood vessels act as sinks that remove metabolites produced by the cells. Metabolites escape or enter the blood flow through the cell junctions in the blood vessel walls and cells convert them into energy to maintain their function. In normal conditions, the vasculature is organised such that every cell receives sufficient levels of vital nutrients to remain alive and perform its normal function. Similarly, cancer cells rely on proximity to blood vessels. Consequently, tumours beyond a certain size (few millimetres) induce angiogenesis – the formation of new blood vessels. However, it is well established that the vascular networks in tumours are highly irregular, i.e. are tortuous, immature and leaky, and result in temporal variations of the blood flow and associated delivery of nutrients.

The consequences of temporal variations in the tumour microenvironment have received little attention and are poorly understood, however, it is clear that such variability requires cells to adapt if they are to survive. In ecology, on the other hand, temporal variations, and the adaptive strategies that might help to deal with them, have been studied to a

great extent. In particular, risk spreading ('bet-hedging') through spontaneous phenotypic variation has been proposed as an evolutionary strategy that allows species to survive in temporally varying environments. Individuals within a species diversify their phenotypes ensuring that a fraction of the population can survive in the face of sudden environmental change.

In this thesis, we use a range of theoretical approaches to investigate whether cancer cells may adopt a risk-spreading strategy in order to cope with changing nutrient levels caused by temporally-varying blood flow. We further aim to investigate the environmental conditions that lead to increased heterogeneity within the cancer cells – one of the reasons that make tumours so difficult to treat [6] – and identify potential therapeutic strategies.

In this chapter, we place our work in context by reviewing the relevant literature. In Section 1.2 we describe the mechanisms of vascular network formation and define the key characteristics of tumour vasculature. We then draw an analogy between tumours and ecological systems and provide a summary of adaptive strategies that are defined in the ecological literature (Section 1.3). Since vessels deliver key nutrients for cells, any change in the blood flow inevitably affects nutrient concentration in the tissue. Therefore, in Section 1.4 we outline the biology of tumour metabolism as well as highlight some of the adaptive responses that cancer cells might utilise when dealing with decreased levels of oxygen. Additionally, we review the mathematical models of metabolism and explain why a more simplified approach might be more suitable as a first step towards a theoretical understanding of evolutionary dynamics in temporally varying environments that arise from irregular blood flow in tumours.

Finally, in Section 1.5, we review mathematical models that investigate inter-species competition in fluctuating environments. We start by looking at consumer-resource models formulated as systems of ordinary differential equations (ODEs), where populations with distinct phenotypes compete for limited resources. Since in real-world situations there is a spectrum of possible phenotypes and a continuous range of environmental conditions, phenotype-structured models formulated in terms of partial differential equations (PDEs) might provide a more suitable framework to study adaptive strategies in tumours. Although such models might capture a more realistic behaviour, they have a nonlocal term and, therefore, are more difficult to analyse. Thus, we review existing PDE models of adaptive dynamics and their discrete analogues, as well as their applications.

We conclude this chapter with an overview of the thesis structure together with a summary of each chapter.

1.2 Tumour vasculature

1.2.1 Angiogenesis

Cancer cells, like other living tissue, rely on oxygen and other nutrients and growth factors in order to maintain their function and grow. The vasculature is the main source of nutrients and it also acts as a sink that removes metabolites, such as lactic acid, produced by cells. Therefore, after reaching a certain size of a few millimetres, tumours must induce angiogenesis – the formation of new blood vessels from existing ones.

There are several mechanisms that govern the formation of new blood vessels observed in mammals during, and post, development. During embryonic development, the initial primitive vascular network is formed via a process known as vasculogenesis. Here, the blood vessels are formed from angioblasts – endothelial-cell precursors – that form a primary network. The network then expands via sprouting (angiogenesis) or intussusception, i.e. transluminal pillar formation [8, 9]. In healthy physiological conditions, newly formed vessels steadily become mature and remain quiescent [10].

The process of angiogenesis relies crucially on the balance between pro- and anti-angiogenic molecules that are produced by cells, as well as connective tissue, i.e. stroma. This balance might be affected by various factors, including metabolic stress (low oxygen levels, high acidity, hypoglycaemia), mechanical stress (pressure exerted by newly differentiated cells), and immune-inflammatory responses [11]. This leads to over-production of pro-angiogenic factors and consequent 'angiogenic switch', triggering formation of new blood vessels via a multi-step process.

Initially, the endothelial junctions in the normally quiescent vessel wall become loose and vascular permeability increases as a response to vascular endothelial growth factors (VEGF) released by cells. This leads to extravasation of plasma proteins and degradation of vascular basement membrane and extracellular matrix, generating a path that enables endothelial cells to migrate into the perivascular tissue. A complex mechanism governs the formation of the 'stalk' that is 'led' by a tip cell sensing the environment and guiding the growth of the cells that will eventually form a new blood vessel. Once this is completed, a lumen forms and the blood is able to flow [12].

1.2.2 Key features of tumour vasculature

Although vasculature formation in tumours relies on similar biological mechanisms as in healthy conditions, the vessels are structurally abnormal, do not mature and continue growing [10]. In particular, the vessel walls may consist partially or entirely of cancer cells, rather than endothelial cells [13]. Blood vessels in tumours may also lack perivascular

cells, which have a protective function and help to maintain quiescence during unexpected changes in oxygenation levels [12]. Furthermore, vessel walls in tumour are characterised by frequent discontinuities and gaps between endothelial cells. This facilitates blood leakages into perivascular tissue, as well as increasing permeability of vessel walls [14].

Unlike healthy organisms where the cells cooperate in order to maintain the function of the whole organ, a cancer cell tends to improve its own immediate environment [7]. Having every cancer cell competing with each other leads to the expression of signals triggering angiogenesis (e.g. VEGF) to vary temporally and spatially in tumours. Thus, on a larger scale the networks of vessels in tumours vary significantly from those observed in healthy tissue (Figure 1.1), as well as between different cancer types, host organs and cancer cell lines [10, 15].

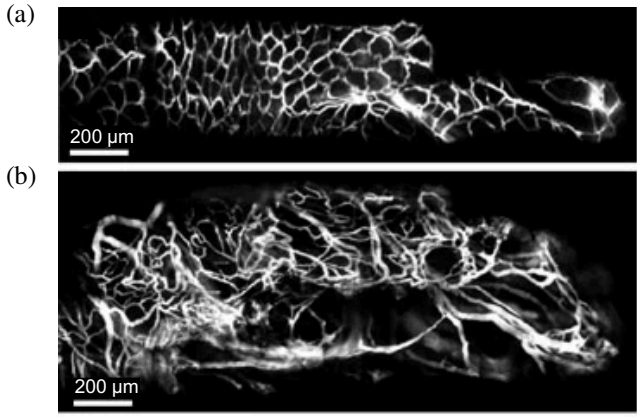

Figure 1.1: Fluorescence imaging of normal **(a)** and tumour **(b)** colon tissue in floxed *Apc* mouse. Reprinted with permission from [16].

Healthy vasculatures demonstrate an orderly branching hierarchy – smaller vessels stem from larger ones and result in a capillary network that ensures homogeneous delivery of nutrients to all regions. Tumour vasculature, on the other hand, does not have an organised structure. Excessive branching and spatial heterogeneity lead to formation of regions with higher vascular density as well as avascular regions. For instance, the outer regions of tumours become more vascularised due to proximity to the existing vessels in the host organ, whereas central regions of the tumours may become avascular [14].

Increased geometric complexity coupled with the abnormal shape of the vessels (varying vessel diameter, bulges, blind ends) affects the blood flow within tumours [16]. On average, the velocities of red blood cells in tumours are much lower compared to healthy tissue and overall perfusion is decreased. The blood flow in solid tumours might undergo stochastic changes in blood flow directions [17]. Moreover, it has been shown that rapidly

proliferating tumour and stromal cells can compress the blood vessel, leading to vessel collapse [18]. Environmental changes, such as development of hypoxia (low oxygen levels) and increased acidity, provide feedback on blood flow and stimulate continuous remodelling of the vasculature [14]. Therefore, such sudden variations in the blood flow, which encompass leakages, flow reversals and occlusions, combined with uneven spatial distribution of vessels, drastically affect the delivery of nutrients, anti-cancer drugs and removal of metabolites.

1.2.3 Spatio-temporal variations in tumour microenvironment

The consequences of spatial and temporal irregularity of the vasculature in tumours have been widely observed and recognised. Since the primary function of blood vessels is the delivery of nutrients, it is possible to assess the dynamics of the flow in tissue by looking at the concentration of molecules, in particular, oxygen. In the tissue, the distribution of oxygen is governed by diffusion and consumption by cells with rates that vary between different cell types and environmental conditions [19]. Low oxygen levels (hypoxia) that arise from the abnormal vasculature are a common feature of all solid tumours, and correlate with poor prognosis, therapy resistance and promote metastasis formation [20].

The diffusion limit of oxygen is around 150–200 micrometers, therefore, cells located beyond that limit experience chronic hypoxia, i.e. constant low levels of oxygen where partial pressure of O_2 is less than 10 mm Hg. Cells existing in hypoxic regions must adapt or they may eventually become necrotic. Such necrotic regions, first observed in lung cancer by Thomlinson and Gray in 1955 [21], impact tumour progression, are associated with poor prognosis and promote resistance to radiotherapy. Cycling, or intermittent, hypoxia is a dynamic type of hypoxia observed to be present in tumours. Here, tumour cells experience cycles of hypoxia followed by re-oxygenation. Cycling hypoxia is classified into two types based on the time scales on which fluctuations occur [22].

Fast fluctuations in oxygen levels occur on timescales ranging from minutes to hours [22, 23], and are associated with instability of red blood cell flux in tumour blood flow caused by irregular tumour vasculature [24]. Such fluctuations were first observed indirectly in mouse tumours by evaluating the fraction of hypoxic cells following radiotherapy [22]. Fast cycling hypoxia was then studied using various techniques – the link between oxygen level oscillations and variations in the red blood cell flux has been made using laser Doppler measurements in both mouse [25] and human tumours [26], as well as by looking directly at the blood vessels and counting labelled red cells passing through over a certain period of time [24, 27]. Finally, non-invasive imaging methods, such as magnetic resonance imaging [28, 29] and optoacoustic tomography [30], are now increasingly used to monitor rapid changes in oxygenation levels. For example, Figure 1.2(a) shows oxygen concentrations in squamous

cell carcinoma xenografts as time progresses [31]. Electron paramagnetic resonance images, taken every 3 minutes, allowed the authors to distinguish between chronic and intermittent hypoxia in different regions of tumour, and to correlate the regions with temporal variations with decreased level of vessel maturation.

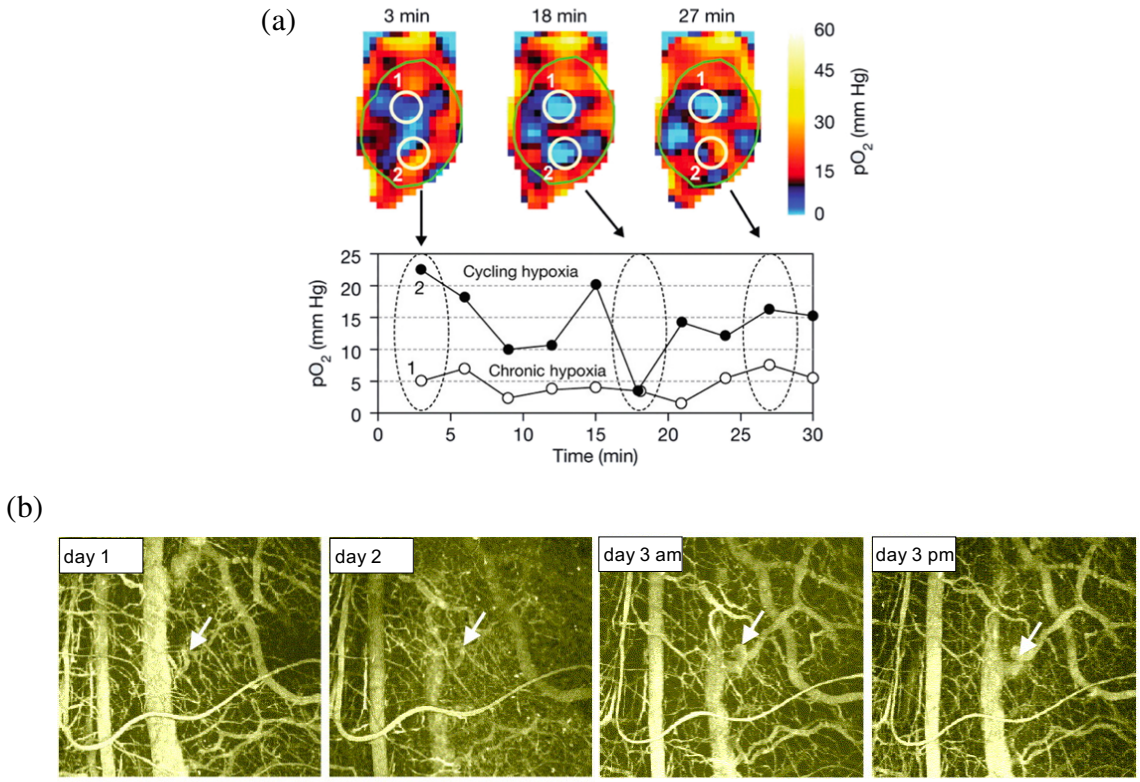

Figure 1.2: **(a)** Top: electron paramagnetic resonance image of a murine SCCVII tumour xenograft with regions of normoxia and hypoxia or anoxia. Bottom: measurements of oxygen level (pO_2) in regions with chronic hypoxia and cycling hypoxia over time. Reprinted with permission from [32]. **(b)** Multi-photon fluorescence imaging of the P22 rat tumour vasculature over 3 days demonstrating vascular remodelling in real time as indicated by arrow. Reprinted with permission from [33].

Fluctuations in oxygen level are also observed on much slower timescales (several days or even weeks). Using intravital microscopy of *in vivo* tumours that grow in window chambers, Tozer et al. [33] were able to track on-going vascular remodelling in real time, as shown in Figure 1.2(b). The authors established the link between slow fluctuations, angiogenesis and vascular remodelling. Fast and slow fluctuations may occur simultaneously in solid tumours and, as a result, yield very complex dynamics of cycling hypoxia [34].

1.2.4 Consequences of intermittent hypoxia

Environmental heterogeneity, both spatial and temporal, imposes different selection pressures and, as a result, will form environmental niches where cells with specific characteristics, i.e. phenotypes, are selected. In order to survive, cells can adapt and even switch their phenotypes [35], altering their motility, proliferation, and resistance to therapy. This complex microenvironmental and evolutionary dynamics results in very heterogeneous tumours [36].

The consequences of chronic hypoxia have been extensively studied, both theoretically and experimentally [37]. Cyclic, or intermittent, hypoxia, however, has only recently gained attention in the scientific community. More and more *in vitro* and *in vivo* studies are becoming available, focussing on the effects that periods of hypoxia and re-oxygenation might impose on different cancer cell lines, including brain, blood and breast cancers. However, it is difficult to consistently compare the experimental data since scientists use different timescales of fluctuations – periods of hypoxia and re-oxygenation may vary from 10 minutes to 7 days – as well as assign different concentrations of oxygen to their definitions of hypoxia and normoxia (reviewed in [1]). Both these factors, i.e. duration and amplitude of fluctuations in oxygen concentration, are known to influence the response of cells.

Experimental studies suggest that chronic and intermittent hypoxia induce different effects on cancer cells [38]. The exact consequences of such dynamics are not well understood, but experimental observations qualitatively suggest that cycling hypoxia promotes angiogenesis [39], selection of stem-like phenotypes [40, 41], inflammation [42, 43], drug resistance [44], migratory abilities and, overall, selects more aggressive pro-metastatic cancer subpopulations [45, 38, 46, 47]. For instance, Louie et al. [40] demonstrated selection of a stem-like subpopulation that was expanded via cycles of hypoxia followed by normoxia. In particular, they maintained a breast cancer cell line repeatedly under hypoxia for 7 days, followed by 2–3 weeks in an oxygenated environment. After the first period of hypoxia they observed a small surviving subpopulation, which demonstrated higher tumorigenicity and enhanced invasiveness. Later, Chen et al. [47] performed a set of experiments where the cancer cells where first grown for 9 days *in vitro* under conditions of cycling hypoxia (24h of hypoxia followed by 24h of normoxia) and were then implanted in mice. The authors observed increased metastasis formation when cells were treated to cycling hypoxia compared to the cells grown in chronic hypoxic or normoxic conditions. Moreover, by analysing cells grown *in vitro*, a higher degree of clonal diversity and phenotypic heterogeneity was observed during intermittent hypoxia.

Despite the progress made by experimental scientists, the consequences of temporal variations in tumour microenvironment remain not fully understood. In particular, various fluctuation timescales and amplitudes might affect cancer cells in certain ways and require

different adaptation strategies [7]. Thus, a more thorough understanding of the consequences of temporal fluctuations in the tumour microenvironment is necessary to underpin the evolutionary dynamics of tumours, shedding light on potential therapeutic strategies that might be employed to minimise the selection of phenotypic heterogeneity and aggressive phenotypes. For example, the concept of vascular normalisation has been proposed to stabilise the cancer environment and could serve as a potential strategy in cancer treatment [48].

1.3 Insights from ecology

1.3.1 Viewing solid tumour as an ecosystem

In 1976, Nowell proposed to view tumours from an eco-evolutionary perspective, arguing that the selection of increasingly abnormal clones is driven by tumour microenvironmental conditions [49]. Therefore, even genetically distinct cancer cells from different tumours are able to express similarities, especially at the latest stages of the disease, i.e. so-called 'lethal' phenotype [50, 51]. In 2000, Hanahan and Weinberg [52] identified six capabilities, now widely known as 'Hallmarks of cancer', which cancer cells must acquire during tumorigenesis in order to enable further colonisation in distant organs, i.e. metastasis. These include sustaining proliferative signalling, evading growth suppressors, resisting cell death, enabling replicative immortality, inducing angiogenesis, and becoming invasive. This concept was extended in 2011 to include two more emerging hallmarks – reprogramming of energy metabolism and evasion of immune destruction [53]. Furthermore, the crucial role of constantly changing tumour microenvironment in the acquisition of these hallmarks and its impact on tumour progression and evolution have been noted.

In nature, ecosystems are composed of living systems, such as animals, fungi, plants, and environmental factors, such as nutrients, soil, climate. These two compartments have a complex underlying network of interactions with different feedbacks. Similarly, solid tumours can be divided into two compartments – the first consisting of cancer, stromal and normal cell populations, and the second representing the tumour microenvironment, including blood flow, pH, oxygen and other molecules [54]. It has been observed, both in patients [55] and *in vivo* [56], that tumours are composed of at least two subpopulations that coexist and have distinct phenotypic properties. For instance, cells at the tumour periphery are characterised by higher proliferation rates, increased motility and acid-producing aerobic glycolysis, whereas at the tumour core cells remain non-motile and have smaller division rates [57, 58, 56]. Such spatial distribution of phenotypes is analogous to that observed in biological invasions of species, for example, during the cane toad invasion in Australia [59].

Alfarouk et al. proposed a similarity between cancer cells surrounding a vessel and a riparian habitat, i.e. zones of vegetation surrounding a river in the desert (Figure 1.3(a)) [60]. In riparian zones, thick vegetation is located along the rivers. However, after a few metres, the vegetation becomes more sparse, consisting mainly of grasses and shrubs. Similarly, cancer cells near and further away from the vessel should have distinct phenotypic properties linked to nutrient availability. In particular, riparian zones are densely populated with highly competitive cells that are adapted to specialised environments and rely on high oxygen concentrations. Cells located further away (xeric), in turn, are comprised of small, phenotypically flexible sub-populations adapted to harsh environments, i.e. hypoxia. Xeric cells are assumed to be less vulnerable to environmental perturbations compared to the riparian cells, and are associated with more therapy-resistant phenotypes. Therefore, we expect to observe different spatially-distributed environmental niches within a solid tumour occupied with phenotypes that are adapted to these particular conditions.

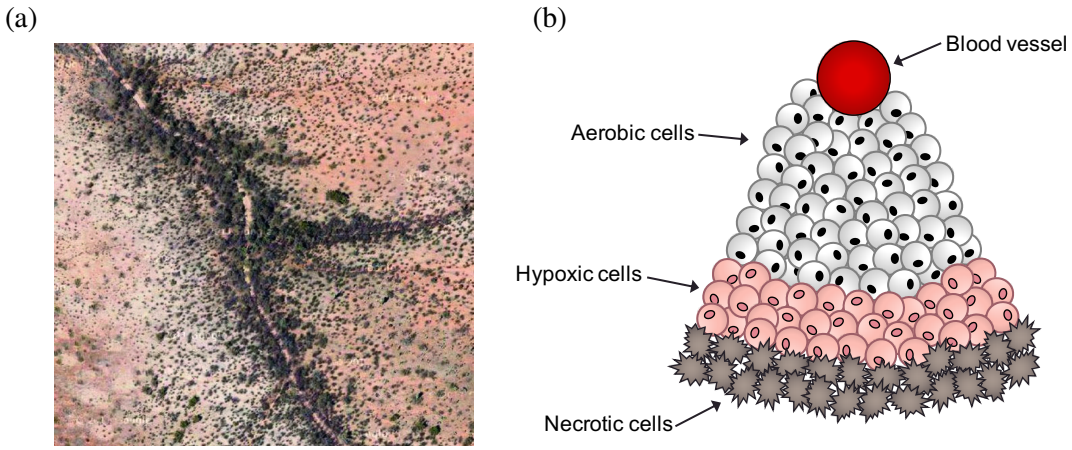

Figure 1.3: **(a)** Riparian habitat in the Sonoran Desert of Arizona. (Reprinted with permission from [60]). **(b)** Schematic representation of cells near the blood vessel. Cells closest to the vessel are adapted to high oxygen conditions, whereas cells located further away are adapted to low oxygen levels, or even undergo necrosis.

The analogy with riparian ecosystems provides an insightful and illustrative picture of the emergence of phenotypic heterogeneity when the blood flow in a vessel is steady. However, as noted in Section 1.2, the blood flow, and subsequent nutrient delivery to tumour cells, is very irregular and prone to temporal fluctuations on a variety of time scales. In particular, cells that are located closest to the periodically occluded vessel will likely experience high amplitude fluctuations, whereas cells located further away will have harsh, but relatively stable, conditions at all times. The consequences of this are unknown and will probably select populations with different adaptive strategies.

1.3.2 The concept of fitness

The reproductive success of an individual in ecology is commonly defined as fitness, and essentially represents the net growth rate in a given environment [61]. Fitness is defined by the genotype of an individual, as well as its phenotype. Genetically identical populations might consist of subpopulations with distinct phenotypes. For example, cells in the human body have the same genetic information, but distinct types (nerve, blood, stem, etc.) and carry out different functions. Similarly, cancer cells demonstrate variation in such characteristics as motility, metabolism, and proliferation rate. Hence, these subpopulations might have different values of fitness in a specific environment.

The relationship between fitness and phenotype can be visualised via fitness curves (Figure 1.4) [62]. Here, the fitness is plotted against the range of phenotypic states and the state with the highest fitness value corresponds to the fittest phenotypic state. In reality, fitness is determined by multiple traits, which then form a so-called adaptive landscape [63]. Such fitness curves and landscapes can be inferred from *in vitro* data by measuring the growth rates of subpopulations of interest in controlled environments. However, measuring fitness from *in vivo* experiments remains extremely difficult.

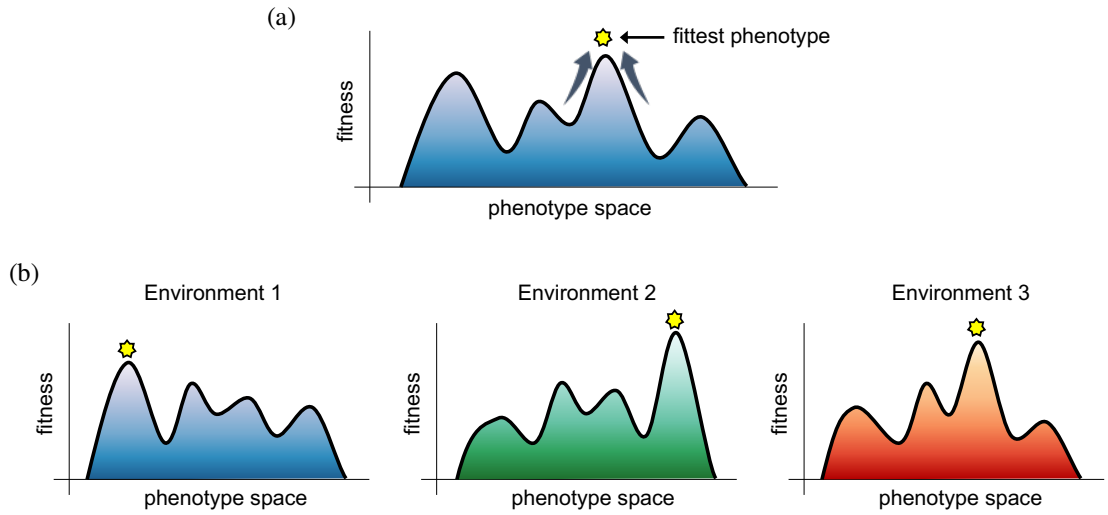

Figure 1.4: **(a)** Schematic representation of fitness curve for a given environment, where fitness values are plotted against phenotype space. The yellow star represents the phenotypic state with highest fitness value. In constant conditions, the fittest phenotype will be selected. **(b)** Schematic representation of fitness curves for different environmental regimes. Here, the fittest phenotype is different for each environment.

In constant environment, the population with the fittest phenotypic state will be selected, i.e. the specialist adapted to this particular condition will survive (Figure 1.4(a)). Here, the mean fitness of the population will tend to the fittest state and the variance

will be minimal. However, it is highly unlikely that in the event of sudden environmental change this phenotypic state will remain fit. Instead, we expect the fitness curve to vary as the environment changes (Figure 1.4(b)) [63]. In other words, each environment will have its own distinct fittest phenotypic state. To deal with such variations, populations deploy adaptive strategies.

1.3.3 Adaptation strategies in dynamic environments

In nature, living species, ranging from bacteria to animals, exist in environmental conditions that exhibit both spatial and temporal heterogeneity. For instance, individuals are faced with periodic fluctuations, such as change of seasons, as well as unpredictable random effects, such as droughts and hurricanes. Individuals undergoing invasion and colonisation are also prone to sudden environmental changes [64]. Such variability requires species to adapt, and this process has received great attention over the last century.

Small organisms with short life spans, such as microbes, provide a useful platform to study adaptation strategies experimentally. Here, scientists can control the environment and measure reproductive success – the fitness. Mathematical models have also provided invaluable insights into the evolution and selection of different adaptive strategies. Based on combined experimental and theoretical knowledge in the ecological literature, two main adaptive strategies have been distinguished that help to understand temporal variations in the environment [65].

1.3.3.1 Phenotypic plasticity

The first strategy is to develop phenotypic plasticity; an individual adjusts its phenotype according to the cues that it senses from the environment [66]. Phenotypic plasticity allows an individual to achieve a greater match between its phenotype and the environmental state. In an ideal scenario, populations would tend to have infinite plasticity but, due to associated costs and limitations, this is not possible [67]. The limitations include lag-time between environmental sensing and response initiation, reliability of sensed cues, as well as costs associated with sensing machinery maintenance and production. Therefore, according to theoretical studies, such a strategy is more suitable for predictable environmental fluctuations where individuals have enough time to respond and the cues are reliable [68]. For instance, by adding significant levels of environmental stochasticity, Ashander et al. theoretically showed that such noise might reduce the ability of phenotypic plasticity to support evolutionary rescue when the conditions are unpredictable [69].

Phenotypic plasticity is not an intrinsic property, rather it can evolve reversibly and irreversibly. Lande, using a quantitative genetic model of plasticity, showed that when a

population is placed in a new environment, its plasticity rapidly increases, allowing the mean phenotype of the population to approach new optimum more efficiently. Afterwards, however, a slow reduction in plasticity is observed if no other environmental fluctuations are present [64]. Moreover, evolution of plasticity is promoted by extreme changes in the environment [70]. Thus, phenotypic plasticity is often suggested to be a characteristic feature of colonising populations [71].

There are examples of phenotypic plasticity in nature. For instance, water fleas (*Daphnia*) are able to grow helmets and spikes when the concentration of kairomones – a sign of a predator – increases [66]. Another common example is the coat of mammals, which changes from season to season in order to promote their camouflage abilities [72]. Phenotypic plasticity has also been observed in cancer. A classic example of plasticity is epithelial-to-mesenchymal transition – a process during which cancer cells acquire the properties of stem cells. As a result, differentiated cells with epithelial phenotype become motile and express markers corresponding to a mesenchymal phenotype [73]. Melanoma cells have been observed to switch between an invasive, slow-proliferating phenotype to a non-motile, fast-proliferating phenotype in response to microenvironmental changes, such as hypoxia and nutrient deprivation [74, 75]. Such plasticity and emergent heterogeneity have been shown to compromise response to therapies, i.e. lead to drug resistance [76].

1.3.3.2 Bet-hedging

An alternative strategy that is more suitable for dealing with irregular and unpredictable changes in the environment is bet-hedging [77, 78, 79], where an individual lowers its variance in fitness at the cost of lower arithmetic mean fitness [80]. Bet-hedging can further be classified into two distinct subtypes [81]. Conservative bet-hedging represents a risk-avoidance strategy where the population acquires a single phenotype that 'always plays it safe' [78, 79]. For instance, egg size variation in fishes reflects such an adaptive strategy. Here, fish produce smaller number of larger eggs, which provide an advantage in poor environmental conditions while remaining unfavourable in good times [70]. On the other hand, diversified bet-hedging represents a risk-spreading strategy, where individuals invest in a variety of strategies. Here, offspring have different phenotypes, each adapted to a specific environment. Therefore, in case of sudden environmental change, at least a fraction of the population will survive and will be able to restore the population [80]. For example, the fairy shrimp, that lives in pools of rainwater, produces eggs that hatch at different times. Eggs that take longer to hatch can wait through the extended dry weather and hatch when the pool reappears [82]. Moreover, bet-hedging can be merged with environmental tracking. In this case, the distribution of phenotypes depends on the cues sensed from the

environment [72]. Even though bet-hedging and phenotypic plasticity are viewed as distinct strategies suitable for specific environmental regimes (predictable vs unpredictable), Xue and Leibler, using a mathematical model of plastic development, demonstrated similarities between environmental bet-hedging and plasticity [66].

Theoretical and mathematical studies have facilitated further exploration of various scenarios where bet-hedging might be beneficial. For instance, a lot of effort has gone into elucidating the role of stochastic phenotype switching when dealing with random environmental fluctuations [83, 84, 85, 86, 87, 88]. Müller et al. investigated the environmental conditions that would lead to the emergence of bet-hedging [89]. In their model, four populations with different adaptation strategies evolved together in an environment that stochastically changed between two discrete states. The authors found that the frequency of stochastic fluctuations affects the success of a particular adaptation strategy. For instance, a rapidly fluctuating environment selects the phenotype adapted to averaged conditions, whereas in a slowly fluctuating environment, having two distinct specialists would be beneficial. The bet-hedger population, which undergoes stochastic phenotypic variations, was shown to be most successful in an intermediately varying environment, noting the importance of timescales when considering adaptation strategies. Moreover, Salathé et al. demonstrated that the success of bet-hedging crucially depends on the symmetry of the fitness landscape, i.e. the fitness cost of maladapted phenotype for a given environment should not be too high [90]. Finally, Martin et al. demonstrated that phenotypic heterogeneity, caused by risk-spreading, might help the expanding populations to deal with environments that vary slowly in both space and time [91].

Bet-hedging is typically proposed to occur within the context of bacterial populations, where experimental [65, 92, 93, 94, 95] and theoretical support [96, 97] for stochastic phenotype switching is available. The classic example of bet-hedging is bacterial persistence. During antibiotic treatment a small fraction of slowly growing bacteria, that are resistant to the antibiotic, is able to survive. After treatment, the original population is restored, resulting in resistance to the antibiotic [98]. Schreiber et al. showed that fluctuations in nutrient levels alter the metabolism of bacteria and promote phenotypic heterogeneity, consistent with the risk-spreading strategy [99]. However, the underlying causes of bet-hedging are not fully understood, and may arise from intrinsic noise of intracellular molecular pathways [100]. Risk spreading strategies have been observed in other organisms, such as fungi and slime moulds [65], and similar phenomena are observed in cancer. In particular, a small drug-resistant population of cells that was able to restore the population after treatment has been identified [101, 102].

Overall, the success of both classes of adaptive strategy depends on costs and they have different advantages in various environmental regimes. Both strategies are hypothesised to be present in tumours. In particular, bet-hedging is thought to be a strategy used by cancer cells in order to deal with fluctuations in their microenvironment arising from irregular vasculature [82, 7]. However, these phenomena in tumours have been studied minimally and, due to being associated with drug resistance and poor prognosis in other systems (bacteria), warrant further theoretical and experimental exploration.

1.4 Tumour metabolism

The examples presented in Section 1.2 illustrate some of the empirical evidence suggesting that temporal variations in the tumour microenvironment caused by blood flow are common events. The insights from ecology, summarised in Section 1.3, suggest that cancer cells might employ different adaptation strategies in order to deal with spatio-temporal variations in nutrient availability caused by irregular vasculature. Therefore, it is important to consider tumour cell metabolism when trying to understand the consequences of such variability.

Metabolism is a fundamental process, in which the cell converts nutrients into the energy that is required to maintain basic functions and for proliferation. Cellular metabolism is extremely complex with hundreds of proteins involved, is maintained through many different pathways, and adaptable depending on microenvironmental conditions and cues. It is well established that cancer metabolism is very different from healthy metabolism, and this shift is associated with cancer progression [103].

1.4.1 Oxidative phosphorylation and glycolysis

There are several mechanisms that convert extracellular nutrients into energy to maintain cellular functions, however, the two primary nutrients are oxygen and glucose. Cells convert these nutrients into adenosine triphosphate (ATP), the so-called 'energy' molecule [104]. The two main pathways that convert glucose into energy – the glycolytic pathway and aerobic respiration – are summarised in Figure 1.5.

Glycolysis is a series of 10 reactions that leads to the conversion of glucose into pyruvate and generates two molecules of ATP and a proton. Once glycolysis is complete, there are two options that depend on the concentration of oxygen. In the absence of oxygen, then pyruvate is metabolised into lactate. On the other hand, if oxygen is abundant, pyruvate is transported to the mitochondria and undergoes oxidative phosphorylation (OXPHOS). Here, pyruvate, together with oxygen, is converted into CO_2, H_2O and ATP molecules. The maximal net production of ATP via OXPHOS is 36 molecules per one glucose and five oxygen molecules [105], whereas glycolysis yields only two molecules of ATP.

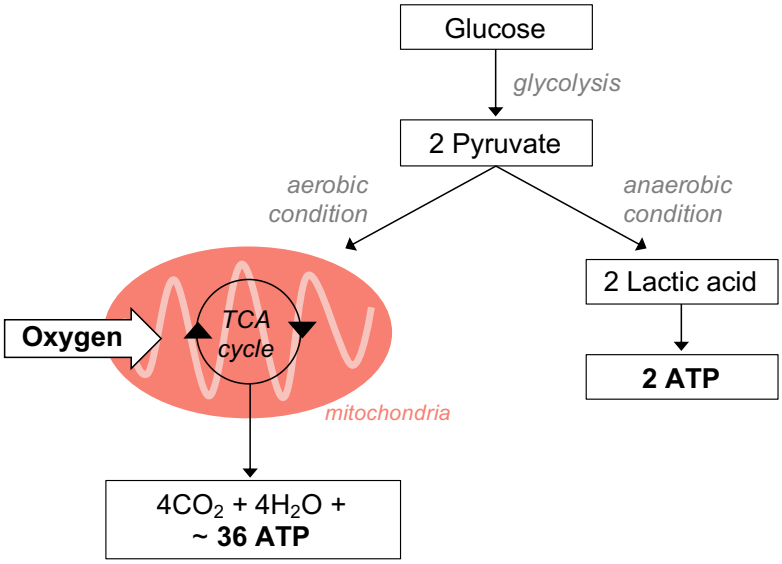

Figure 1.5: Schematic representation of pathways that convert glucose into adenosine triphosphate – oxidative phosphorylation on the left and glycolysis on the right.

In normal physiological conditions, i.e. when both oxygen and glucose are abundant, non-proliferating cells use glycolysis to obtain pyruvate, which is then converted into ATP via the aerobic pathway. This route is the most efficient way of generating energy, however, it is relatively slow [106]. When oxygen is scarce or cells require extra energy, e.g. during division, the cells can up-regulate glycolysis – a less efficient but faster process of energy generation. This is known as the Pasteur effect [107]. Elevated glycolysis leads to increased production of lactic acid, which cells then pump into extracellular space. Hence, prolonged periods of hypoxia lead to decreased levels of pH, which is toxic to normal cells. If glucose is also unavailable, the cells might switch to another food source, for example, glutamine or fatty acids, or become quiescent [58].

Cancer cells, on the other hand, have been observed to rely mostly on glycolysis, even in the presence of oxygen. This was noted by Otto Warburg about 100 years ago, and is known as the Warburg effect [108]. The Warburg effect is now commonly observed using positron emission tomography-based imaging of the uptake of ^{18}F-fluorodeoxyglucose [109]. Cancer cells have been shown to produce over 50% of ATP from glucose and higher levels of glycolysis have been linked to poorer prognosis [103]. Moreover, imaging glycolysis is used in the clinic for tumour diagnosis and treatment monitoring.

The reasons behind the preference for anaerobic glycolysis in cancer cells are not fully elucidated yet, but several hypotheses exist trying to explain the benefits of utilising this less efficient, and eventually toxic, metabolic pathway. In particular, decreased mitochondrial function is linked with reduced production of reactive oxygen species (ROS), which

can be toxic to cells, and increased production of anabolic substrates, i.e. building blocks of proliferating cells [104]. Epstein et. al suggested that OXPHOS and glycolysis provide energy for different types of energy demands [106]. In particular, they suggest that aerobic metabolism provides energy for baseline energy demand, whereas glycolytic metabolism is used to meet short-timescale energy requirements. In particular, the authors hypothesise that the Warburg effect is a response to the increased energy demand for membrane transport activity required for elevated cell division, growth and migration. Moreover, the use of glycolysis results in the development of a highly acidic environment, which is associated with some highly invasive tumours [110, 57]. Finally, recent theoretical studies have suggested that the Warburg effect can be linked to temporal fluctuations in the tumour microenvironment and acts as an adaptive strategy [111, 82].

1.4.2 Cellular adaptations to hypoxia

Since oxygen is one of the main nutrients for any living cell, hypoxia triggers a set of responses that help cells deal with the absence of crucial nutrients, both chronic and transient. In return, cells switch from aerobic respiration to glycolysis during hypoxia. Here, we will highlight three main adaptive mechanisms that cancer cells can utilise in order to deal with hypoxia. These processes occur on different timescales, and we will compare them to the typical lifespan of a cancer cell.

One of the main cellular responses to hypoxia is expression of genes. For instance, up-regulation of hypoxia-inducible factors (HIF) triggers a cascade of molecular reactions that allow cancer cells to survive low oxygen levels. Activation of HIF-1 has two main implications. First, it promotes glycolysis by activating genes responsible for extracellular glucose transport, such as glucose transporters (GLUT), as well as enzymes that promote breakdown of glucose inside the cell. Secondly, HIF-1 inhibits oxidative phosphorylation at the mitochondria. Therefore, the net result is a switch from OXPHOS to glycolysis for energy generation [104], which can be observed experimentally using tumour-on-chip microfluidic devices [112].

Expression of genes, such as HIF-1 and GLUT, is a relatively fast process and occurs on timescales much shorter than the average lifespan of a tumour cell [113]. Furthermore, experimental studies show that the responses of HIF-1 in chronic and cycling hypoxia are different. When cells are exposed to hypoxia, the level of HIF-1 rises quickly and becomes stabilised within hours. After a few days it decreases to a lower level. In cyclic hypoxia, however, the response of HIF-1 is enhanced and stabilisation of HIF-1 occurs at much greater levels [114].

Another way for cells to respond to environmental stress is to undergo epigenetic modifications. Epigenetic response can be transient (e.g. histone acetylation), designed to deal with acute stress, or heritable, such as DNA methylation. Such epigenetic modifications are initiated by sensing the extracellular environment and altering cellular metabolism. For instance, oxygen deprivation induces stabilisation of HIF1 and enhanced glycolysis. Glycolysis, in turn, increases the acidity of the tumour microenvironment and leads to further epigenome alterations [115]. Heritable epigenetic variations occur on timescales that are slower, compared to the expression of genes. The timescale of this process is comparable to the lifespan of a tumour cell.

Finally, cells can acquire genetic mutations that occur on very long timescales [116], and lead to permanent change in the genome and, hence, cell behaviour. These different adaptation strategies that occur on three distinguishable timescales might be useful for cancer cells when dealing with fluctuations in the tumour microenvironment that occur at different frequencies.

1.4.3 Mathematical models of cancer cell metabolism

So far, we have highlighted two molecular pathways through which cells obtain energy. In particular, we considered oxygen and glucose as the main nutrients, however, cells can utilise other molecules, such as glutamine, in order to generate energy and produce building blocks required for the formation of new cells. In other words, this brief introduction to metabolism covers only a small fraction of all processes that constitute cellular metabolism. In reality, the full picture comprises very complex networks of interactions and feedbacks, which are usually elucidated using *in vitro* and *in vivo* studies.

Experimental studies alone, however, are a quite expensive and time consuming way to investigate the underlying mechanisms of metabolism and their impact on disease development and progression. Mathematical models, on the other hand, provide a flexible tool to investigate different hypotheses and scenarios that might not be possible yet to test experimentally. Over the last decades, mathematical modelling has provided a deeper mechanistic understanding of cancer dynamics, as well as contributed to the development of novel therapeutic strategies [117, 118]. Crucially, the success of mathematical modelling in cancer research relies on an interdisciplinary collaboration between biologists, clinicians and mathematicians, as well as a thorough understanding of the underlying biological processes.

Below, we review existing mathematical models of tumour growth and metabolism. These approaches are very diverse, ranging from well-mixed to spatial, from models formulated in terms of ordinary differential equations to those couched in the framework of hybrid cellular-automata. Moreover, each model is tailored to a specific problem, starting

from avascular tumour growth [119, 120, 121, 122] towards models that incorporate vasculature and angiogenesis [123, 124, 125], and beyond. Since we are interested in blood vessels being the main source of microenvironmental fluctuations, this overview focuses on the models that integrate tumour metabolism and vasculature in some form.

Continuum models. Mathematical models of tumour metabolism were originally framed in terms of deterministic partial differential equations that look at nutrient transport in space. Such models usually consist of several compartments that represent populations of cells and diffusible molecules, i.e. nutrients, which are supplied by the blood vessels. Cells can comprise one population, or be subdivided into several subpopulations with different metabolic phenotypes, e.g. Warburg vs Pasteur. These compartments are linked via nonlinear processes representing metabolic interactions, such as nutrient consumption, which is often modelled via Michaelis-Menten form. Such PDE models can be solved numerically and sometimes are mathematically tractable.

The classic Krogh cylinder model provides the basic framework for studying nutrient gradients along a single vessel [126]. It was originally used to analyse oxygen transport into tissue from capillaries. In this model, oxygen diffuses from the vessel into a surrounding finite cylindrical tissue region. At the outer boundary of the cylinder, a zero flux boundary condition is applied, assuming that this tissue cylinder is surrounded by an array of equivalent cylinders and, since they are identical, there is no exchange of oxygen across the domain boundary.

The Krogh cylinder model was later extended to study the cylindrical perivascular tissue that surrounds the blood vessel in tumours – a tumour cord [127, 128]. Such structures have been observed in the clinic, with a mean cord radius of around 100 μm [129], and are usually surrounded by regions of necrosis. In the model developed by Bertuzzi and colleagues, the population of cells is assumed to be a continuous medium structured by age, which represents the proliferative potential of each cell [127]. Cells can move within the cord, and their proliferative status depends on the oxygen level, which is modelled by a reaction-diffusion equation. Oxygen is supplied by the blood vessel, diffuses through tissue and is consumed by cells, which is modelled via a saturating term. For simplicity, the authors did not include cellular death, such as apoptosis (natural cell death) and necrosis (hypoxia-induced cell death). In agreement with experimental data, the model predicts that cells located closest to the blood vessel are in a proliferative state and, thus, result in an increased density. Cells on the outer edge of the cylinder are, in turn, in a quiescent state due to decreased oxygen availability.

Astanin and Tosin extended the tumour cord model and incorporated the basics of tumour metabolism in it [130]. In this model, the proliferation of cells depends on the amount of energy available that is regulated by nutrients. For simplicity, the authors assume that the tumour cells are unable to switch to glycolysis and only aerobic respiration takes place. Hence, the production of ATP is proportional to the oxygen consumption rate and governs proliferation and death when the ATP concentration is excessive or insufficient, respectively. This model was later adapted to incorporate glucose dynamics to more accurately model the Warburg effect [131]. Here, the population of cancer cells was split into two subpopulations – aerobic (oxidative) and anaerobic (glycolytic). The aerobic cells could undergo a spontaneous irreversible metabolic switch and become glycolytic. The concentrations of oxygen and glucose were modelled via reaction-diffusion equations, where the consumption of both nutrients was determined by the metabolic phenotype of the cell. As a result, the authors observed that the glycolytic subpopulation out-competed the oxidative population and spread inhomogeneously within the entire tumour cord.

The assumption of irreversibility of switching between aerobic and the anaerobic phenotypes has been relaxed in other models. In particular, in [132] and [122], authors made an assumption that a cell can return to normal metabolism after hypoxia is over. Both sets of assumptions are motivated by experimental evidence, and they each may hold depending on cell line type and environmental conditions of the experiment.

Hybrid individual-based models. Recently, individual-based models, whereby cells are modelled as individual agents either on- or off-lattice, have gained increasing attention. Such models allow tracking the behaviour of individual cells, as well as their interactions with the microenvironment, which is modelled via reaction-diffusion partial differential equations (PDEs). Furthermore, such a modelling approach allows one to capture cellular heterogeneity – an important feature of tumours. In [133], Gerlee and Anderson modelled the emergence of the glycolytic phenotype which, as they found, was regulated by oxygen concentration and the extracellular matrix. In their model, oxygen and glucose were supplied from the nearby stationary vasculature, and the dynamics of pH and extracellular matrix were also incorporated. Cells in the model demonstrated different metabolic phenotypes, ranging from oxidative to glycolytic, and were able to change phenotype while undergoing mutations upon division.

Robertson-Tessi et al. further explored the impact of metabolic heterogeneity on tumour growth and therapy response and the emergence of a glycolytic, acid-resistant phenotype by incorporating vasculature and drift in phenotypic space [58]. Here, the authors model a 2D slice of tissue, composed of normal cells and blood vessels, which are modelled as point

sources of nutrients (oxygen, glucose) and sinks of lactic acid. Normal cells resemble the Pasteur phenotype, i.e. obtain most of their energy via OXPHOS, and a small fraction via glycolysis. Cancer cells, however, demonstrate increased glycolysis on top of the energy generated from the oxidative pathway. Therefore, the phenotype of tumour cells is characterised by two continuous traits – increased glycolysis and acid-resistance. In the model, cancer cells can drift in phenotypic space equally in both directions. This phenotypic change is random and occurs upon division. Furthermore, when hypoxia develops in a region of interest, new vessels are added to the grid, modelling angiogenesis. Similarly, vessels can degrade over time due to surrounding tumour growth. This model is quite complex and captures in detail different processes that occur in solid tumours, including metabolism and angiogenesis, and provides important insights on how to tackle phenotypic heterogeneity therapeutically.

Modelling temporal variations of nutrient supply. Even though the existing models provide some insight into the evolutionary processes in tumours, behind most of these models lies the assumption of a steady blood flow, which does not represent a biologically complete picture. Until now, very minimal effort has been made to theoretically study the effect of temporal variations in nutrient availability on cancer progression and evolution [7] with only a few studies available that tackle this problem. For example, Gravenmier et al. presented a discrete non-spatial model that addressed the emergence of the Warburg phenotype as a conservative bet-hedging strategy that evolves in response to stochastic fluctuations in oxygen concentration [82]. In this model, two subpopulations, Warburg and Pasteur-like, are considered, and glucose uptake by cells is governed by oxygen availability without explicitly modelling glucose concentration. Even though this model emphasises the role of fluctuations in oxygen concentration in the selection of a more aggressive, glycolytic phenotype, it omits several important features, such as feedback from acid production from the anaerobic pathway, spatial structure and the phenotypic heterogeneity of cancer cells. Thus, it is crucial to develop further mathematical models with the aim of exploring the role of potential adaptive strategies.

1.5 Mathematical models of competing populations in dynamic environments

Taking into account the very sparse experimental data and the lack of theoretical studies, it is crucial to develop a mathematical model that can account for the impact of variable nutrient availability on tumours. It will help us to understand the underlying biological processes, as well as identify more efficient treatment strategies. However, even though existing

mathematical models of tumour metabolism provide a good starting point, incorporation of dynamic changes in oxygen and other nutrients is a non-trivial task. This is due to the very complex non-linear dynamics of tumour metabolism, as well as the lack of systematic experimental evidence of cellular response to intermittent hypoxia. Therefore, in this thesis we propose to develop a set of mathematical models that aim at a more qualitative description of the emergent evolutionary dynamics in temporally fluctuating environments. In particular, instead of modelling cell metabolism explicitly, we adapt existing models of species competition from ecology and assign different phenotypic traits to the cancer cell populations via an environment-dependent fitness function.

1.5.1 Ordinary differential equation (ODE) models of species competition

The basic model of species competition is a predator-prey model, also known as the Lotka-Volterra model [134]. Equations (1.1) and (1.2) describe the competition between two species with population sizes $N_1(t)$ and $N_2(t)$, where t is time:

$$\frac{dN_1}{dt} = r_1 N_1 \left(1 - \frac{N_1 + c_{12}N_2}{K_1}\right) \tag{1.1}$$

$$\frac{dN_2}{dt} = r_2 N_2 \left(1 - \frac{N_2 + c_{21}N_1}{K_2}\right). \tag{1.2}$$

These two competitors are assumed to undergo logistic growth described by the growth rates r_1 and r_2, and carrying capacities K_1 and K_2; the positive coefficients c_{12} and c_{21} reflect the effect of competition, for example, for the available resource. In constant conditions, i.e. in the case where growth rates, competition parameters and carrying capacity will remain constant, coexistence of both species and competitive exclusion of each one specie are possible outcomes depending on the parameter values. The Lotka-Volterra equations can be extended to consider n species, and have been extensively used to model different problems in the field of mathematical biology.

In order to study the competition between populations i and j in time-dependent conditions, the simplest modification would be to consider time-dependent parameter values r_i, K_i and c_{ij}. This approach was used extensively in a number of mathematical models [135, 136, 137, 138, 139, 140, 141]. These types of models commonly address the question, motivated by studies of phytoplankton, raised by Hutchinson in 1961 [142] – how can a large number of species competing for the same resources coexist in an unstructured environment? In particular, Lotka-Volterra models with time-dependent parameters focussed on identifying temporal environmental regimes that might promote coexistence of populations that, in constant conditions, would lead to competitive exclusion.

The observations made by these models were quite heterogeneous. For example, May and Macarthur argued that environmental variability acts as a destabilising force and does not promote coexistence of sufficiently similar competitors [141]. A set of other studies, on the other hand, suggested that temporal variations promote coexistence [135, 136, 138]. Namba noted that the possibility of coexistence in seasonally fluctuating environments depends highly on the phase differences between growth rates and competition terms of the two populations [140]. All these models, however, differ in the underlying assumptions and the time-dependent regimes assigned to the parameters and, as a result, the observed dynamics are sensitive to these. Furthermore, by considering variability in parameters such as growth rate and carrying capacity, it is difficult to represent these quantities in terms of biologically measurable parameters [143].

Consumer-resource models, on the other hand, provide a useful framework to study species coexistence. Here, the dynamics of consumer species and resources are explicitly modelled, and particular attention is paid to defining the response of consumers to resource consumption (i.e. growth rate of consumers) and the way the resources are consumed by consumers. Coexistence is crucially influenced by the quality of available resources (substitutable vs essential), spatio-temporal distribution of resources throughout the environment, and foraging traits of consumers [144]. Consumer-resource models were used to model coexistence in both steady [145] and temporally variable [146, 147] environmental conditions, as well as in well-mixed and spatially-resolved settings [148].

1.5.2 Competition between generalists and specialists

The problem of generalist-specialist competition comprises a class of models investigating a bet-hedging strategy. Here, competition occurs between populations that differ in their consumption strategies in response to available resources. Specialists consume one resource and proliferate very efficiently when their preferable resource is in abundance. The generalist is able to consume several resources and, thus, is adapted to a range of environmental conditions, but has slower growth compared to specialists. Specialists are known to do better in steady environments, whereas the generalist is expected to do better when the resources fluctuate. Competition between a generalist and two specialists and their potential coexistence have been studied previously using a Lotka-Volterra model with time-dependent carrying capacity term [149], as well as by considering a resource-consumer model with time-dependent growth of resource species [147].

A comparison between generalists and specialists can be made in the context of cancer cells and their metabolic preferences, as well as proliferative abilities [7]. Theoretical studies of generalists and specialists suggest that temporal variations in the environment

are likely to promote within-patch coexistence [147]. Therefore, temporal variations in resource supply caused by irregular vasculature might promote the observed phenotypic heterogeneity in solid tumours and, in some conditions, select a bet-hedger population. To demonstrate this concept, here we provide an illustrative study by adapting and analysing the generalist-specialist model developed by Abrams [147].

1.5.2.1 Model description

We consider a well-mixed model of three distinct populations of cells competing for two resources, which is summarised in Figure 1.6. Here, two specialists, U_1 and U_2, each consume their preferred resource, R_1 and R_2, respectively. The generalist, V, however, consumes both resources. In this model, we assume that the resources enable the populations to grow linearly. This simplifying assumption allows us to analyse the model, as well as more accurately relate the resources to cancer dynamics (although this is still a simplification).

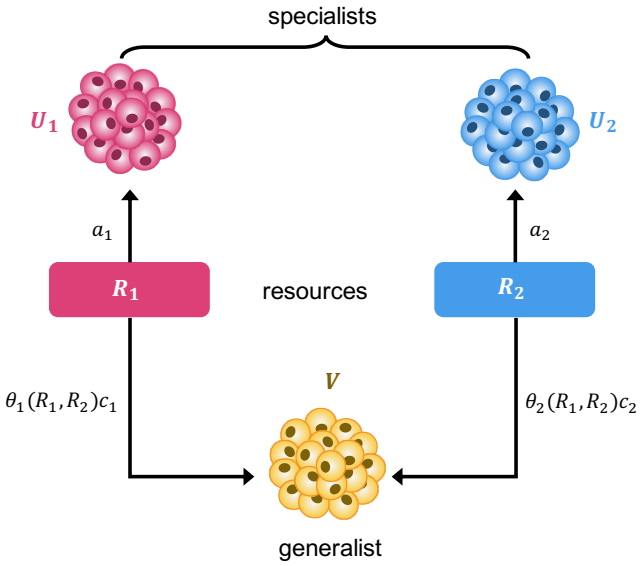

Figure 1.6: Schematic representation of the generalist-specialists model, Equations (1.3)–(1.7). U_1 and U_2 are specialists that consume resources R_1 and R_2, respectively. The growth of specialists depends linearly (with growth rates a_1 and a_2) on the population size and level of resource. V is the generalist population that consumes both resources with proportions θ_1 and θ_2. The growth rate of the generalist is determined by c_1 and c_2.

In this model, U_1 consumes resource R_1 from which it grows with the constant rate, a_1. Moreover, we assume natural death of cells with rate d_1. A similar relationship between the specialist U_2 and resource R_2 is assumed. γ_1 and γ_2 are the conversion terms. As shown in Figure 1.6, the growth of the generalist, V, depends on both resources. c_1 and c_2 are the proportions of resource R_1 and R_2, respectively, that are converted to V. The two

functions, $\theta_1(R_1, R_2)$ and $\theta_2(R_1, R_2)$ represent how much of each resource the generalist consumes, i.e. the dietary preference of a generalist. The resources are supplied by the source terms, $S_i(t)$, which are time-dependent and represent the fluctuating or constant blood flow. The resources are consumed by specialists with rate constants b_1 and b_2, and by the generalist with rates g_1 and g_2. Therefore, we use the following system of ODEs to model the dynamics of the specialists, generalist and two resources:

$$\frac{dU_1}{dt} = a_1 U_1 R_1 - d_1 U_1 \tag{1.3}$$

$$\frac{dU_2}{dt} = a_2 U_2 R_2 - d_2 U_2 \tag{1.4}$$

$$\frac{dR_1}{dt} = S_1(t) - \gamma_1 a_1 b_1 R_1 U_1 - \theta_1(R_1, R_2) g_1 R_1 V \tag{1.5}$$

$$\frac{dR_2}{dt} = S_2(t) - \gamma_2 a_2 b_2 R_2 U_2 - \theta_2(R_1, R_2) g_2 R_2 V \tag{1.6}$$

$$\frac{dV}{dt} = \theta_1(R_1, R_2) g_1 c_1 R_1 V + \theta_2(R_1, R_2) g_2 c_2 R_2 V - d_3 V. \tag{1.7}$$

For simplicity, we consider $a_1 = a_2 = 1$, $b_1 = b_2 = 1$, $\gamma_1 = \gamma_2 = 1$, $g_1 = g_2 = 1$, $c_1 = c_2 = 1$ and $d_1 = d_2 = d_3 = d$ in the numerical simulations and analysis presented below.

As mentioned before, the functions $\theta_1(R_1, R_2)$ and $\theta_2(R_1, R_2)$ denote the nutritional preferences of the generalist. We consider two scenarios for the adaptive behaviour of a generalist:

- **Non-adaptive generalist:** consumes the same proportions of resources at all times:

$$\theta_1(R_1, R_2) \equiv \bar{\theta}_1 \in \mathbb{R}_{>0} \quad \text{and} \quad \theta_2(R_1, R_2) \equiv \bar{\theta}_2 \in \mathbb{R}_{>0}. \tag{1.8}$$

  In particular, we assume that $\bar{\theta}_1, \bar{\theta}_2 \in [0, 1]$, such that $\bar{\theta}_1 + \bar{\theta}_2 \leq 1$. This definition represents a conservative bet-hedging strategy, where an individual is able to grow from both resources, but pays a cost by having a reduced growth rate compared to a specialist.

- **Adaptive generalist:** can assess the environmental conditions and adapt their intake of resources according to the availability of the resources. Hence, the parameters that determine the food preference of the generalist are functions of the resource levels:

$$\theta_1(R_1, R_2) = \frac{\Theta_1 R_1}{R_1 + R_2} \quad \text{and} \quad \theta_2(R_1, R_2) = \frac{\Theta_2 R_2}{R_1 + R_2}, \tag{1.9}$$

  where $\Theta_1 \in [0, 1]$ and $\Theta_2 \in [0, 1]$ are constant parameters that determine the factor at which the generalist grows slower than specialists. This guarantees that $\theta_1(R_1, R_2) + \theta_2(R_1, R_2) \leq 1$ at all times. This definition of $\theta_1(R_1, R_2)$ and $\theta_2(R_1, R_2)$ represents an adaptive bet-hedging strategy, whereby and individual can sense the environment

and adapt its nutrient uptake accordingly. The generalist still pays a cost by having a reduced proliferation potential compared to a specialist.

In order to link this model to cancer, we can assume that the two resources represent oxygen and glucose, which are supplied by the vasculature that is prone to temporal vessel occlusions. The three populations of cells then represent cells with different metabolic preferences. Two specialists correspond to fully oxidative and glycolytic phenotypes, whereas the generalist relies on both nutrients.

We solve the Equations (1.3)–(1.7) numerically in MATLAB. The details of the numerical setup are provided in Section A.3 in Appendix A.

1.5.2.2 Competition with constant nutrient supplies

First, we study the competition outcomes in the case where nutrient supply is constant:

$$S_1(t) \equiv \bar{S} \geq 0 \quad \text{and} \quad S_2(t) \equiv \bar{S} \geq 0. \tag{1.10}$$

The simplicity of this consumer-resource model allows us to determine the steady states when the nutrient is supplied constantly. In Appendix A, we non-dimensionalise the system of Equations (1.3)–(1.7) and characterise the linear stability of the steady states for both non-adaptive and adaptive generalists, in the presence of resources.

Figure 1.7(a) – (b) illustrates the predicted outcomes for different combinations of parameters that define nutrient preference. The different colours represent competition outcomes predicted by linear stability analysis (see Section A.2 in Appendix A). When the generalist is non-adaptive (Figure 1.7(a)), the specialists out-compete the generalist for any $\bar{\theta_1} + \bar{\theta_2} < 1$, as shown in white. The population dynamics when only two specialists survive is shown in Figure 1.7(c) The coexistence of both specialists and a generalist (Figure 1.7(d)) is possible only in a narrow range of parameters as shown by the green line and, hence, is biologically unlikely. Similarly for the adaptive generalist (Figure 1.7(b)), only specialists survive for any $\Theta_1 + \Theta_2 < 1$. These results agree with our expectations that specialists are selected in constant environments.

1.5.2.3 Competition with periodically-fluctuating nutrient supplies

Now we assume that both nutrients are supplied in a time-dependent manner. In particular, we consider periodically fluctuating source terms defined as a sinusoidal wave given by

$$S_1 = I_{mean} + \Delta I \, \sin\left(\frac{2\pi t}{T}\right), \tag{1.11}$$

$$S_2 = I_{mean} + \Delta I \, \sin\left(\frac{2\pi t}{T} - \phi\right), \tag{1.12}$$

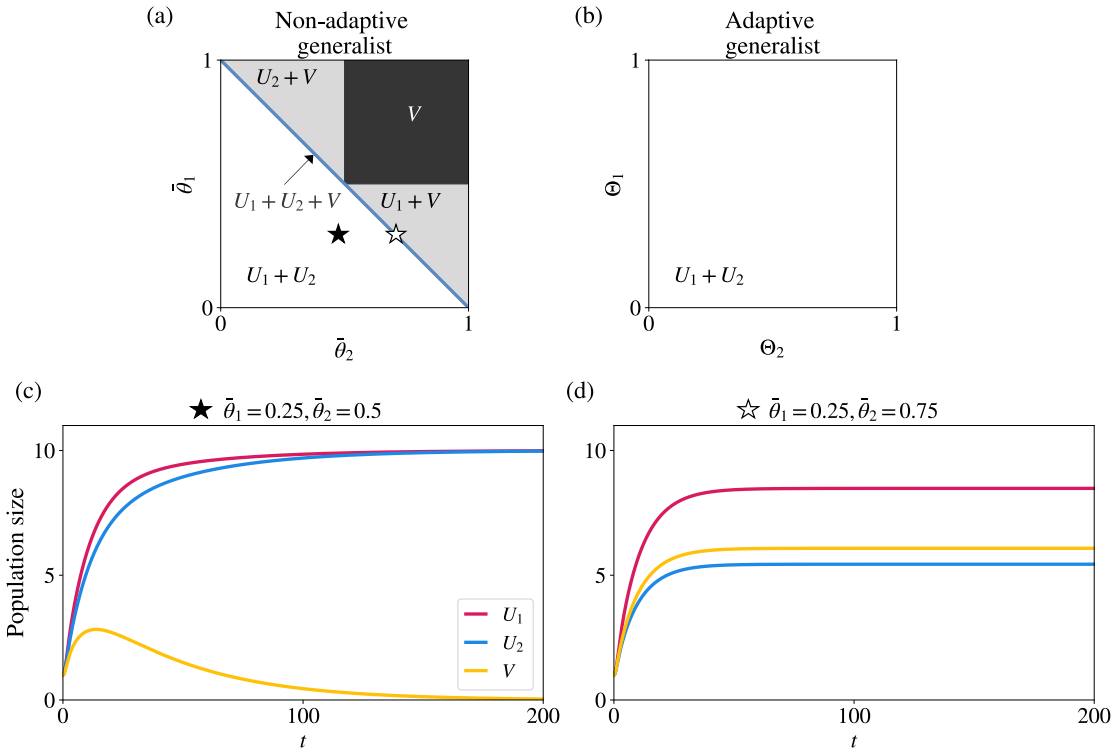

Figure 1.7: **(a)** Outcomes of the non-adaptive generalist model (Equations (1.3)–(1.7) with Equations (1.8) and (1.10)) predicted analytically for different values of $\bar{\theta_1}$ and $\bar{\theta_2}$. Colours represent competition outcomes: black – survival of generalist; white – survival of both specialists; grey – survival of one specialist and the generalist; blue – coexistence of all three populations. Stars denote the parameter sets that were used to generate the plots in **(c)** and **(d)**. **(b)** Outcomes of the adaptive generalist model (Equations (1.3)–(1.7) with Equation (1.9)) predicted analytically for different values of Θ_1 and Θ_2, where both specialists survive in all cases. **(c)** An example of the population dynamics when the two specialists out-compete the generalist. (d) Sample of population dynamics when all three populations coexist. Parameter values used here: $d = 0.1$, $\bar{S} = 1$.

where T is the period, ΔI is the half-amplitude, and I_{mean} is the mean value of $S_i(t)$. Moreover, we assume that the source terms fluctuate out of phase between two extreme values, i.e. $\phi = \pi$.

Non-adaptive generalist. When assessing the fluctuating environment, we split $\bar{\theta}_i$, $i \in \{1, 2\}$, into 25 values and for each combination of $\bar{\theta}_1$ and $\bar{\theta}_2$ and we solve numerically Equations (1.3)–(1.7) and note the average population sizes over the last period. By comparing the averages, we obtain the competition outcome. If one of the population sizes is below 0.001, this population is considered extinct. Each simulation runs until $t = t_{max} = 5000$. Moreover, we consider different fluctuation regimes by choosing different

values of half-amplitude, ΔI, and period of fluctuations, T, while keeping $I_{mean} = 1$.

Numerical simulations (see Figure A.1 in Appendix A) suggest that periodic fluctuations in the supply of resources do not promote the selection of the generalist population. Instead, for any combination of the nutrient preferences such that $\bar{\theta}_1 + \bar{\theta}_2 < 1$, the two specialists always survive for any environmental regimes. When $\bar{\theta}_1 + \bar{\theta}_2 = 1$ we, similarly to the constant environment case, observe coexistence of all three populations. See Figure A.2 in Appendix A for an example of population dynamics in this case. Therefore, a conservative generalist strategy might not be beneficial in this particular scenario. This observation is consistent with the original results from Abrams [147].

Adaptive generalist. Now we study how competition is affected by a periodically fluctuating nutrient source in the case of an adaptive generalist. As before, we split the parameters that determine the nutrient uptake proportions, Θ_1 and Θ_2, into 25×25 values and simulate the model for $t = t_{max} = 10000$. At the end of each realisation we note the average population sizes over the last period of fluctuations and using it we define the competition outcome. We consider different fluctuation regimes with $T \in \{10, 100, 500\}$ and $\Delta I \in \{0.2, 0.9\}$, while keeping $I_{mean} = 1$. The resulting outcomes are summarised in Figure 1.8(a).

Small amplitude fluctuations do not drastically change the outcome of competition and the results are similar to those for the steady environment. As the amplitude increases, the environment becomes more favourable for the generalist population. In particular, when the fluctuations have high amplitude, the generalist can out-compete both specialists. It is important to note that harsh fluctuations (higher amplitude, smaller frequency) promote transient coexistence of all three species. The parameters Θ_1 and Θ_2 determine the proportions of the three coexisting populations. However, no transient coexistence is observed when the environment fluctuates slowly ($T = 500$). An example of the population dynamics in the case where the generalist survives, transient coexistence is observed and the two specialists survive are shown in Figures 1.8(b), (c) and (d), respectively.

In accordance with our assumption, the adaptive generalist can vary its nutrient preference and, therefore, can potentially shift from more specialised phenotypes. To investigate the adaptive dynamics of the generalist population, we compare the values of Θ_1 and Θ_2 that define the uptake proportion of each resource for the cases where resources are supplied periodically with small and high amplitudes. This is shown in Figure 1.9.

When the amplitude of fluctuations in the nutrient supply is relatively low (Figure 1.9(a)), the specialists out-compete the generalist. The nutrient preference of the generalist does not vary much. The population V maintains a 'generalist' phenotype, i.e. it consumes both resources with roughly the same proportion throughout the time. On the other hand,

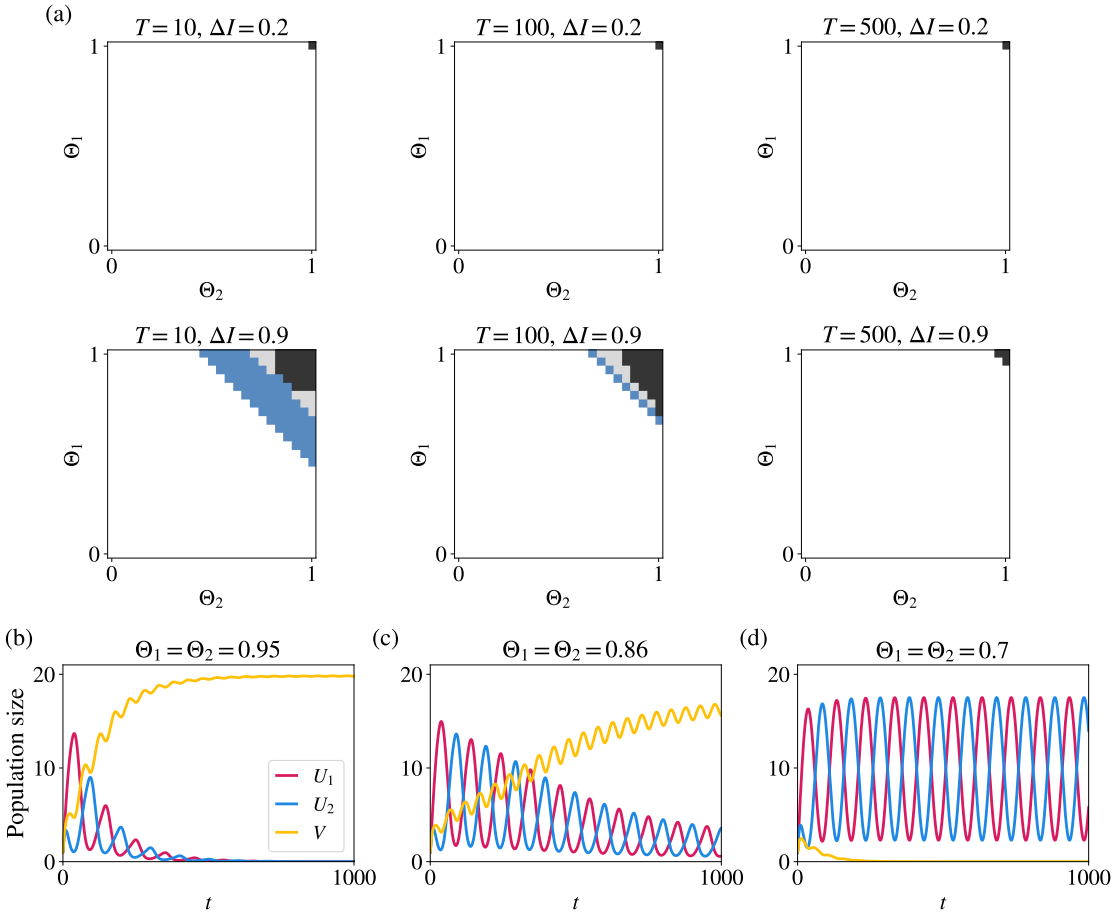

Figure 1.8: **(a)** Outcomes of the adaptive generalist model obtained by solving numerically Equations (1.3)–(1.7) with Equation (1.9) when the nutrient supply is defined by Equation (1.11). The simulations were run until $t_{max} = 10000$. Colours represent competition outcomes: black – survival of generalist; white – survival of both specialists; grey – survival of one specialist and the generalist; blue – coexistence (transient) of all three populations. Simulations carried out for 25×25 equally spaced (Θ_1, Θ_2) pairs. **(b)** – **(d)** Examples of the population dynamics when the generalist out-competes the specialists **(b)**, three populations transiently coexist **(c)**, and specialists out-compete the generalist **(d)**. Parameter values used here: $d = 0.1$.

when the populations experience high-amplitude fluctuations in their environment, it is the generalist population that survives (Figure 1.9(b)). In this case, the generalist essentially 'switches' between two phenotypes that are more specialised to a given resource.

1.5.2.4 Summary

We have investigated competition between a generalist and two specialist populations for two resources when the nutrient supply fluctuates periodically in time. In particular, we considered gradual changes in the environment.

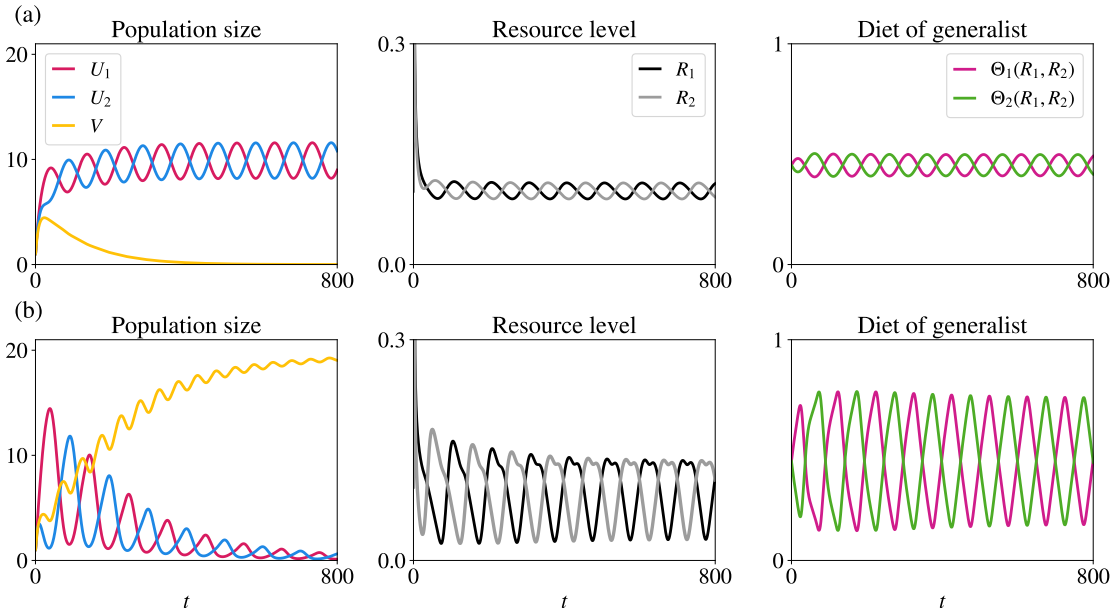

Figure 1.9: **(a)** Dynamics of population sizes (right), resource levels (middle) and dynamics of functions $\Theta_1(R_1, R_2)$ and $\Theta_2(R_1, R_2)$ given by Equation (1.9) under low-amplitude fluctuations ($\Delta I = 0.2$) obtained by solving numerically Equations (1.3)–(1.7) with Equation (1.11). **(b)** Same as **(a)**, but for high-amplitude fluctuations with $\Delta I = 0.9$. Parameter values used here: $d = 0.1$, $T = 100$, $I_{mean} = 1$.

We find that the non-adaptive generalist is not a successful strategy as in a fluctuating environment the specialists still out-compete the generalist. The fluctuation periods and amplitudes do not affect the competition outcomes for a generalist, which is inferior to specialist, i.e. pays the cost for being able to grow from both resources. Furthermore, the fluctuations do not affect the probability of coexistence of all three populations.

The adaptive strategy, whereby the generalist adjusts its nutrient uptake according to the immediate environment, promotes the generalist when the nutrient is supplied periodically. High amplitude fluctuations that occur with intermediate frequencies can select for a generalist switches between two specialised phenotypes. We also observed that faster, high-amplitude fluctuations allow all three species to coexist transiently for a longer time period across a much wider range of parameter values. Even though the coexistence observed is transient, it is still relevant when thinking about the emergence of phenotypic heterogeneity tumours, which are constantly evolving and almost never are in a steady state.

In this brief demonstration of generalist-specialist behaviour we only considered a limited set of parameters such as death rate, d_i, variation in growth from each resource, phase shift between the resource supply rates, ϕ. Furthermore, we only considered one form of the generalist dietary preferences given by Equation (1.9). However, it is known that functional

responses affect the success of adaptive strategy [144]. Thus, it would be useful to explore a wider range of parameters and assumptions that might affect the competition between the three populations.

Our results are consistent with those from the original model [147], which focussed mainly on the likelihood of coexistence when varying parameters values, such as the death rates, d_i. We further explored the impact of amplitude and period of fluctuations, which play an important role when evaluating a particular adaptive strategy. In particular, we observe that fluctuations occurring on intermediate timescales are more efficient at selecting a generalist population. This is in agreement with recent theoretical works that identified environmental conditions that lead to the evolution of a generalist [150, 151].

1.5.3 Phenotype-structured models of adaptive dynamics

The models of adaptive dynamics formulated in terms of ODEs provide insights on the behaviour of averaged populations. In other words, the specific characteristics of individuals within one population are hidden. In the ODE framework, heterogeneity within the population can be represented by considering a number of compartments with specific behaviours, but within each compartment there can be no variation.

In order to account for more detailed intra-population heterogeneity, one must consider the so-called structured population dynamic equations, which are usually formulated in terms of integro-differential (IDEs) or non-local partial differential equations. Here, the population of cells is structured by a continuous variable, which can represent a measurable physical characteristic of each cell. Sometimes, these traits cannot be measured experimentally, but aid conceptual understanding of the underlying system. For example, the structured variable can represent the age, spatial position, or level of gene expression. Such IDEs and PDEs have been widely applied to a range of biological problems in ecology, epidemiology and beyond [152].

We begin with a simple example that illustrates the general form of a model that governs the dynamics of a single structured population. We consider a structure variable, i.e. phenotypic trait, $x \in \mathbb{R}$. We assume that the growth rate, $p(x)$, is dependent on cell phenotype and proliferation is limited by the total population size, $\rho(t)$. The dynamics of such a structured population follows the logistic equation:

$$\begin{cases} \dfrac{\partial n(x,t)}{\partial t} = p(x)n(x,t) - \rho(t)n(x,t), \\ \\ \rho(t) = \displaystyle\int_{\mathbb{R}} n(x,t)\mathrm{d}x, \\ \\ n(x,0) = n^0(x) > 0 \quad \text{for all } x. \end{cases} \tag{1.13}$$

One of the benefits of using such deterministic models is the ability to study the asymptotic (long-time) behaviour of the solutions. Thus, assuming that $p(x)$ is positive at all times and that the initial population distribution satisfies $n^0(x) > 0$, it is possible to show [153] that the population size will converge to some constant value and the population density will concentrate as a Dirac mass at the phenotype x^∞ that represents the evolutionary stable strategy (i.e. the fittest phenotypic state with highest value of $p(x)$):

$$\rho(t) \to \rho^\infty = p(x^\infty), \quad n(x,t) \to p(x^\infty)\delta(x - x^\infty) \quad \text{as} \quad t \to \infty. \tag{1.14}$$

Starting from this simple example, it is possible to generalise the model to a higher number of interacting populations, as well as study their dynamics when their environment is subject to change [153].

In the example above (Equation (1.13)), the selected phenotype x^∞ is naturally selected under conditions that all traits are present initially. However, when dealing with biologically realistic scenarios, some traits, or phenotypes, can develop over time as a response to environmental changes. Therefore, x becomes a variable that can evolve in time. The mathematical approaches governing adaptive dynamics can be generalised to a reaction-diffusion-advection equations with the general form

$$\frac{\partial n(x,t)}{\partial t} + \underbrace{\frac{\partial}{\partial x}\left\{v(x)n(x,t)\right\}}_{\substack{\text{stress-induced} \\ \text{adaptation}}} = \underbrace{\beta \frac{\partial^2 n(x,t)}{\partial x^2}}_{\substack{\text{spontaneous} \\ \text{phenotypic variation}}} + \underbrace{\left\{p(x,t) - d(x,t)\rho(t)\right\} n(x,t)}_{\text{fitness}}, \tag{1.15}$$

where

$$\rho(t) = \int_{\mathbb{R}} n(x,t)\mathrm{d}x \quad \text{and} \quad n(x,0) = n^0(x). \tag{1.16}$$

Here, the phenotypic variation is modelled via diffusion and advection operators. The diffusion term represents spontaneous, random heritable phenotypic variation that occurs at rate $\beta \in \mathbb{R}_+$. The advection (also called drift) term models the fact that phenotypic variation is more likely to be biased in a certain direction. For instance, administration of chemotherapy might select resistant phenotypes [154]. $v(x)$ determines the direction and magnitude of bias – it can be constant or dependent on phenotypic trait. Finally, the nonlocal term can be interpreted as the fitness of an individual in phenotypic state x in a given environment [153]. The fitness function can be determined from empirical observations or by fitting to data. It is usually formulated either as a polynomial [155] or a sum of Gaussian functions corresponding to different fitness peaks [156]. In order for the population to have one uni-modal population (i.e. one fitness peak), the function $p(x,t)$ must be strictly concave. However, the cases where the population can be bi- or multi-modal have also been investigated [157].

Mathematical models formulated in terms of IDEs and non-local parabolic PDEs like those considered here have been increasingly used to achieve a more in-depth theoretical understanding of the mechanisms underlying phenotypic adaptation in a variety of biological contexts. For instance, both predator-prey [158] and generalist-specialist [159] models with phenotypic trait have been developed and analysed. Moreover, the dynamics of consumer-resource competition has been investigated in a spatial context by introducing spatial structure [160]. Furthermore, it is possible to incorporate both spatial and phenotypic structure, as was done, for example, by Alfaro et al. [161, 162]. They investigated biological invasions involving Darwinian evolution using reaction-diffusion models. Furthermore, several studies assumed that motility is an evolving trait and investigated the implications of this assumption in the problem of biological invasions, as well as random dispersal of species [163, 164, 165, 166, 167, 168].

IDEs and nonlocal PDEs have been recently applied to model cancer evolutionary dynamics. For instance, by linking the phenotype to the level of drug resistance of a cell, a number of studies looked at the emergence of drug resistance in tumours [169, 170, 171, 172, 154, 173]. Here, the phenotypic variations were modelled via both diffusion and advection terms, and the emergence of drug resistance was assessed in both well-mixed and spatial contexts. Such phenotype-structured models were later combined with optimal control theory to provide insights into therapy scheduling in order to minimise tumour burden and, at the same time, keep the side-effects associated with chemotherapy to a minimum [174, 175, 176]. Furthermore, phenotype-structured models have been applied to study blood cancers. Here, the populations were structured by the self-renewal ability of stem cells and clonal selection was investigated [177, 178].

Emergence of phenotypic heterogeneity in solid tumours has also been approached via phenotype-structured IDEs and PDEs. In particular, by the modelling spatial distribution of oxygen, Lorenzi et al. demonstrated the evolution of phenotypic heterogeneity in various 3D geometries, including tumour spheroids and real vascularised human liver tumour structures obtained via computer tomography [179]. Here, the phenotype represented the expression level of a hypoxia-responsive gene, thus being linked to metabolic state. Villa et al. used a similar approach to study phenotypic heterogeneity in vascularised tumours [180]. The authors considered a 2D geometry and modelled blood vessels as point sources of oxygen. As an extension, movement of cells in physical space was modelled via a diffusion term. In both works the authors assumed that oxygen delivery via blood vessels is steady and the role of temporal variations in the blood flow was not investigated.

Temporal variations in the environment have been approached recently in well-mixed models of one phenotype-structured population [181, 182, 183, 184, 185, 186, 187]. For

example, Lorenzi et al. considered that the fitness function, which governs the proliferation and death of population, undergoes periodic fluctuations in time [182]. The population is structured by the trait defining how fit an individual is in a given environment. The authors observed that the population enters an unstable and fluctuation-driven phenotypic state and undergoes oscillation in population size, mediated by the synergism between rate of phenotypic variation and frequency of environmental fluctuations. Other works (cited above) also assume that environmental change is reflected via a time-dependent fitness function, i.e. levels of resources were not modelled explicitly and no interactions between the population and environment, which might affect the temporal dynamics, were considered.

1.5.4 Discrete phenotype-structured models

Deterministic models have undeniable advantages when the task is to model the behaviour of population-level phenomena. Continuum models are amenable to asymptotic analysis, which allows for a more in-depth theoretical understanding of the underlying dynamics. This allows a complete exploration of parameter space and gives the opportunity to perform simulations with large population sizes. However, population-scale phenomenological assumptions make it more difficult to incorporate the finer details of phenotypic adaptation by single individuals. Moreover, such models cannot capture adaptive phenomena that are driven by stochastic effects in the evolutionary paths of single individuals. This is particularly relevant at low population levels, which are commonly observed when risk-spreading adaptive strategies occur and when populations are faced with novel environments during colonisation.

Continuum phenotype-structured PDEs and IDEs can be derived from first principles as the appropriate limits of discrete stochastic models that track the evolution of single individuals [188, 189]. The corresponding discrete models permit the representation of individual-scale adaptive mechanisms, and account for possible stochastic inter-individual variability in evolutionary trajectories. Such individual-based models have been successfully applied to study evolutionary cancer dynamics and compared to their continuum analogues [190, 191].

The development of a discrete phenotype-structured model begins with the identification of microscopic properties of the population. It is necessary to define how the adaptive traits of an individual affect their birth and death rates, as well as the process of phenotypic variation. Furthermore, it is essential to determine how an individual with specific phenotype interacts with other individuals and the environment. Therefore, for each phenotypic state and environmental condition, the probabilities of birth, death and phenotypic variation are defined, and the population evolves as a Markov process – the likelihood of events

depend only on the current state of the population and environment [188]. Spontaneous phenotypic variation, which is modelled via a diffusion term in a continuum approximation, is calculated as a discrete-time branching random walk on a space of phenotypes [192].

Furthermore, discrete phenotype-structured models can be extended in order to incorporate space. It is also possible to consider hybrid models, where the population dynamics is modelled via a discrete process, and the distribution of abiotic factors is approximated via partial differential equations. Several computational frameworks, such as Hybrid Automata Library [193], Chaste [194] and PhysiCell [195], exist that allow easy and computationally-efficient implementation of algorithms that comprise an individual-based model.

1.6 Thesis structure

This literature review provides the empirical evidence for temporal variations of nutrients in solid tumours that are caused by unstable blood flow. These variations occur at a range of timescales and amplitudes, and are likely to require cancer cells to adapt in different ways. For instance, risk-spreading strategies, such as spontaneous phenotypic variation, are known to help the populations of individuals to survive through such temporally-varying conditions. Thus, in this thesis, we investigate whether cancer cells could utilise such an adaptive strategy by developing a set of phenotype-structured partial differential equation models.

This thesis consists of four main chapters. In each chapter we develop and analyse a range of spatially well-mixed phenotype-structured (both continuum and discrete) models of increasing biological complexity for the competition of tumour subpopulations for resources (oxygen), which are supplied periodically in time.

In Chapter 2, we present a system of nonlocal PDEs modelling the evolutionary dynamics of two phenotype-structured cancer cell populations exposed to fluctuating nutrient level. The phenotypic state of every cell is described by a continuous variable that provides a simple representation of its metabolic phenotype. The cells are grouped into two competing populations that undergo heritable, spontaneous phenotypic variations at different rates. By considering a prescribed oxygen level, we analyse long-term behaviour of the solutions and identify the environmental regimes that favour selection of each population. The results suggest that when nutrient levels undergo small and slow oscillations, it is evolutionarily more convenient to rarely undergo spontaneous phenotypic variations. Conversely, under relatively large and fast periodic oscillations in the nutrient levels, which bring about alternating cycles of starvation and nutrient abundance, higher rates of spontaneous phenotypic variation confer a competitive advantage. At the end of this chapter, we discuss how the

environmental regimes that are characterised by different amplitudes and timescales can create distinct environmental niches that will select a specific adaptation strategy.

Having gained a solid theoretical understanding of the model, we then add several layers of biological complexity in Chapter 3 by modelling oxygen dynamics explicitly. In particular, we include cell-environment feedback, such as consumption. Additionally, we study the impact of fitness costs associated with the phenotype that is adapted to oxygen-scarce environments, i.e. the decreased energy yield during glycolysis. We first consider a simplified model, where oxygen consumption is linear. Analysis of this simplified model, together with numerical simulations, shows, that the results from the original model carry through to this more biologically realistic setting. We then consider a full model where oxygen consumption is dependent on the phenotype of the cell. Our model supports the idea that under chronic-hypoxic conditions lower rates of phenotypic variation lead to a competitive advantage, whereas higher rates of phenotypic variation can confer a competitive advantage under cycling-hypoxic conditions. In the latter case, the numerical results obtained show that bet-hedging evolutionary strategies, whereby cells switch between oxidative and glycolytic phenotypes, can spontaneously emerge. Furthermore, we demonstrate that phenotype-dependent interactions between cells and the environment can amplify the fluctuations in oxygen level. At the end of this chapter, we relate our findings to the emergence of phenotypic heterogeneity within solid tumours caused by on-going angiogenesis.

In Chapter 4, motivated by the presence of small populations that are commonly observed in cancer, we present a corresponding stochastic individual-based model for the coevolution of two competing phenotype-structured cell populations that are exposed to time-varying nutrient levels and undergo spontaneous, heritable phenotypic variations with different probabilities. We compare the individual-based model and its continuum analogue, focussing on scenarios whereby the predictions of the two models differ. These differences arise in the presence of low probabilities of phenotypic variation, and become more apparent when the two populations are characterised by less fit initial mean phenotypes and smaller initial levels of phenotypic heterogeneity. Finally, we apply our modelling framework to the problem of metastasis formation in distant organs, highlighting the importance of stochastic events and increased adaptation in this multi-step process.

In Chapter 5, we present preliminary results investigating the effect of the shape of fitness landscapes on selection of a population with higher rates of phenotypic variation. In particular, by solving numerically the system of PDEs modelling the competition of two populations in prescribed environments, we study how the shape of fitness peaks, i.e. the width, makes the adaptive strategy more or less successful.

We conclude the thesis in Chapter 6 where we present a summary of the main results and outline potential extensions of the work. As additional extensions, we mention the development of a model with a more accurate depiction of cancer metabolism, incorporation of other cell-environment feedback mechanisms, a spatially-structured model and reaction-diffusion-advection model in order to study the phenotypic adaptation that occurs on faster timescales (gene expression).

Chapter 2

Competition of phenotype-structured populations in prescribed environments

2.1 Introduction

Pronounced spatial variations in the molecular properties of cancers have been well recognised and are often ascribed to evolution driven by genetic mutations ('branching clonal evolution'). An alternative hypothesis is that the cancer cells are simply evolving to adapt to spatial and temporal variations in microenvironmental conditions that result from heterogeneous blood flow. The vascular structure in tumours is highly disordered and is constantly re-modelled via processes such as sprouting angiogenesis and vascular regression and dilation [11]. As a consequence, there can be spatial and temporal variations in the delivery of oxygen to regions of tumour, leading to alternating periods of oxygen-deprivation and re-oxygenation [24].

In nature, organisms of various scales, ranging from bacteria to animals, also exist in fluctuating environments. For example, in order to cope with changes in nutrient availability, they are required to adapt. When the fluctuations are regular and the populations have sufficient time to sense and react to the changes, a highly plastic phenotype, in which individuals acquire different traits based on environmental cues, is an optimal strategy [66]. An alternative strategy that is more suitable for irregular and unpredictable changes is risk spreading, which is also known as bet-hedging [77]. Here, the population diversifies such that each sub-population is adapted to a specific environment. This ensures that at least some fraction of the population will survive in the face of sudden environmental changes [79]. Phenotypic heterogeneity, a characteristic feature of a risk spreading strategy, is observed in many systems.

The direct causes of temporal variations on the selection of cancer cells and their adaptive strategies have not been investigated yet, and mathematical modelling provides a unique opportunity to study the impact of intermittent hypoxia on tumour progression. An obvious place to start would be to consider tumour metabolism, as it is likely to be directly affected by fluctuations in oxygen levels – one of the main nutrients for any cell. Detailed cell-based models of tumour metabolism have been developed in order to study the emergence of phenotypic heterogeneity in solid tumours [58]. These types of models contain a large number of parameters where most of them are estimated from experimental literature. Similarly, modelling assumptions are also based on experimental evidence. However, lack of understanding of the impact of cycling hypoxia on the cancer cell cycle makes it very difficult to extract robust results on the effect of this phenomenon from complex, cell-based models. Therefore, we approach this problem from the ecological point of view by considering abstract models that rely on qualitative understanding of the underlying biology and allow a mathematical analysis.

Most of the abstract ecological models that have been developed to explore the dynamics of phenotypic changes in fluctuating environments view the environment and an individuals phenotype as binary – the environment switches between two extreme conditions and individuals jump between two antithetical phenotypic states that are each adapted to the external environmental conditions [94, 89, 85]. However, in many cases of biological and ecological interest *Natura non facit saltus*, and it might therefore be relevant to consider the occurrence of intermediate environmental conditions and the existence of a spectrum of possible phenotypic states.

In light of these considerations, in this chapter we present a novel mathematical model for the evolutionary dynamics of two competing phenotype-structured populations in periodically fluctuating environments. In Section 2.2 we develop the new model. Here, the nutrient level represents the environmental state. The phenotypic state of each individual is represented by a continuous variable, and the phenotypic fitness landscape of the populations evolves in time due to variations in the concentration of a nutrient. In order to assess the evolutionary role that spontaneous phenotypic variations play in environmental adaptation, we focus on the case where the two populations undergo spontaneous phenotypic variations with different probabilities. In Section 2.3 we exploit the analytical tractability of the governing equations to investigate its long-term behaviour. We then validate our findings in Section 2.4 by solving the model equations numerically for a range of environmental conditions.

The work contained in this chapter was carried out in collaboration with Prof. Tommaso Lorenzi (Politecnico di Torino, Italy). He developed the methodology presented in Section

2.3. The results presented in Sections 2.2 – 2.5 have been published in the following paper:

A. Ardaševa, R. A. Gatenby, A. R. A. Anderson, H. M. Byrne, P. K. Maini, T. Lorenzi, 2020, 'Evolutionary dynamics of competing phenotype-structured populations in periodically-fluctuating environments', Journal of Mathematical Biology, 80, 775–807.

2.2 Mathematical model

2.2.1 Population and nutrient dynamics

We study the evolutionary dynamics of two competing phenotype-structured populations in a well-mixed system. Individuals within the two populations reproduce asexually, die and undergo spontaneous phenotypic variation. We assume the two populations differ only in the rate at which they undergo spontaneous phenotypic variation. We label the population undergoing phenotypic variations at a higher rate by the letter H, while the other population is labelled by the letter L.

We represent the phenotypic state of each individual by a continuous variable $x \in \mathbb{R}$, and we describe the phenotype distributions of the two populations at time $t \in [0, \infty)$ by means of the population density functions $n_H(x,t) \geq 0$ and $n_L(x,t) \geq 0$. We define the size of population H, the size of population L and the total number of individuals inside the system at time t, respectively, as

$$\rho_H(t) = \int_{\mathbb{R}} n_H(x,t)\, \mathrm{d}x, \quad \rho_L(t) = \int_{\mathbb{R}} n_L(x,t)\, \mathrm{d}x, \quad \rho(t) = \rho_H(t) + \rho_L(t). \tag{2.1}$$

We further define, respectively, the mean phenotypic state and the related variance of each population $i \in \{H, L\}$ at time t as

$$\mu_i(t) = \frac{1}{\rho_i(t)} \int_{\mathbb{R}} x\, n_i(x,t)\, \mathrm{d}x, \quad \sigma_i^2(t) = \frac{1}{\rho_i(t)} \int_{\mathbb{R}} x^2\, n_i(x,t)\, \mathrm{d}x - \mu_i^2(t). \tag{2.2}$$

In the mathematical framework of our model, the function $\sigma_i^2(t)$ provides a measure of the level of phenotypic heterogeneity in the i^{th} population. Finally, we introduce a function $S(t) \geq 0$ to model the concentration of a nutrient that is equally available to the two populations at time t, which we assume is prescribed.

The evolution of the population density functions is governed by the following system of non-local parabolic PDEs

$$\begin{cases} \dfrac{\partial n_H}{\partial t} = \beta_H \dfrac{\partial^2 n_H}{\partial x^2} + R\big(x, S(t), \rho(t)\big)\, n_H, \\[2ex] \dfrac{\partial n_L}{\partial t} = \beta_L \dfrac{\partial^2 n_L}{\partial x^2} + R\big(x, S(t), \rho(t)\big)\, n_L, \end{cases} \quad \text{for } (x,t) \in \mathbb{R} \times (0, \infty). \tag{2.3}$$

In the system of PDEs (2.3), the diffusion terms model the effects of spontaneous phenotypic variation, which occur at rates $\beta_H > 0$ and $\beta_L > 0$, with

$$\beta_H > \beta_L. \tag{2.4}$$

2.2.2 Fitness function and biological assumptions

The functional $R\big(x, S(t), \rho(t)\big)$ models the fitness of individuals in the phenotypic state x at time t under the environmental conditions given by the nutrient concentration $S(t)$ and the total number of individuals $\rho(t)$ – i.e. the functional $R\big(x, S(t), \rho(t)\big)$ can be seen as the phenotypic fitness landscape of the two populations at time t. We define this fitness functional as

$$R\big(x, S(t), \rho(t)\big) = p(x, S(t)) \; - \; d\rho(t). \tag{2.5}$$

Definition (2.5) translates into mathematical terms the following biological ideas: (i) all else being equal, individuals die due to interpopulation and intrapopulation competition at rate $d\rho(t)$, with the parameter $d > 0$ being related to the carrying capacity of the system in which the two populations are contained; (ii) individuals in the phenotypic state x proliferate and die under natural selection at rate $p(x, S(t))$ (i.e. the function $p(x, S)$ is a net proliferation rate). We focus on the following biological assumptions:

Assumption 1. Phenotypic variants with $x \to 0$ have a competitive advantage over the other phenotypic variants when the nutrient concentration is high.

Assumption 2. Phenotypic variants with $x \to 1$ are favoured over the other phenotypic variants when the nutrient concentration is low.

We then define the net proliferation rate as

$$p\big(x, S(t)\big) = \gamma \, \frac{S(t)}{\kappa + S(t)} \, \left(1 - x^2\right) \; + \; \zeta \left(1 - \frac{S(t)}{\kappa + S(t)}\right) \left[1 - (1 - x)^2\right], \tag{2.6}$$

with $0 < \zeta \leq \gamma$. The parameters γ and ζ model, respectively, the maximum proliferation rate of the phenotypic variants best adapted to nutrient-rich and nutrient-scarce environments. Here, the parameter κ represents the nutrient concentration at which the reaction rate is half of the maximal value. The defined net proliferation rate function ensures that when the nutrient is high (i.e. $S \to \infty$), cells in the phenotypic state $x = 0$ will have the highest fitness. On the other hand, when the nutrient is absent (i.e. $S \to 0$), cells in the phenotypic state $x = 1$ will proliferate at the highest rate. The functional form of Equation (2.6) is chosen in order to facilitate mathematical analysis, and it is possible to use other variants, depending on the biological problem and available data. For discussion, see Chapter 5.

Definition (2.6) ensures analytical tractability of the model and leads to a fitness functional that is close to the approximate fitness landscapes which can be inferred from experimental data through regression techniques – see, for instance, Equation (1) in [155]. In fact, after a little algebra, definition (2.6) can be rewritten as

$$p\big(x, S\big) = \gamma\, g(S) - h(S)\,(x - \varphi(S))^2 \tag{2.7}$$

with

$$g(S) = \frac{S}{\kappa + S} + \frac{\zeta^2\kappa^2}{\gamma(\kappa + S)(\gamma S + \zeta\kappa)}, \quad \varphi(S) = \frac{\zeta\kappa}{\gamma S + \zeta\kappa} \tag{2.8}$$

and

$$h(S) = \frac{\gamma S + \zeta\kappa}{\kappa + S}. \tag{2.9}$$

Under the environmental conditions defined by the nutrient concentration S, the function $0 \leq \varphi(S) \leq 1$ represents the fittest phenotypic state, $\gamma\, g(S) > 0$ is the maximum fitness, and $h(S)$ can be seen as a nonlinear selection gradient that quantifies the intensity of natural selection. Throughout this section we will refer to $g(S)$ as the rescaled maximum fitness. The form of $p(x, S)$ given by Equation 2.7 implies that the net proliferation rate of each cell depends on how close its phenotypic state, x, is to the fittest phenotypic variant, $\phi(S)$, for a given environment.

In accordance with our biological assumptions, equation (2.7) shows that definition (2.6) is such that the fittest phenotypic state $\varphi(S)$ belongs to the interval $[0, 1]$ for any nutrient concentration $S \geq 0$, i.e. $\varphi : \mathbb{R}_{\geq 0} \to [0, 1]$. In particular, under starvation conditions (i.e. if $S = 0$) the fittest phenotypic state is $\varphi(0) = 1$, while increasing nutrient concentrations correspond to values of the fittest phenotypic state closer to 0, i.e. $\varphi'(S) < 0$ for all $S \geq 0$ and $\varphi(S) \to 0$ as $S \to \infty$. Furthermore, the fact that the function $p(x, S)$ is negative for values of x sufficiently far from the fittest phenotypic state $\varphi(S)$ captures the idea that less fit variants are driven to extinction by natural selection. These observations are illustrated by the plots in Figure 2.1.

In this chapter, for simplicity, we assume that there is no cost associated with the phenotype adapted to a nutrient-scare environment:

$$\zeta = \gamma. \tag{2.10}$$

Therefore, definitions (2.8) and (2.9) become, respectively,

$$g(S) = \frac{1}{\kappa + S}\left(S + \frac{\kappa^2}{\kappa + S}\right), \quad \varphi(S) = \frac{\kappa}{\kappa + S} \quad \text{and} \quad h(S) \equiv \gamma. \tag{2.11}$$

Moreover, since we assume the function $S(t)$ to be given, we use the notation

$$g(t) \equiv g(S(t)) \quad \text{and} \quad \varphi(t) \equiv \varphi(S(t)).$$

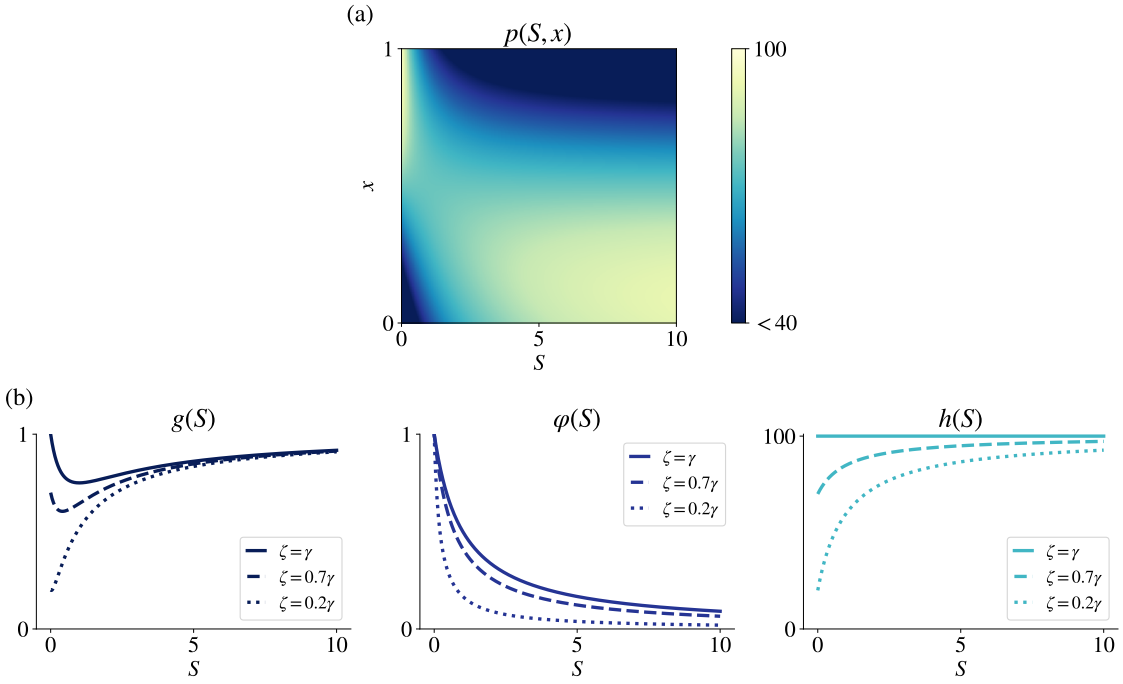

Figure 2.1: (a) The plot of the net proliferation rate $p(S, x)$ defined by Equation (2.6) [or equivalently by Equation (2.7)] with $\gamma = 100$ and $\zeta = 50$. (b) The rescaled maximum fitness $g(S)$ and the fittest phenotypic state $\varphi(S)$ defined by Equation (2.8), along with the selection gradient $h(S)$ defined by Equation (2.9), are plotted against the nutrient concentration S, for $\gamma = 100$, $\kappa = 1$ and different values of the parameter ζ.

2.3 Analysis of long-term solutions

In order to obtain an analytical description of the evolutionary dynamics, we focus on a biological scenario whereby the initial phenotype distributions of the two populations are Gaussians, that is, we study the behaviour of the solution to the system of non-local parabolic equations (2.3) subject to the initial condition given by the pair $n_H(x, 0)$ and $n_L(x, 0)$ with

$$n_i(x, 0) = \rho_i^0 \sqrt{\frac{v_i^0}{2\pi}} \exp\left[-\frac{v_i^0}{2}\left(x - \mu_i^0\right)^2\right] \quad \text{for} \quad i \in \{H, L\}, \tag{2.12}$$

where $\rho_i^0 \in \mathbb{R}_{>0}$, $v_i^0 \in \mathbb{R}_{>0}$ and $\mu_i^0 \in \mathbb{R}$. The choice of initial condition (2.12) is consistent with much of the previous work on the mathematical analysis of the evolutionary dynamics of continuous traits, which relies on the prima facie assumption that population densities are Gaussians [196].

Proposition 1. *Under assumptions* (2.5), (2.7) *and* (2.11), *the system of non-local PDEs* (2.3)

subject to the initial condition (2.12) *admits the exact solution*

$$n_i(x,t) = \rho_i(t)\sqrt{\frac{v_i(t)}{2\pi}}\exp\left[-\frac{v_i(t)}{2}(x-\mu_i(t))^2\right] \quad \textit{for} \quad i \in \{H,L\}\,, \tag{2.13}$$

with the population size, $\rho_i(t)$*, the mean phenotypic state,* $\mu_i(t)$*, and the inverse of the related variance,* $v_i(t) = 1/\sigma_i^2(t)$*, being solutions of the Cauchy problem*

$$\begin{cases} v_i'(t) = 2\left(h(t) - \beta_i v_i^2(t)\right), \\ \mu_i'(t) = \dfrac{2h(t)}{v_i(t)}\left(\varphi(t) - \mu_i(t)\right), \\ \rho_i'(t) = \left(F_i(t) - d\rho(t)\right)\rho_i(t), \qquad \textit{for } i \in \{H,L\}\,, \\ v_i(0) = v_i^0, \quad \mu_i(0) = \mu_i^0, \quad \rho_i(0) = \rho_i^0, \\ \rho(t) = \rho_H(t) + \rho_L(t), \end{cases} \tag{2.14}$$

where

$$F_i(t) \equiv F_i(t, v_i(t), \mu_i(t)) = \gamma\, g(t) - \frac{h(t)}{v_i(t)} - h(t)\left(\mu_i(t) - \varphi(t)\right)^2, \tag{2.15}$$

and $'$ *denotes* t *derivative.*

Proof. Substituting the definitions (2.5), (2.7) and (2.11) into the non-local PDE (2.3) for $n_i(x,t)$ yields

$$\frac{\partial n_i}{\partial t} = \beta_i \frac{\partial^2 n_i}{\partial x^2} \;+\; \left[\gamma g(t) - \gamma(x-\varphi(t))^2 - d\rho(t)\right] n_i, \quad n_i \equiv n_i(x,t). \tag{2.16}$$

Building upon the results presented in [175, 190, 182], we make the ansatz (2.13) and substituting this ansatz into Equation (2.16) we find

$$\begin{aligned} \frac{\rho_i'}{\rho_i} + \frac{v_i'}{2v_i} \;=\; & \frac{v_i'}{2}(x-\mu_i)^2 - \mu_i' v_i (x-\mu_i) + \beta_i\left[v_i^2(x-\mu_i)^2 - v_i\right] \\ & + \gamma\, g(t) - h(t)\,(x-\varphi(t))^2 - d\rho. \end{aligned} \tag{2.17}$$

Equating the coefficients of the zero-order, first-order and second-order terms in x in Equation (2.17) produces a system of ordinary differential equations (ODEs). Namely, the second-order terms in x yield the following ODE for v_i alone

$$v_i' + 2\beta_i v_i^2 = 2h(t). \tag{2.18}$$

Moreover, equating the coefficients of the first-order terms in x, and eliminating v_i' from the resulting equation, yields

$$\mu_i' = \frac{2h(t)(\varphi - \mu_i)}{v_i}. \tag{2.19}$$

Lastly, choosing $x = \mu_i$ in Equation (2.17) gives

$$\frac{\rho_i'}{\rho_i} + \frac{v_i'}{2v_i} = -\beta_i v_i + \gamma\, g - h(t)(\mu_i - \varphi)^2 - d\rho \tag{2.20}$$

and eliminating v_i' from the above equation we find

$$\rho_i' = (F_i - d\rho)\,\rho_i, \tag{2.21}$$

with the function $F_i(t)$ being defined according to Equation (2.23). Under the initial condition (2.12), we have

$$v_i(0) = v_i^0, \quad \mu_i(0) = \mu_i^0 \quad \text{and} \quad \rho_i(0) = \rho_i^0.$$

Imposing these initial conditions on the system of ODEs (2.18)–(2.21), we arrive at the Cauchy problem (2.14) for the functions $v_i(t)$, $\mu_i(t)$ and $\rho_i(t)$. □

Since in this chapter we assume $\gamma = \zeta$, substituting the definition of $h(t) = \gamma$ leads to the following set of ODEs:

$$\begin{cases} v_i'(t) = 2\left(\gamma - \beta_i v_i^2(t)\right), \\ \mu_i'(t) = \dfrac{2\gamma}{v_i(t)}\left(\varphi(t) - \mu_i(t)\right), \\ \rho_i'(t) = \left(F_i(t) - d\rho(t)\right)\rho_i(t), \qquad \text{for } \ i \in \{H, L\}, \\ v_i(0) = v_i^0, \quad \mu_i(0) = \mu_i^0, \quad \rho_i(0) = \rho_i^0, \\ \rho(t) = \rho_H(t) + \rho_L(t), \end{cases} \tag{2.22}$$

where

$$F_i(t) \equiv F_i(t, v_i(t), \mu_i(t)) = \gamma\, g(t) - \frac{\gamma}{v_i(t)} - \gamma\left(\mu_i(t) - \varphi(t)\right)^2. \tag{2.23}$$

2.3.1 Constant environment

Focussing on the case of constant environment, we let the nutrient concentration be constant and thus we make the assumption

$$S(t) \equiv \overline{S} \geq 0, \tag{2.24}$$

which implies that

$$g(t) \equiv \overline{g} \quad \text{and} \quad \varphi(t) \equiv \overline{\varphi}. \tag{2.25}$$

In this case, our main results are summarised by Theorem 2.

Theorem 2. *Under assumptions* (2.4), (2.5), (2.7), (2.11) *and the additional assumption* (2.24), *the solution of the system of PDEs* (2.3) *subject to the initial condition* (2.12) *is of the Gaussian form* (2.13) *and satisfies the following:*

(i) if

$$\sqrt{\beta_L} \geq \sqrt{\gamma}\,\overline{g} \tag{2.26}$$

then

$$\lim_{t\to\infty} \rho_H(t) = 0 \quad \textit{and} \quad \lim_{t\to\infty} \rho_L(t) = 0; \tag{2.27}$$

(ii) if

$$\sqrt{\beta_L} < \sqrt{\gamma}\,\overline{g} \tag{2.28}$$

then

$$\lim_{t\to\infty} \rho_H(t) = 0, \quad \lim_{t\to\infty} \rho_L(t) = \frac{\sqrt{\gamma}}{d}\left(\sqrt{\gamma}\,\overline{g} - \sqrt{\beta_L}\right) \tag{2.29}$$

and

$$\lim_{t\to\infty} \mu_L(t) = \overline{\varphi}, \quad \lim_{t\to\infty} \sigma_L^2(t) = \sqrt{\frac{\beta_L}{\gamma}}. \tag{2.30}$$

Proof. Under the additional assumption (2.24), Proposition 1 ensures that the population density function $n_i(x,t)$ is of the Gaussian form (2.13) with the population size, $\rho_i(t)$, the mean phenotypic state, $\mu_i(t)$, and the inverse of the related variance, $v_i(t) = 1/\sigma_i^2(t)$, being governed by the Cauchy problem (2.22) with $g(t) \equiv \overline{g}$ and $\varphi(t) \equiv \overline{\varphi}$.

In this framework, we divide the proof of Theorem 2 into four steps. We study the asymptotic behaviour of $v_i(t)$, $\mu_i(t)$ and $F_i(t)$ for $t \to \infty$ (Step 1). We show that $\rho_i(t)$ is non-negative and uniformly bounded (Step 2). Finally, we prove claim (2.27) (Step 3), and we conclude with the proof of claims (2.29) and (2.30) (Step 4).

Step 1: asymptotic behaviour of $v_i(t)$, $\mu_i(t)$ and $F_i(t)$ for $t \to \infty$. Solving the separable first-order ODE $(2.22)_1$ for $v_i(t)$ and imposing the initial condition $(2.22)_4$ gives

$$v_i(t) = \sqrt{\frac{\gamma}{\beta_i}}\,\frac{\sqrt{\gamma/\beta_i} + v_i^0 - \left(\sqrt{\gamma/\beta_i} - v_i^0\right)\exp\left(-4\sqrt{\gamma\,\beta_i}\,t\right)}{\sqrt{\gamma/\beta_i} + v_i^0 + \left(\sqrt{\gamma/\beta_i} - v_i^0\right)\exp\left(-4\sqrt{\gamma\beta_i}\,t\right)}, \tag{2.31}$$

which implies that

$$v_i(t) \to \sqrt{\frac{\gamma}{\beta_i}} \quad \text{exponentially fast as } t \to \infty. \tag{2.32}$$

Moreover, solving the ODE $(2.22)_2$ for $\mu_i(t)$ by the integrating factor method and imposing the initial condition $(2.22)_4$ yields

$$\mu_i(t) = \mu_i^0 \exp\left(-2\gamma\int_0^t \frac{\mathrm{d}s}{v_i(s)}\right) + \overline{\varphi}\left[1 - \exp\left(-2\gamma\int_0^t \frac{\mathrm{d}s}{v_i(s)}\right)\right], \tag{2.33}$$

from which, using the positivity of $v_i(t)$, we find that

$$\mu_i(t) \to \overline{\varphi} \quad \text{exponentially fast as } t \to \infty. \tag{2.34}$$

Lastly, noting that, under the additional assumption (2.24), the function $F_i(t)$ defined by Equation (2.23) reads as

$$F_i(t) = \gamma\,\overline{g} - \frac{\gamma}{v_i(t)} - \gamma\,(\mu_i(t) - \overline{\varphi})^2\,, \tag{2.35}$$

the asymptotic results (2.32) and (2.34) allow us to conclude that

$$F_i(t) \to \gamma\,\overline{g} - \sqrt{\gamma\,\beta_i} \quad \text{exponentially fast as } t \to \infty. \tag{2.36}$$

Step 2: non-negativity and boundedness of $\rho_i(t)$. Solving the ODE $(2.22)_3$ for ρ_i and imposing the initial condition $(2.22)_4$ yields

$$\rho_i(t) = \rho_i^0 \exp\left[\int_0^t (F_i(s) - d\rho(s))\,\mathrm{d}s\right]. \tag{2.37}$$

This result, along with the positivity of ρ_i^0, implies that

$$\rho_i(t) \geq 0 \quad \text{for all } t \geq 0. \tag{2.38}$$

Moreover, substituting Equation (2.35) into the ODE $(2.22)_3$ for ρ_i yields

$$\rho_i'(t) = \left[\gamma\,\overline{g} - \frac{\gamma}{v_i(t)} - \gamma\,(\mu_i(t) - \overline{\varphi})^2\right]\rho_i(t) - d\,(\rho_i(t) + \rho_j(t))\;\rho_i(t), \tag{2.39}$$

with $j = L$ if $i = H$ and $j = H$ if $i = L$. Estimating from above the right-hand side of the latter ODE by using the non-negativity of $\rho_j(t)$ [cf. the uniform lower bound (2.38)], the positivity of $v_i(t)$ [cf. expression (2.31)] and the fact that $\overline{g} < 2$ [cf. definition (2.11)], we obtain the differential inequality

$$\rho_i'(t) \leq (2\gamma - d\,\rho_i(t))\,\rho_i(t),$$

which gives the uniform upper bound

$$\rho_i(t) \leq \max\left\{\rho_i^0, \frac{2\,\gamma}{d}\right\} \quad \text{for all } t \geq 0. \tag{2.40}$$

Step 3: proof of claim (2.27)**.** Combining the asymptotic result (2.36) with the expression (2.37) for ρ_i we find that

$$\rho_i(t) \sim C\rho_i^0 \exp\left[\left(\gamma\overline{g} - \sqrt{\gamma\,\beta_i}\right)t - d\int_0^t \rho(s)\,\mathrm{d}s\right] \quad \text{as } \; t \to \infty, \tag{2.41}$$

for some positive constant C. Since the function $\rho(t)$ is non-negative [*cf.* the uniform lower bound (2.38)], the asymptotic relation (2.41) ensures that

$$\text{if} \quad \sqrt{\beta_i} \geq \sqrt{\gamma}\,\overline{g} \quad \text{then} \quad \lim_{t\to\infty} \rho_i(t) = 0. \tag{2.42}$$

Under assumption (2.4) and the additional assumption (2.26), claim (2.27) follows from the asymptotic result (2.42).

Step 4: proof of claims (2.29) **and** (2.30)**.** As long as $\rho_H(t) > 0$, we can compute the quotient of $\rho_L(t)$ and $\rho_H(t)$ through Equation (2.37). In so doing we find

$$\frac{\rho_L(t)}{\rho_H(t)} = \frac{\rho_L^0}{\rho_H^0} \exp\left[\int_0^t (F_L(s) - F_H(s))\,\mathrm{d}s\right]. \tag{2.43}$$

Using the limit (2.36) for F_i, we then have

$$\frac{\rho_L(t)}{\rho_H(t)} \sim C \exp\left[\sqrt{\gamma}\,\left(\sqrt{\beta_H} - \sqrt{\beta_L}\right) t\right] \quad \text{as} \quad t \to \infty, \tag{2.44}$$

for some positive constant C. Under assumption (2.4), the asymptotic relation (2.44) gives

$$\lim_{t\to\infty} \frac{\rho_L(t)}{\rho_H(t)} = \infty$$

and, since ρ_L is uniformly bounded from above [cf. the uniform upper bound (2.40)], we conclude that

$$\rho_H(t) \to 0 \quad \text{exponentially fast as } t \to \infty. \tag{2.45}$$

We can rewrite the ODE $(2.22)_3$ for ρ_L as

$$\rho_L'(t) = \left[\left(\gamma\overline{g} - \sqrt{\gamma\,\beta_L} + \eta(t)\right) - d\rho_L(t)\right]\rho_L(t), \tag{2.46}$$

where the function $\eta(t)$ is defined as

$$\eta(t) = \left(\sqrt{\gamma\,\beta_L} - \frac{\gamma}{v_L(t)}\right) - \gamma\,(\mu_L(t) - \overline{\varphi})^2 - d\rho_H(t).$$

Using the asymptotic results (2.32), (2.34) and (2.45), we see that

$$\eta(t) \to 0 \quad \text{exponentially fast as } t \to \infty. \tag{2.47}$$

Solving the ODE (2.46) complemented with the initial condition $\rho_L(0) = \rho_L^0$ yields [190]

$$\rho_L(t) = \frac{\rho_L^0 \exp\left[\displaystyle\int_0^t \left(\gamma\overline{g} - \sqrt{\gamma\,\beta_L} + \eta(s)\right)\mathrm{d}s\right]}{1 + d\,\rho_L^0 \displaystyle\int_0^t \exp\left[\int_0^s \left(\gamma\overline{g} - \sqrt{\gamma\,\beta_L} + \eta(z)\right)\mathrm{d}z\right]\mathrm{d}s}. \tag{2.48}$$

The result (2.47) ensures that in the asymptotic regime $t \to \infty$ we have

$$\exp\left[\int_0^t \left(\gamma\overline{g} - \sqrt{\gamma\,\beta_L} + \eta(s)\right)\mathrm{d}s\right] \sim C\,\exp\left[\left(\gamma\overline{g} - \sqrt{\gamma\,\beta_L}\right) t\right]$$

and, under the additional assumption (2.28), we also have

$$\int_0^t \exp\left[\int_0^s \left(\gamma\overline{g} - \sqrt{\gamma\,\beta_L} + \eta(z)\right)\mathrm{d}z\right]\mathrm{d}s \sim C\,\frac{\exp\left[\left(\gamma\overline{g} - \sqrt{\gamma\,\beta_L}\right)\,t\right]}{\gamma\overline{g} - \sqrt{\gamma\,\beta_L}},$$

for some positive constant C. These asymptotic relations, along with the expression (2.48) for ρ_L, allow us to conclude that

$$\lim_{t\to\infty} \rho_L(t) = \frac{\gamma\overline{g} - \sqrt{\gamma\,\beta_L}}{d}. \tag{2.49}$$

Claims (2.29) and (2.30) follow from the asymptotic results (2.45) and (2.49), and the asymptotic results (2.34) and (2.32) with $i = L$. □

The asymptotic results established by Theorem 2 provide a mathematical formalisation of the idea that in constant environments:

1. populations undergoing spontaneous phenotypic variation at a rate that is too large compared to the maximum fitness will ultimately go extinct [cf. point (i) in Theorem 2];

2. *ceteris paribus*, if at least one population undergoes spontaneous phenotypic variation at a rate sufficiently small compared to the maximum fitness [cf. point (ii) in Theorem 2] then:

   2(a). the population with the lower rate of phenotypic variation will outcompete the other population;

   2(b). the equilibrium phenotype distribution of the surviving population will be unimodal with the mean phenotype corresponding to the fittest phenotypic state and the related variance being directly proportional to the rate of phenotypic variations.

Biologically, we can interpret our results as follows. If the rate of heritable, spontaneous phenotypic variations is too high (Assumption (2.26)), then we might expect to observe extinction of both populations. For instance, this is observed in many biological asexually reproducing systems that accumulate too many deleterious mutations and undergo mutational meltdown [197]. However, if the rate of phenotypic variation is relatively small compared to the maximal proliferation rate (Assumption (2.28)), then we expect the population with the lower rate of phenotypic variation to be selected. The surviving cells will obtain the fitness state corresponding to the fittest phenotypic state for a given environment. In other words, a specialist population is selected in a constant environment, which is in agreement with the ecological literature [198].

2.3.2 Periodically fluctuating environment

We now focus on the case of environments that undergo fluctuations with period $T > 0$, and we assume the nutrient concentration to be Lipschitz continuous and T-periodic, i.e. we let $S : [0, \infty) \to \mathbb{R}_{\geq 0}$ satisfy the assumptions

$$S \in \mathrm{Lip}([0, \infty)) \quad \text{and} \quad S(t + T) = S(t) \quad \text{for all } t \geq 0, \tag{2.50}$$

which implies that the functions $g(t)$ and $\varphi(t)$ satisfy the assumptions

$$g, \varphi \in \mathrm{Lip}([0, \infty)), \;\; g(t + T) = g(T) \;\text{ and }\; \varphi(t + T) = \varphi(T) \;\text{ for all } t \geq 0. \tag{2.51}$$

Our main results are summarised by Theorem 5, the proof of which relies on the results established by Lemma 3 and Lemma 4.

Lemma 3. *Under assumptions* (2.5), (2.7), (2.11) *and* (2.50), *the unique real periodic solution of the problem*

$$\begin{cases} u_i'(t) = 2\sqrt{\gamma\,\beta_i}\,\left(\varphi(t) - u_i(t)\right), & \text{for } t \in (0, T), \\ u_i(0) = u_i(T), \end{cases} \tag{2.52}$$

is

$$\begin{aligned} u_i(t) = {} & \frac{2\sqrt{\gamma\beta_i}\exp\left(-2\sqrt{\gamma\beta_i}t\right)}{\exp\left(2\sqrt{\gamma\beta_i}\,T\right) - 1} \int_0^T \exp\left(2\sqrt{\gamma\beta_i}\,s\right)\varphi(s)\,\mathrm{d}s \\ & + 2\sqrt{\gamma\beta_i}\exp\left(-2\sqrt{\gamma\beta_i}\,t\right)\int_0^t \exp\left(2\sqrt{\gamma\beta_i}\,s\right)\varphi(s)\,\mathrm{d}s, \end{aligned} \tag{2.53}$$

and satisfies the integral identity

$$\frac{1}{T}\int_0^T u_i(t)\,\mathrm{d}t = \frac{1}{T}\int_0^T \varphi(t)\,\mathrm{d}t. \tag{2.54}$$

Lemma 4. *Let*

$$\Lambda_i = \sqrt{\beta_i} + \frac{\sqrt{\gamma}}{T}\int_0^T \left(u_i(s) - \varphi(s)\right)^2\,\mathrm{d}s \quad \text{for} \quad i \in \{H, L\}, \tag{2.55}$$

and

$$Q_i(t) = \gamma\,g(t) - \sqrt{\gamma\beta_i} - \gamma\left(u_i(t) - \varphi(t)\right)^2 \tag{2.56}$$

with $u_i(t)$ given by Equation (2.53). *Under assumptions* (2.5), (2.7), (2.11), (2.50) *and the additional assumption*

$$\Lambda_i < \frac{\sqrt{\gamma}}{T}\int_0^T g(t)\,\mathrm{d}t,$$

the unique real non-negative periodic solution of the problem

$$\begin{cases} w_i'(t) = \left(Q_i(t) - d\,w_i(t)\right)w_i(t), & \text{for } t \in (0, T), \\ w_i(0) = w_i(T), \end{cases} \tag{2.57}$$

is

$$w_i(t) = \frac{d^{-1}\exp\left(\int_0^t Q_i(s)\,\mathrm{d}s\right)}{\dfrac{\int_0^T \exp\left(\int_0^s Q_i(z)\,\mathrm{d}z\right)\mathrm{d}s}{\exp\left(\int_0^T Q_i(s)\,\mathrm{d}s\right)-1} + \int_0^t \exp\left(\int_0^s Q_i(z)\,\mathrm{d}z\right)\mathrm{d}s} \tag{2.58}$$

and satisfies the integral identity

$$\frac{1}{T}\int_0^T w_i(t)\,\mathrm{d}t = \frac{1}{d}\left(\frac{\gamma}{T}\int_0^T g(t)\,\mathrm{d}s - \sqrt{\gamma}\,\Lambda_i\right). \tag{2.59}$$

The proofs of Lemmas 3 and 4 can be obtained by solving the ODEs (2.52) and (2.57) using the integrating factor technique. We refer the reader to Appendices (A.3) and (A.4) in [182] for the complete proofs.

Theorem 5. *Under assumptions* (2.4), (2.5), (2.7), (2.11) *and the additional assumptions* (3.29), *the solution of the system of PDEs* (2.3) *subject to the initial condition* (2.12) *is of the Gaussian form* (2.13) *and satisfies the following:*

(i) if

$$\min\{\Lambda_H, \Lambda_L\} \;\geq\; \frac{\sqrt{\gamma}}{T}\int_0^T g(t)\,\mathrm{d}t \tag{2.60}$$

then

$$\lim_{t\to\infty}\rho_H(t) = 0 \quad \textit{and} \quad \lim_{t\to\infty}\rho_L(t) = 0; \tag{2.61}$$

(ii) if

$$\min\{\Lambda_H, \Lambda_L\} \;<\; \frac{\sqrt{\gamma}}{T}\int_0^T g(t)\,\mathrm{d}t, \tag{2.62}$$

and

$$i = \arg\min_{k\in\{H,L\}}\Lambda_k, \quad j = \arg\max_{k\in\{H,L\}}\Lambda_k \tag{2.63}$$

then

$$\rho_j(t)\to 0 \quad \textit{and} \quad \rho_i(t)\to w_i(t) \quad \textit{as } t\to\infty, \tag{2.64}$$

and

$$\mu_i(t)\to u_i(t) \quad \textit{and} \quad \sigma_i^2(t)\to\sqrt{\frac{\beta_i}{\gamma}} \quad \textit{as } t\to\infty, \tag{2.65}$$

with $w_i(t)$ and $u_i(t)$ given by Equations (2.58) *and* (2.53), *respectively.*

Proof. Proposition 1 ensures that the population density function $n_i(x,t)$ is of the Gaussian form (2.13) with the population size, $\rho_i(t)$, the mean phenotypic state, $\mu_i(t)$, and the inverse of the related variance, $v_i(t) = 1/\sigma_i^2(t)$, being governed by the Cauchy problem (2.22).

In this framework, we prove Theorem 5 in 4 steps. In Step 1 we study the asymptotic behaviour of $v_i(t)$, $\mu_i(t)$ and $F_i(t)$ for $t \to \infty$. In Step 2 we show that $\rho_i(t)$ is non-negative and uniformly bounded. In Step 3 we prove claim (2.61). Finally, in Step 4 we prove claims (2.64) and (2.65).

Step 1: asymptotic behaviour of $v_i(t)$, $\mu_i(t)$ and $F_i(t)$ for $t \to \infty$. Since the ODE $(2.22)_1$ does not depend on $S(t)$, the expression (2.31) of $v_i(t)$ obtained in the proof of Theorem 2 still holds and

$$v_i \to \sqrt{\frac{\gamma}{\beta_i}} \quad \text{exponentially fast as } t \to \infty. \tag{2.66}$$

Moreover, using the asymptotic result (2.66) along with the linear ODE $(2.22)_2$ for $\mu_i(t)$ one can easily show that

$$\mu_i(t) \to u_i(t) \quad \text{exponentially fast as } t \to \infty \tag{2.67}$$

where $u_i(t)$ is a T-periodic solution of the ODE (2.52). Lemma 3 ensures that $u_i(t)$ is given by Equation (2.53). Lastly, for $F_i(t)$ defined according to Equation (2.23), the asymptotic results (2.66) and (2.67) allow us to conclude that

$$F_i(t) \to \gamma\, g(t) - \sqrt{\gamma\, \beta_i} - \gamma \left(u_i(t) - \varphi(t)\right)^2 \quad \text{exponentially fast as } t \to \infty. \tag{2.68}$$

Step 2: non-negativity and boundedness of $\rho_i(t)$. Proceeding in a similar way as in the proof of Theorem 2 (cf. Step 2 in the proof of Theorem 2), one can prove that

$$0 \leq \rho_i(t) \leq \max\left\{\rho_i^0, \frac{2\,\gamma}{d}\right\} \quad \text{for all } t \geq 0. \tag{2.69}$$

Step 3: proof of claim (2.61). Solving the ODE $(2.22)_3$ for ρ_i and imposing the initial condition $(2.22)_4$ yields

$$\rho_i(t) = \rho_i^0 \exp\left[\int_0^t \left(F_i(s) - d\rho(s)\right) \mathrm{d}s\right], \tag{2.70}$$

with $F_i(t)$ defined according to Equation (2.23). Combining the asymptotic result (2.68) with the expression (2.70) for $\rho_i(t)$ gives

$$\begin{aligned} \rho_i(t) \quad \sim \quad C\,\rho_i^0 \exp\Bigg[\gamma \int_0^t g(s)\,\mathrm{d}s - \sqrt{\gamma\,\beta_i}\,t - \gamma \int_0^t \left(u_i(s) - \varphi(s)\right)^2 \mathrm{d}s \\ -d\int_0^t \rho(s)\,\mathrm{d}s\Bigg] \quad \text{as } t \to \infty, \end{aligned} \tag{2.71}$$

for some positive constant C. Hence, using the fact that the functions $g(t)$, $\varphi(t)$ and $u_i(t)$ are T-periodic, and considering $\mathrm{m} \to \infty$ we find

$$\rho_i(t) \sim C \exp\left[\gamma\,\mathrm{m}\int_0^T g(t)\,\mathrm{d}t - \mathrm{m}\,T\sqrt{\gamma\,\beta_i} - \gamma\,\mathrm{m}\int_0^T \left(u_i(t)-\varphi(t)\right)^2\,\mathrm{d}t - d\int_0^t \rho(s)\,\mathrm{d}s\right] \quad \text{as } t\to\infty, \tag{2.72}$$

for some positive constant C. Since the function $\rho(t)$ is non-negative [cf. the uniform lower bound (2.69)], the asymptotic relation (2.72) ensures that if

$$\sqrt{\beta_i} + \frac{\sqrt{\gamma}}{T}\int_0^T \left(u_i(t)-\varphi(t)\right)^2\,\mathrm{d}t \geq \frac{\sqrt{\gamma}}{T}\int_0^T g(t)\,\mathrm{d}t$$

then

$$\lim_{t\to\infty} \rho_i(t) = 0. \tag{2.73}$$

This proves that if assumption (2.60) is satisfied then claim (2.61) is verified.

Step 4: proof of claims (2.64) **and** (2.65)**.** Let $j = L$ if $i = H$ and $j = H$ if $i = L$. As long as $\rho_j(t) > 0$, we can compute the quotient of $\rho_i(t)$ and $\rho_j(t)$ through (2.70). In so doing, using the asymptotic relation (2.71) for $\rho_i(t)$ and $\rho_j(t)$ and considering $\mathrm{m} \to \infty$ we obtain

$$\frac{\rho_i(t)}{\rho_j(t)} \sim C \exp\left[\mathrm{m}\,T\sqrt{\gamma}\left(\Lambda_j - \Lambda_i\right)\right] \quad \text{as } t\to\infty, \tag{2.74}$$

for some positive constant C, with Λ_i and Λ_j defined according to Equation (2.55). Choosing

$$j = \underset{k\in\{H,L\}}{\arg\max}\,\Lambda_k \quad \text{and} \quad i = \underset{k\in\{H,L\}}{\arg\min}\,\Lambda_k, \tag{2.75}$$

the asymptotic relation (2.74) allows us to conclude that

$$\lim_{t\to\infty}\frac{\rho_i(t)}{\rho_j(t)} = \infty, \quad \text{for } j = \underset{k\in\{H,L\}}{\arg\max}\,\Lambda_k \text{ and } i = \underset{k\in\{H,L\}}{\arg\min}\,\Lambda_k. \tag{2.76}$$

Since ρ_i is uniformly bounded from above [*cf.* the uniform upper bound (2.69)], the asymptotic result (2.76) implies that

$$\rho_j(t) \to 0 \quad \text{exponentially fast as } t\to\infty \quad \text{for } j = \underset{k\in\{H,L\}}{\arg\max}\,\Lambda_k. \tag{2.77}$$

We can rewrite the ODE $(2.22)_3$ for ρ_i with $i = \underset{k\in\{H,L\}}{\arg\min}\,\Lambda_k$ as

$$\rho_i'(t) = \left[\gamma g(t) - \sqrt{\gamma\,\beta_i} - \gamma\,\left(u_i(t)-\varphi(t)\right)^2 + \eta(t) - d\rho_i(t)\right]\rho_i(t), \tag{2.78}$$

where the function $\eta(t)$ is defined as

$$\eta(t) = \left(\sqrt{\gamma\,\beta_i} - \frac{\gamma}{v_i(t)}\right) + \gamma\,\left[(u_i(t)-\varphi(t))^2 - (\mu_i(t)-\varphi(t))^2\right] - d\rho_j(t)$$

with $j = \underset{k\in\{H,L\}}{\arg\max}\,\Lambda_k$. Using the asymptotic results (2.66), (2.67) and (2.77) we see that $\eta(t) \to 0$ exponentially fast as $t \to \infty$. Hence, $\rho_i(t) \to \tilde{\rho}_i(t)$ as $t \to \infty$, with $\tilde{\rho}_i(t)$ being the solution of the ODE

$$\tilde{\rho}_i' = f(\tilde{\rho}_i, t), \tag{2.79}$$

with

$$f(\tilde{\rho}_i, t) = \left[\gamma g(t) - \sqrt{\gamma\,\beta_i} - \gamma\,(u_i(t)-\varphi(t))^2 - d\tilde{\rho}_i\right]\tilde{\rho}_i,$$

subject to an initial condition $0 < \tilde{\rho}_i(0) < \infty$. We note that: (i) the function $\tilde{\rho}_i(t)$ is uniformly bounded as it satisfies the upper and lower bounds

$$0 \le \tilde{\rho}_i(t) \le \max\left\{\tilde{\rho}_i(0), \frac{2\,\gamma}{d}\right\} \quad \text{for all } t \ge 0;$$

(ii) the function f is Lipschitz continuous in the first variable; (iii) the function f is Lipschitz continuous and T-periodic in the second variable, since g, φ and u_i are T-periodic Lipschitz continuous functions of t [cf. assumptions (2.51) and expression (2.53)]. Therefore, the conditions of Massera's Convergence Theorem [199, 200] are satisfied and this allows us to conclude that

$$\tilde{\rho}_i(t) \longrightarrow w_i(t) \quad \text{as } t \to \infty, \tag{2.80}$$

with $w_i(t)$ being a non-negative T-periodic solution of the ODE (2.57). Under the additional assumption (2.62), that is,

$$\Lambda_i < \frac{\sqrt{\gamma}}{T}\int_0^T g(t)\,\mathrm{d}t,$$

Lemma 4 ensures that $w_i(t)$ is given by Equation (2.58). Claims (2.64) and (2.65) follow from the asymptotic results (2.77) and (2.80), the asymptotic result (2.67) and the result (2.66) with $i = \underset{k\in\{H,L\}}{\arg\min}\,\Lambda_k$. □

Since the functions $u_i(t)$ and $w_i(t)$ are T-periodic and satisfy the integral identities (2.54) and (2.59), respectively, the results established by Theorem 5 show that the long-term limits of the size and the mean phenotypic state of the surviving population are periodic functions of time with period T and mean values given by Equations (2.54) and (2.59), respectively.

Using the ODE (2.52) for $u_i(t)$ one can easily obtain

$$\frac{\mathrm{d}}{\mathrm{d}t}\,(u_i-\varphi)^2 = 4\,\gamma\,\sqrt{\gamma\,\beta_i}\left[\frac{1}{2}\,\frac{1}{\sqrt{\gamma\,\beta_i}}\,(\varphi-u_i)\,\frac{\mathrm{d}\varphi}{\mathrm{d}t} - (u_i-\varphi)^2\right].$$

Integrating both sides of the above equation with respect to t between 0 and T, and using the fact that $u_i(T) - \varphi(T) = u_i(0) - \varphi(0)$, yields

$$\frac{1}{T}\int_0^T (u_i(t) - \varphi(t))^2 \, \mathrm{d}t = \frac{1}{2\sqrt{\gamma\,\beta_i}}\,\frac{1}{T}\int_0^T (\varphi(t) - u_i(t))\,\varphi'(t)\,\mathrm{d}t. \tag{2.81}$$

Therefore, definition (2.55) can be rewritten as

$$\Lambda_i = \sqrt{\beta_i} + \frac{1}{2\sqrt{\beta_i}}\,\frac{1}{T}\int_0^T (\varphi(t) - u_i(t))\,\varphi'(t)\,\mathrm{d}t. \tag{2.82}$$

If $S \equiv \bar{S}$ then $g(t) \equiv \overline{g}$ and $\varphi(t) \equiv \overline{\varphi}$ (i.e. $\varphi' \equiv 0$). In this case

$$\frac{\sqrt{\gamma}}{T}\int_0^T g(t)\,\mathrm{d}t = \overline{g}$$

and (2.82) allow one to see that $\Lambda_i = \sqrt{\beta_i}$. Hence, if S is constant then the results of Theorem 5 reduce to the results of Theorem 2. Moreover, the first term in the expression (2.82) for Λ_i is clearly a monotonically increasing function of β_i, whereas the factor in front of the integral in the second term is a monotonically decreasing function of β_i. Hence, if the mean value of the $T-$periodic function $(\varphi(t) - u_i(t))\,\varphi'(t)$ is sufficiently small then $\Lambda_H > \Lambda_L$, while if such a mean value is sufficiently large then $\Lambda_H < \Lambda_L$. We expect the latter scenario to occur when the variability and the rate of change of $S(t)$ are sufficiently high so as to cause substantial and sufficiently fast variations in the value of $\varphi(t)$.

The asymptotic results established by Theorem 5 formalise mathematically the idea that in periodically fluctuating environments:

1. populations undergoing spontaneous phenotypic variations at a rate too large compared to the mean value of the maximum fitness will ultimately go extinct [cf. point (i) in Theorem 5];

2. *ceteris paribus*, if at least one population undergoes spontaneous phenotypic variations at a rate sufficiently small compared to the mean value of the maximum fitness, then the following behaviours are possible:

   2(a). when environmental conditions are relatively stable, the population with the lower rate of phenotypic variation will outcompete the other population;

   2(b). when environmental conditions undergo drastic changes, either both populations go extinct or the population with the higher rate of phenotypic variations will outcompete the other population;

   2(c). the phenotype distribution of the surviving population will be unimodal, and both the population size and the mean phenotype will become periodic;

2(d). ultimately, the population size and the mean phenotype will both oscillate with the same period as the fluctuating environment, and the mean value (with respect to time) of the mean phenotype will be the same as the mean value of the fittest phenotypic state with the related variance being directly proportional to the rate of phenotypic variations.

We can interpret these analytical results as follows. Similar to the case where the environment is constant (Theorem 2), when the rate of the phenotypic variation is relatively high the population might become extinct. Furthermore, we formally show that if the environmental conditions undergo mild fluctuations, then the population with the lower rate of phenotypic variations is selected. In this case, a more specialised population survives. However, if the environment undergoes drastic changes (i.e. cells experience periods of harsh and good conditions), then the population with the higher rate of phenotypic variations has a competitive advantage and survives. Moreover, in this case we expect higher level of phenotypic heterogeneity. This observation is consistent with experimental studies in which cells grown under intermittent hypoxia demonstrated phenotypic diversity [47].

2.4 Results of numerical simulations

In this section, we construct numerical solutions to the system of non-local parabolic PDEs (2.3) subject to the initial condition (2.12).

2.4.1 Numerical methods and set-up of numerical simulations

The above model has a set of parameters that can be chosen in order to represent certain biological experimental systems (e.g. *in vitro* experiments). However, in order to uniquely recover a parameter set given available, error-free data, one must perform structural identifiability analysis [202]. There exist various methods for the analysis of global identifiability for nonlinear systems, reviewed and compared in [203, 204]. However, such analysis is beyond the scope of this thesis and will remain as future work.

The parameter values used to carry out the numerical simulations are chosen in order to demonstrate the behaviour expected from the analysis and are listed in Table 2.1. In order to capture the fact that rates of heritable spontaneous phenotypic variations are small, in general, and much smaller than maximum proliferation rates, in particular, we assume $\beta_i \ll \gamma$ for $i \in \{H, L\}$. Furthermore, given the values of γ and β_i, we fix the value of d to be such that the long-term limit (2.29) of the size of the population L is approximatively 10^4, which is consistent with biological data from the existing literature regarding *in vitro* cell populations [205].

We remark that the value of the parameter β_L and the range of values of the parameter β_H reported in Table 2.1 are such that neither condition (2.26) nor condition (2.60) are met in all cases on which we report in this section. This ensures that the two populations do not simultaneously go extinct. We relax this assumption only in Figure 2.3 in order to demonstrate complete extinction.

Parameter	**Description**	**Value / Value range**
γ	Maximum proliferation rate	100
d	Death rate due to competition	0.01
β_L	Rate of phenotypic variations of population L	0.01
β_H	Rate of phenotypic variations of population H	[0.01, 0.1]
κ	Half-maximum concentration of nutrient	1

Table 2.1: Parameter values used to carry out numerical simulations.

In this chapter, we consider both populations to have the same initial phenotypic distribution (2.12) with $v_i^0 = 20$, $\mu_i^0 = 0$ and $\rho_i^0 \approx 800$ for $i \in \{H, L\}$.

The method for constructing numerical solutions to the system of non-local parabolic PDEs (2.3) is based on an explicit finite difference scheme in which a three-point stencil is used to approximate the diffusion terms and an explicit finite difference scheme is used for the reaction term [201]. We use the MATLAB built-in solver ODE45 to solve numerically the Cauchy problem (2.22) for $v_i(t)$, $\mu_i(t)$ and $\rho_i(t)$. We validate the numerical scheme by comparing the solutions of PDEs (2.3) and ODEs (2.22) with the explicit solutions for the inverse of variance, mean phenotype and population size given by Equations (2.31), (2.33) and (2.37), respectively. Particularly, we demonstrate the comparison between the PDEs and ODEs in Figure 2.5.

In order to choose the discretisation values, i.e. the time step, Δt, phenotype step, Δx, and the phenotype interval, $[-L, L]$, we used the convergence test results presented in Figure 2.2. Here, we calculated the difference between the solutions of the system of PDEs (2.3) and the analytic solutions given by Equations (2.31), (2.33) and (2.37). We considered the difference between the total population size values at the end of the simulation

$$E_1 = \left| \rho^a(t_f) - \rho^{pde}(t_f) \right|, \tag{2.83}$$

and the maximal difference between population densities at the end of the simulation

$$E_2 = \max\left(\left| n_L^a(x, t_f) - n_L^{pde}(x, t_f) \right| \right), \tag{2.84}$$

where ^{a} denotes analytical and ^{pde} denotes numerical solutions. We choose the final time to be $t_f = 40$ as at this time the solutions are sufficiently close to their equilibrium value.

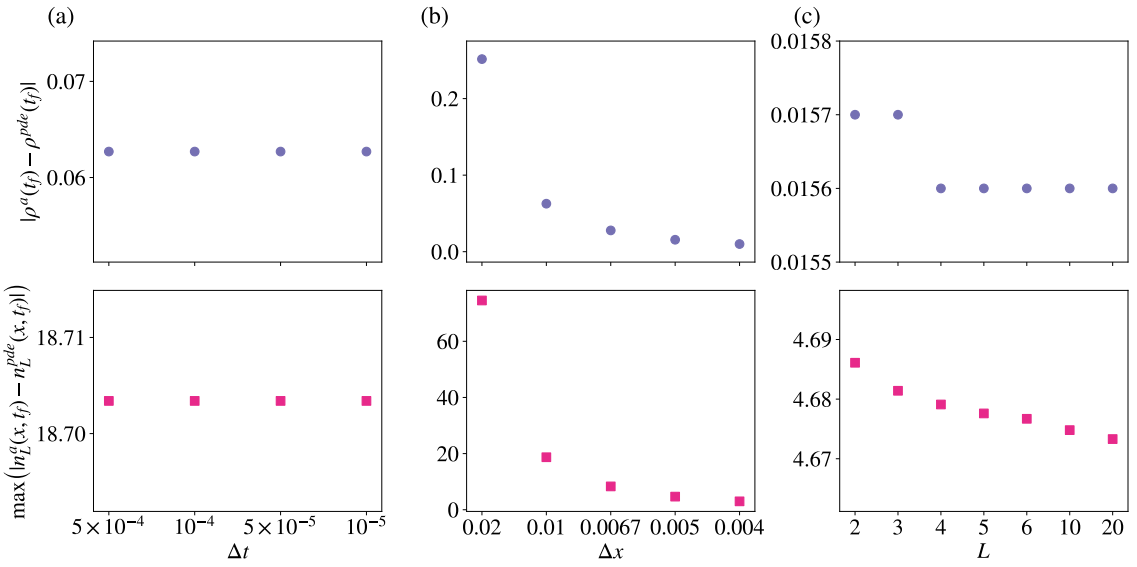

Figure 2.2: **(a)** Plot of the differences between analytical (Equations (2.31), (2.33), and (2.37)) and numerical (Equations (2.3)) solutions for the total population size defined in Equation (2.83) (top) and the population density given by Equation (2.84) for different time steps, Δt. Here, the environment is constant with $S = 1$. We use parameter values defined in Table 2.1 with $\Delta x = 0.01$. **(b)** Same as **(a)** but for different phenotype step size, Δx, with $\Delta t = 0.0001$. **(c)** Same as **(b)** but for different phenotype domain interval defined as $[-L, L]$ with $\Delta x = 0.005$ and $\Delta t = 0.0001$.

Based on the results in Figure 2.2, we select a uniform discretisation consisting of 2000 points on the interval $[-5, 5]$ (corresponding to $\Delta x = 0.005$) as the computational domain of the independent variable x and impose no flux boundary conditions. Moreover, we assume $t \in [0, t_f]$, with $t_f > 0$ being the final time of simulation, and we discretise the interval $[0, t_f]$ with the uniform step $\Delta t = 0.0001$ (unless stated otherwise in figure caption).

2.4.2 Demonstration of analytical results

We consider the following definition of the nutrient concentration

$$S(t) = M + A \sin\left(\frac{2\pi t}{T}\right). \tag{2.85}$$

In definition (2.85), the parameter $M > 0$ represents the mean nutrient concentration, while the parameter $A \geq 0$ models the semi-amplitude of the oscillations of the nutrient concentration, which have period $T > 0$. We consider only values of M and A such that $S(t) \geq 0$, i.e. $0 \leq A \leq M$.

First, we consider the case where the rate of phenotypic variations satisfies the assumption (2.26), i.e. the two populations undergo spontaneous phenotypic variations with very

high rate. In this case, according to Theorem 2, we expect extinction of both populations, as is demonstrated in Figure 2.3.

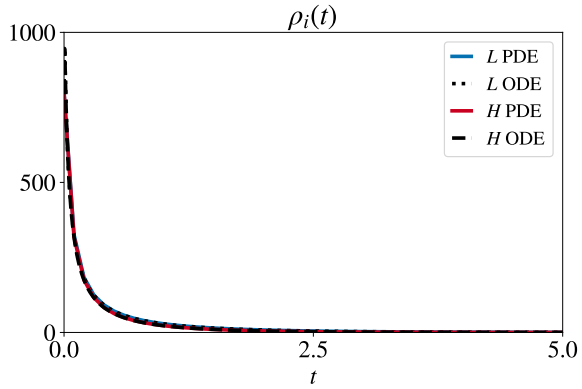

Figure 2.3: Plot of population sizes $\rho_H(t)$ and $\rho_L(t)$ obtained by computing numerically the integrals of the components of the numerical solution of the system of PDEs (2.3) subject to the initial condition (2.12). The dotted and dashed lines highlight, respectively, $\rho_L(t)$ and $\rho_H(t)$ obtained by solving numerically the Cauchy problem (2.22). The nutrient concentration $S(t)$ is defined according to Equation (2.85) with $M = 100$ and $A = 0$. The rates of phenotypic variation are chosen to satisfy Equation (2.26): $\beta_H = 100.5$, $\beta_L = 100$. We use $\Delta t = 10^{-7}$ and other parameters as listed in Table 2.1.

We then explore three prototypical scenarios exemplified by different values of the parameter A. In particular, we choose $M = 1$ and compare the numerical solutions obtained for $A = 0$ (i.e. constant nutrient concentration), $A = 0.5$ (i.e. lower nutrient variability) and $A = 1$ (i.e. higher nutrient variability). Figure 2.4 displays plots of the nutrient concentration $S(t)$ (top row), the rescaled maximum fitness $g(t)$ (middle row) and the fittest phenotypic state $\varphi(t)$ (bottom row) corresponding to these choices of the parameter A. These plots show that, as one would expect, higher nutrient variability brings about more pronounced variations in the rescaled maximum fitness and the fittest phenotypic state.

Figure 2.5 shows a comparison between the exact solutions (2.13) – with $v_i(t)$, $\mu_i(t)$ and $\rho_i(t)$ obtained by solving numerically the Cauchy problem (2.22) – and the numerical solutions of the system of non-local parabolic PDEs (2.3) subject to the initial condition (2.12). In agreement with the results established by Proposition 1, for all values of A considered, there is a perfect match between the population sizes obtained by computing numerically the integrals of the components of the numerical solution of the system of PDEs (2.3) (solid lines in the top row of Figure 2.5) and the population sizes obtained by solving numerically the Cauchy problem (2.22) (dashed and dotted lines in the top row of Figure 2.5). Similarly, there is excellent agreement between the population density functions obtained by solving numerically the system of PDEs (2.3) (solid lines in the bottom row of Figure 2.5) and the

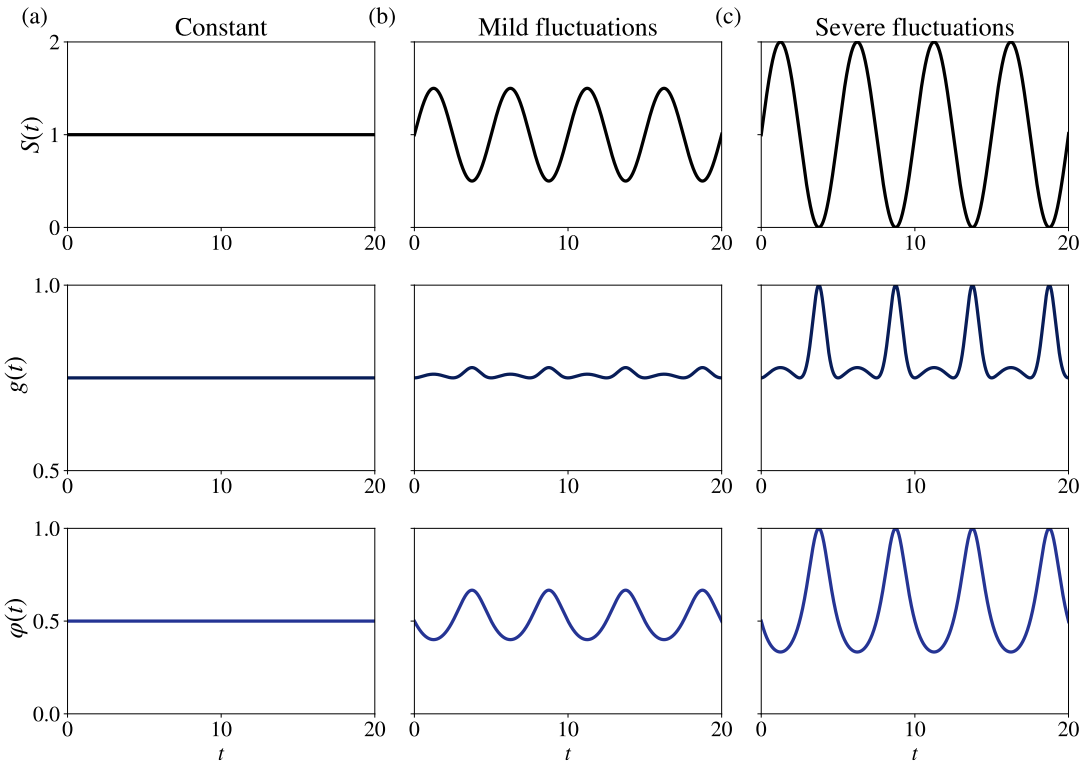

Figure 2.4: **(a)** Plots of the nutrient concentration $S(t)$ (top panel) defined according to Equation (2.85) with $M = 1$ and $A = 0$, the corresponding rescaled maximum fitness $g(t)$ (central panel), and fittest phenotypic state $\varphi(t)$ (bottom panel) defined according to Equation (2.11). **(b)** Same as column **(a)** but with $A = 0.5$ and $T = 5$. **(c)** Same as column **(b)** but with $A = 1$ and $T = 5$.

population density functions (2.13) with $v_i(t)$, $\mu_i(t)$ and $\rho_i(t)$ given by the numerical solutions of the Cauchy problem (2.22) (dashed and dotted lines in the bottom row of Figure 2.5).

In accord with the results of Theorem 2, when the nutrient concentration is constant (i.e. $S(t) \equiv M$), the population with the lower rate of phenotypic variation (population L) outcompetes the other population (Figure 2.5(a)). The size of the surviving population, $\rho_L(t)$, reaches the asymptotic value (2.29) and the phenotype distribution at the end of the simulations, $n_L(x, t_f)$, is Gaussian with mean and variance equal to the asymptotic values (2.30).

In agreement with the results established by Theorem 5, a similar outcome is observed in the presence of a low nutrient variability (Figure 2.5(b)). In fact, in this case $\Lambda_L < \Lambda_H$. On the other hand, when the nutrient variability is sufficiently high (Figure 2.5(c)), the population with the higher rate of phenotypic variation (population H) outcompetes the other population. This is due to the fact that in this case the condition condition

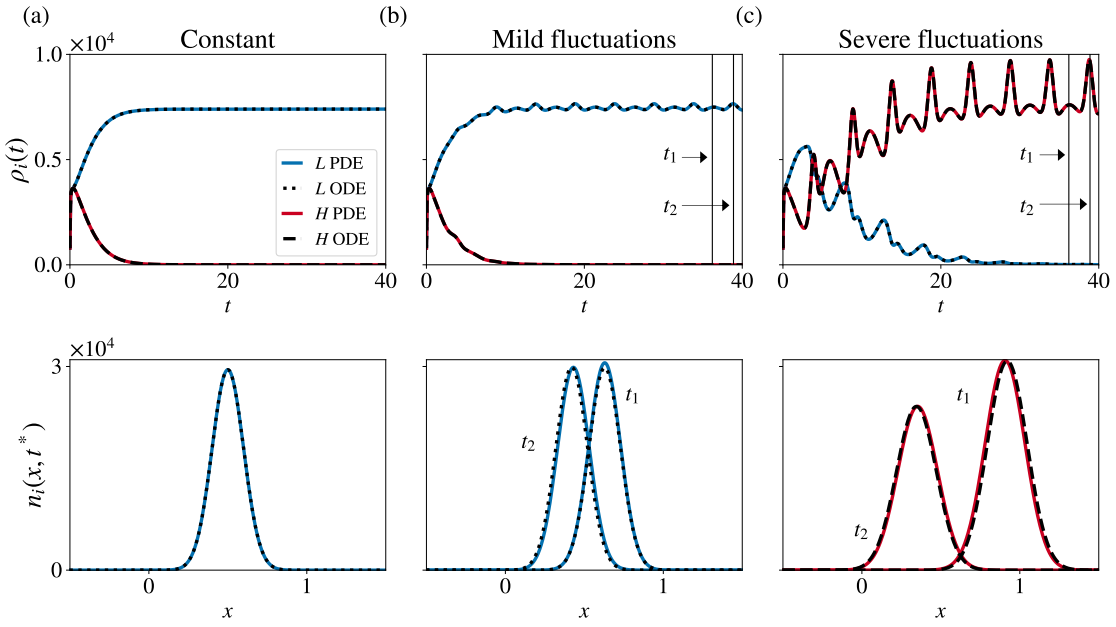

Figure 2.5: **(a)** Plots of the population sizes (top row) $\rho_H(t)$ (red line) and $\rho_L(t)$ (blue line) obtained by computing numerically the integrals of the components of the numerical solution of the system of PDEs (2.3) subject to the initial condition (2.12). The dotted and dashed lines highlight, respectively, $\rho_L(t)$ and $\rho_H(t)$, obtained by solving numerically the Cauchy problem (2.22). The nutrient concentration $S(t)$ is defined according to Equation (2.85) with $M = 1$ and $A = 0$. Plots of the corresponding phenotype distribution of the surviving population at $t = t_f$ obtained by solving numerically the system of PDEs (2.3) subject to the the initial condition (2.12). The dotted and dashed lines correspond to the exact phenotype distributions (2.13) with $v_i(t)$, $\mu_i(t)$ and $\rho_i(t)$ given by the numerical solutions of the Cauchy problem (2.22). The values of the model parameters are as listed in Table 2.1 with $\beta_H = 0.025$. **(b)** Same as **(a)** but for $A = 0.5$. **(c)** Same as **(a)** but for $A = 1$. In **(b)** and **(c)**, the phenotype distributions are plotted at $t = t_1$ and $t = t_2$ as indicated in the plots on the top panel.

$\Lambda_H < \Lambda_L$ is satisfied. As expected, since $A > 0$, both the size and the mean phenotype of the surviving population become T-periodic, with mean values given by Equations (2.54) and (2.59), respectively. Moreover, the phenotype distribution of the surviving population remains Gaussian with variance given by Equation (2.65). This implies that if population H outcompetes population L then the variance of the phenotype distribution (i.e. the level of phenotypic heterogeneity) will be ultimately larger than in the case where population L is selected.

Taken together, these results demonstrate that when the nutrient concentration is constant, or in the presence of a low level of nutrient variability, it is evolutionarily more desirable to rarely undergo spontaneous phenotypic variation, since environmental conditions are stable. Conversely, when nutrient variability is high (i.e. alternating cycles of

starvation and nutrient abundance occur), higher rates of spontaneous phenotypic variation constitute a competitive advantage, as they allow for a quicker adaptation to changeable environmental conditions, and higher levels of phenotypic heterogeneity emerge.

2.4.3 Survey of environmental conditions and competition outcomes

Exploiting the results of the analysis of the evolutionary dynamics in Section 2.3, we can further assess the range of environmental conditions under which higher rates of spontaneous phenotypic variation will represent a source of competitive advantage, i.e. when population H survives. In more detail, as shown by the asymptotic results established by Theorem 5, provided that condition (2.60) is not satisfied (i.e. at least one population survives), the outcome of competition between population H and population L in periodically fluctuating environments can be predicted by computing the value of the quantities Λ_H and Λ_L given by equation (2.55). In particular, the population characterised by the lower value of this quantity will ultimately be selected. Therefore, we computed Λ_H and Λ_L for different values of the period of the nutrient oscillations, T, and different values of the rate of spontaneous phenotypic variations, β_H. We used the values of the other evolutionary parameters shown in Table 2.1 and considered possible values of the environmental parameters M and A corresponding to three different scenarios: an environment in which the nutrient is abundant and undergoes small-amplitude periodic oscillations, i.e. M is relatively large and A is relatively small (Figure 2.6(a)); an environment in which the nutrient is scarce and undergoes small-amplitude periodic oscillations, i.e. M and A are both relatively small (Figure 2.6(b)); and an environment in which periodic oscillations can induce a sufficiently high variability of nutrient concentration, i.e. $M = A$ and different values of A are allowed (Figure 2.6(c)).

The results obtained are summarised by the plots in Figure 2.6. As we would expect, if the nutrient concentration undergoes low-amplitude periodic oscillations, then $\Lambda_L < \Lambda_H$ for all values of T and β_H considered (Figure 2.6(a) and Figure 2.6(b)). In this case population L is selected. On the other hand, when periodic oscillations can bring about sufficiently high levels of nutrient variability, there is a region of the β_H–T plane where $\Lambda_H < \Lambda_L$ (Figure 2.6(c)). Here, the population H is selected. When the value of A is either low or high, this region is small and concentrated in the bottom left corner of the plane. For intermediate values of A the region where $\Lambda_H < \Lambda_L$ is wider and such that the smaller the value of T (i.e. the higher the frequency of the nutrient oscillations) the wider the range of values of β_H that belong to it.

Furthermore, we can investigate how the fluctuations in the nutrient level affect the phenotypic distribution of each population at any given time point by constructing numer-

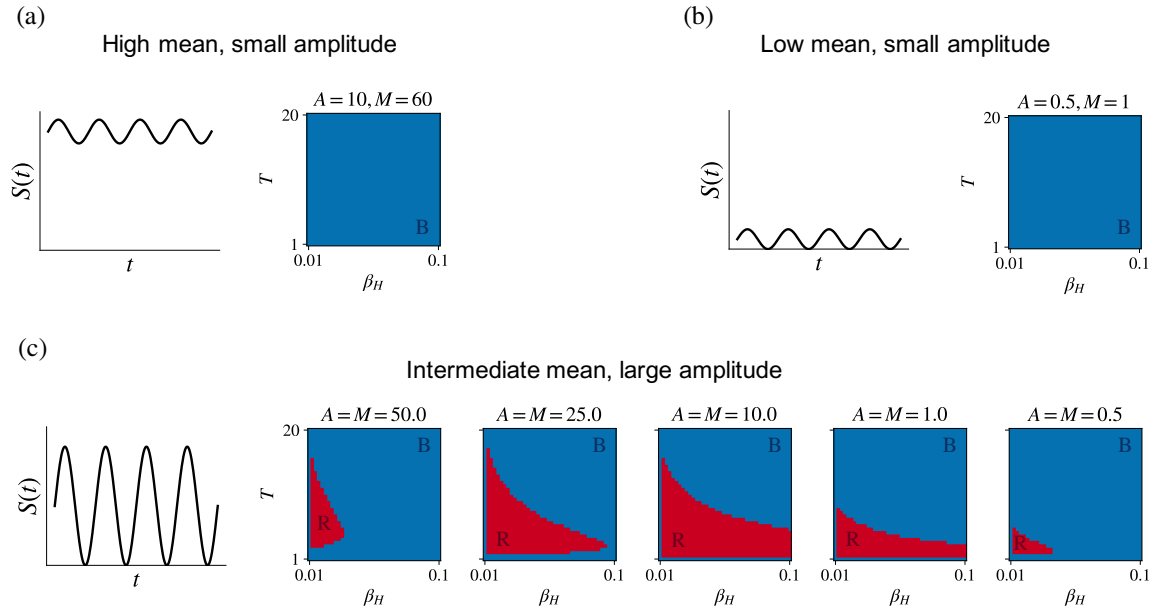

Figure 2.6: **(a)** Qualitative dynamics of the nutrient concentration, $S(t)$, defined according to Equation (2.85) with $M = 60$ and $A = 10$, and corresponding plot of $\mathrm{sgn}\,(\Lambda_H - \Lambda_L)$ as a function of $\beta_H \in (\beta_L, 0.1]$, with $\beta_L = 0.01$, and $T \in [1, 20]$. The quantities Λ_H and Λ_L are computed using Equation (2.55) and the values of the other model parameters are as listed in Table 2.1. The blue (marked by letter B) points in the $\beta_H - T$ plane correspond to $\mathrm{sgn}\,(\Lambda_H - \Lambda_L) = 1$, i.e. population L survives, whereas the red points (marked by letter R) correspond to $\mathrm{sgn}\,(\Lambda_H - \Lambda_L) = -1$, i.e. population H survives. **(b)** Same as panel **(a)** but with $M = 1$ and $A = 0.5$. **(c)** Same as panel **(b)** but with $M = A$ and $A \in \{0.5, 1, 10, 25, 50\}$.

ical solutions to the system of non-local PDEs (2.1) subject to initial condition (2.12) with $S(t)$ defined according to Equation (2.85). This is demonstrated by the plots in Figure 2.7, which show sample dynamics of the nutrient concentration $S(t)$, the phenotype distributions, $n_H(x,t)$ and $n_L(x,t)$, and the population sizes, $\rho_H(x,t)$ and $\rho_L(x,t)$, for different values of semi-amplitude, A, and mean, M, of fluctuations.

When the nutrient is abundant and experiences fluctuations of relatively low level (Figure 2.7(a)) population L outcompetes population H. This is due to the fact that, as shown by the Figure 2.8(a), the fittest phenotypic state $\varphi(t)$ undergoes very small periodic oscillations and its value remains close to 0 (i.e. the value of the phenotypic variable x corresponding to the fittest phenotypic state when nutrient is scarce). Moreover, the rescaled maximum fitness $g(t)$ undergoes very small periodic oscillations and its value remains close to 1.

When the nutrient level is uniformly low and undergoes relatively small oscillations (Figure 2.7(d)) population L is selected against population H. This is due to the fact

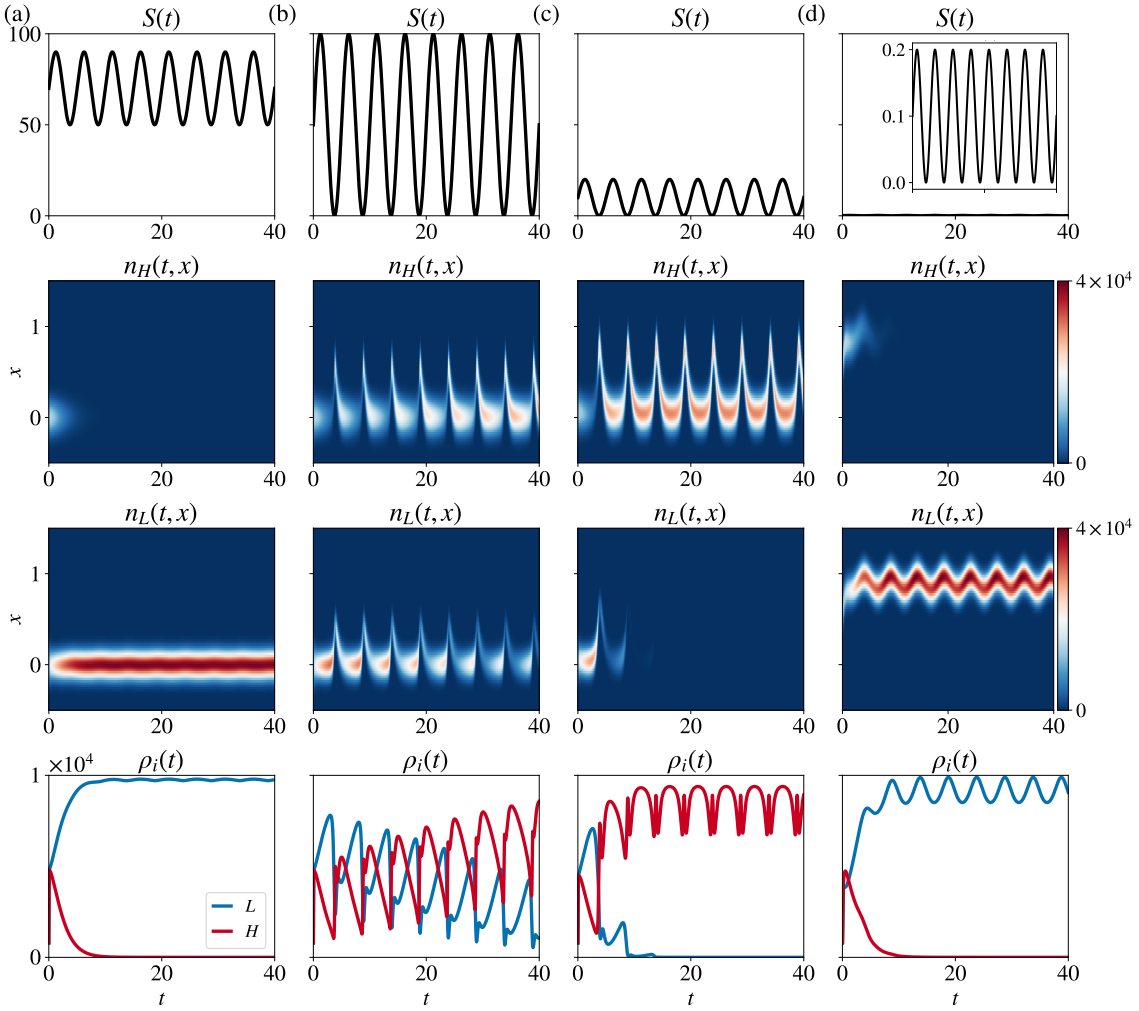

Figure 2.7: **(a)** Plots of the nutrient concentration $S(t)$ (first row), the phenotype distributions $n_H(x,t)$ (second row) and $n_L(x,t)$ (third row), and the population sizes $\rho_H(t)$ (fourth row, red line) and $\rho_L(t)$ (fourth row, blue line) obtained by solving numerically the system of PDEs (2.3), where $S(t)$ is defined according to Equation (2.85) with $T = 5$, $A = 20$ and $M = 70$. The values of the model parameters are as listed in Table 2.1 with $\beta_H = 0.025$. **(b) - (d)** Same as column **(a)** but for $A = M = 50$ (column **(b)**), $A = M = 10$ (column **(c)**), and $A = M = 0.1$ (column **(d)**).

that, as shown by the Figure 2.8(d), both the fittest phenotypic state $\varphi(t)$ and the rescaled maximum fitness $g(t)$ undergo small periodic oscillations and their values remain close to 1. We recall that $x = 1$ is the value of the phenotypic variable corresponding to the fittest phenotypic state when nutrient is scarce.

For the cases when the populations experience fluctuations of relatively high level (Figure 2.7(b) and Figure 2.7(c)) population H outcompetes population L. This is due to the fact that, as shown by Figure 2.8(b) and Figure 2.8(c), the fittest phenotypic state $\varphi(t)$

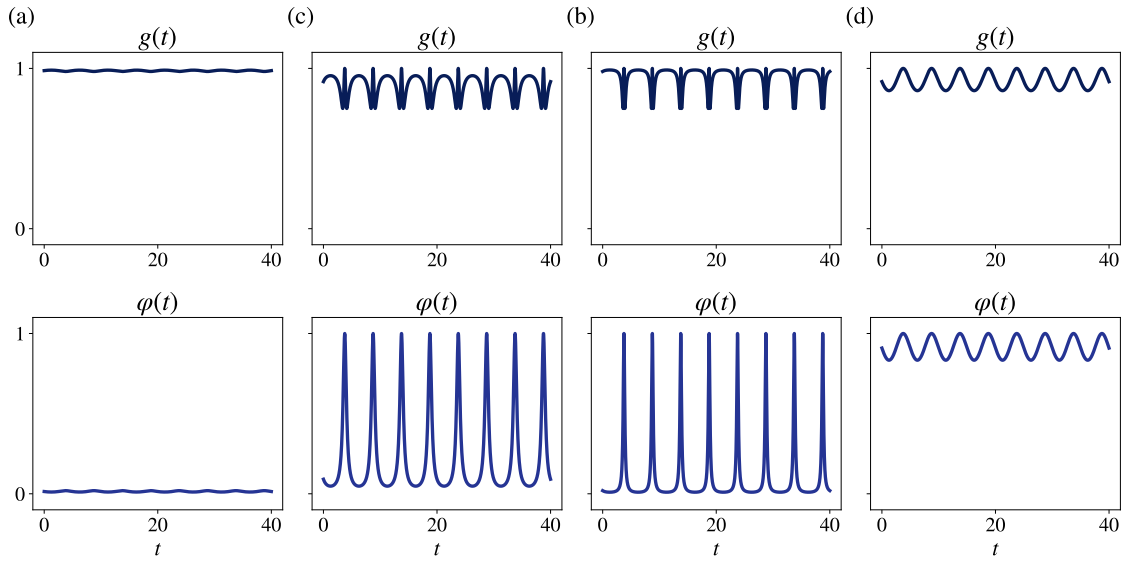

Figure 2.8: **(a)** Plot of the corresponding rescaled maximum fitness $g(t)$ (top row) and fittest phenotypic state $\varphi(t)$ (bottom row) defined according to Equation (2.11) with the nutrient concentration $S(t)$ defined according to Equation (2.85) with $M = 70$, $A = 20$ and $T = 5$. **(b)** – **(d)** Same as column **(a)** but with $A = M = 50$ (column **(b)**), $A = M = 10$ (column **(c)**), and $A = M = 0.1$ (column **(d)**).

fluctuates periodically between 1 and a positive value close to 0. Moreover, the rescaled maximum fitness $g(t)$ undergoes small periodic oscillations and its value remains close to 1.

Note that in all cases the phenotype distribution of the surviving population remains unimodal with maximum at the mean phenotypic state. Ultimately, both the size and the mean phenotypic state of the surviving population oscillate periodically with the same period as the nutrient concentration, $S(t)$. Furthermore, when the populations experience fluctuations of relatively high level (i.e. Figure 2.7(b) and Figure 2.7(c)), the mean phenotypic state of the surviving population (i.e. population H) undergoes rapid transitions between 1 and a positive value close to 0. This can be biologically seen as the emergence of a bet-hedging behaviour.

2.5 Discussion

In this chapter, we have presented a mathematical model, which describes the evolutionary dynamics of two asexual phenotype-structured populations competing in periodically oscillating environments. The two populations undergo spontaneous phenotypic variations at different rates and their fitness landscapes are dynamically sculpted by fluctuations in the nutrient levels.

Our analytical results formalise the idea that distinct environmental regimes will select different adaptation strategies, as summarised in Figure 2.9. In particular, when nutrient levels experience small and slow periodic oscillations, and thus environmental conditions are relatively stable, it is evolutionarily more efficient to rarely undergo spontaneous phenotypic variations. Conversely, under relatively large and fast periodic oscillations in the nutrient levels, which lead to alternating cycles of starvation and nutrient abundance, higher rates of spontaneous phenotypic variations can confer a competitive advantage, as they may allow for a quicker adaptation to changeable environmental conditions. In the latter case, our results predict higher levels of phenotypic heterogeneity than those observed in slowly fluctuating environments. Finally, our results suggest that bet-hedging evolutionary strategies, whereby individuals switch between antithetical phenotypic states, can naturally emerge in the presence of relatively large and fast nutrient fluctuations leading to drastic environmental changes.

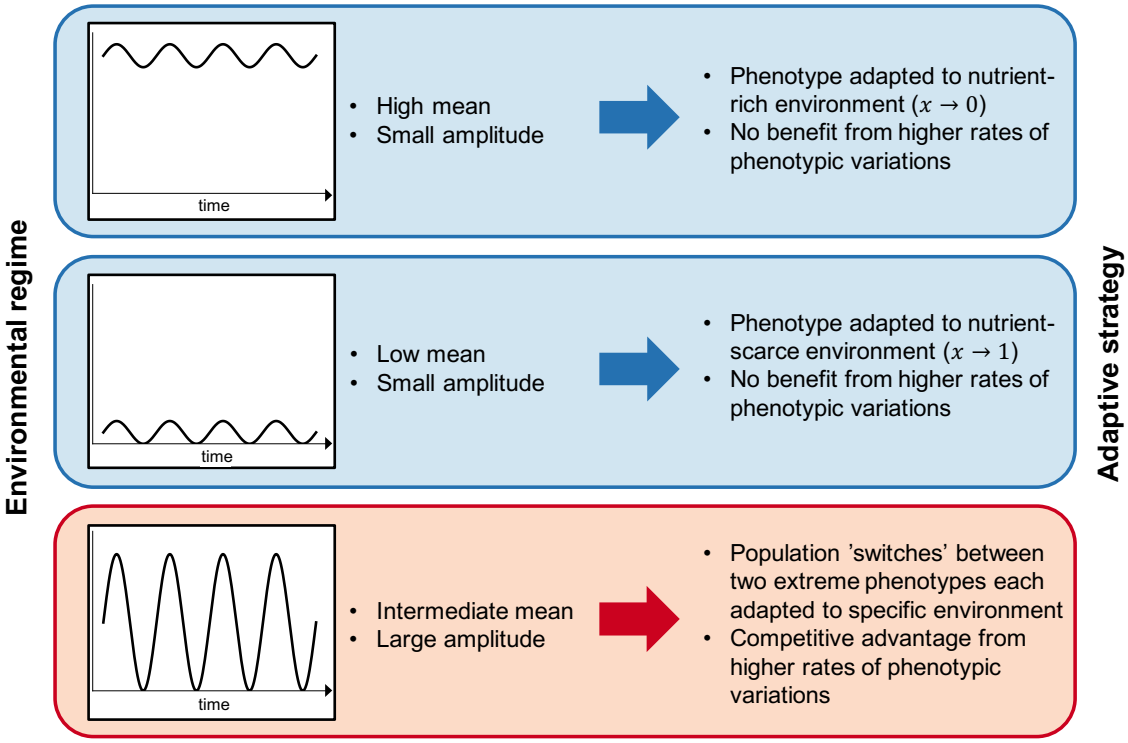

Figure 2.9: Schematic representation of the environmental regimes (left) and the corresponding adaptive strategies (right). The benefit from higher rates of spontaneous variations (bottom box) depends on the period of fluctuations, i.e. oscillations must be slow enough such that cells have time to change their phenotype.

The results of this chapter are consistent with existing mathematical models that look at adaptive strategies in fluctuating environments. In particular, our observation that a population, which switches between two specialised phenotypes, is selected when nutrient

levels undergo high-amplitude fluctuations, is consistent with the results of the generalist-specialist model, presented in Section 1.5.2, and in the original model from [147]. Furthermore, our results are in agreement with studies by Müller et al. [89], where the authors observed that a bet-hedger population that switches between two phenotypes is selected when environmental fluctuations occur on intermediate timescales. Furthermore, we showed how the mean value of fluctuations, together with the amplitude, affect the competitive advantage of spontaneous phenotypic variations. In this chapter we considered periodic environmental fluctuations, but we also showed that our results hold when using stochastic environmental variations between two extreme environments (e.g. $S = 0$ and $S = 1$). Exploration of other environmental regimes remains as future work.

The generality of the model and the robustness of the results make our conclusions applicable to a broad range of asexual populations evolving in fluctuating environments. Here, our aim is to apply the developed model to cancer cell populations in temporally varying environments due to irregular blood flow. To do so, we introduced several biological assumptions as a first step towards a more biologically realistic model. If we assume that $S(t)$ in our model represents the oxygen level at time t, then the phenotypic variants best adapted to oxygen-rich environments, and thus displaying a regular metabolism, are those with $x \to 0$. On the other hand, the phenotypic variants best adapted to oxygen-low environments – i.e. the phenotypic variants that proliferate through the consumption of glucose, which is usually abundant – correspond to $x \to 1$. Even though still a simplified scenario, these assumptions allow us to adapt the fitness landscape to more accurately represent tumour metabolism.

The focus of this chapter has been on the case where the maximum proliferation rate of the phenotypic variants best adapted to nutrient-rich environments (i.e. the parameter γ) and the maximum proliferation rate of the phenotypic variants best adapted to nutrient-scarce environments (i.e. the parameter ζ) are the same. In practice, in the realistic scenario of tumour metabolism, as well as other biological systems, the ability to survive in harsh environments comes with a fitness cost. In particular, anaerobic glycolysis is far less efficient in terms of produced energy than oxidative phosphorylation [105]. Therefore, the proliferation rate of glucose-dependent phenotypic variants might be lower than that of phenotypic variants best adapted to oxygenated environments. Therefore, it is necessary to extend our analytical results to the case where $\zeta < \gamma$.

Another natural extension of the model is consideration of the feedback from the populations on the nutrient level. In fact, most existing models of evolutionary dynamics in a fluctuating environment do not account for this feedback. However, changes in the population dynamics are known to affect the outcome of interspecies competition in the presence

of time variations in the availability of nutrients [206]. In the context of solid tumours, an example of a negative feedback mechanism that regulates population growth is nutrient consumption, which is known to vary across different cell lines and environmental conditions [19].

Therefore, in Chapter 3 we use the modelling framework developed in this chapter to study the evolution of cancer cell populations exposed to fluctuating oxygen levels. In particular, we present an extended model where oxygen dynamics are modelled explicitly via an ordinary differential equation. We assume that oxygen is supplied by the blood vessel, decays naturally and is consumed by the cells at rates which depend on their metabolic phenotype. Thus, in Chapter 3, we investigate the impact of the fitness cost on the competition outcomes. We aim also to understand how the interplay between the cells and their environment affects the selection of populations with higher rates of phenotypic variation and, hence, promotes phenotypic heterogeneity.

Chapter 3

Competition of phenotype-structured populations with cell-environment interactions

3.1 Introduction

Experimental and clinical studies show that oscillations in oxygen levels in solid tumours can occur on a variety of timescales, ranging from minutes to weeks [11, 22]. Temporal variations may lead to the emergence of regions of normoxia (i.e. high oxygen levels), chronic hypoxia (i.e. sustained low oxygen levels) and regions with fluctuating levels of oxygen (i.e. transient periods of low and relatively higher oxygen levels) [34].

The evolutionary consequences of these spatial and temporal variations can be profound. In order to survive, cancer cells in a poorly perfused region that is hypoxic, acidic and lacks growth factors require a different phenotype compared to cancer cells in a well-perfused, physiological environment. Furthermore, rapid, stochastic changes in environmental conditions apply additional selection forces. Here, cells must be able to adapt rapidly to unpredictable and potentially lethal environmental conditions. Furthermore, hypoxic and acidic environments generate genotoxic conditions and the transition from hypoxic to normoxic conditions can generate bursts of oxygen free radicals that induce widespread tissue and cellular damage [207].

Previous empirical and theoretical work has suggested that temporal variations in oxygen levels may drive cancer cells to adapt [7, 198]. Further, such adaptation can substantially impact the evolutionary dynamics of cancer by increasing clonal diversity, promoting metastasis and supporting more plastic phenotypic variants [45, 47, 40, 1]. In particular, it has been hypothesised that cancer cell populations could utilise risk spreading through stochastic phenotype switching, which is also known as bet-hedging, as an adaptive strategy to survive in the harsh, constantly changing environmental conditions associated with

intermittent hypoxia [7, 82]. However, in order to apply the developed framework to the specific application, we have to account for the specific details of the interactions between cells and the resource, that can shape the environment and, therefore, affect competition outcomes.

In Chapter 2, for simplicity, we assumed that the cells exist in prescribed conditions and do not interact with their environment. However, in reality, this is not the case. Cells can consume the available resources, become involved in cell signalling, which promotes or inhibits various cellular activities, such as angiogenesis, and can also exert physical pressure on the surroundings, leading to occlusion of the blood vessels. Various mathematical models have accounted for such feedback mechanisms, both positive and negative. In particular, this question has been addressed using structured consumer-resource models formulated in terms of a renewal equation [208]. Here, the resource dynamics is represented using an ordinary differential equation [209, 210, 211]. Such models are analytically tractable and have provided insights into the impact of feedback on the stability of behaviours. For instance, models of this form have been used to study cannibalism in fish populations [212, 213], as well as modelling the consumption of algae by *Daphnia magna* [214, 210]. These models demonstrate the importance of considering feedback mechanisms when studying the competitive behaviour of structured populations.

In this chapter, we aim to investigate whether cancer cells might utilise spontaneous phenotypic variations as an adaptive strategy in order to deal with temporal variations in oxygen concentrations. In particular, we extend the modelling framework developed in Chapter 2 by including a more detailed description of tumour metabolism in the fitness function. We model the oxygen dynamics via an ordinary differential equation where oxygen is supplied in a time-dependent manner by blood vessels and is consumed by the cells at rates determined by their phenotype. We use this model to examine the consequences of cell-environment feedback and how it shapes the formation of environmental niches within solid tumours.

We begin this chapter by explaining how we extend the mathematical model from the previous chapter (Section 3.2). We then consider a simplified model, in which oxygen consumption is modelled via a linear term. Under this assumption that the long time system dynamics can be described by a coupled system of PDEs, which we present in Section 3.3. We then solve numerically the full model, coupling the dynamics of the PDEs to the ODE governing the oxygen dynamics and accounting for phenotype-dependent consumption. The simulation results are outlined in Section 3.4. By considering a specific set of parameter values obtained from the literature, we identify timescales on which spontaneous phenotypic variation can be a successful adaptive strategy (Section 3.5). Finally, we explain how

these mathematical results can shed light on the evolutionary processes that underpin the emergence of phenotypic heterogeneity in vascularised tumours (Section 3.6).

The work contained in this chapter was carried out in collaboration with Prof. Tommaso Lorenzi (Politecnico di Torino, Italy). He contributed to the analysis of simplified model, presented in Appendix B, and to overall supervision of this work. The results presented in Sections 3.2, 3.3.1, 3.4 and 3.6 have been published in the following paper:

A. Ardaševa, R. A. Gatenby, A. R. A. Anderson, H. M. Byrne, P. K. Maini, T. Lorenzi, 2020, 'A mathematical dissection of the adaptation of cell populations to fluctuating oxygen levels', Bulletin of Mathematical Biology, 82, 81.

3.2 Mathematical model

In this chapter, we build on the modelling framework developed in Chapter 2 where cells are grouped into two populations, H and L, which differ only in the rates at which the cells undergo phenotypic variations. Cells in each group can proliferate, die, undergo spontaneous phenotypic variations, and compete for oxygen. The oxygen concentration in the system is denoted by $S(t)$. Based on the observation that glucose levels in biological tissues are usually sufficiently high not to represent a limiting factor for the proliferation of cells [82], for the sake of simplicity, we do not model the dynamics of the glucose concentration.

We represent the phenotypic state with a continuous variable on a finite domain $x \in [0,1]$, which represents the metabolic state of the cell (see Section 3.2.1). We describe the phenotype distributions of the two cell populations at time t by means of the population density functions $n_H(x,t)$ and $n_L(x,t)$. We define the size of populations H and L, and the total number of cells inside the system at time t, respectively, as

$$\rho_H(t) := \int_0^1 n_H(x,t)\,\mathrm{d}x, \quad \rho_L(t) := \int_0^1 n_L(x,t)\,\mathrm{d}x \tag{3.1}$$

and

$$\rho(t) := \rho_H(t) + \rho_L(t). \tag{3.2}$$

Moreover, we define the mean phenotype and the phenotypic variance of population $i \in \{H, L\}$ at time t, respectively, as

$$\mu_i(t) := \frac{1}{\rho_i(t)} \int_0^1 x\, n_i(x,t)\,\mathrm{d}x, \quad \sigma_i^2(t) := \frac{1}{\rho_i(t)} \int_0^1 x^2\, n_i(x,t)\,\mathrm{d}x - \mu_i^2(t). \tag{3.3}$$

We describe the evolution of the two cell populations through the system of conservation equations for the population density functions:

$$\begin{cases} \dfrac{\partial n_H}{\partial t} = \beta_H \dfrac{\partial^2 n_H}{\partial x^2} \; + \; R\big(x, S(t), \rho(t)\big)\, n_H, \\ \\ \dfrac{\partial n_L}{\partial t} = \beta_L \dfrac{\partial^2 n_L}{\partial x^2} \; + \; R\big(x, S(t), \rho(t)\big)\, n_L, \end{cases} \qquad \text{for } (x,t) \in (0,1) \times (0,\infty), \tag{3.4}$$

subject to no-flux boundary conditions, i.e.

$$\frac{\partial n_i(0,t)}{\partial x} = 0 \quad \text{and} \quad \frac{\partial n_i(1,t)}{\partial x} = 0 \quad \text{for all} \quad t \in (0,\infty), \quad i \in \{H, L\}. \tag{3.5}$$

The function, $R(x, S(t), \rho)$ represents, as before, the fitness of cells and is given by Equation (2.5) with the net proliferation rate, $p(x, S)$, defined by Equation (2.7). We consider the maximum proliferation rate, $g(S)$, non-linear selection gradient, $h(S)$, and fittest phenotypic state, $\varphi(S)$ to be given by Equations (2.8) and (2.9), respectively. We keep our assumption (2.4) that population H undergoes spontaneous phenotypic variations at a higher rate compared to the population L.

3.2.1 Biological assumptions

As summarised by the schematic in Figure 3.1, the phenotypic state, x, represents the metabolic state of each cell. In particular, we make the following assumptions:

Assumption 1. Cells in the phenotypic state $x = 0$ have a fully oxidative metabolism and produce energy through aerobic respiration only. Oxidative cells consume oxygen.

Assumption 2. Cells in the phenotypic state $x = 1$ express a fully glycolytic metabolism and produce energy through anaerobic glycolysis only. Glycolytic cells do not consume oxygen.

Assumption 3. Cells in other phenotypic states $x \in (0, 1)$ produce energy via aerobic respiration and anaerobic glycolysis, and higher values of x correlate with a less oxidative and more glycolytic metabolism.

To incorporate into the model the fitness cost associated with a less efficient glycolytic metabolism [215], we assume that

$$\gamma \geq \zeta > 0. \tag{3.6}$$

A sample of plots of the function $p\big(x, S\big)$ for different values of the oxygen concentration, S, and of the quotient, γ/ζ, is displayed in Figure 3.2. If $\gamma/\zeta = 1$, then there is no fitness cost associated with glycolytic metabolism, whereas increasing values of $\gamma/\zeta > 1$ correspond to larger fitness costs of glycolytic metabolism.

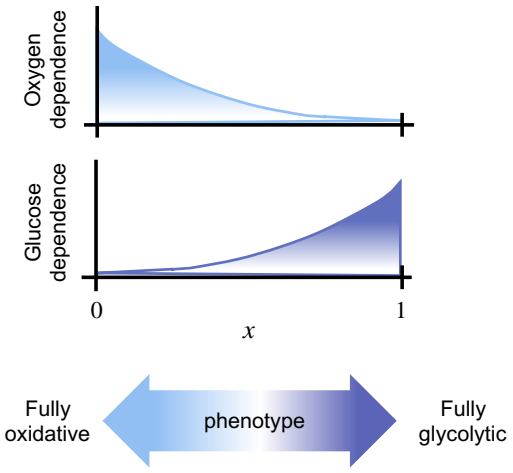

Figure 3.1: Schematic diagram illustrating the relationship between the cell phenotype variable $x \in [0,1]$ and the dependence on oxygen and glucose for energy production for different phenotypic variants.

3.2.2 Oxygen dynamics

We describe the oxygen dynamics via the following equation for $S(t)$:

$$\frac{\mathrm{d}S}{\mathrm{d}t} = I(t) - \eta\, S - \int_0^1 q(x,S)\,[n_H(x,t) + n_L(x,t)]\,\mathrm{d}x, \quad t \in (0,\infty) \tag{3.7}$$

which is coupled with the system of non-local PDEs (3.4). In the ODE (3.7), the parameter $\eta > 0$ represents the rate of natural decay of oxygen and the non-negative function $I(t)$ models the rate at which oxygen is supplied to the system. The last term on the right-hand side of Equation (3.7) models the rate of oxygen consumption by the cells. Here, the non-negative function $q(x,S)$ is the consumption rate of cells in phenotypic state x, and we take it to be

$$q(x,S) := \theta\,\gamma\,\frac{S}{1+S}\,(1-x^2), \tag{3.8}$$

based on the following argument. Cells in the phenotypic state $x = 1$ (i.e. fully glycolytic phenotype) produce energy through anaerobic glycolysis only and, therefore, they do not consume any oxygen (i.e. $q(1,S) = 0$ for any S). However, cells in the phenotypic state $x = 0$ (i.e. fully oxidative phenotype) consume oxygen at a rate proportional to their division rate, with constant of proportionality $\theta > 0$ (i.e. $q(0,S) = \theta\, p(0,S) = \theta\,\gamma\,\frac{S}{1+S}$). Finally, the rate at which oxygen is consumed by cells in phenotypic state $x \in (0,1)$ is a fraction of the consumption rate of cells in the phenotypic state $x = 0$, and higher values of x correlate with lower oxygen consumption (i.e. $q(x,S) = q(0,S)(1-x^2)$ for $x \in (0,1)$).

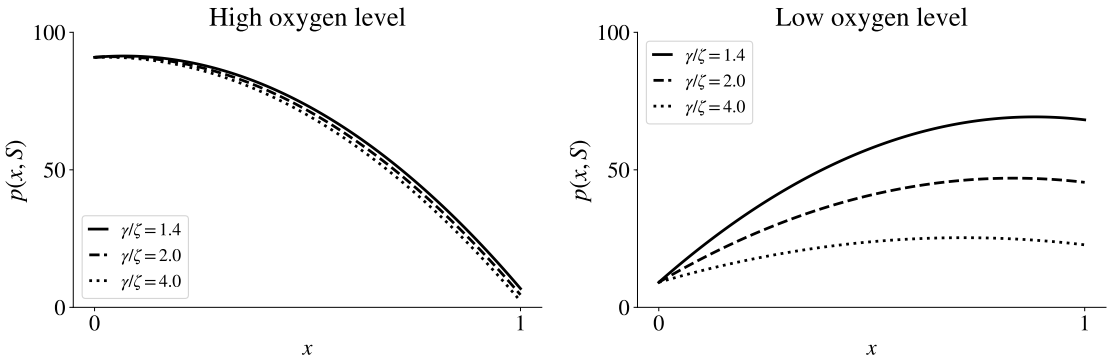

Figure 3.2: Plot of the cell division rate $p(x, S)$ defined according to Equation (2.7) in the case of a relatively high oxygen level (i.e. $S = 10$) and a relatively low oxygen level (i.e. $S = 0.1$), for increasing values of the fitness cost associated with glycolytic metabolism (i.e. increasing values of the quotient $\gamma/\zeta \geq 1$). Here, $\gamma = 100$, $\kappa = 1$.

3.3 Simplified model

In order to obtain a detailed analytical description of the evolutionary dynamics of the two cell populations, we first consider a simplified scenario whereby the ODE for $S(t)$ is decoupled from the system of non-local parabolic PDEs (3.4). In particular, we let the evolution of the oxygen concentration $S(t)$ be governed by the following Cauchy problem

$$\begin{cases} \dfrac{\mathrm{d}S}{\mathrm{d}t} = I(t) - \Theta S, & \\ & t \in (0, \infty), \\ S(0) = S^0 \geq 0, & \end{cases} \tag{3.9}$$

where the effects of oxygen consumption and oxygen decay are both encapsulated in the parameter $\Theta > 0$. Moreover, to facilitate analysis, we extend the interval $[0, 1]$ to $\mathbb{R}$ and re-define the population-level quantities accordingly, i.e. we use the definitions (2.1) and (2.2) from Chapter 2. The fact that the function $p(x, S)$ is negative for values of x sufficiently far from the $x \in [0, 1]$ ensures that less fit variants outside this region are driven to extinction by natural selection. Finally, we consider initial conditions of the Gaussian form defined by Equation (2.12). This allows us to use the result established by Proposition 1, which can be proved through the method that we previously employed in Section 2.3 (see Appendix B).

3.3.1 Analysis results

We use the approaches outlined in the proofs of Theorems 2 and 5 to analyse the long-term behaviour of the solutions.

In the case where the inflow of oxygen is constant, i.e. the source term $I(t)$ in the ODE (3.9) satisfies the following

$$I(t) \equiv I_S, \tag{3.10}$$

our main results are summarised by Theorem 6, where the functions g, φ and h are defined according to Equations (2.8) and (2.9), and we use the definitions

$$S^\infty := \frac{I_S}{\Theta}, \quad \rho_L^\infty := \frac{\gamma\, g(S^\infty) - \sqrt{h(S^\infty)\,\beta_L}}{d}, \quad \mu_L^\infty := \varphi(S^\infty). \tag{3.11}$$

Theorem 6. *Under assumptions* (2.4) *and* (3.6) *and the additional assumption* (3.10)*, the solution of the system of non-local PDEs* (3.4) *posed on* $\mathbb{R} \times (0, \infty)$*, subject to the initial condition* (2.12) *and complemented with the Cauchy problem* (3.9) *is of the Gaussian form* (2.13) *and satisfies the following:*

(i) if

$$\sqrt{h(S^\infty)\,\beta_L} \geq \gamma\, g(S^\infty)$$

then

$$\lim_{t\to\infty} \rho_H(t) = 0 \quad \textit{and} \quad \lim_{t\to\infty} \rho_L(t) = 0; \tag{3.12}$$

(ii) if

$$\sqrt{h(S^\infty)\,\beta_L} < \gamma\, g(S^\infty)$$

then

$$\lim_{t\to\infty} \rho_H(t) = 0, \quad \lim_{t\to\infty} \rho_L(t) = \rho_L^\infty \tag{3.13}$$

and

$$\lim_{t\to\infty} \mu_L(t) = \mu_L^\infty, \quad \lim_{t\to\infty} \sigma_L^2(t) = \sqrt{\frac{\beta_L}{h(S^\infty)}}. \tag{3.14}$$

Theorem 6 suggests that when the oxygen level is constant and the rate of phenotypic variation is relatively small, we expect the population with lower rate of phenotypic variation to survive. In this case, the cells will attain the fittest phenotypic state, i.e. a specialist population will be selected.

In the case where the inflow of oxygen undergoes periodic oscillations, i.e. the source term $I(t)$ in the ODE (3.9) satisfies the following assumptions

$$I \in \mathrm{Lip}([0,\infty)) \quad \text{and} \quad I(t+T) = I(t) \quad \text{for all} \quad t \geq 0, \tag{3.15}$$

our main results are summarised by Theorem 7, where $\tilde{S}(t)$ is the unique non-negative T-periodic solution of the problem

$$\begin{cases} \dfrac{\mathrm{d}\tilde{S}}{\mathrm{d}t} = I(t) - \Theta\tilde{S}, \quad t \in (0,T), \\ \\ \tilde{S}(0) = \tilde{S}(T), \end{cases} \tag{3.16}$$

$\tilde{v}_i(t)$ is the unique real positive T-periodic solution of the problem

$$\begin{cases} \dfrac{\mathrm{d}\tilde{v}_i}{\mathrm{d}t} = 2\left(h(\tilde{S}) - \beta_i \tilde{v}_i^2\right), \quad t \in (0,T), \\ \\ \tilde{v}_i(0) = \tilde{v}_i(T), \end{cases} \tag{3.17}$$

$\tilde{\mu}_i(t)$ is the unique real T-periodic solution of the problem

$$\begin{cases} \dfrac{\mathrm{d}\tilde{\mu}_i}{\mathrm{d}t} = \dfrac{2h(\tilde{S})}{\tilde{v}_i}\left(\varphi(\tilde{S}) - \tilde{\mu}_i\right), \quad t \in (0,T), \\ \\ \tilde{\mu}_i(0) = \tilde{\mu}_i(T), \end{cases} \tag{3.18}$$

$\tilde{\rho}_i(t)$ is the unique real non-negative T-periodic solution of the problem

$$\begin{cases} \dfrac{\mathrm{d}\tilde{\rho}_i}{\mathrm{d}t} = \left(F_i(\tilde{S}, \tilde{v}_i, \tilde{\mu}_i) - d\tilde{\rho}_i\right)\tilde{\rho}_i, \quad t \in (0,T), \\ \\ \tilde{\rho}_i(0) = \tilde{\rho}_i(T), \end{cases} \tag{3.19}$$

and

$$\Lambda_i := \frac{1}{T}\int_0^T \frac{h(\tilde{S}(z))}{\tilde{v}_i(z)}\,\mathrm{d}z + \frac{1}{T}\int_0^T \left(\tilde{\mu}_i(z) - \varphi(\tilde{S}(z))\right)^2 h(\tilde{S}(z))\,\mathrm{d}z \quad \text{for} \quad i \in \{H, L\}\,. \tag{3.20}$$

In Equations (3.17)–(3.20), the functions g, φ and h are defined according to Equation (2.8) and (2.9). Moreover, the function F_i in Equation (3.19) is defined according to Equation (2.23).

Theorem 7. *Under assumptions* (2.4)-(3.6) *and the additional assumption* (3.15)*, the solution of the system of non-local PDEs* (3.4) *posed on* $\mathbb{R}\times(0,\infty)$*, subject to the initial condition* (2.12) *and complemented with the Cauchy problem* (3.9) *is of the Gaussian form* (2.13) *and satisfies the following:*

(i) if

$$\min\{\Lambda_H, \Lambda_L\} \;\geq\; \frac{\gamma}{T}\int_0^T g(\tilde{S}(t))\,\mathrm{d}t \tag{3.21}$$

then

$$\lim_{t\to\infty}\rho_H(t) = 0 \quad \textit{and} \quad \lim_{t\to\infty}\rho_L(t) = 0; \tag{3.22}$$

(ii) if

$$\min\{\Lambda_H, \Lambda_L\} < \frac{\gamma}{T}\int_0^T g(\tilde{S}(t))\,\mathrm{d}t \tag{3.23}$$

and

$$i = \arg\min_{k\in\{H,L\}} \Lambda_k, \quad j = \arg\max_{k\in\{H,L\}} \Lambda_k, \tag{3.24}$$

then

$$\rho_i(t) \to \tilde{\rho}_i(t), \quad \rho_j(t) \to 0 \quad as\ t \to \infty, \tag{3.25}$$

and

$$\mu_i(t) \to \tilde{\mu}_i(t), \quad \sigma_i^2(t) \to \frac{1}{\tilde{v}_i(t)} \quad as\ t \to \infty. \tag{3.26}$$

Theorem 7 suggests that when the oxygen level oscillates periodically, we expect the population that minimises Λ_i, given by the definition (3.20), to survive and have a periodic solution. Moreover, the variance (i.e. the level of phenotypic heterogeneity) will also vary periodically in time.

The proofs of Theorems 6 and 7 are presented in Appendix B.

3.3.2 Demonstration of analysis results

Here we present numerical simulations illustrating the results of the long-term ($t \to \infty$) analysis presented in Section 3.3.1.

3.3.2.1 Numerical setup

We use the numerical scheme to obtain the numerical solutions of the PDEs (3.4) detailed in Section 2.4.1. We use the `ode15s` solver in MATLAB to solve the ODEs (3.16) – (3.19). We use this particular solver as we might expect a more stiff system due to time-dependent parameters. We compare the numerical approximations of the PDEs with the ODEs to validate the approximations. In all the simulations presented in this section we use the parameter values listed in Table 3.1,which are chosen in order to demonstrate the analytic results. We consider the initial conditions of both cell populations as being given by Equation (2.12) where $v_i^0 = 20$, $\mu_i^0 = 0$, and $\rho_i^0 \approx 800$ for $i \in \{H, L\}$. The initial condition for the oxygen concentration is given by $S(0) = I(0)$.

Parameter	**Description**	**Value range**
γ	Maximum proliferation rate of oxidative cells	100
ζ	Maximum proliferation rate of glycolytic cells	[25,100]
d	Death rate due to competition	0.01
β_L	Rate of phenotypic variations of population L	0.01
β_H	Rate of phenotypic variations of population H	0.025
Θ	Oxygen consumption term	[1, 100]
κ	Michaelis constant	1

Table 3.1: Parameter values used to carry out the numerical simulations in Section 3.3.2.

3.3.2.2 Main results

We consider the following definition of the oxygen inflow concentration

$$I(t) = M + A \sin\left(\frac{2\pi t}{T}\right), \tag{3.27}$$

where M is the mean oxygen concentration, A is the amplitude and T is the period of oscillation. The values are chosen such that $A \leq M$. We start by exploring three prototypical scenarios exemplified by different values of the parameter A. We choose $M = 10$ and let $A = 0$ (i.e. constant environment), $A = 1$ (i.e. mild fluctuations) and $A = 10$ (i.e. severe fluctuations).

The plots in the top row of Figure 3.3 show the inflow of oxygen as a function of time. In (a), oxygen is supplied constantly, whereas in (b) and (c) oxygen inflow undergoes periodic oscillations of low and high amplitude, respectively. The bottom row in Figure 3.3 shows the resulting dynamics of the oxygen concentration for given $I(t)$. As expected, higher variability in the oxygen inflow leads to higher amplitude fluctuations in the oxygen concentration. Figure 3.4 shows a comparison between the solutions of $v_i(t)$, $\mu_i(t)$, $\rho_i(t)$

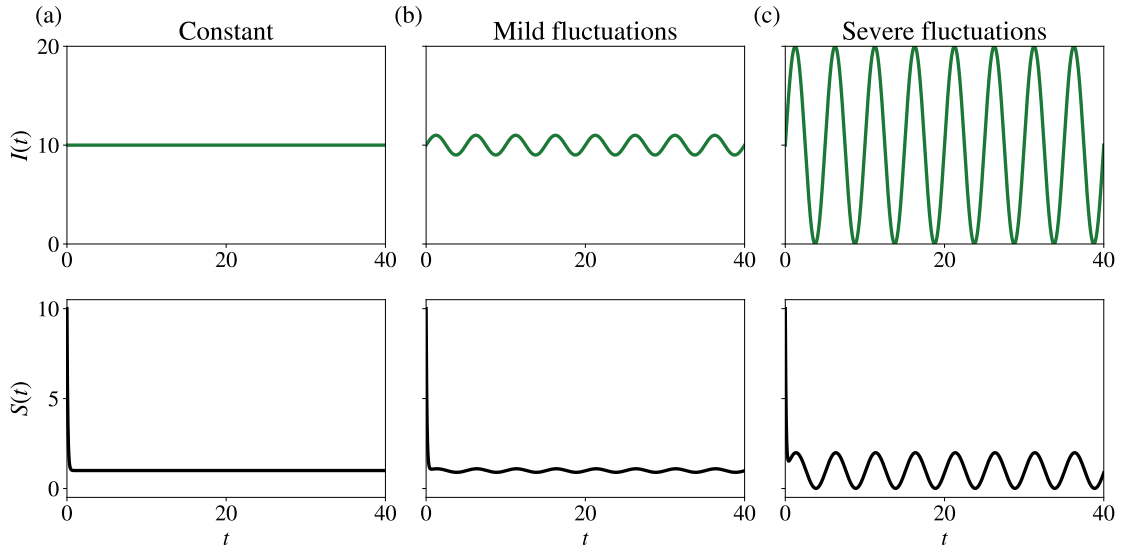

Figure 3.3: **(a)** Dynamics of oxygen inflow $I(t)$ (first row) and oxygen concentration $S(t)$ obtained by solving numerically the ODE (3.9) with oxygen inflow given by Equation (3.27) with $A = 0$, $M = 10$, $T = 5$. **(b)** – **(c)** Same as column **(a)** but for $A = 1$ (column **(b)**) and $A = 10$ (column **(c)**). $\Theta = 10$, $\zeta = 50$, and other parameter values are defined as in Table 3.1.

and the resulting phenotype distributions at given times $t = t^*$, $n_i(x, t^*)$, obtained by solving numerically the Cauchy problem (2.22) and the system of PDEs (3.4) with Equation

(3.9). We observe an excellent agreement between the population sizes, mean phenotypes, variances and population densities over time.

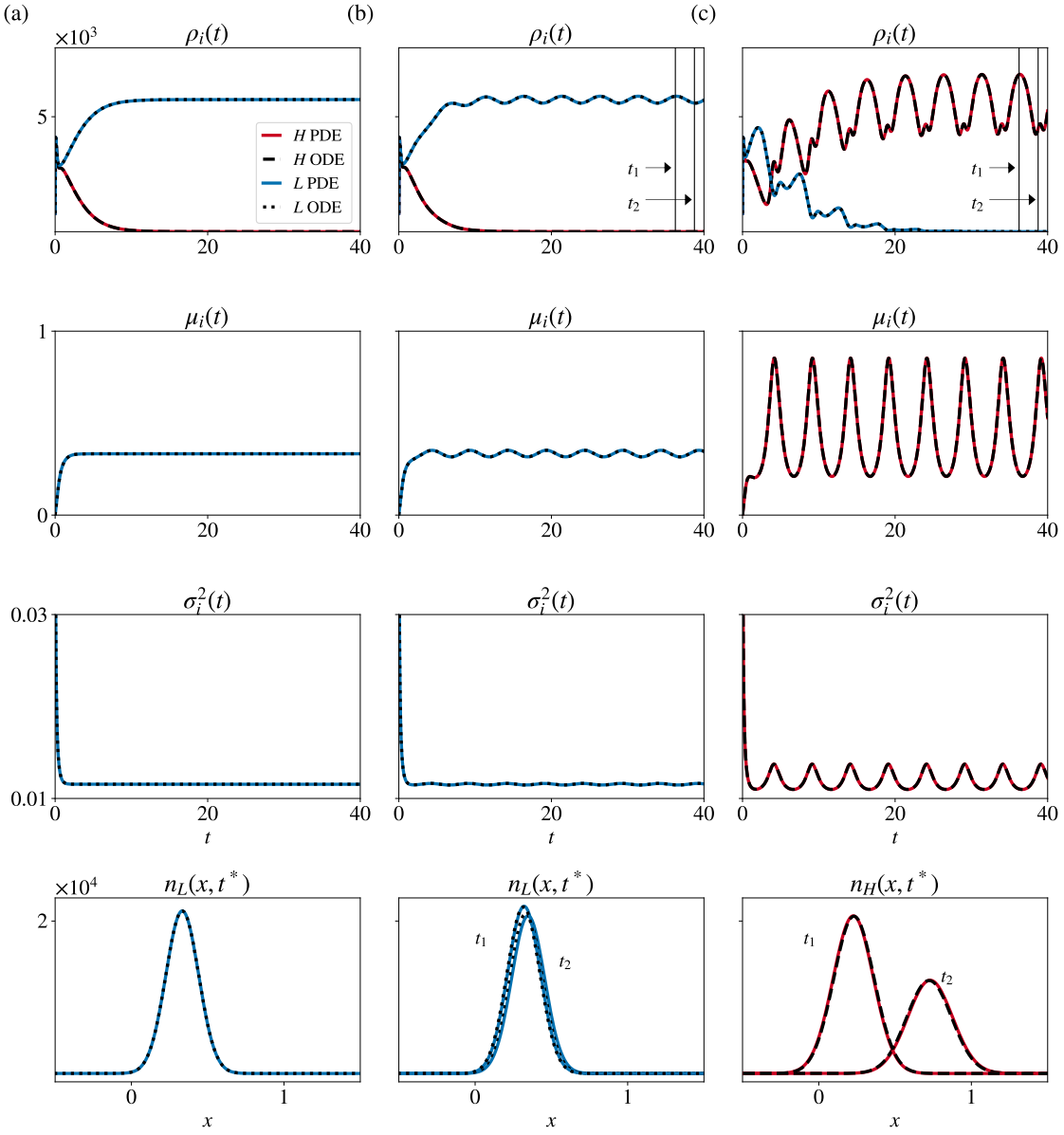

Figure 3.4: **(a)** Plots of population sizes $\rho_i(t)$, mean phenotype $\mu_i(t)$ of the surviving population, the variance $\sigma_i^2(t)$ of phenotypic distribution of the surviving population, and the corresponding phenotype distributions $n_i(x, t^*)$ at the end of simulation $t^* = 40$. Blue and red lines correspond to populations L and H, respectively, obtained by computing numerically the solutions of the system of PDEs (3.4) coupled with Equation (3.9) where nutrient supply is given by Equation (3.27) subject to the initial conditions (2.12). The dotted and dashed lines highlight populations H and L, respectively, obtained by solving numerically the Cauchy problem (2.22) with Equation (3.9). Here, $A = 0$, $M = 10$, $T = 5$, $\zeta = 50$, $\Theta = 10$ and other parameters as listen in Table 3.1. **(b)**–**(c)** Same as **(a)** but with $A = 1$ **(b)** and $A = 10$ **(c)**.

In agreement with the results established by Theorem 6, when the inflow of the nutrient is constant (i.e. $I(t) \equiv M$), the population with lower rate of phenotypic variations survives (Figure 3.4(a)). The size of the population L reaches the asymptotic value (3.13) and the phenotype distribution $n_L(x, t_1)$ is Gaussian with mean and variance equal to the asymptotic values (3.14).

A similar outcome is observed in the presence of mild fluctuations (Figure 3.4(b)) in accord with the results of Theorem 7, where the condition $\Lambda_L < \Lambda_H$ is satisfied and the population L survives. When the nutrient variability is high, we observe that population H survives (Figure 3.4(c)). In this case, the condition $\Lambda_L > \Lambda_H$ is satisfied. In both scenarios, the size of the surviving population, mean phenotype and variance of the phenotypic distribution become T-periodic. In Figure 3.4(c), when the environment is oxygen-rich, the population size is the highest (e.g. at t_1) and the population acquires the oxidative phenotype with the variance being at its lowest. On the contrary, when the oxygen level is low, the resulting population size is low (e.g. at t_2) and the population moves towards a more glycolytic phenotype with higher variance. Therefore, the phenotypic heterogeneity is increased in the case of larger nutrient variability, and is at its highest when the population size is small, i.e. during the period of hypoxia.

Exploiting the results of the analysis of the evolutionary dynamics, we can further investigate the range of environmental conditions under which higher rates of phenotypic variations represent a competitive advantage. We assume that the inflow of nutrient fluctuates between 0 and some positive value such that $A = M$. Additionally, we look at the impact of the nutrient consumption term Θ and maximum proliferation rate of glycolytic cells ζ. Therefore, for every combination of parameters $\{A, T, \Theta, \zeta\}$ we compute the quantities Λ_L and Λ_H given by Equation (3.20). The population characterised by the lower value of this quantity will ultimately be selected, as predicted by Theorem 7. We compute the quantities required to calculate Λ_i, i.e. $\hat{v}_i(t)$, $\hat{\mu}_i(t)$, $\hat{h}(t)$ and $\hat{\varphi}(t)$, by solving numerically the Cauchy problem (2.22) and ODE describing oxygen dynamics given by Equation (3.9). We use the values of other parameters as defined in Table 3.1. The results are summarised by the plots in Figure 3.5, where blue points correspond to the case where population L survives and red to the case where population H survives. The value of Θ increases from left to right and the value of ζ decreases from top to bottom.

When the nutrient consumption rate is small (e.g. $\Theta = 1$, first column in Figure 3.5), the population L survives for any given environment and values of ζ. In this case, very little nutrient is consumed and a build-up occurs. Therefore, the populations experience an oxygenated environment and the population with lower rate of phenotypic variation survives as suggested by Theorem 6.

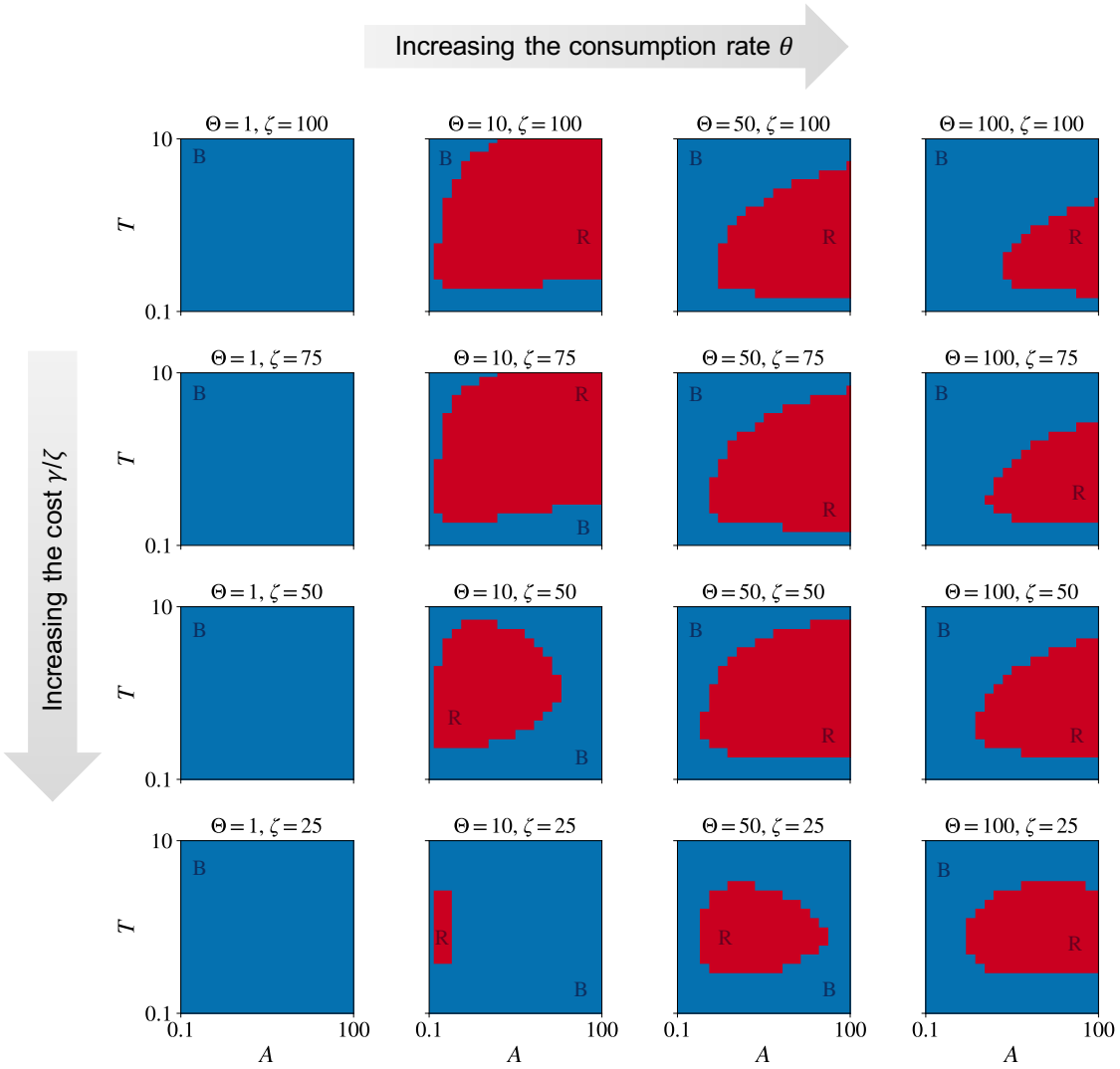

Figure 3.5: Plots of $\text{sgn}(\Lambda_H - \Lambda_L)$ as a function of $A \in [0.1, 100]$ and $T \in [1, 20]$ for different values of $\Theta \in \{1, 10, 50, 100\}$ and $\zeta \in \{25, 50, 75, 100\}$. The quantities Λ_H and Λ_L are computed using the Equation (3.20) and the values of the other model parameters as listed in Table 3.1. The blue points (marked by letter B) in the $\beta_H - T$ plane correspond to $\text{sgn}(\Lambda_H - \Lambda_L) = 1$ (i.e. $\Lambda_L < \Lambda_H$), whereas the red points (marked by letter R) correspond to $\text{sgn}(\Lambda_H - \Lambda_L) = -1$ (i.e. $\Lambda_H < \Lambda_L$).

As the magnitude of the consumption term increases, the environmental regimes where the population with higher rate of phenotypic variation is favoured appear. In general, the population H survives when both amplitude A and period T are at intermediate values. The range of favourable environments for population H depends on the maximum proliferation rate of glycolytic cells and nutrient consumption term. In particular, when there is no cost for being in the glycolytic state, i.e. $\gamma = \zeta$, the largest 'opportunity window' appears when θ is relatively small. However, when the cost for being glycolytic is large, e.g. $\zeta = 25$,

the largest 'opportunity window' exists at larger values of Θ. Thus, depending on the characteristics of the cell line (such as oxygen consumption rate and proliferation rate under hypoxia), we expect to observe the population with higher rates of phenotypic variation, and hence higher phenotypic heterogeneity, in regions characterised by different environmental conditions.

3.4 Model with phenotype-dependent consumption

In this section, we present the results of numerical simulations of the mathematical model defined by the non-local PDEs (3.4) coupled with the ODE (3.7) in Section 3.2.2. We combine these numerical results with the analytical results obtained for a simplified version of the model presented in Section 3.3, and discuss their biological relevance. In more detail, Section 3.4.1 provides a description of the numerical methods employed and the set-up of the numerical simulations. In Section 3.4.2, we consider the case where the inflow of oxygen is constant, i.e. we assume

$$I(t) = I_S \geq 0 \quad \text{for all } t \geq 0, \tag{3.28}$$

while in Section 3.4.3 we study the case where the oxygen inflow undergoes periodic oscillations of period $T > 0$, i.e. we assume

$$I(t+T) = I(t) \quad \text{for all } t \geq 0. \tag{3.29}$$

In particular, to construct numerical solutions we consider the case where

$$I(t) = \max\left(0, A\sin\left(\frac{2\pi t}{T}\right)\right), \tag{3.30}$$

with $A > 0$ modelling the amplitude of the periodic fluctuations in oxygen inflow. Definition (3.30) corresponds to a biological scenario in which oxygen inflow is periodically interrupted due to, for instance, the periodic blockage of a blood vessel.

3.4.1 Numerical setup

We use a uniform discretisation, based on the results of the convergence tests in Section 2.4.1, consisting of 200 points on the interval $[0, 1]$ (i.e. $\Delta x = 0.005$) as the computational domain of the independent variable x. We assume $t \in [0, t_f]$, with $t_f = 40$ being the final time of simulations, and we discretise the time interval $[0, t_f]$ with the uniform step size $\Delta t = 0.0001$. The method we use for constructing numerical solutions to the system of non-local parabolic PDEs (3.4) subject to no-flux boundary conditions is based on a three-point finite difference explicit scheme for the diffusion terms and an explicit finite difference

scheme for the reaction terms [201]. Moreover, numerical solutions to the ODE (3.7) are constructed using the explicit Euler method.

The nutrient concentration is presented in non-dimensional form and the dimensionless parameter values listed in Table 3.2 are used to carry out numerical simulations in order to demonstrate the qualitative behaviour of the system. The values of the rates of phenotypic variation, β_i, maximum proliferation rate of oxidative cells, γ, and death rate due to intra- and inter-population competition, d, are the same as those used in Sections 2.4 and 3.3. In summary, we define the rates of phenotypic variation β_H and β_L so that they are consistent with typical times required by cells to acquire a glycolytic phenotype through epigenetic changes [113]. Moreover, we choose the value of the maximum cell division rate of fully oxidative phenotypic variants γ such that $\gamma \gg \beta_H$, in order to capture the fact that phenotypic variations occur on a slower time scale than cell division. Furthermore, to explore the effect of the cost of glycolytic metabolism on the evolutionary dynamics of the cells and on the dynamics of oxygen, we consider different values of ζ such that $\gamma/\zeta \in [1, 4]$. Since the rate at which cells consume oxygen varies between cell lines and depends on a variety of environmental factors, including the pH level [19], we consider a range of values for the rate of consumption of oxygen, θ, that is, $\theta \in [10^{-5}, 10^{-3}]$, to investigate also the influence this parameter has on the cell and oxygen dynamics. Finally, we choose the value of the rate of natural decay of oxygen, η, to be consistent with the values used by other authors, such as [216].

Parameter	**Description**	**Value range**
β_H	Rate of phenotypic variation of cells in population H	2.5×10^{-2}
β_L	Rate of phenotypic variation of cells in population L	10^{-2}
γ	Maximum cell division rate of fully oxidative cells	100
ζ	Maximum cell division rate of fully glycolytic cells	[25,100]
d	Death rate due to competition	10^{-2}
θ	Consumption rate of oxygen	$[10^{-5}, 10^{-3}]$
η	Rate of natural decay of oxygen	10^{-4}
κ	Half-maximum concentration of oxygen	1
$\rho_i(0)$	Initial size of population i	800
$\mu_i(0)$	Initial mean phenotype of population i	0
$v_i(0)$	Initial inverse of variance of population i	{20, 100}

Table 3.2: Parameter values used in numerical simulations.

We let the initial cell population density functions $n_i(x, 0)$ with $i \in \{H, L\}$ be given by Equation (2.12) with ρ_i^0, μ_i^0 and v_i^0 as listed in Table 3.2 and define the initial oxygen concentration as $S(0) = I(0)$.

3.4.2 Constant oxygen inflow

The numerical solutions presented in Figure 3.6 show that when the oxygen inflow is constant (i.e. when the function $I(t)$ is defined according to Equation (3.28)), cell population L outcompetes cell population H, which eventually goes extinct. Moreover, the population density function $n_L(x,t)$ is unimodal, attaining its maximum at the mean phenotype. Furthermore, since the oxygen concentration $S(t)$ converges to an equilibrium value, the population size $\rho_L(t)$ also converges to an equilibrium value. The equilibrium value of $\rho_L(t)$ is approximately equal to the asymptotic value ρ_L^∞ given by definition (3.13) in Section 3.3.1, which is obtained by studying the long-time behaviour of the solutions to a simplified version of the model (Theorem 6 in Section 3.3.1). This is consistent with the analytical results that we presented in Section 2.3.

The results displayed in Figure 3.6 also show that larger values of the oxygen consumption rate θ lead to smaller equilibrium values of the oxygen concentration S and, therefore, smaller final values of ρ_L and larger final values of μ_L. Moreover, the numerical results summarised by the plots in Figure 3.7 demonstrate that larger values of the fitness cost associated with glycolytic metabolism, γ/ζ, correspond to smaller final values of ρ_L and μ_L. The plots in Figure 3.7 also show that lower values of I_S, which lead to smaller equilibrium values of S for a given value of θ, correlate with a weaker impact of the value of the quotient γ/ζ on the final values of ρ_L and μ_L. All these findings are consistent with the way in which the equilibrium values of the population size, ρ_L^∞, and the mean phenotype, μ_L^∞, obtained through the analysis of the simplified model considered in Section 3.3.1 depend on the equilibrium value of the oxygen concentration, S^∞, and on the quotient γ/ζ (Theorem 7 in Section 3.3.1).

Furthermore, as shown in Figure 3.8, we can observe scenarios of population dynamics where population H initially has the advantage and drives the size of population L to very low numbers. After some time, the population H decreases, eventually becoming extinct, and the population L is restored and approaches its asymptotic value given by Equation (3.13). The presence of such initial transient dynamics is dependent on the initial characteristics of each population, such as initial mean phenotype and variance. Even though in the long-term limit the population with higher rate of phenotypic variation becomes extinct, there is a possibility that in a stochastic setting, population L might become extinct due to stochasticity in birth-death processes, which is very important at low population sizes. Therefore, it is necessary to consider a discrete model to explore the likelihood of the population with higher rate of phenotypic variation surviving in constant environments (see Chapter 4).

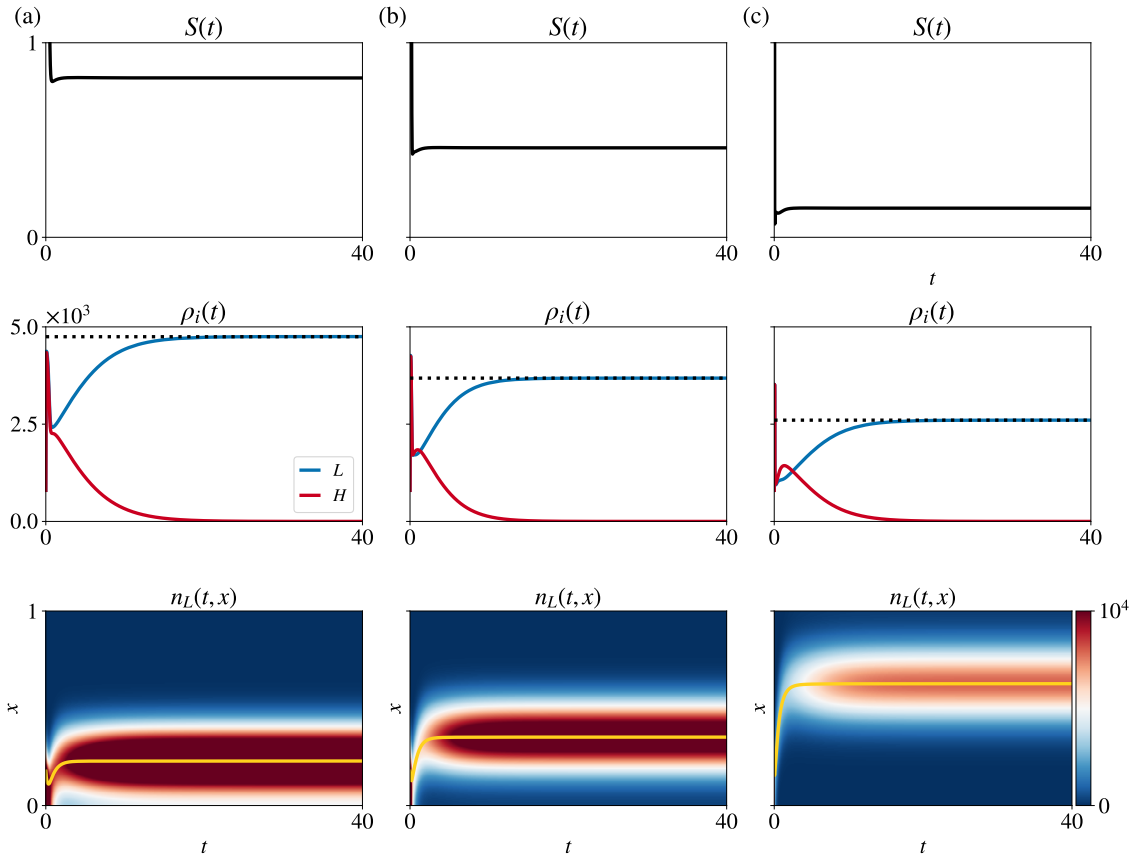

Figure 3.6: **(a)** Dynamics of the oxygen concentration $S(t)$ (first row), the population sizes $\rho_H(t)$ (second row, red line) and $\rho_L(t)$ (second row, blue line), and the population density function $n_L(t,x)$ (third row) obtained by solving numerically Equations (3.4) and (3.7) with the oxygen inflow $I(t)$ defined via Equation (3.28) with $I_S = 10$. The dotted lines in the second column highlight the asymptotic value ρ_L^∞ given by definition (3.13) in Section 3.3.1, while the yellow lines in the third column highlight the mean phenotype $\mu_L(t)$ obtained by solving PDEs. The consumption rate of oxygen is $\theta = 5 \times 10^{-5}$, the maximum cell division rate of fully glycolytic phenotypic variants is $\zeta = 25$, $v_i(0) = 20$, and the values of the other parameters are given in Table 3.2. **(b)**, **(c)** Same as column **(a)** but for $\theta = 10^{-4}$ (column **(b)**) and $\theta = 5 \times 10^{-4}$ (row **(c)**).

Taken together, these results indicate that lower rates of heritable, spontaneous phenotypic variation constitute a source of competitive advantage under constant oxygen inflow. Furthermore, the negative feedback that regulates the growth of cell populations through oxygen consumption shapes, in a nonlinear way, the evolutionary dynamics of the cells. In particular, larger values of the rate of oxygen consumption, θ, lead to the emergence of lower oxygenated environments whereby phenotypic variants that rely to a larger extent on anaerobic glycolysis for energy production are ultimately selected. Finally, all other things being equal, larger values of the fitness cost associated with glycolytic metabolism, γ/ζ, are to be expected to promote the selection of less glycolytic phenotypic variants and to reduce

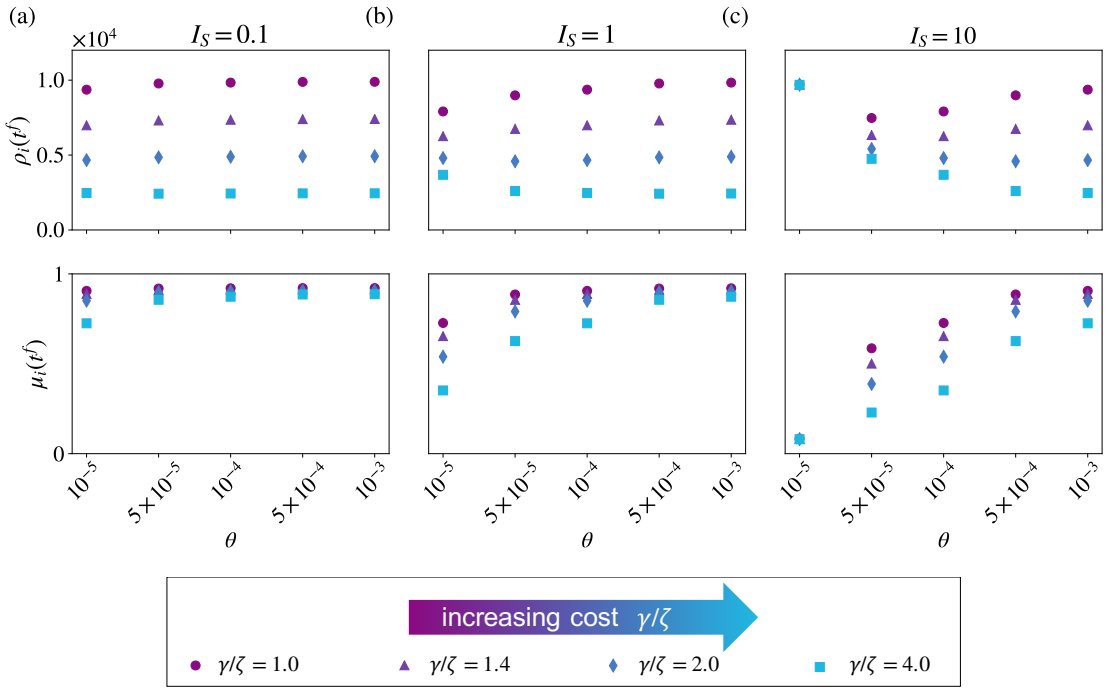

Figure 3.7: **(a)** Values of the population size $\rho_L(t)$ and the mean phenotype $\mu_L(t)$ at $t_f = 40$ (i.e. at the end of numerical simulations) obtained by solving numerically Equations (3.4) and (3.7) with the oxygen inflow $I(t)$ defined via Equation (3.28) with $I_S = 0.1$ and for different values of the consumption rate of oxygen, θ, and different values of the cost associated with glycolytic metabolism, γ/ζ, obtained by changing the value of the maximum cell division rate of fully glycolytic phenotypic variants, ζ, and keeping the value of the maximum cell division rate of fully oxidative phenotypic variants, γ, constant (i.e. $\gamma = 100$). The parameter values used are as listed in Table 3.2. **(b)**, **(c)** Same as column **(b)** but for $I_S = 1$ (column **(b)**) and $I_S = 10$ (column **(c)**).

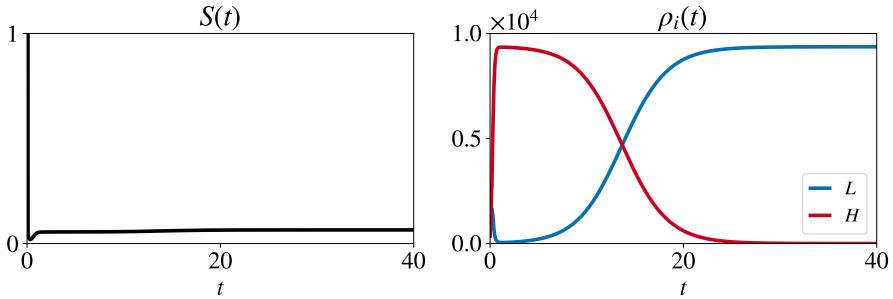

Figure 3.8: Dynamics of the oxygen concentration $S(t)$ (left) and the population sizes $\rho_H(t)$ and $\rho_L(t)$ (right), obtained by solving numerically Equations (3.4) and (3.7) with the oxygen inflow $I(t)$ defined via Equation (3.28) with $I_S = 10$. Parameter values used here: $\theta = 10^{-3}$, $v_i(0) = 100$, and others as listed in Table 3.2.

the equilibrium size of cell populations exposed to constant oxygen inflow.

3.4.3 Periodic oxygen inflow

The numerical solutions presented in Figure 3.9 show how the system evolves when the oxygen inflow undergoes periodic oscillations (e.g. when the function $I(t)$ is defined according to Equation (3.30)): if the oxygen concentration is relatively stable (low-amplitude oscillations), the cell population L outcompetes cell population H, which eventually goes extinct; if the oxygen concentration undergoes drastic, high-amplitude variations, then cell population L is outcompeted by cell population H and ultimately goes extinct. Moreover, the population density function of the surviving cell population, $n_i(x,t)$, is unimodal with maximum at the mean phenotype. Since the oxygen concentration $S(t)$ becomes T-periodic, after an initial transient, the population size $\rho_i(t)$ of the surviving population also converges to a T-periodic function. Such a T-periodic function is approximately equal to the solution $\tilde{\rho}_i(t)$ of the problem (3.25) in Section 3.3.1, which is obtained by studying the long-time behaviour of the solutions to a simplified version of the model (Theorem 7 in Section 3.3.1). This is in line with the analytical results presented in Section 2.3.

The results displayed in Figure 3.9 also show that the consumption rate of oxygen, θ, has a crucial impact on the dynamics of the oxygen concentration $S(t)$ and, therefore, on the outcome of the competition between the two cell populations. In fact, *ceteris paribus*, for sufficiently small (Figure 3.9(a)) or sufficiently large (Figures 3.9(d) and 3.9(e)) values of θ the function $S(t)$ is bounded well above zero or undergoes small oscillations while remaining close to zero, respectively. This brings about relatively stable oxygen concentrations in presence of which cell population L outcompetes cell population H. On the other hand, for intermediate values of θ (Figures 3.9(b) and 3.9(c)) the function $S(t)$ oscillates between small and relatively larger values. This results in more drastic variations of the oxygen concentration, which lead to cell population L being outcompeted by cell population H. As we would expect, when $S(t)$ remains away from zero or undergoes small oscillations while remaining close to zero, the mean phenotype of the surviving population $\mu_L(t)$ undergoes small oscillations and its value remains close, respectively, either to the fully oxidative phenotypic state $x = 0$ (Figure 3.9(a)) or to the fully glycolytic phenotypic state $x = 1$ (Figures 3.9(d) and 3.9(e)). By contrast, when $S(t)$ oscillates between small and relatively larger values, the mean phenotype of the surviving population $\mu_H(t)$ undergoes rapid and large amplitude transitions between phenotypic states closer to $x = 0$ and phenotypic states closer to $x = 1$ (Figures 3.9(b) and 3.9(c)).

The numerical results in Figure 3.9 refer to the case where there is no cost associated with glycolytic metabolism (i.e. $\gamma/\zeta = 1$) and both the amplitude A and the period T of the

fluctuations in oxygen inflow in Equation (3.30) are relatively large. However, the numerical results summarised by the plots in Figure 3.10 demonstrate that similar conclusions about how the oxygen consumption rate θ affects the outcome of the competition between the two cell populations hold when different values of the parameters γ/ζ, A and T are considered, provided that the value of A is sufficiently large.

The results summarised in Figure 3.10 also show that, for relatively large values of A, when θ is sufficiently high (second to fourth columns in Figure 3.10), larger values of γ/ζ correspond to a wider range of values of the parameters A and T under which transient coexistence between the two cell populations is observed. Moreover, these results show that for sufficiently large values of θ, larger values of γ/ζ increase the likelihood that cell population H will ultimately outcompete cell population L. As illustrated by the sample dynamics presented in Figure 3.11, this gives rise to smaller cell numbers, more pronounced variations in the mean phenotype of the surviving cell population and higher levels of phenotypic heterogeneity. On the other hand, the plots in the first column of Figure 3.10 show that for relatively small values of A and θ the outcome of the competition between the two cell populations is only weakly affected by the quotient γ/ζ.

Taken together, these results indicate that, when oxygen inflow undergoes periodic oscillations, chronic hypoxia and cycles of hypoxia followed by re-oxygenation can spontaneously emerge depending on the rate at which oxygen is consumed by the cells. In this biological scenario, the evolutionary fate of cell populations that undergo heritable, spontaneous phenotypic variations at different rates depends crucially upon the rate at which cells consume oxygen, θ, and the fitness costs associated with glycolytic metabolism, γ/ζ. Overall, cell populations undergoing phenotypic variations at lower rates are to be expected to be selected when the oxygen concentration remains, on average, relatively high or under chronic-hypoxic conditions. By contrast, cell populations with higher rates of phenotypic variation will outcompete other cell populations under alternating periods of hypoxia and re-oxygenation. In the latter case, the surviving cells adopt a bet-hedging strategy switching between oxidative and glycolytic metabolic phenotypes. Moreover, when oxygen levels fluctuate between zero and sufficiently large values, higher θ and γ/ζ can favour the transient coexistence of competing populations of cells that undergo heritable, spontaneous phenotypic variations at different rates.

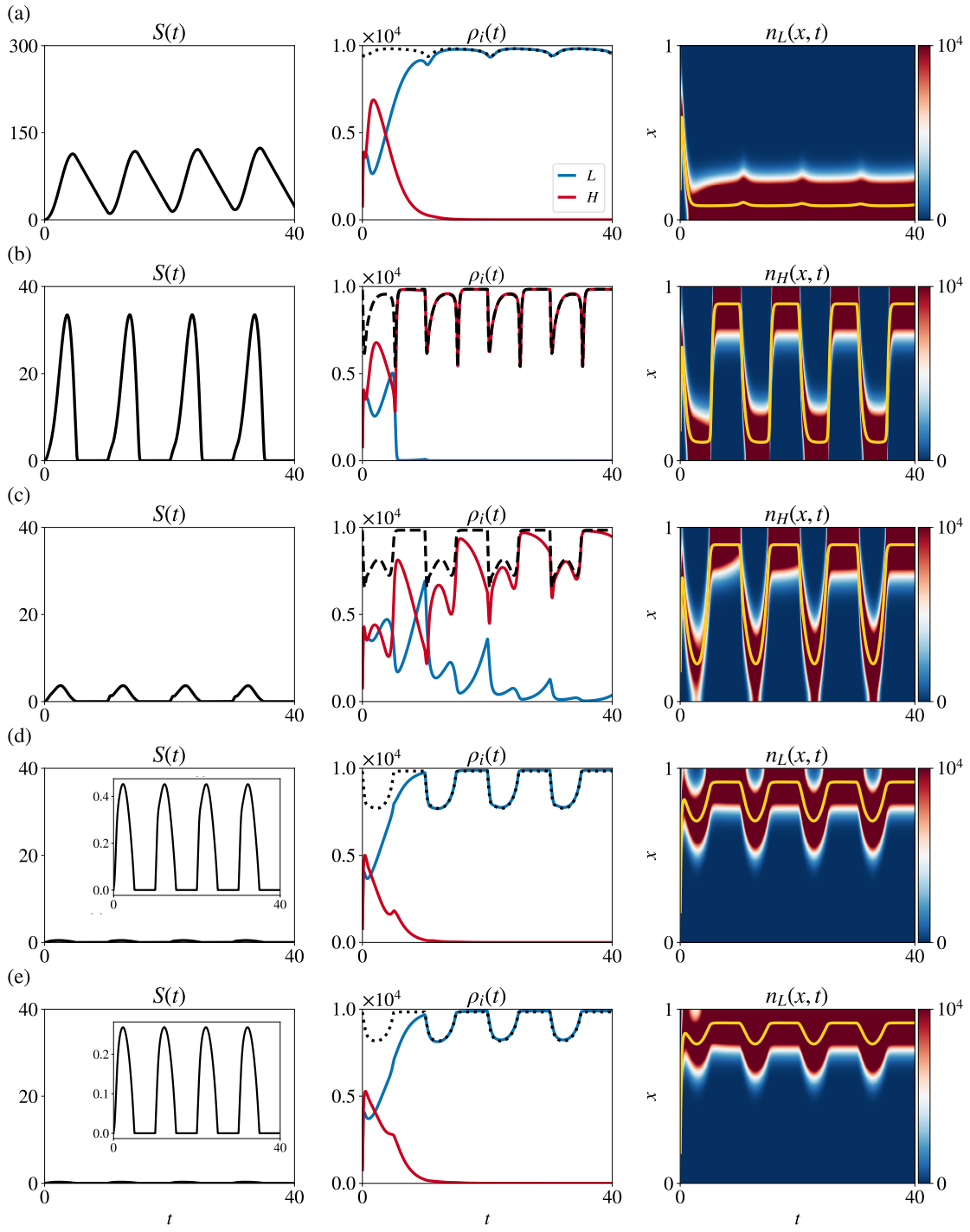

Figure 3.9: **(a)** Dynamics of the oxygen concentration (left), the population sizes (middle), and the population density of the surviving population (right) obtained by solving numerically Equations (3.4) and (3.7) with the oxygen inflow $I(t)$ defined via Equation (3.30) with $A = 60$ and $T = 10$. The dotted (or dashed) lines in the second column highlight the T-periodic solution of surviving population $\tilde{\rho}_L(t)$ (or $\tilde{\rho}_H(t)$) of the problem (3.25) in Section 3.3.1, while the yellow lines in the third column highlight the mean phenotype of the surviving population $\mu_i(t)$. Here, $\theta = 2 \times 10^{-5}$, $\zeta = \gamma$, and the values of the other parameters are defined in Table 3.2. **(b)** – **(e)** Same as row **(a)** but for $\theta = 5 \times 10^{-5}$ (row **(b)**), $\theta = 10^{-4}$ (row **(c)**), $\theta = 5 \times 10^{-4}$ (row **(d)**) and $\theta = 10^{-3}$ (row **(e)**).

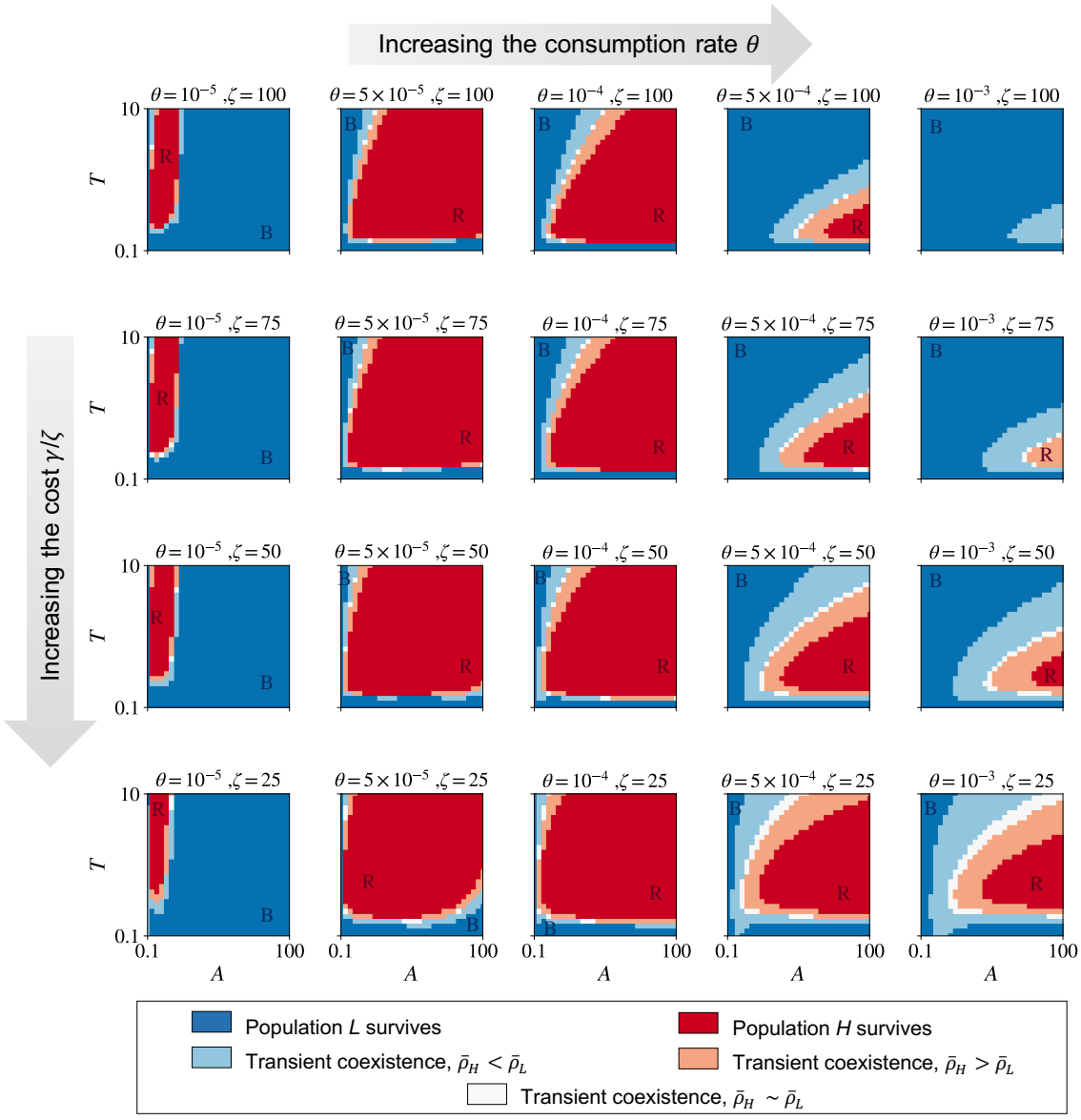

Figure 3.10: Summary of the results of numerical solutions of Equations (3.4) and (3.7) with the oxygen inflow $I(t)$ defined via Equation (3.30) for different values of A and T. Different columns correspond to different values of the consumption rate of oxygen θ, and different rows correspond to different values of the maximum cell division rate of fully glycolytic phenotypic variants. The blue points in the A–T plane correspond to parameter combinations for which $\bar{\rho}_H$ and $\bar{\rho}_L$ (i.e. the mean values of $\rho_H(t)$ and $\rho_L(t)$ computed over the last period of $I(t)$) are, respectively, smaller than 100 and larger than 1000 (i.e. $\rho_H(t)$ will eventually converge to zero), while the red points correspond to parameter combinations for which the same quantities are, respectively, larger than 1000 and smaller than 100 (i.e. $\rho_L(t)$ will eventually converge to zero). Lighter regions highlight the parameter combinations for which both $\bar{\rho}_H$ and $\bar{\rho}_L$ are considerably larger than 100 and $\bar{\rho}_H < \bar{\rho}_L$ (light blue regions), $\bar{\rho}_H > \bar{\rho}_L$ (pink regions) or $\bar{\rho}_H \approx \bar{\rho}_L$ (white regions) – i.e. for these parameter combinations, transient coexistence occurs for longer times although only one population will ultimately survive. The values of the other parameters are given in Table 3.2.

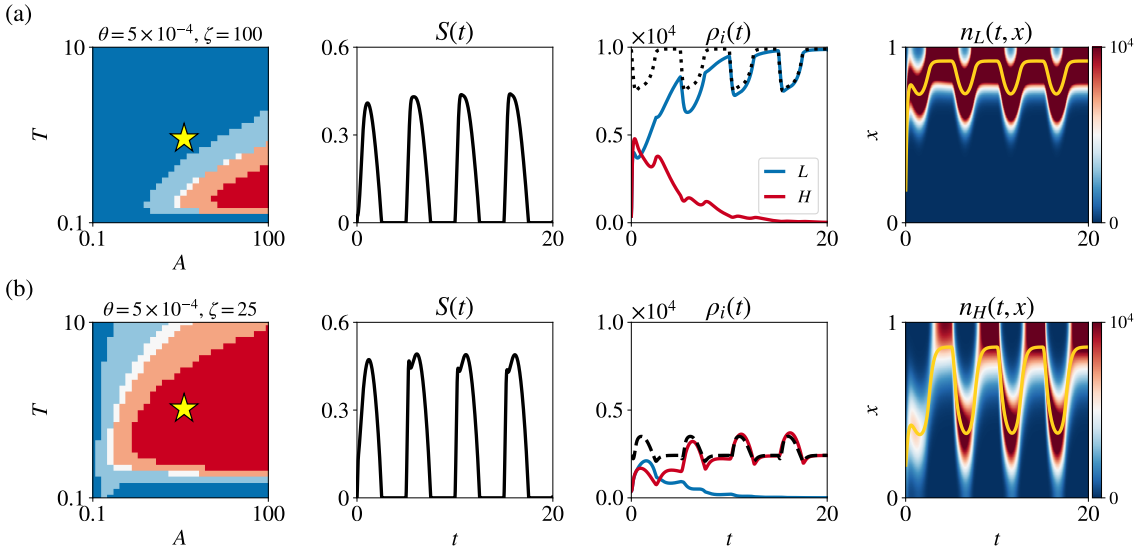

Figure 3.11: **(a)** The plot in the first column is the same as the plot in the fourth column of Figure 3.10, and the yellow star highlight the parameter values corresponding to the numerical results displayed here. The subsequent plots show the dynamics of the oxygen concentration $S(t)$ (second column), the population sizes $\rho_H(t)$ and $\rho_L(t)$ (third column), and the population density function of the surviving population $n_i(t,x)$ (fourth column) obtained by solving numerically Equations (3.4) and (3.7) with oxygen inflow $I(t)$ defined via Equation (3.30) with $A = 50$ and $T = 5$. The dotted (or dashed) lines in the third column highlight the T-periodic solution $\tilde{\rho}_L(t)$ (or $\tilde{\rho}_H(t)$) of the problem (3.25), while the yellow lines in the fourth column highlight the mean phenotype $\mu_i(t)$ obtained by solving the PDEs. The consumption rate of oxygen is $\theta = 5 \times 10^{-4}$, the maximum cell division rate of fully glycolytic phenotypic variants is $\zeta = \gamma$, and the values of the other parameters are defined as in Table 3.2. **(b)** Same as row **(a)** but for $\zeta = 0.25\gamma$.

3.5 Investigating the timescales of fluctuations

In this chapter we have investigated the population dynamics of cells that undergo spontaneous phenotypic variations when oxygen is supplied constantly or periodically in time. The parameters were chosen to demonstrate the qualitative behaviour of the system. In particular, we were interested in defining the environmental regimes that lead to selection of population with higher rates of phenotypic variation. Additionally, we investigated the impact of cellular feedback on the environment, as well as fitness costs associated with glycolytic phenotype. All these parameters are known to be cell line and environment-dependent. In this section, we use the model to define the timescales at which heritable, spontaneous phenotypic variations might confer a competitive advantage to cancer cells. We do so by considering a particular set of realistic parameter values obtained from the literature. We note that we have not performed a structural identifiability analysis and this remains as future work.

3.5.1 Choice of parameter values

In accordance with existing literature [171], we choose the rate of phenotypic variation β_H reported in Table 3.3. We assume that the rate of phenotypic variations of population L is on order of magnitude smaller that β_H (i.e. $\beta_L = 0.1\beta_H$.)

We estimate the maximum proliferation rate of cells in fully oxidative phenotype ($x = 0$), $\gamma = 0.86$ day^{-1}, from existing literature [120, 19]. Furthermore, we assume that the maximum proliferation rate of fully glycolytic cells ($x = 1$) is defined as $\zeta = 0.76\gamma = 0.68$ day^{-1} [19].

We consider a biological scenario scenario where cancer cells occupy 1 mm^3 volume of space. Assuming that the average diameter of a cell is approximately 20 μm, we estimate that the maximum number of cells that can occupy such volume of space is 1.25×10^5. Since the approximate carrying capacity of the system can be defined as

$$\frac{\gamma}{d} \approx 1.25 \times 10^5, \tag{3.31}$$

we deduce the value of the death rate due to inter- and intra-population competition, d.

In this setup, we assume that the oxygen is supplied (term $I(t)$ in the Equation (3.7)) by the blood vessel. We denote by I_v the average amount of oxygen released from a single healthy blood vessel and use the value measure by [217]. From Krogh cylinder model [126], we know that oxygen diffusion limit is about 100 – 200 μm. Thus, using average value of cell size and cylindrical geometry, we estimate that a single vessel can support around 200 cells. Thus, the parameter α defines the number of vessels required in order to maintain

1.25×10^5 cells. The values of oxygen consumption rate, θ, Michaelis constant, κ, and rate of natural decay, ν, are obtained from the literature.

The full list of parameter values used in this section are summarised in Table 3.3. We use the numerical scheme to solve the system of PDEs (3.4) coupled with an ODE for oxygen dynamics (3.7) and the initial conditions as described in Section 3.4.1.

Parameter	**Value**	**Unit**	**Reference**
β_H	0.01	day^{-1}	[171]
β_L	0.001	day^{-1}	Model specific
γ	0.86	day^{-1}	[120, 19]
ζ	0.66	day^{-1}	[19]
d	6.9×10^{-5}	cell^{-1} day^{-1}	Model specific
θ	1.73×10^{-8}	mmol cell^{-1}	[19]
κ	7×10^{-3}	mmol	[19]
ν	0.24	day^{-1}	[218]
I_v	1.5×10^{-4}	mmol day^{-1}	[217]
α	625	–	Model specific

Table 3.3: Parameter values used in numerical simulations.

3.5.2 Results

Figure 3.12 shows the dynamics of oxygen (top) and population dynamics (bottom) for different regimes of environmental fluctuations when we use the maximum proliferation rates that are realistic for bacterial populations. Here, we assume that oxygen inflow varies according to Equation (3.30) between $I_{min} = 0$ and $I_{max} = \alpha I_v$. The simulation results suggest that for this particular parameter set it is impossible to observe a scenario where the population H survives.

Thus, it remains as future work to fully explore the parameter space to determine the extent to which the behaviour observed in Section 3.4.3 occurs and to then see how realistic those parameters are in the context of human cancers. It may well be the case that for biologically realistic parameters, this behaviour will require inclusion of additional feedback mechanisms, which is beyond the scope of this thesis. However, if we increase the values of the maximum proliferation rates for oxidative and glycolytic variants, we can observe scenarios whereby the population L becomes extinct. In particular, here we consider values of γ and ζ that are consistent with the proliferation rates of bacteria [219].

Figure 3.13 shows that fast fluctuations in oxygen supply ($T = 1$ and $T = 7$ days), result in mild fluctuations experienced by the cells. In both cases, the population with the lower rate of phenotypic variation survives. Slower variations in the supply of oxygen ($T = 14$ and $T = 21$ days), on the other hand, provide favourable conditions for the population with

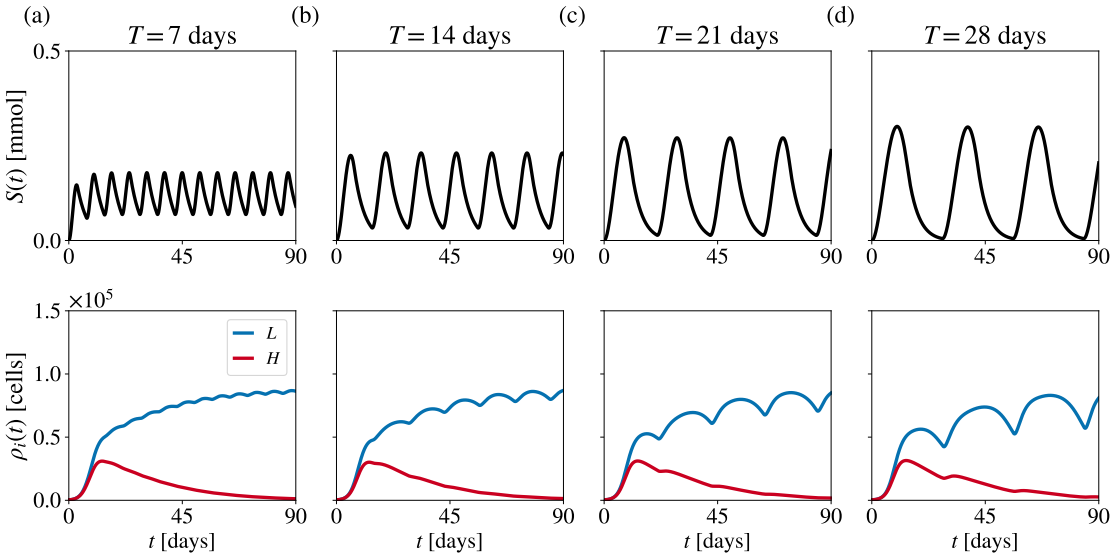

Figure 3.12: **(a)** The dynamics of the oxygen concentration (top) and the population sizes (bottom) obtained by solving numerically Equations (3.4) and (3.7) with the oxygen inflow $I(t)$ defined by Equation (3.30) with $A = \alpha I_v$ and period of oscillation $T = 1$ day. The values of the parameters are given in Table 3.3. **(b)** – **(d)** Same as column **(a)** but for $T = 7$ days (column **(b)**), $T = 14$ days (column **(c)**), and $T = 21$ days (column **(d)**).

the higher rate of phenotypic variation. In this case, the environment undergoes extended periods of starvation followed by re-oxygenation conditions and population H ultimately survives. Moreover, longer periods of fluctuation result in higher amplitude oscillations in oxygen concentration. This is due to the fact that when fluctuations are slow, individuals have more time to adapt and entirely switch their phenotype. Therefore, in accordance with the observations from Figure 3.11, the cost for being in a glycolytic phenotype enhances the severity of the environmental fluctuations.

3.6 Application of the results to the emergence of phenotypic heterogeneity in vascularised tumours

In small tumours, cancer cells receive growth factors and nutrients via diffusion from blood vessels in adjacent normal tissue. However, this process supports limited tumour growth, to a diameter of a few millimetres. Further expansion requires intratumoural blood flow and, therefore, selects for cancer cells with an 'angiogenic' phenotype. This results in growth of blood vessels (i.e. sprouting angiogenesis) into the tumour. However, unlike normal tissue, a tumour cannot perform the coordinated functions required for vascular maturation. Thus, while intratumoural blood flow enables the nutrient transport into the tumour [11], the tangled, uncoordinated vascular structure typically results in regions of

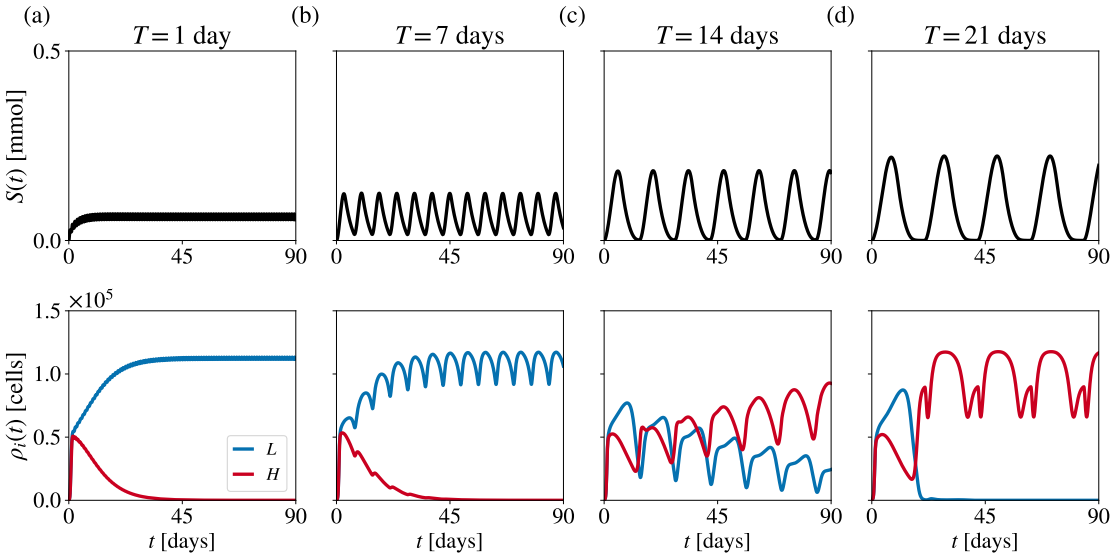

Figure 3.13: **(a)** The dynamics of the oxygen concentration (top) and the population sizes (bottom) obtained by numerically solving Equations (3.4) and (3.7) with the oxygen inflow $I(t)$ defined by Equation (3.30) with $A = \alpha I_v$ and period of oscillation $T = 1$ day. The values of the parameters are given in Table 3.3 with $\gamma = 8.64$ day^{-1} and $\zeta = 6.57$ day^{-1}. **(b)** – **(d)** Same as column **(a)** but for $T = 7$ days (column **(b)**), $T = 14$ days (column **(c)**), and $T = 21$ days (column **(d)**).

disordered blood flow with stochastic (but often frequent) changes in microenvironmental conditions. Thus, cancer cells at the tumour-host interface, which invade adjacent normal tissue and often transiently acquire normal vessels, may have relatively stable environments, (the left region of the scheme displayed in Figure 3.14). By contrast, deeper regions of the tumour, characterised by limited oxygen diffusion, suffer from chronic hypoxia (the right region of the scheme displayed in Fig. 3.14). Moreover, regions that require angiogenesis are often subject to variable blood flow and associated microenvironmental conditions. The nonlinear interplay between vascular remodelling, associated with on-going angiogenesis, and oxygen consumption by the cells brings about alternating periods of hypoxia and re-oxygenation in vascularised regions in the tumour interior (the central region of the scheme displayed in Fig. 3.14).

The results of our theoretical study indicate that such an expected spatio-temporal variability in oxygen concentration across a tumour can create distinct ecological niches in which different phenotypic variants undergoing heritable, spontaneous, phenotypic variation at different rates can be selected, and that this can also foster the emergence of phenotypic intratumour heterogeneity (the plots of the phenotype distributions $n_i(x,t)$ in the lower part of Figure 3.14). In particular, cell populations characterised by a lower rate of phenotypic variation and a more oxidative metabolism can be expected to colonise the oxygenated

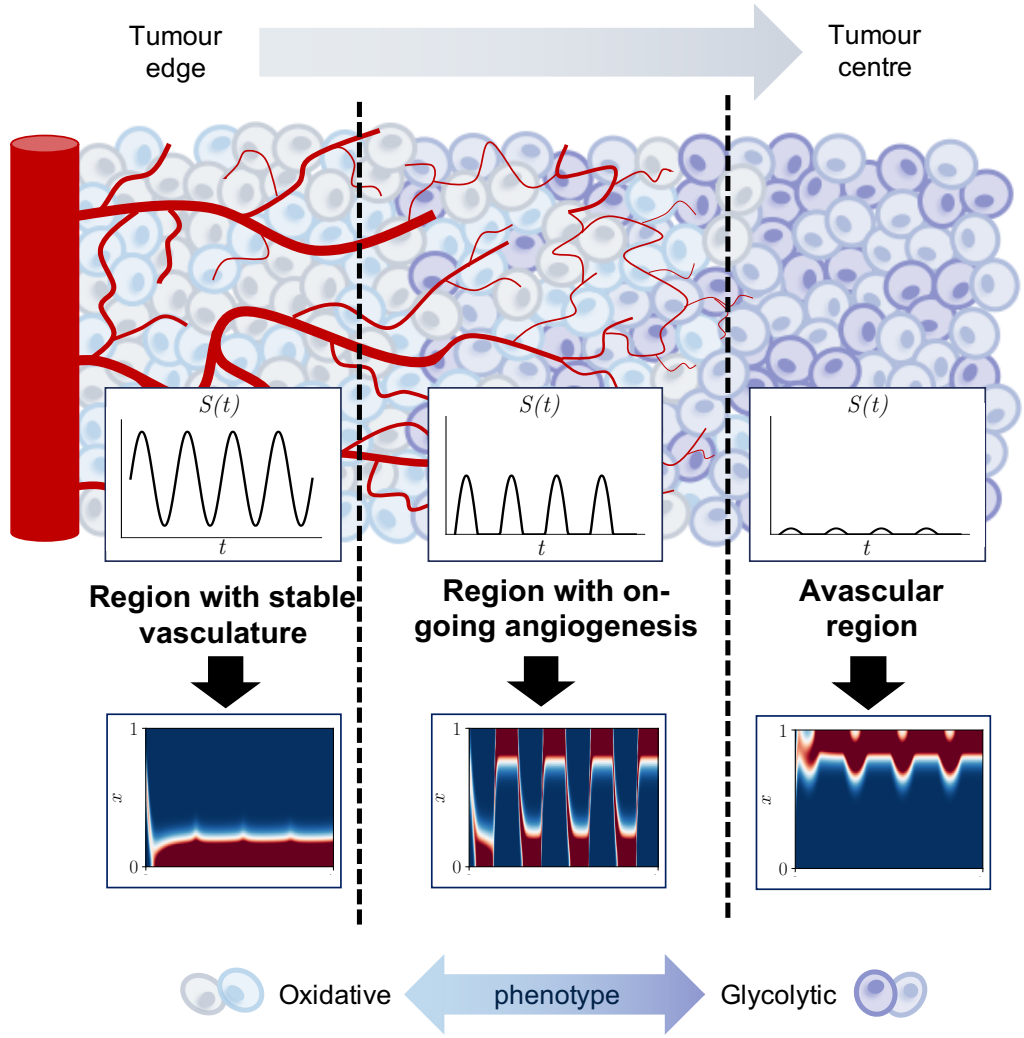

Figure 3.14: Application of the results to the emergence of phenotypic heterogeneity in vascularised tumours. In the plots in the bottom row, blue colour represents lower values of population density, whereas red colours correspond to higher density.

regions with relatively stable vasculature at the edge of tumour; cell populations characterised by higher rates of phenotypic variation that switch between oxidative and glycolytic metabolism are likely to populate regions of on-going angiogenesis at an intermediate distance from the tumour edge; cell populations characterised by lower rates of phenotypic variation and a more glycolytic metabolism can be expected to colonise central, avascular regions of the tumour where chronic hypoxia occurs.

3.7 Discussion

In this chapter, we have extended the mathematical model presented in Chapter 2 in order to investigate whether bet-hedging strategies might be beneficial for cancer cells subject to

constant and periodically-oscillating oxygen inflow. We assumed that oxygen dynamics are governed by an ordinary differential equation, where oxygen is supplied by the blood vessel, decays naturally and is consumed by cells.

We started by investigating a simplified model, where natural decay and consumption are represented by a single linear term and occur at constant rate. Under this simplifying assumption, we were able to study the asymptotic behaviour of model solutions and explore the qualitative dynamics of the system. We then looked at a more realistic but analytically non-tractable case, where cells consume oxygen with rates that depend on their phenotype. For both constant and periodically fluctuating oxygen inflow, there is excellent agreement between numerical simulations of the full model and analytical results from the simplified model. This agreement shows both the robustness of the biological conclusions drawn from the simulation results and the idea that the key features of the analytical results that we derived previously carry through when additional biological complexity is incorporated into the model. Furthermore, because our results persist across a range of values of the consumption rate of oxygen, θ, and the fitness cost associated with glycolytic metabolism, γ/ζ, we conclude that they are applicable to a variety of cancer cell lines under different environmental conditions, such as different levels of acidity [19].

In summary, the simulation results generated from our model indicate that nonlinear interactions between cells and oxygen can lead naturally to the occurrence of chronic hypoxia, and cycles of hypoxia and re-oxygenation depending on the rate at which oxygen is consumed by the cells. Moreover, the model supports the idea that under chronic hypoxia, lower rates of phenotypic variation constitute a source of competitive advantage. On the other hand, higher rates of phenotypic variation can confer a competitive advantage when oxygen levels are time-varying and the fitness costs associated with glycolytic metabolism are higher. In this case, the model demonstrates that bet-hedging strategies, where cells switch between oxidative and glycolytic metabolic phenotypes, can spontaneously emerge. In particular, higher rates of phenotypic variations confer a competitive advantage when the environmental fluctuations occur on slower timescales. Such fluctuations may to occur due to on-going angiogenesis and vascular remodelling, as well as during early tumour development.

These results provide a theoretical basis for previous experimental results, such as those presented by [40] and [47], showing that intermittent hypoxia can trigger the emergence of different phenotypic properties in cancer cell populations. We expect intermittent hypoxia to promote higher levels of phenotypic heterogeneity, which is known to affect the efficacy of therapies [5, 6]. Hence, our observations support the concept of 'vascular normalisation' to stabilise the cancer environment and bring levels of phenotypic heterogeneity to a

minimum as a key strategy in cancer treatment [48]. Furthermore, in line with previous theoretical studies indicating that periodically fluctuating environments can promote coexistence of competing populations [220], our results suggest that, when the environmental conditions within the tumour switch between oxygen-poor and oxygen-rich, higher rates of oxygen consumption by cells and higher fitness costs associated with glycolytic metabolism can promote transient coexistence of competing cell populations that undergo heritable, spontaneous phenotypic variations at different rates. Finally, we have discussed how our mathematical results shed light on the evolutionary processes underlying the emergence of phenotypic heterogeneity in vascularised tumours.

In this chapter, we observed that, under certain conditions, a transient coexistence might occur between populations with higher and lower rates of phenotypic variations when oxygen supply is both constant (Figure 3.6) and periodic (Figure 3.9). Furthermore, under certain initial conditions, we observed that population H might drive population L to very low numbers even when oxygen supply is constant (Figure 3.8). In the deterministic setting, population L will always recover and its population size will approach the long-term limit, as predicted. However, this might not be the case in a discrete setting where cells undergo stochastic birth-death processes. Therefore, it is likely that the discrete and continuum models might lead to different competition outcomes even when the environmental conditions are steady. We investigate this in Chapter 4 by developing and studying a corresponding discrete individual-based model of two competing phenotype-structured populations.

Chapter 4

Individual-based model for the competition of phenotype-structured populations

4.1 Introduction

Continuum models formulated in terms of integro-differential and nonlocal partial differential equations have been successfully used to study the evolutionary dynamics of cancer cell populations that are structured by physiological traits. Such models provided insights into the development of drug resistant clones during chemotherapy administration [169, 170, 172, 176, 173], emergence of phenotypic heterogeneity in solid tumours [179, 180], as well as the adaptive strategies employed by cancer cells in temporally varying environments [182], which is the focus of this thesis.

One of the main advantages of deterministic continuum models is that they are amenable to mathematical analysis, allowing for an in-depth theoretical understanding of the underlying dynamics and full exploration of the parameter space. Additionally, continuum models are computationally cost-effective, i.e. it is possible to perform numerical simulations for large numbers of cells even at the scale of the whole organ. However, such continuum models are usually defined on the basis of population-scale phenomenological assumptions. This makes it more difficult to incorporate the details of phenotypic adaptation by individuals. Moreover, such models cannot capture adaptive phenomena that are driven by stochastic effects during the evolution of individual cells. This is particularly relevant at low population levels.

Small populations of cells are common in cancers and affect dramatically disease progression and the response of the tumour to therapies. For instance, by administering anti-cancer drugs, it is possible to drive tumours beyond clinically detectable levels. However, a small number of surviving cells that are resistant to the drug usually remain and lead to relapse

of the disease, and eventually, may prove to be lethal [221]. Similarly, tumour cells are able to colonise distant organs. These colonies begin as micrometastases – single cells or small clusters of cells – that subsequently expand into clinically detectable metastasis, and often lead to patient death [222]. Therefore, when studying the evolutionary dynamics of cancer cells in temporally varying environments, it is important to consider scenarios where the number of cells is small.

Furthermore, small population sizes are commonly observed when risk-spreading adaptive strategies occur [89]. As shown in Figure 3.8 in Chapter 3, the populations placed in a new environment can decrease in size. In a deterministic setting, such populations will always recover. However, the validity of a continuum approach at low population numbers may be called into question as stochastic effects play a more pronounced role. Ideally, we want to derive deterministic continuum models from first principles (i.e. as the appropriate limit of discrete stochastic models that track the evolution of single individuals), which permit representation of individual-scale adaptive mechanisms, and account for stochastic inter-individual variability in evolutionary trajectories [189, 188]. Therefore, the goal of this study is to derive the deterministic model as a large population scale limit of a discrete, stochastic system, so that we can investigate the validity of the deterministic model when cell densities are small.

In light of these considerations, we develop a stochastic individual-based (IB) model for the evolutionary dynamics of two competing phenotype-structured cell populations that are exposed to time-varying nutrient levels as described in Chapters 2 and 3. In this model, every cell is viewed as an individual agent whose phenotypic state is modelled by a discrete variable. Cells proliferate, die and undergo phenotypic variations according to a set of rules that correspond to a discrete-time branching random walk on the space of phenotypic states [190, 192]. As before, we assume that the cell proliferation rate depends on nutrient levels, and its concentration is governed by a difference equation in which a sink term models nutrient consumption by the cells.

This chapter is organised as follows. We begin by describing the individual-based model in Section 4.2. We then show formally that the deterministic continuum counterpart of this stochastic IB model comprises a system of non-local PDEs for the cell population density functions (i.e. the cell distribution over the space of phenotypic states) coupled to an ordinary differential equation for the nutrient concentration (Section 4.3). In Section 4.5 we carry out numerical simulation of individual-based model, implemented using on open-source framework Hybrid Automata Library [193]. We compare the IB model and its continuum analogue, exploring scenarios in which differences between the two models emerge due to stochastic effects not captured by the deterministic continuum model. Finally, as an

illustrative example, we interpret our results in the context of the early stage of metastatic colonisation of distant organs by cancer cells (Section 4.6).

This work has been done under the co-supervision of Prof. Tommaso Lorenzi (Politecnico di Turino, Italy). The results presented in Sections 4.2 – 4.6 have been published in the following paper:

A. Ardaševa, R. A. Gatenby, A. R. A. Anderson, H. M. Byrne, P. K. Maini, T. Lorenzi, 2020, 'A comparative study between discrete and continuum models for the evolution of competing phenotype-structured cell populations in dynamical environments', Physical Review E, 102(4), 042404.

4.2 Stochastic individual-based model

We model the evolutionary dynamics of two competing cell populations in a well-mixed system. Cells in the two populations proliferate (i.e. divide), die and undergo spontaneous, heritable phenotypic variations. We assume that the two populations differ only in their probability of phenotypic variation. The population undergoing phenotypic variations with a higher probability is labelled by the letter H, while the other population is labelled by the letter L.

We consider two different scenarios for nutrient dynamics. First, we assume that nutrient concentration is prescribed (Section 4.4), which is analogous to the modelling framework studied in Chapter 2. Here, the phenotypic state of every cell at time $t \in [0, t_f] \subset \mathbb{R}^+$ is characterised by a variable $x \in \mathbb{R}$. Afterwards, we consider a scenario whereby cells consume nutrient according to their phenotypic state (Section 4.5). This is identical to the approach used in Chapter 3. In this case, we limit the phenotypic domain to $x \in [0, 1] \subset \mathbb{R}^+$.

We represent each cell as an agent that occupies a position on a lattice. We discretise the time variable and the phenotypic state via $t_h = h\tau \in [0, t_f]$ and $x_j = j\chi \in \mathbb{R}$, where $h, j \in \mathbb{N}_0$, and $\tau \in \mathbb{R}_*^+$ and $\chi \in \mathbb{R}_*^+$ are the time- and phenotype-step, respectively. In Section 4.4 we let $x_j \in [-5, 5]$ and in Section 4.5 we assume $x_j \in [0, 1]$. We introduce the dependent variable $N_{i,j}^h \in \mathbb{N}_0$ to represent the number of cells of population $i \in \{H, L\}$ on lattice site j (i.e. in the j^{th} phenotypic state) at time-step h. The density of population i, the size of population i, and the total number of cells are defined, respectively, as follows

$$n_i(t_h, x_j) = n_{i,j}^h := N_{i,j}^h \, \chi^{-1}, \tag{4.1}$$

$$\rho_i(t_h) = \rho_i^h := \sum_j N_{i,j}^h \quad \text{and} \quad \rho(t_h) = \rho^h := \sum_i \rho_i^h. \tag{4.2}$$

We further define the mean phenotype of population i and the related standard deviation, respectively, as

$$\mu_i(t_h) = \mu_i^h := \frac{1}{\rho_i^h} \sum_j x_j \, N_{i,j}^h \tag{4.3}$$

and

$$\sigma_i(t_h) = \sigma_i^h := \left(\frac{1}{\rho_i^h} \sum_j x_j^2 \, N_{i,j}^h - \left(\mu_i^h\right)^2 \right)^{\frac{1}{2}}. \tag{4.4}$$

Finally, the nutrient concentration at time-step h is modelled by the discrete, non-negative function $S(t_h) = S^h$.

4.2.1 Phenotypic variations

We account for spontaneous, heritable phenotypic variations by allowing cells to update their phenotypic states according to a random walk. In particular, between the time-steps h and $h+1$, every cell in population $i \in \{H, L\}$ either enters a new phenotypic state, with probability $\lambda_i \in [0, 1]$, or remains in its current phenotypic state, with probability $1 - \lambda_i$. Since we assume phenotypic variations to occur randomly due to non-genetic instability, rather than selective pressures [223], we assume that a cell of population i in phenotypic state x_j that undergoes a phenotypic variation enters into either of the phenotypic states $x_{j\pm1}$ with probabilities $\lambda_i/2$, as demonstrated in Figure 4.1. No-flux boundary conditions are implemented by aborting any attempted phenotypic variation of a cell if it requires moving into a phenotypic state outside the intervals $[0, 1]$ or $[-5, 5]$, depending on the problem.

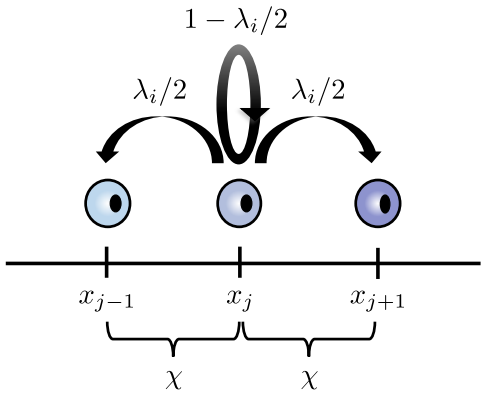

Figure 4.1: Schematic representation of the algorithmic rules governing the phenotypic variation.

4.2.2 Cell division and death

Cells divide, die or remain quiescent with probabilities that depend on their phenotypic states, the total number of cells and the nutrient concentration. We assume that a dividing cell is replaced by two identical cells that inherit the phenotypic state of the parent cell (i.e. the progenies are placed on the same lattice site as their parent), while a dying cell is removed from the population.

Following the assumptions introduced in Chapter 2, in order to translate into mathematical terms the idea that larger population sizes correspond to more intense competition between cells, at every time-step h we allow cells to die due to intra-population and inter-population competition at a rate proportional to the total cell number ρ^h, with constant of proportionality $d > 0$.

We denote by $p(x_j, S^h)$ the division rate of a cell in the j^{th} phenotypic state. In line with assumptions made in Chapters 2 and 3, we assume that cells in phenotypic state $x \to 0$ are adapted to nutrient-rich conditions (i.e. fully oxidative), whereas cells in the phenotypic state $x \to 1$ are adapted to nutrient-scarce environment (i.e. fully glycolytic). Therefore, following the modelling strategies defined in Chapters 2 and 3, we define the cell division rate $p(x_j, S^h)$ as follows

$$p(x_j, S^h) := \gamma \frac{S^h}{\kappa + S^h}(1 - x_j^2) + \zeta \left(1 - \frac{S^h}{\kappa + S^h}\right)[1 - (1 - x_j)^2]. \tag{4.5}$$

In Equation (4.5), γ and ζ are the maximal proliferation rates of cells in phenotypic states $x = 0$ and $x = 1$, respectively, and κ is the Michaelis constant of the nutrient. After a little algebra, Equation (4.5) can be rewritten as

$$p(x_j, S^h) = \gamma g(S^h) - h(S^h)(x_j - \varphi(S^h))^2, \tag{4.6}$$

where

$$g(S^h) := \frac{S^h}{\kappa + S^h} + \frac{\zeta^2 \kappa^2}{\gamma(\kappa + S^h)(\gamma S^h + \zeta\kappa)}, \tag{4.7}$$

$$\varphi(S^h) := \frac{\zeta\kappa}{\gamma S^h + \zeta\kappa} \quad \text{and} \quad h(S^h) := \frac{\gamma S^h + \zeta\kappa}{\kappa + S^h}. \tag{4.8}$$

Under these assumptions, between time-steps h and $h + 1$, a cell in the j^{th} phenotypic state may divide with probability

$$\mathcal{P}_b := \tau\, p(x_j, S^h), \tag{4.9}$$

die with probability

$$\mathcal{P}_d := \tau\, d\, \rho^h, \tag{4.10}$$

or remain quiescent (i.e. do not divide nor die) with probability

$$\mathcal{P}_q := 1 - \tau \left(p(x_j, S^h) + d\,\rho^h \right). \tag{4.11}$$

Notice that we are implicitly assuming that the time-step τ is sufficiently small that the probabilities $\mathcal{P}_b$, $\mathcal{P}_d$ and $\mathcal{P}_q$ satisfy $0 \leq \mathcal{P}_i \leq 1$ for all $i \in \{b, d, q\}$.

4.2.3 Nutrient dynamics

We consider two scenarios corresponding to different levels of biological complexity. In the first scenario (see Paragraph **a** below), we focus on the case of a controlled environment whereby the nutrient concentration S^h is a given function (i.e. the dynamic of the nutrient is decoupled from the dynamic of the cells). In the second scenario (see Paragraph **b** below), we let the evolution of S^h be governed by a difference equation that is coupled with the dynamics of the cells, in order to explore how the evolutionary dynamics of the cells is shaped by the negative feedback that regulates the growth of the two populations through nutrient consumption.

a. Prescribed nutrient concentration. In order to consider both constant and periodically oscillating given levels of nutrient, we follow Chapter 2 by letting S^h be a discrete function defined as

$$S^h := M + A \sin\left(\frac{2\pi t_h}{T}\right), \tag{4.12}$$

where $M > 0$ is the mean nutrient level, while the parameter $0 \leq A \leq M$ models the amplitude of possible oscillations of the nutrient level, which have period $T > 0$.

b. Nutrient concentration co-evolving with the cells. Following Chapter 3, we describe the nutrient dynamics via the following difference equation for S^h

$$S^{h+1} = S^h + \tau\Big[I^h - \eta S^h - \theta\gamma \frac{S^h}{1+S^h} \sum_j (1-x_j)^2 \left(N^h_{H,j} + N^h_{L,j} \right) \Big]. \tag{4.13}$$

In Equation (4.13), the parameter $\eta > 0$ represents the rate of natural decay of the nutrient, while the last term on the right-hand side of Equation (4.13) models the rate of nutrient consumption by the cells and is based on the assumptions given in Section 3.2.2. The discrete, non-negative function I^h on the right-hand side of Equation (4.13) models the rate at which the nutrient is supplied to the system. When the nutrient inflow is constant we let

$$I^h \equiv \bar{I} \geq 0, \tag{4.14}$$

while to model the case where the nutrient inflow undergoes periodic oscillations we use the definition

$$I^h := \max\left(0, A\sin\left(\frac{2\pi t_h}{T}\right)\right), \tag{4.15}$$

with the parameters $T > 0$ and $A > 0$ modelling, respectively, the period and the amplitude of the oscillations.

4.2.4 Computational implementation

Numerical simulations of the IB model are performed using the open-source Java library Hybrid Automata Library [193]. At each time-step, we follow the procedures summarised in Figure 4.2 and described hereafter to simulate phenotypic variations as well as cell division and death. All random numbers mentioned below are real numbers drawn from the standard uniform distribution on the interval $(0, 1)$ using the Java function `Rand.Double()`. We validate the individual-based model by comparing the dynamics of population sizes, mean phenotype and phenotypic distribution in time with the numerical solutions of the continuum model (see Section 4.3). The numerical simulations of the continuum model are obtained as described in Sections 2.4.1 and 3.4.1.

a. Computational implementation of phenotypic variations. For each cell in population i, a random number, r_1, is generated and used to determine whether the cell undergoes a phenotypic variation (i.e. $0 \leq r_1 < \lambda_i$) or not (i.e. $\lambda_i \leq r_1 \leq 1$). If the cell undergoes a phenotypic variation, then a second random number, r_2, is generated. If $0 \leq r_2 < 1/2$, then the cell moves into the phenotypic state to the left of its current state, whereas if $1/2 \leq r_2 \leq 1$ then the cell moves into the phenotypic state to the right of its current state. No-flux boundary conditions are implemented by aborting attempted phenotypic variations that would move a cell into a phenotypic state outside the prescribed interval ($[0, 1]$ or $[-5, 5]$).

b. Computational implementation of cell division and death. For each population, the number of cells in each phenotypic state is counted. The size of each cell population and the total number of cells are then computed via Equation (4.2). Equations (4.9)–(4.11) are used to calculate the probabilities of cell division, death and quiescence for every phenotypic state. For each cell, a random number, r_3, is generated and cell fate is determined by comparing this number with the probabilities of division, death and quiescence corresponding to the phenotypic state of the cell. If $0 \leq r_3 < \mathcal{P}_d$, then the cell is considered dead and is removed from the population. If $\mathcal{P}_d \leq r_3 < \mathcal{P}_d + \mathcal{P}_b$, then the cell undergoes

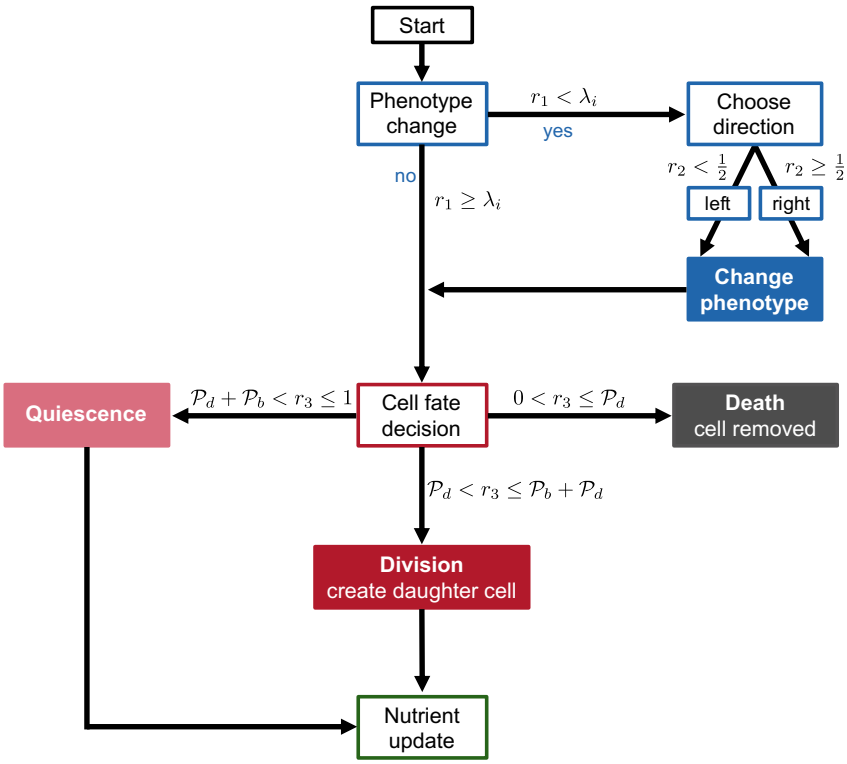

Figure 4.2: Flowchart illustrating the procedure underlying the computational implementation of the stochastic IB model for each cell at every time-step. Once all cells have undergone both the phenotype-change step and the fate-decision step, the total number of cells is computed and the nutrient level is updated.

division and an identical daughter cell is created. Finally, if $\mathcal{P}_d + \mathcal{P}_b \leq r_3 < 1$, then the cell remains quiescent (i.e. does not divide nor die).

c. Computational implementation of nutrient dynamics. If the evolution of nutrient is governed by the difference equation (4.13), then at each time-step the number of cells of the two populations in every phenotypic state is counted and used to evaluate the last term on the right-hand side of Equation (4.13), in order to update the nutrient concentration. Otherwise, the nutrient concentration is updated according to definition (4.12).

d. Parameter values and initial conditions. For consistency with previous mathematical studies of the evolutionary dynamics of phenotype structured populations, simulations are carried out under the assumption that the initial phenotype distribution of population i for the IB model is of the form

$$n_{i,j}^0 = a_i \left(\frac{b}{2\pi}\right)^{\frac{1}{2}} \exp\left[-\frac{b}{2}(x_j - c)^2\right], \tag{4.16}$$

with $i \in \{H, L\}$. In Equation (4.16), the parameter a_i is related to the initial size of population i, while the parameters b and c are related, respectively, to the inverse of the initial standard deviation and the initial mean phenotype of the two populations. The initial population density $n_i(x, 0)$ for the continuum model is defined as the continuum analogue of Equation (4.16) (see Equation (2.12)). We assume the nutrient concentration to be non-dimensionalised and use the dimensionless parameter values listed in Table 4.1 to carry out numerical simulations of the IB and PDE models. The parameter values are consistent with those used in Chapters 2 and 3 in order to demonstrate the qualitative behaviour of the system.

Parameter	**Description**	**Values**
λ_H	Probability of phenotypic variation of population H	[0.05, 1]
λ_L	Probability of phenotypic variation of population L	[0.02, 0.2]
γ	Maximum proliferation rate of oxidative cells	100
ζ	Maximum proliferation rate of glycolytic cells	50
d	Death rate due to competition	0.01
θ	Consumption rate of nutrient	$[10^{-5}, 10^{-3}]$
κ	Michaelis constant	1
η	Rate of natural decay of nutrient	10^{-3}
χ	Phenotype-step	[0.032, 0.01, 0.0032]
τ	Time-step	$[10^{-3}, 10^{-4}, 10^{-5}]$
t_f	Final time	[10, 40, 60]

Table 4.1: Parameter values used in numerical simulations.

The methods employed to numerically solve the equations of the related continuum model are described in Section 2.4.1 (when the nutrient level is prescribed) and in Section 3.4.1 (when nutrient co-evolves with the cells and we assume phenotype-dependent consumption).

4.3 Formal derivation of the corresponding continuum model

Using a method analogous to that employed in [190, 191], we are using mean field assumption to show that the system of non-local PDEs (2.3) presented in Chapter 2 can be formally derived as the appropriate continuum limit of our discrete model.

In the case where the dynamics of the cells is governed by the rules described in Section 4.2, the principle of mass balance yields the following difference equations

$$n_{i,j}^{h+1} = \Big\{2\,\tau\,p(x_j, S^h) + \Big[1 - \tau\,\Big(p(x_j, S^h) + d\rho^h\Big)\Big]\Big\} \times \Big[\frac{\lambda_i}{2} n_{i,j+1}^h + \frac{\lambda_i}{2} n_{i,j-1}^h + (1-\lambda_i)\, n_{i,j}^h\Big],$$

for $i \in \{H, L\}$, which can be rewritten as

$$n_{i,j}^{h+1} = (1 + \tau\ p(x_j, S^h) - \tau\ d\ \rho^h)\Big[\frac{\lambda_i}{2} n_{i,j+1}^h + \frac{\lambda_i}{2} n_{i,j-1}^h + (1-\lambda_i) n_{i,j}^h\Big]. \tag{4.17}$$

Using the fact that the following relations hold for τ and χ sufficiently small

$$t_h \approx t, \quad t_{h+1} \approx t+\tau, \quad x_j \approx x, \quad x_{j\pm1} \approx x \pm \chi, \tag{4.18}$$

$$n_{i,j}^h \approx n_i(x,t), \quad S^h \approx S(t), \tag{4.19}$$

$$n_{i,j}^{h+1} \approx n_i(x,t+\tau), \quad n_{i,j\pm1}^h \approx n_i(x\pm\chi,t), \tag{4.20}$$

$$\rho_i^h \approx \rho_i(t) := \int_0^1 n_i(x,t)\,\mathrm{d}x, \tag{4.21}$$

$$\rho^h \approx \rho(t) := \int_0^1 n_H(x,t)\,\mathrm{d}x + \int_0^1 n_L(x,t)\,\mathrm{d}x, \tag{4.22}$$

Equation (4.17) can be formally rewritten in the approximate form

$$n_i(x,t+\tau) = \Big(1+\tau R(x,S(t),\rho(t))\Big)\Big[\frac{\lambda_i}{2}n_i(x+\chi,t)+\frac{\lambda_i}{2}n_i(x-\chi,t)+(1-\lambda_i)n_i(x,t)\Big], \tag{4.23}$$

with

$$R(x,S(t),\rho(t)) := p(x,S(t)) - d\rho(t). \tag{4.24}$$

If the function $n_i(x,t)$ is twice continuously differentiable with respect to the variable x, for χ sufficiently small we can use the Taylor expansions

$$n_i(x\pm\chi,t) = n_i \pm \chi\frac{\partial n_i}{\partial x} + \frac{\chi^2}{2}\frac{\partial^2 n_i}{\partial x^2} + h.o.t.\ , \tag{4.25}$$

where $n_i \equiv n_i(x,t)$. Substituting Equation (4.25) into Equation (4.23) and dividing both sides of the resulting equation by τ, after a little algebra we find

$$\frac{n_i(x,t+\tau)-n_i(x,t)}{\tau} = R(x,S(t),\rho(t))n_i(x,t) + \frac{\lambda_i\chi^2}{2\tau}\frac{\partial^2 n_i(x,t)}{\partial x^2} + R(x,S(t),\rho(t))\frac{\lambda_i\chi^2}{2}\frac{\partial^2 n_i(x,t)}{\partial x^2} + h.o.t.\ .$$

If, in addition, the function $n_i(x,t)$ is continuously differentiable with respect to the variable t, letting $\tau \to 0$ and $\chi \to 0$ in such a way that $\dfrac{\lambda_i\chi^2}{2\tau} \to \beta_i > 0$, from the latter equation we formally obtain

$$\frac{\partial n_i(x,t)}{\partial t} = \beta_i\frac{\partial^2 n_i(x,t)}{\partial x^2} \ + \ R\big(x,S(t),\rho(t)\big)\,n_i(x,t),$$

which gives the system of non-local PDEs (2.3) complemented with the zero-flux boundary conditions which follow from the fact that the attempted phenotypic variation of a cell is aborted if it requires moving into a phenotypic state that is outside the computational domain.

4.4 Competition in prescribed environment

We study the case where nutrient concentration is given and defined via Equation (4.12) with the initial value of nutrient being $S^0 = M$. This is a scenario analogous to the one presented in Chapter 2. We fix the values of M and T and consider three different values of A that correspond to distinct environmental regimes: constant nutrient level (i.e. no oscillations), mild nutrient fluctuations (i.e. small-amplitude oscillations) and severe nutrient fluctuations (i.e. large-amplitude oscillations).

The results presented in Figure 4.3 show that, for all values of A considered, there is an excellent quantitative match between the numerical simulations of the IB and continuum models. In agreement with the analytical results that we presented in Section 2.3, when the nutrient concentration is constant, population L outcompetes population H (Figure 4.3(a)). The same outcome is observed in the presence of mild nutrient fluctuations (Figure 4.3(b)). By contrast, population L is outcompeted by population H when severe nutrient fluctuations occur (Figure 4.3(c)). In all cases, the phenotype distribution of the surviving population is unimodal and attains its maximum at the mean phenotype (left column in Figure 4.3). Moreover, when the nutrient level is constant, the size and the mean phenotype of the surviving population converge to stable values. On the other hand, in the presence of T-periodic nutrient fluctuations, the size and mean phenotype of the surviving population converge to T-periodic functions.

4.5 Competition in co-evolving environment

Here we assume that the oxygen concentration co-evolves with the cells and its dynamics is governed by Equation (4.13). This is a scenario analogous to the one presented in Chapter 3.

4.5.1 Base-case results

We first assume that the supply rate of nutrient is constant (i.e. we define the term I^h via Equation (4.14)) and consider different values of the nutrient consumption rate θ. The results displayed in Figure 4.4(a)–(b) show excellent quantitative agreement between numerical simulations of the IB and continuum models, both for relatively low and relatively high values of θ. As expected, based on the results we presented in Section 3.4.2, population L out-competes population H, which eventually goes extinct. Moreover, since the nutrient concentration converges to smaller equilibrium values for larger values of the nutrient consumption rate, higher values of θ correspond to decreasing equilibrium sizes of population

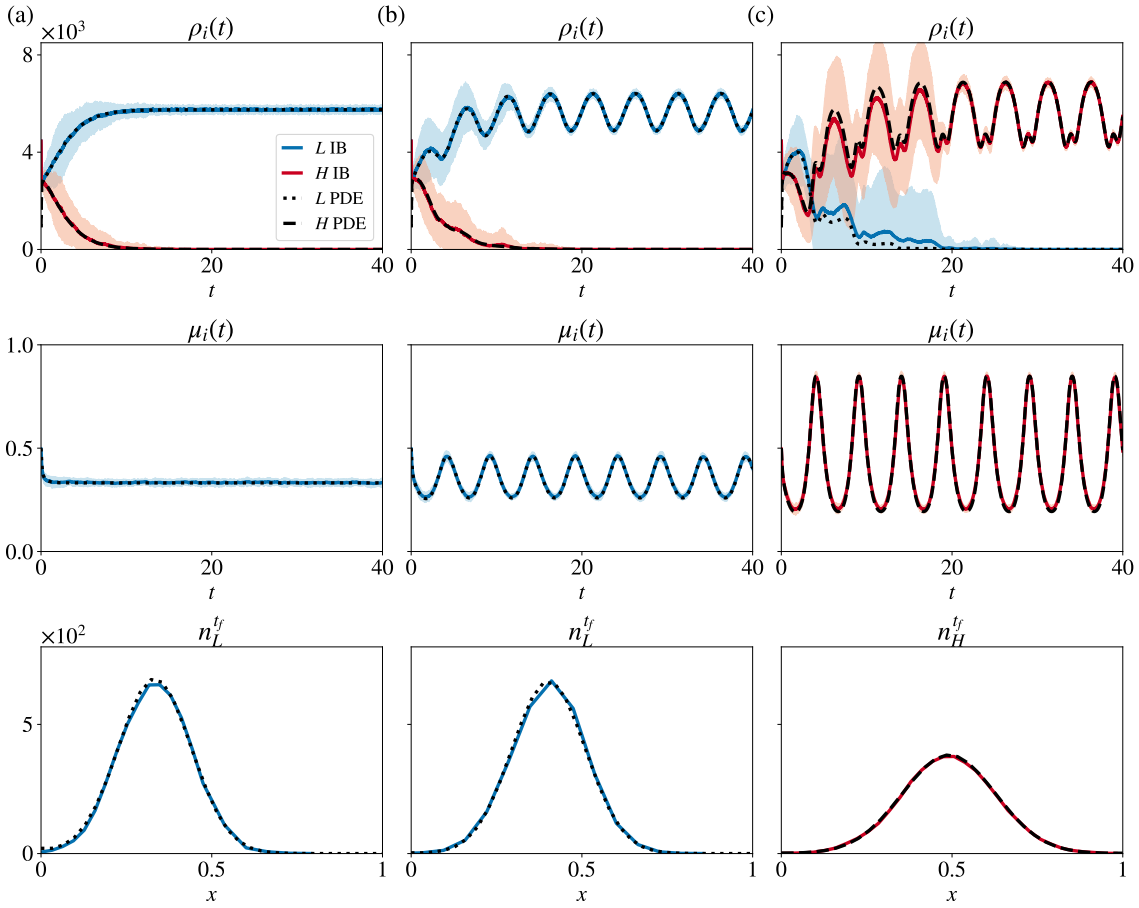

Figure 4.3: Comparison between numerical simulations of the IB (solid, coloured lines) and continuum (broken, black lines) models in the case where the nutrient concentration is prescribed and defined via Equation (4.12). **(a)** Dynamics of the population sizes (top row), the mean phenotype of the surviving population (middle row) and the phenotype distribution at $t = t_f$ (bottom row) in the case where $M = 1$, $T = 5$ and $A = 0$ in Equation (4.12). Here, $a_H = a_L = 800$, $b = 10$ and $c = 0.5$ in Equation (4.16), and the values of the other parameters are those listed in Table 4.1 with $\lambda_H = 0.05$, $\lambda_L = 0.02$, $\tau = 10^{-3}$ and $\chi = 0.032$. The results from the IB model correspond to the average over 30 realisations and the related variance is displayed by the coloured areas surrounding the curves. **(b)**–**(c)** Same as **(a)** but for $A = 0.5$ (row **(b)**) and $A = 1$ (row **(c)**).

L and equilibrium values of the mean phenotype which are closer to 1 (i.e. the fittest phenotypic state in nutrient-scarce environments). In all cases, the phenotype distribution of the surviving population is unimodal and attains its maximum at the mean phenotype.

We then let the supply rate of nutrient undergo periodic oscillations (i.e. we define the term I^h via Equation (4.15)) and, informed by the numerical results presented in Section 3.4.3, we consider different values of the consumption rate θ that lead to the emergence of either mild (i.e. small-amplitude) or severe (i.e. large-amplitude) fluctuations in the nutrient concentration S^h. The results displayed in Figure 4.4(c)–(d) demonstrate that, both for

mild and severe fluctuations in the nutrient concentration, the size and the mean phenotype of the surviving population converge to positive T-periodic functions. When nutrient levels undergo smaller fluctuations, population L survives (see Figure 4.4(d)). However, when nutrient levels undergo larger fluctuations, population H ultimately outcompetes population L (see Figure 4.4(c)). In both cases, the phenotype distribution of the surviving population is unimodal and attains its maximum at the mean phenotype. Moreover, excellent agreement between numerical simulations of the IB and continuum models is observed.

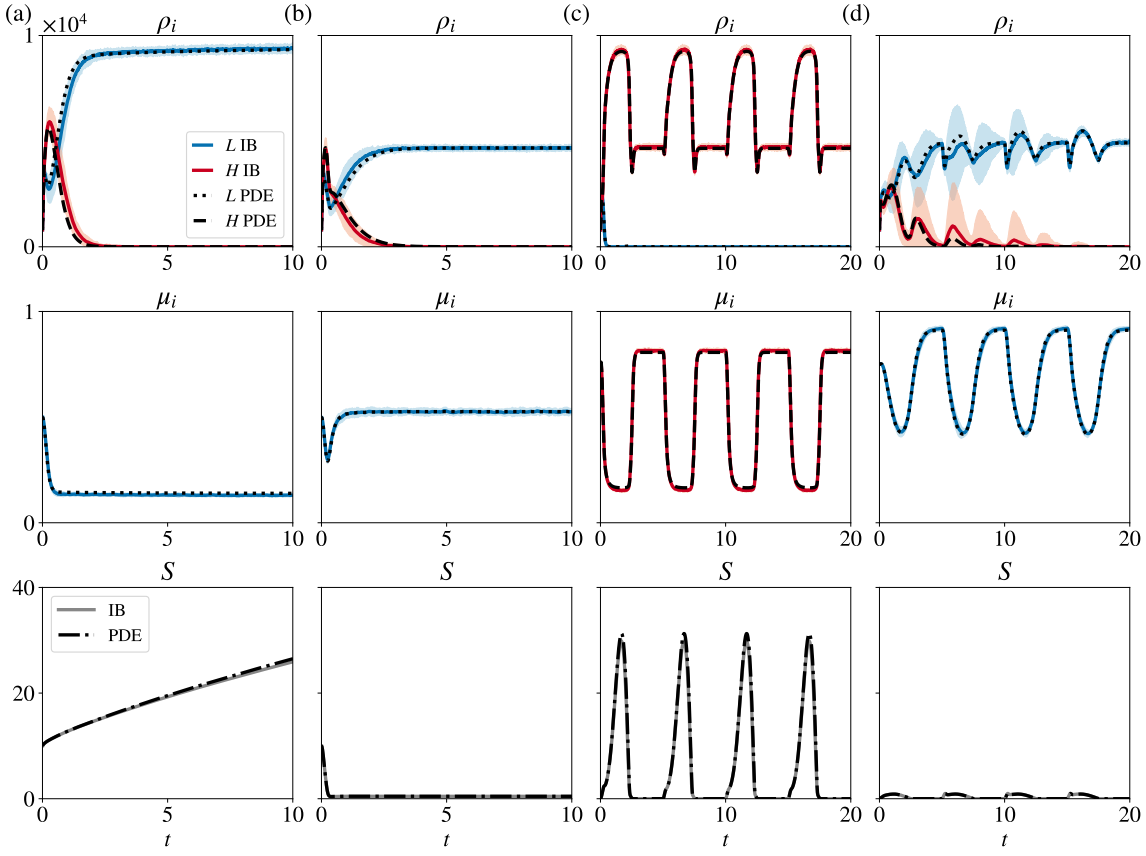

Figure 4.4: **(a)**–**(b)** Comparison between numerical simulations of the IB (solid, coloured lines) and continuum (broken, black lines) models in the case where the evolution of the nutrient concentration is governed by the difference equation (4.13) whereby the term I^h is defined via Equation (4.14) with $\bar{I} = 10$. Dynamics of the population sizes (top panel), mean phenotype of the surviving population (central panel) and nutrient level (bottom panel) in the case where $\theta = 10^{-5}$ in **(a)** and $\theta = 10^{-4}$ in **(b)**. Here, $a_H = a_L = 800$, $b = 10$ and $c = 0.5$ in Equation (4.16), $\tau = 10^{-3}$, and $\chi = 0.032$, and the values of the other parameters are those listed in Table 4.1 with $\lambda_H = 1$ and $\lambda_L = 0.2$. The results from the IB model correspond to the average over 30 realisations and the related variance is displayed by the coloured areas surrounding the curves. **(c)**–**(d)** Same as **(a)** but when the term I^h is defined via Equation (4.14) with $A = 200$, $T = 5$, $\lambda_H = 0.4$, $\lambda_L = 0.02$, $c = 0.5$, $\theta = 2 \times 10^{-4}$ in **(c)** and $\theta = 0.001$ in **(d)**.

4.5.2 Sensitivity analysis of the probabilities of phenotypic variation

Based on the analytical results presented in Sections 2.3 and 3.3.1 for the continuum model, we expect smaller values of λ_H and λ_L (i.e. the probabilities of phenotypic variation) to correlate with longer transient intervals in the dynamics of the sizes of the two cell populations. To test this hypothesis, we focus on the case where the supply rate of nutrient is constant (i.e. when the term I^h is defined via Equation (4.14)). We carry out numerical simulations of the IB model assuming

$$\lambda_i = \varepsilon \, L_i, \tag{4.26}$$

with L_i fixed and $\varepsilon \in \{1, \ldots, 10\}$. As summarised by the plots in Figure 4.5, smaller values of ε bring about longer transient intervals (i.e. larger values of t_{tr} in Figure 4.5(d)) during which the two populations coexist before population L ultimately out-competes population H.

The results displayed in Figure 4.5(a)–(c) indicate that the size of population L decreases during the transient, defined as the early part of the population trajectory, before approaching steady state. Moreover, longer transients correlate with lower minimum values of the size of population L (i.e. smaller ρ_L^{min} in Figure 4.5(d)), which creates the bottleneck effects that bring about both lower regularity of the density functions of the two populations, and more pronounced demographic stochasticity which is more likely to come into play. This suggests that lower probabilities of phenotypic variation may create conditions for the emergence of differences between predictions of the IB and continuum models.

To investigate this further, we compare numerical simulations of the IB model with numerical solutions of the continuum model in the setting of Figure 4.4(a) and 4.4(b) (i.e. defining the nutrient supply term, I^h, via Equation (4.14) and considering different values of θ) but using lower values of the probabilities of phenotypic variation λ_H and λ_L. The results, summarised in Figure 4.6, demonstrate that while excellent quantitative agreement between numerical simulations of the IB model and numerical solutions of the continuum model is obtained for relatively large values of θ (see Figure 4.6(b)), significant differences in the behaviour of the two models can be observed for relatively low values of θ (see Figure 4.6(a)).

This is because, when lower values of λ_H and λ_L are considered, relatively small values of nutrient consumption rate θ correspond to a longer initial phase of cell dynamics during which the size of population L decays and the size of population H grows. After this initial phase, the numerical solutions of the continuum model exhibit trend inversion, with the size of population L converging to a stable positive value and the size of population H decaying to zero. Numerical simulations of the IB model, however, demonstrate that there

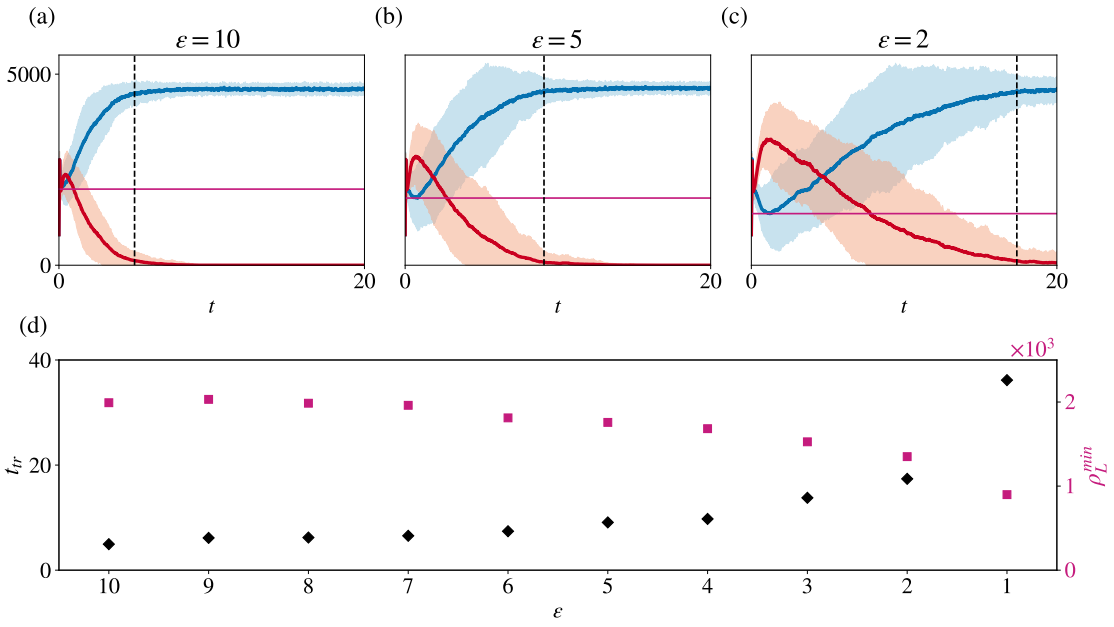

Figure 4.5: **(a)**–**(c)** Numerical simulations of the IB model in the case where the probabilities of phenotypic variation, λ_H and λ_L, are defined by Equation (4.26) with $L_H = 0.05$, $L_L = 0.02$, and $\varepsilon = 10$ (panel **(a)**), $\varepsilon = 5$ (panel **(b)**), and $\varepsilon = 2$ (panel **(c)**). Simulations are run until $t_f = 40$. The black dashed lines highlight the time t_{tr} such that $\rho_L^{t_f} - \rho_L^{t_{tr}} < 100$, while the solid pink lines highlight the value of $\rho_L^{min} := \min_h \rho_L^h$. **(d)**. Plots of t_{tr} (black diamonds) and ρ_L^{min} (pink squares) as functions of $\varepsilon \in \{1, \dots, 10\}$. The evolution of the nutrient concentration is governed by the difference equation (4.13), whereby the term I^h is defined by Equation (4.14) with $\bar{I} = 10$. Here, $a_H = a_L = 800$, $b = 1000$ and $c = 0.5$ in Equation (4.16), and the values of the other parameters are as listed in Table 4.1 with $\theta = 0.001$, $\tau = 10^{-3}$, and $\chi = 0.032$. These results correspond to the average over 30 realisations and the related variance is displayed by the coloured areas surrounding the curves in panels **(a)**–**(c)**.

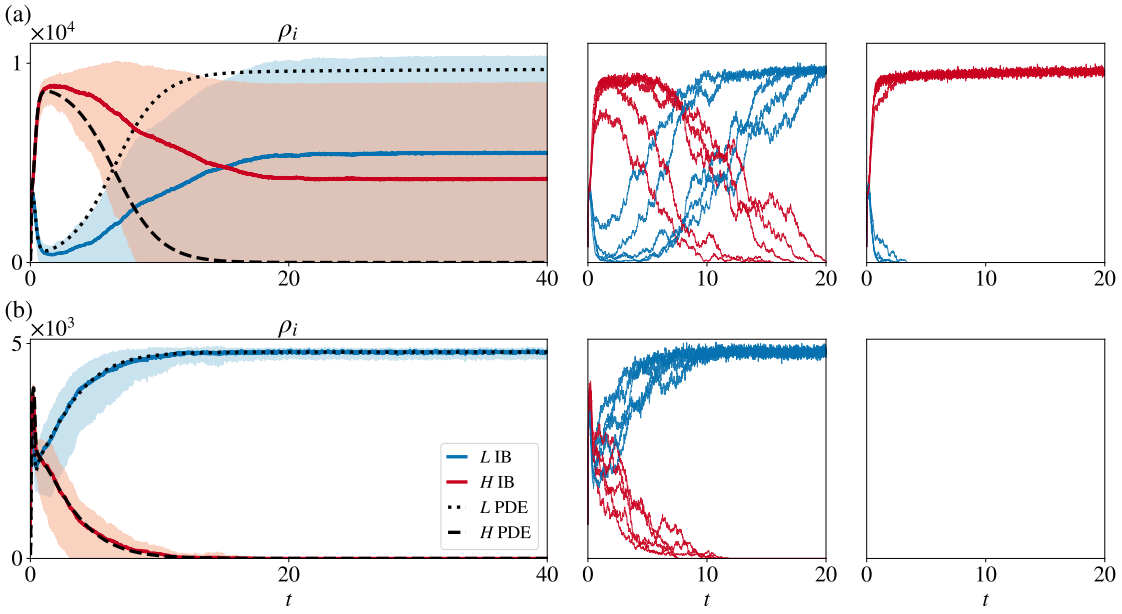

Figure 4.6: **(a)** Comparison between numerical simulations of the IB (solid, coloured lines in the left panel) and continuum (broken, black lines in the left panel) models under the parameter setting of Figure 4.4(a) but with $\lambda_H = 0.05$, $\lambda_L = 0.02$, $\tau = 10^{-3}$, and $\chi = 0.032$. The results from the IB model correspond to the average over 30 realisations and the related variance is displayed by the coloured areas surrounding the curves. The plots in the central and right panels show the dynamics of the sizes of the two populations for single realisations of the IB model that match with (central panel) or differ from (right panel) numerical solutions of the continuum model. **(b)** Same as **(a)** for the parameter setting of Figure 4.4(b) but with $\lambda_H = 0.05$ and $\lambda_L = 0.02$.

are realisations whereby, due to stochastic effects, the aftermath of the initial phase of cell dynamics is the extinction of population L and the survival of population H (see right panel of Figure 4.6(a)).

Such differences persist when smaller values of the time-step, τ, and the phenotype-step, χ, are considered. More specifically, lower time- and phenotype-steps correlate with a more drastic decay in the size of the population L, which then becomes more prone to extinction due to demographic stochasticity, as demonstrated in Figure 4.7. Since this trend is observed for lower values of τ and χ, from now on we use larger values ($\tau = 10^{-3}$ and $\chi = 0.032$) in order to minimise computational time.

Differences between the discrete and the continuum models are also observed when the supply rate of nutrient undergoes periodic oscillations (i.e. when the term I^h is defined via Equation (4.15)) and different values of θ are considered, provided that lower values of λ_H and λ_L are chosen (Figure 4.8). In this case, for values of nutrient consumption rate, θ, leading to the emergence of severe fluctuations in the nutrient level (i.e. when

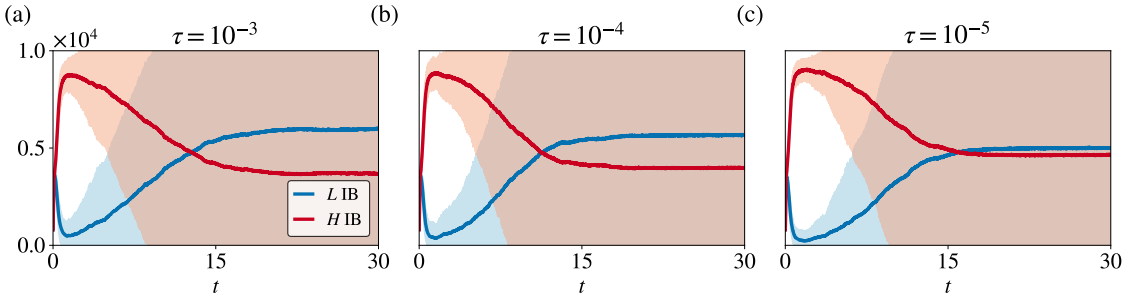

Figure 4.7: **(a)** Numerical simulations of the IB model under the parameter setting of Figure 4.5(a) but with $\tau = 10^{-3}$ and $\chi = 0.032$. The results from the IB model correspond to the average over 10 realisations and the related variance is displayed by the coloured areas surrounding the curves. **(b)**–**(c)** Same as **(a)** but with $\tau = 10^{-4}$ and $\chi = 0.01$ **(b)** and $\tau = 10^{-5}$ and $\chi = 0.0032$ **(c)**.

population H is ultimately selected according to the continuum model), there is an excellent quantitative agreement between the two models. On the other hand, for values of θ leading to the emergence of mild fluctuations in nutrient levels (i.e. when the continuum model predicts that population L will ultimately be selected after an initial phase of population size contraction), there are realisations of the IB model in which population L is outcompeted by population H.

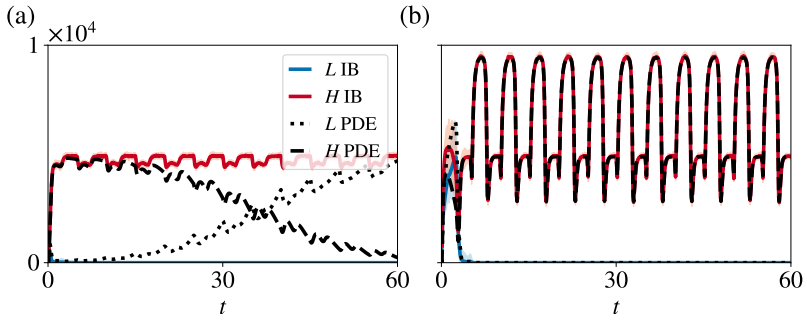

Figure 4.8: **(a)** Comparison between numerical simulations of the IB (solid, coloured lines) and continuum (broken, black lines) models in the case where the evolution of the nutrient concentration is governed by the difference equation (4.13) whereby the term I^h is defined via Equation (4.14) with $A = 60$, $T = 5$, $\lambda_H = 0.05$, $\lambda_L = 0.02$, $\theta = 10^{-3}$ and other parameter values are as listed in Table 4.1. **(b)** Same as **(a)** but with $\theta = 5 \times 10^{-5}$.

4.5.3 Sensitivity analysis of the initial standard deviation and the initial mean phenotype

Based on the analytical and numerical results presented in Sections 3.3.1 and 3.4.2, we anticipate stronger bottleneck effects in the dynamics of the sizes of the two cell populations

arising from the choice of initial conditions. In particular, the time it takes for the two populations to reach the equilibrium values in their size and mean phenotype depends on the initial standard deviation, $\sigma^0_{H,L}$, distances between the initial mean phenotypes, $\mu^0_{H,L}$, and the equilibrium value of the fittest phenotypic state $\varphi(S^\infty)$, which is computed by substituting the long-time limit S^∞ of the nutrient concentration into Equation (4.8). Since the results presented in Section 4.5.2 demonstrate that stronger bottleneck effects may promote the emergence of differences between the predictions of the two models, we expect that larger values of $|\mu^0_H - \varphi(S^\infty)|$ and $|\mu^0_L - \varphi(S^\infty)|$, along with smaller values of σ^0_H and σ^0_L, will increase the likelihood of observing differences between numerical simulations of the IB and continuum models.

To test this hypothesis, we first suppose that the nutrient supply rate is constant. We then carry out numerical simulations for different values of the parameters b and c in Equation (4.16). We recall that larger values of b correlate with lower σ^0_H and σ^0_L, and in the setting considered here, lower values of c correspond to higher $|\mu^0_H - \varphi(S^\infty)|$ and $|\mu^0_L - \varphi(S^\infty)|$ (i.e. less fit initial mean phenotypes). The plots presented in Figure 4.9(a) reveal excellent quantitative agreement between numerical simulations of the IB and continuum models for sufficiently large values of σ^0_H and σ^0_L, regardless of the values of $|\mu^0_H - \varphi(S^\infty)|$ and $|\mu^0_L - \varphi(S^\infty)|$ (i.e. independently of the value of c). On the other hand, and consistent with our expectations, the numerical results presented in Figure 4.9(b) show that, for sufficiently small values of σ^0_H and σ^0_L, higher $|\mu^0_H - \varphi(S^\infty)|$ and $|\mu^0_L - \varphi(S^\infty)|$ (i.e. lower values of c) correlate with longer transients during which stochastic effects can lead to the emergence of differences between the cell dynamics exhibited by the two models.

We now suppose that the nutrient supply rate undergoes periodic oscillations and perform numerical simulations for different values of the parameter c (i.e. the initial mean phenotype of the two populations), which correspond to different values of the quantities $|\mu^0_H - < \varphi >|$ and $|\mu^0_L - < \varphi >|$, where

$$< \varphi >:= \frac{1}{2}\left(\min_{t_h \in [0,T]} \tilde{S}^h + \max_{t_h \in [0,T]} \tilde{S}^h\right) \tag{4.27}$$

with $\tilde{S}^h$ being the positive T-periodic function to which S^h converges as $h \to \infty$. In the setting considered here, smaller values of c correspond to higher $|\mu^0_H - < \varphi >|$ and $|\mu^0_L - < \varphi >|$ (i.e. less fit initial mean phenotypes). The results presented in Figure 4.10b indicate that excellent quantitative agreement is observed between numerical simulations of the IB and continuum models when the consumption rate θ is such that the nutrient level undergoes severe fluctuations (i.e. when population H is ultimately selected according to the continuum model), regardless of the values of $|\mu^0_H - < \varphi >|$ and $|\mu^0_L - < \varphi >|$ (i.e. independently of the value of c). On the other hand, the results presented in Figure 4.10a

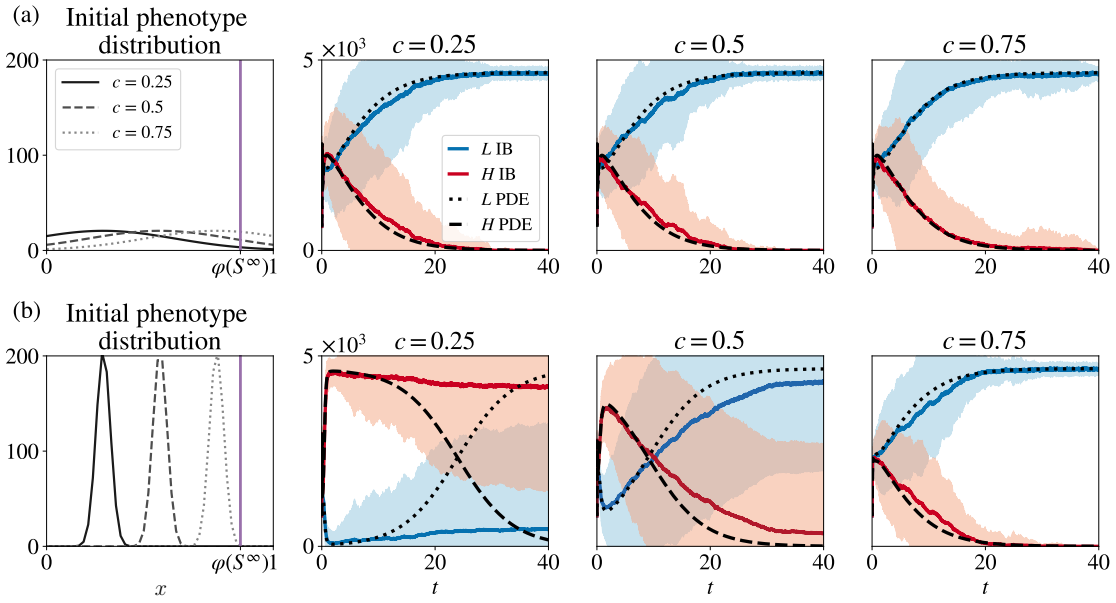

Figure 4.9: **(a)** Comparison between numerical simulations of the IB (solid, coloured lines in columns 2 – 4) and continuum (broken, black lines in columns 2 – 4) models in the case where the initial phenotype distributions of the two populations are defined as shown by the plots in the first panel, corresponding to different values of c in Equation (4.16). The purple line in the first panel highlights the equilibrium value of the fittest phenotypic state $\varphi(S^\infty)$, which is computed by substituting into Equation (4.8) the long-time limit S^∞. The evolution of S^h is governed by the difference equation (4.13), whereby the term I^h is defined via Equation (4.14) with $\bar{I} = 10$. Here, $a_H = a_L = 800$ and $b = 10$ in Equation (4.16), and the values of the other parameters are listed in Table 4.1 with $\lambda_H = 0.05$, $\lambda_L = 0.02$, $\theta = 10^{-3}$, $\tau = 10^{-3}$, and $\chi = 0.032$. The results from the IB model correspond to the average over 30 realisations and the related variance is displayed by the coloured areas surrounding the curves. **(b)** Same as **(a)** but for $b = 1000$.

show that, when θ is such that the nutrient level undergoes mild fluctuations (i.e. when the continuum model predicts population L to be ultimately selected after an initial phase of population size contraction), good quantitative agreement between numerical simulations of the IB and continuum models is observed only if $|\mu_L^0 - < \varphi >|$ and $|\mu_H^0 - < \varphi >|$ are sufficiently small (i.e. only if c is sufficiently large). Indeed, larger values of these distances correlate with longer transients during which stochastic effects may drive discrepancies between the cell dynamics of the two models.

4.5.4 Sensitivity analysis of the initial population sizes

Motivated by the numerical results presented in Section 4.5.3, we hypothesise that differences between numerical simulations of the IB and continuum models, which are observed for sufficiently large values of $|\mu_i^0 - \varphi(S^\infty)|$ (i.e. sufficiently small c) and sufficiently small

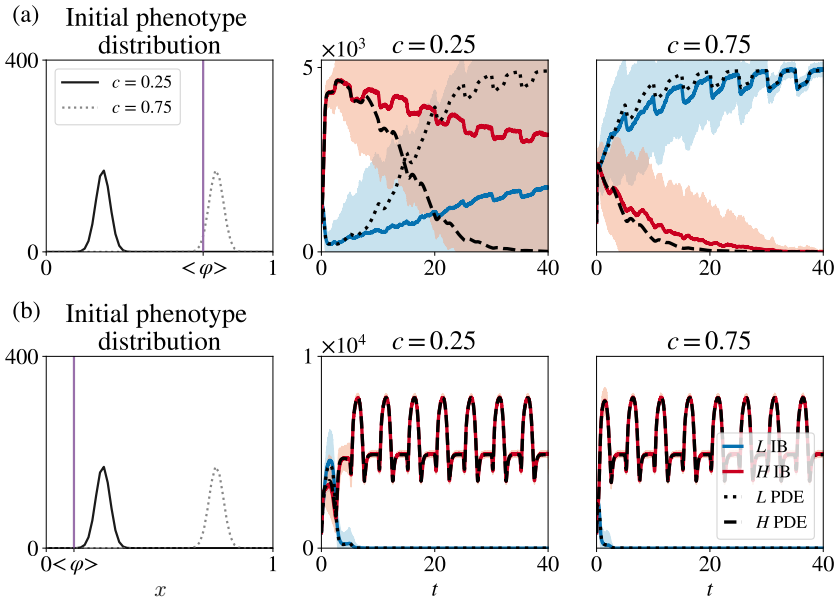

Figure 4.10: **(a)** Comparison between numerical simulations of the IB (solid, coloured lines in the central and right columns) and continuum (broken, black lines in the central and right columns) models in the case where the initial phenotype distributions of the two populations are the same, and defined as shown by the plots in the left panel, which correspond to different values of the parameter c in Equation (4.16). The purple line in the first column highlights the value of the quantity $< \varphi >$ defined according to Equation (4.27). The evolution of S^h is governed by the difference equation (4.13), whereby the term I^h is defined via Equation (4.15) with $A = 30$ and $T = 5$. Numerical simulations are carried out assuming $a_H = a_L = 800$ and $b = 1000$ in Equation (4.16), and using the parameter values listed in Table 4.1 with $\lambda_H = 0.05$, $\lambda_L = 0.02$, $\theta = 10^{-3}$, $\tau = 10^{-3}$, and $\chi = 0.032$. The results from the IB model correspond to the average over 30 realisations and the related variance is displayed by the coloured areas surrounding the curves. **(b)** Same as **(a)** but for $\theta = 5 \times 10^{-5}$.

values of σ_i^0 (i.e. sufficiently high b), will be amplified when smaller initial sizes of population L are considered and the initial total number of cells is held fixed. Indeed, lower values of ρ_L^0 may exaggerate stochastic effects associated with small population sizes in the course of the population bottleneck that occurs in the initial phase of the cell dynamics (i.e. when the size of population L decays). To test this hypothesis, we focus on the case where the nutrient inflow rate is constant and carry out numerical simulations for which the parameters a_H and a_L (i.e. the parameters linked to the initial population sizes) in Equation (4.16) are related as follows

$$a_H = \nu Z \quad \text{and} \quad a_L = (1 - \nu)Z, \tag{4.28}$$

with Z fixed and for increasing values of $0 < \nu < 1$.

The results presented in Figure 4.11 show that higher values of ν lead to a sharper bottleneck in population L and longer transient intervals during which the two populations coexist. For all admissible values of ν, the solutions of the continuum model are such that the size of population L evolves to a stable positive value and population H becomes extinct. By contrast, for ν sufficiently large there are realisations for the IB models whereby population H outcompetes population L. Moreover, the size of population H may undergo small stochastic fluctuations about a stable positive value that is larger than that about which the size of population L fluctuates – i.e. the mean size of population H is higher than the mean size of population L.

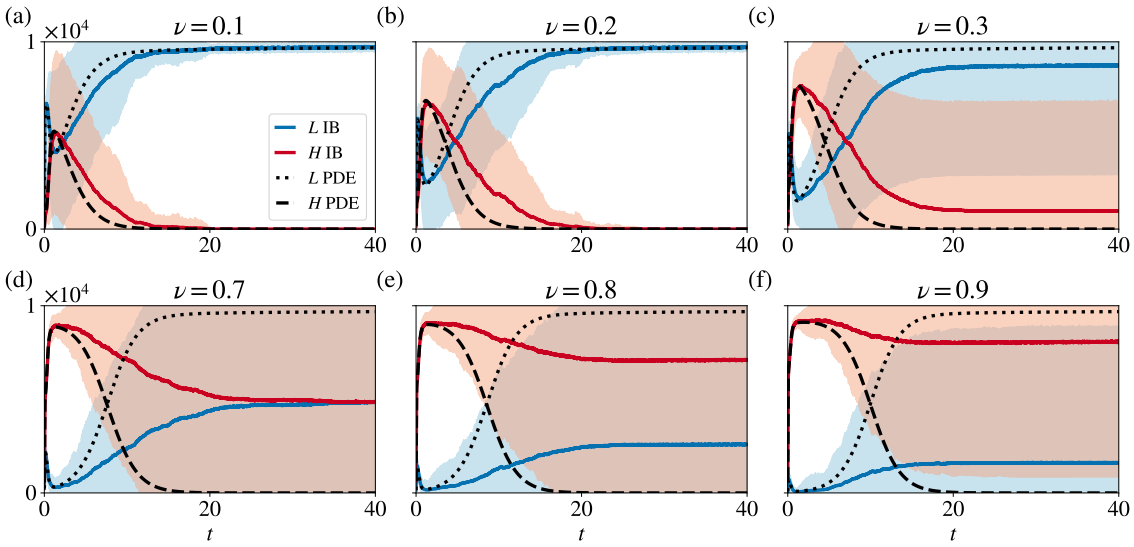

Figure 4.11: **(a)** Comparison between numerical simulations of the IB (solid, coloured lines) and continuum (broken, black lines) models in the case where a_i in Equation (4.16) is defined via Equation (4.28) with $Z = 800$ and $\nu = 0.1$. The evolution of the nutrient concentration is governed by the difference equation (4.13), whereby the term I^h is defined via Equation (4.14) with $\bar{I} = 10$. Numerical simulations are carried out assuming $b = 1000$ and $c = 0.5$ in Equation (4.16), and using the parameter values listed in Table 4.1 with $\lambda_H = 0.05$, $\lambda_L = 0.02$, $\theta = 10^{-3}$, $\tau = 10^{-3}$, and $\chi = 0.032$. The results from the IB model correspond to the average over 30 realisations and the related variance is displayed by the coloured areas surrounding the curves. **(b)**–**(f)** Same as **(a)** but for $\nu = 0.2$ (panel **(b)**), $\nu = 0.3$ (panel **(c)**), $\nu = 0.7$ (panel **(d)**), $\nu = 0.8$ (panel **(e)**), and $\nu = 0.9$ (panel **(f)**).

Analogous results pertain when a periodic nutrient inflow defined via Equation (4.15) is considered, provided that values of θ leading to the emergence of mild fluctuations in the nutrient level are chosen (i.e. when the continuum model predicts population L to be ultimately selected after an initial phase of population size contraction) along with sufficiently high $|\mu_L^0 - < \varphi >|$ and $|\mu_H^0 - < \varphi >|$.

4.6 Application to the mathematical modelling of metastatic colonisation

The results presented in Section 4.5 lead us to conclude that significant differences between the predictions made by the stochastic IB model and the corresponding deterministic continuum model can arise due to the occurrence of bottleneck effects, which may be encountered during the early stage of colonisation of new habitats by invasive species across a wide range of ecological scenarios. Metastasis – the process where cancer cells colonise distant organs – is an example of such an ecological scenario. Therefore, as an illustrative example, here we demonstrate the implications of such differences between the two modelling approaches when studying *in silico* the metastatic colonisation of distant organs by cancer cells.

4.6.1 Essentials of the biological problem

Metastasis is a multi-step process where cancer cells encounter a number of restrictive bottlenecks. In particular, cancer cells have to leave their primary tumour site, survive in the blood circulation and, ultimately, extravasate into a new organ. Afterwards, the invaders are required to settle in, engineer supportive niches, and eventually establish themselves over in the local tissue. During the course of such a multifaceted process, cancer cells need to sequentially acquire different phenotypic characteristics and ultimately adapt to the environmental conditions of distant organs, which may be significantly different from those of the primary tumour [224, 225, 226].

Cancer cells have been reported to undergo spontaneous, heritable phenotypic variation [227], which may facilitate adaptation to unpredictable environmental changes, such as those faced during the colonisation of a new niche following extravasation [35]. Since metastases are seeded by single cancer cells or small cell clusters, which originate from the primary site, the adaptive process undergone by cancer cells during the early stages of colonisation may be strongly impacted by demographic stochasticity.

4.6.2 Definition and calibration of the model

We use the stochastic IB model presented in Section 4.2 and its deterministic continuum analogue derived in Section 4.3 to investigate the role that spontaneous, heritable phenotypic changes play in the evolutionary dynamics of cancer cells during the early stages of colonisation of a distant organ upon extravasation. In particular, we model the dynamics of cancer cells within a small metastatic lesion that is embedded in a 1 mm^3 portion of tissue and we assume the metastatic lesion to consist of two competing populations of cancer cells which undergo spontaneous, heritable phenotypic changes with different probabilities.

As before, the population with the lower probability of phenotypic variation is labelled by the index L, while the other population is labelled by the index H. In keeping with the existing literature [171], we choose the value of the probability of phenotypic variation λ_H reported in Table 4.2 and we estimate the probability of phenotypic variation λ_L to be one order of magnitude smaller than λ_H (i.e. $\lambda_L = 0.1\lambda_H$).

We keep our assumptions from Chapter 3 by assigning the metabolic state of the cell to their phenotypic trait, i.e. cells in $x \to 0$ are fully oxidative, while cells in $x \to 1$ are fully glycolytic. We estimate the maximum proliferation rates of fully oxidative and fully glycolytic phenotypic variants, γ and ζ, respectively, from the literature. Since glucose is an inefficient energy source compared to oxygen, we have that $\zeta < \gamma$ [105].

Letting the average diameter of a cell be about 20 μm, we estimate the maximum number of cells that can be accommodated in 1 mm^3 of tissue to be $K = 1.25 \times 10^5$ [172], and we assume that only 1% of them can be cancer cells since, during the early stage of metastatic colonisation, other cells that are present in the tissue prior to cancer cell extravasation will leave a very limited amount of space available for cancer cells to invade. Hence, using the fact that the approximate carrying capacity for our model in oxygen-rich environments is γ/d, we estimate the value of the death rate due intra- and inter-population competition d as follows

$$\frac{\gamma}{d} \approx \frac{K}{100} \quad \Longrightarrow \quad d \approx 100\,\frac{\gamma}{K}.$$

We assume the phenotype distributions of the two cell populations at time $t_h = 0$ to be of the form given by Equation (4.16) with the values of the parameters a_H, a_L, b and c corresponding to a biological scenario whereby the two cell populations are both small and mainly composed of cells in the fully oxidative phenotypic state $x_j = 0$ (cf. the values of the parameters a_H, a_L, b and c listed in Table 4.2).

We let the function S^h represent the concentration of oxygen available to cancer cells at time t_h. The dynamics of S^h are governed by the difference equation (4.13) whereby the term I^h models the rate at which cancer cells are supplied with oxygen by blood vessels found in the tissue. Here, the parameter η is the rate of natural decay of oxygen, the value of which is estimated based on [218], κ is the Michaelis constant of oxygen and θ is a conversion factor for cell consumption of oxygen, the values of which are chosen consistent with those reported in [19]. Making the simplifying assumption that oxygen supply from blood vessels is constant over time, we define I^h via Equation (4.14). Furthermore, denoting by I_v the average amount of oxygen released from a single healthy blood vessel, the value of which is chosen based on the experimental measurements reported in [217], we use the following definition of the term $\bar{I}$ in Equation (4.14)

$$\bar{I} := \alpha\, I_v. \tag{4.29}$$

The parameter $\alpha > 0$ in Equation (4.29) models the level of tissue oxygenation, which is known to be organ-specific – viz. lungs and bones are, respectively, highly- and poorly-oxygenated organs [228].

In summary, the parameter values used to carry out numerical simulations of the IB model are those shown in Table 4.2 and the parameter values of the corresponding continuum model are defined accordingly. We note that structural identifiability analysis of this model has not been performed and remains as future work. The used parameter values are identical to those shown in Table 3.3 (Section 3.5), except for the values of maximal growth rate of oxidative and glycolytic phenotypic variants, γ and ζ, respectively.

Parameter	**Value**	**Unit**	**Reference**
γ	0.66	day^{-1}	[19]
ζ	0.5	day^{-1}	[19]
d	5.2 $\times 10^{-4}$	day^{-1} cells^{-1}	Model specific
K	1.25 $\times 10^{5}$	cells	[172]
θ	8.2 $\times 10^{-9}$	mmol cells^{-1}	[19]
κ	2.1 $\times 10^{-3}$	mmol	[19]
η	0.24	day^{-1}	[218]
I_v	1.5 $\times 10^{-4}$	mmol day^{-1}	[217]
α	{0.01, 1, 10 }	–	Model specific
λ_H	0.02	day^{-1}	[171]
λ_H	0.002	day^{-1}	Model specific

Table 4.2: Parameter values used in numerical simulations.

Finally, we assume that the initial population of cells is homogeneous and fully oxidative with $b = 1000$ and $c = 0$. We use $\tau = 10^{-3}$ day and $\chi = 0.032$, and run simulations until $t_f = 365$ days. To obtain the numerical solutions of the IB model, we use the method described in Section 4.2. To solve the continuum system of PDEs we use the approach outlined in Section 3.4.1.

4.6.3 Results

In this section, we present some results from the numerical simulations of the IB model.

4.6.3.1 Sensitivity analysis of the level of host tissue oxygenation

We expect lower values of α in Equation (4.29) (i.e. lower levels of tissue vascularisation) to correlate with a lower saturation value of the oxygen concentration. On the basis of the simulation-assisted analysis carried out in Chapter 3, we can foresee that lower saturation values of the oxygen concentration will bring about cancer cell populations of smaller size and will favour glycolytic phenotypic variants (i.e. cells in phenotypic states $x_j \to 1$) over

oxidative phenotypic variants (i.e. cells in phenotypic states $x_j \to 0$). Under the biological conditions corresponding to the initial phenotype distributions considered here, the initial mean phenotype of the two cancer cell populations is the fully oxidative phenotypic state $x_j = 0$ and, therefore, lower values of α will correspond to initial mean phenotype of lower fitness. Hence, based on the results of the sensitivity analysis presented in Section 4.5, we expect smaller α to make it more likely that differences between the IB model and its continuum counterpart will emerge. This is confirmed by the results presented in Figure 4.12.

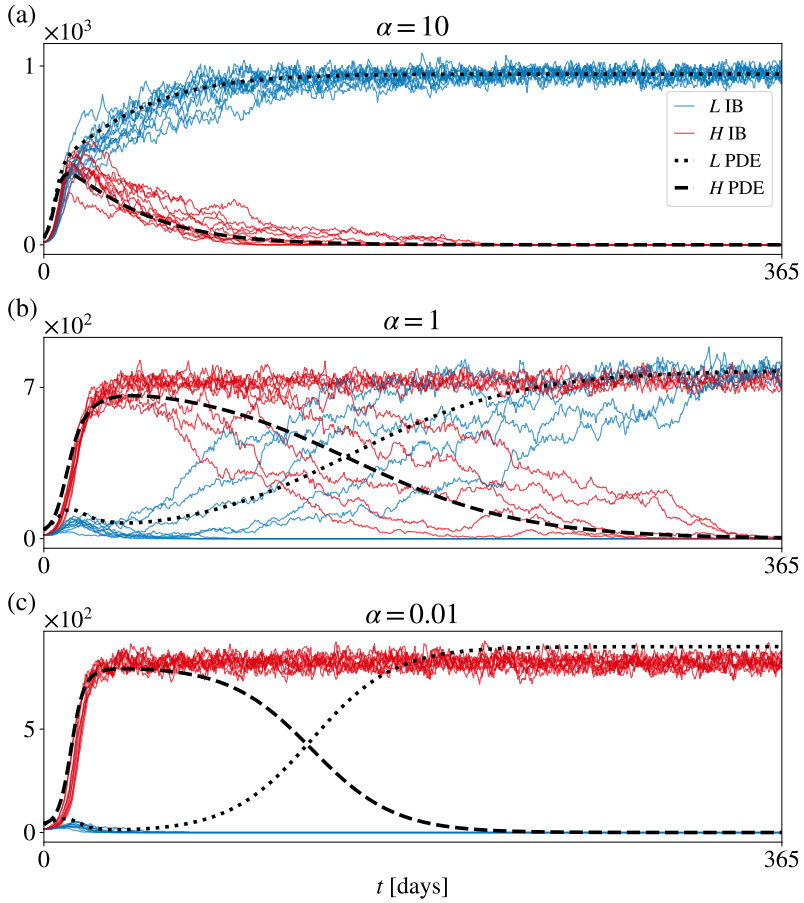

Figure 4.12: **(a)** Comparison between numerical simulations of population sizes of the IB (solid, coloured lines) and continuum (broken, black lines) models, in the case where realistic parameter values corresponding to the early stages of metastatic colonisation of distant organs by cancer cells are considered (cf. parameter values as listed in Table 4.2). The evolution of the oxygen concentration is governed by the difference equation (4.13) whereby the term I^h is defined by Equation (4.14) with $\bar{I}$ defined according to Equation (4.29) with $\alpha = 10$. Here, $a_i = 25$. **(b), (c)** Same as **(a)** but for $\alpha = 1$ and $\alpha = 0.01$, respectively.

The sample dynamics of the size of the cell populations H and L displayed in Figure 4.12

demonstrate that when α is sufficiently large there is excellent quantitative agreement between the discrete and continuum models (see Figure 4.12(a)). On the other hand, the match between the two models deteriorates as the value of α decreases. This discrepancy arises because, in contrast with the deterministic continuum model, the IB model predicts that population L may be driven to extinction by demographic stochasticity, resulting in the survival of population H (see Figures 4.12(b) and 4.12(c)).

These results communicate the biological notion that higher probabilities of spontaneous, heritable phenotypic changes may constitute a competitive advantage for cancer cells during the early stage of metastatic colonisation of poorly-oxygenated distant organs. The same results act also as a proof of concept for the idea that whilst stochastic effects associated with small cell numbers, which cannot be captured by deterministic continuum models formulated as non-local PDEs, can be, at a first approximation, neglected when modelling the metastatic colonisation of highly-oxygenated distant organs, such as the lungs, they become particularly relevant when considering poorly-oxygenated organs, such as the bones. This supports the idea that particular care should be taken when selecting the mathematical modelling approach employed to describe processes such as the biological colonisation of new habitats.

4.6.3.2 Sensitivity analysis of the carrying capacity of the host tissue

In Section 4.6.3.1, we assumed that approximately 1% of space is available to the cancer cells once they extravasate into a distant organ. This makes the carrying capacity of the cancer cell population to be around 1000 cells. However, in reality, there is likely to be even less space and resource available for the invaders. Therefore, here we consider lower values of carrying capacity for the population of cancer cells, i.e. higher values of the death rate due to intra- and inter-population competition, d:

$$d = \omega \frac{\gamma}{K}, \tag{4.30}$$

where ω is the fraction of space available for cancer cells. In particular, we consider $\omega \in \{0.005, 0.001, 0.0005, 0.0001\}$. Here, we assume that the host tissue is well oxygenated, i.e. $\alpha = 10$.

When the carrying capacity of cancer cells is relatively large (i.e. higher value of ω), the solutions of the IB and continuum models demonstrate good agreement (Figure 4.13(a)). In this case, population L outcompetes the population with higher rate of phenotypic variation. Furthermore, even though the initial size of each population is very small, consisting of only three cells, none of the populations becomes extinct due to demographic noise. This is due to the fact that the probability of death, defined by Equation (4.10), is directly proportional

to the death rate, d, and the total population size at given time step, ρ^h. Since at the beginning of the simulation ρ^h is small, and d is relatively small as well, the probability of a death event is extremely small.

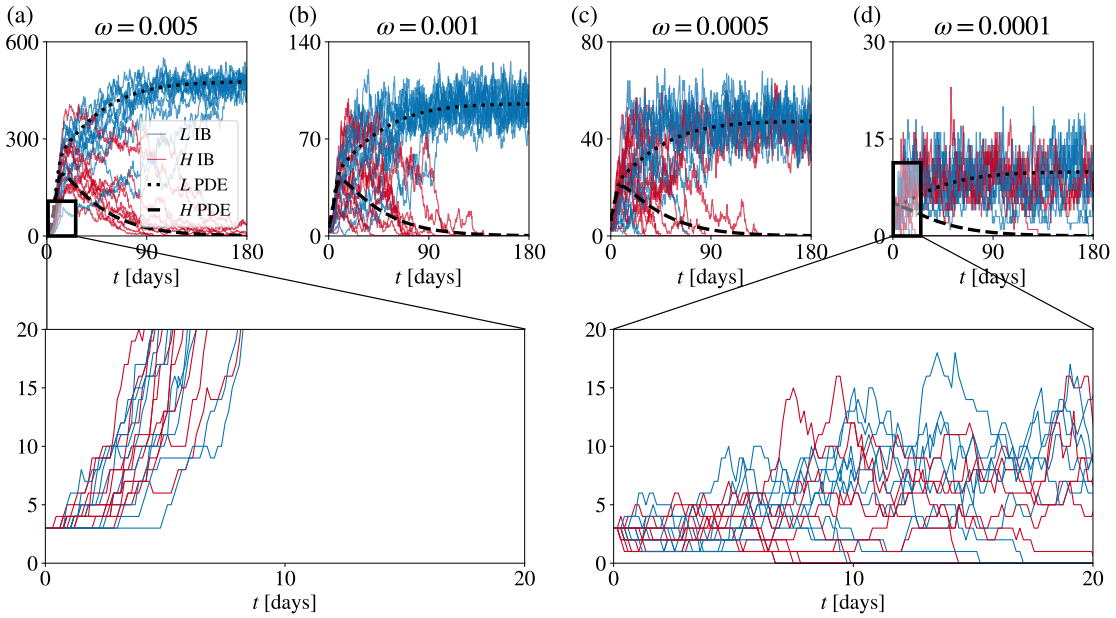

Figure 4.13: Top row: **(a)** Comparison between numerical simulations of population sizes of the IB (solid, coloured lines, 10 realisations) and continuum (broken, black lines) models when $\omega = 0.005$ in Equation (4.30), $a_i = 3$ and other parameters as given by Table 4.2. The evolution of the oxygen concentration is governed by the difference equation (4.13) whereby the term I^h is defined by Equation (4.14) with $\bar{I}$ defined according to Equation (4.29) with $\alpha = 10$. **(b)** – **(d)** Same as **(a)** but for $\omega = 0.001$ **(b)**, $\omega = 0.0005$ **(c)**, and $\omega = 0.0001$ **(d)**. Plots in the bottom row show close-up population dynamics from **(a)** and **(d)**.

As the amount of space available for the invaders decreases, i.e. the value of ω increases, demographic stochasticity becomes more important (Figures 4.13(b) – (d)). Here, due to higher values of d, the probability of death event (Equation 4.10) is larger and we can observe extinction of one population at the beginning of the simulation. Both population H and L can be affected by this. By decreasing the carrying capacity even further ($\omega = 0.00005$), it is possible to observe extinction of both populations, as demonstrated in Figure 4.14, both in cases where the host tissue is well oxygenated (Figure 4.14(a)) and poorly oxygenated (Figure 4.14(b)). Even though eventually both populations become extinct, some populations can survive for a relatively long period of time. This time might be sufficient for the cancer cells to adapt and engineer the environment in order to increase their carrying capacity. For example, this can be achieved by switching to glycolysis and producing lactic acid. In this case, cancer cells can lower the environmental pH, which is

toxic to normal, non-acid resistant cells.

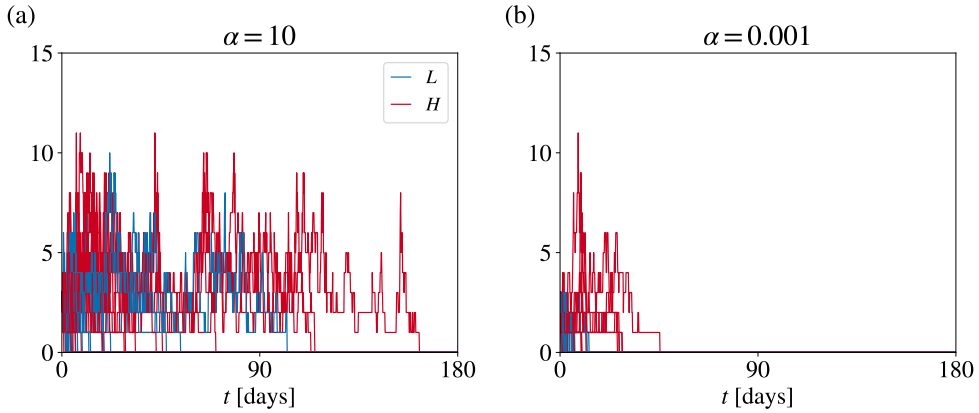

Figure 4.14: **(a)** Population dynamics in well oxygenated medium ($\alpha = 10$) obtained via the IB model (20 realisations) when $\omega = 0.005$ in Equation (4.30), $a_i = 3$ and the other parameters are as listed in Table 4.2. **(b)** Same as **(a)** but with $\alpha = 0.001$.

These results further support the idea that stochastic processes are very important when studying metastasis formation, and the appropriate modelling framework must be used in order to capture the full behaviour of the system.

4.7 Discussion

In this chapter, we developed a stochastic IB model for the evolutionary dynamics of two competing phenotype-structured cell populations that are exposed to time-varying nutrient levels and undergo spontaneous, heritable phenotypic variations with different probabilities. We formally derived the deterministic continuum counterpart of this model and carried out a systematic comparison between numerical simulations of the IB and continuum models.

We presented base-case results that demonstrate an excellent quantitative match between the outcomes of the two models. These results agree with our previous analytical and numerical results for the related deterministic continuum models presented in Chapters 2 and 3. Moreover, we investigated the importance of stochastic effects in driving differences between the predictions made by the two models. The results indicate that stochastic effects associated with small population sizes, which are crucial in population bottlenecks, can lead to significant differences between the two models. In particular, these differences arise in the presence of low probabilities of phenotypic variation, and are more apparent when the two populations are characterised by less fit initial mean phenotypes and smaller initial levels of phenotypic heterogeneity. When there is agreement between the two modelling approaches, this depends on the initial proportions of the two populations.

The results obtained indicate that bottleneck effects, which are crucial during the colonisation of new habitats by invasive species, can lead to significant differences between the two models. In fact, more prominent population bottlenecks bring about sharper drops in cell numbers. This correlates with both lower regularity of the density functions of the two populations and more pronounced demographic stochasticity, which cause a reduction in the quality of the approximations employed in the formal derivation of the deterministic continuum model from the stochastic IB model (cf. the approximations given by Equations (4.20)–(4.22) and (4.25)). In particular, bottleneck effects emerge in the presence of lower probabilities of phenotypic variation, and are more apparent when the two populations are characterised by less fit initial mean phenotypes and smaller initial levels of phenotypic heterogeneity. The emergence of these effects, and thus the agreement between the two modelling approaches, also depends on the initial sizes of the two populations.

Finally, considering suitably parameterised versions of the IB and continuum models, we demonstrated how such differences may impact on the mathematical modelling of the early stage of metastatic colonisation of distant organs by cancer cells. During colonisation, cancer cells are faced with unpredictable, and potentially lethal, environmental conditions. Our results demonstrate that higher rates of spontaneous phenotypic variations may be advantageous for cancer cells that are faced with sudden environmental changes during metastasis. This is consistent with observations from the ecological literature, where populations with higher adaptive abilities (e.g. higher plasticity) are favoured when placed in new environments [64, 69].

The generality of our assumptions make the discrete modelling framework considered here applicable to a broad range of asexual organisms exposed to dynamically changing environments. Such a modelling framework, along with the related method for formally deriving corresponding continuum models, could be readily extended to incorporate additional biological effects related to spatial structure, such as cell movement, inter-cellular spatial interactions, nutrient diffusion and the presence of multiple sources of nutrient distributed across the spatial domain. These extension will enable us to establish conditions under which a deterministic continuum model can be used to approximate the dynamics of an inherently stochastic system. This will ultimately help unravel the impact, and different sources, of stochasticity on the emergence of spatio-temporal evolutionary patterns in a variety of living systems [58, 229].

Chapter 5

Investigating the shape of fitness landscape

5.1 Introduction

It is well established that the tumour microenvironment is extremely heterogeneous, both spatially and temporally [7]. In particular, variations in oxygen level – the main energy source for cells – occur on various timescales and with different amplitudes [22]. Even though the presence of intermittent hypoxia is a widely acknowledged phenomenon, the consequences of such environmental dynamics on tumour progression remain unknown. In this thesis, we theoretically investigated whether cancer cells could utilise a risk-spreading strategy when dealing with such dynamic conditions.

In particular, we have developed a set of mathematical models, of increasing biological complexity, in order to study whether cancer cells could benefit from heritable, spontaneous phenotypic variations. In Chapter 2, we introduced a modelling framework consisting of two phenotype-structured populations competing for a limiting nutrient. We extended this model in Chapter 3 by incorporating interactions between cancer cells and their microenvironment. Finally, we developed a corresponding discrete individual-based model in Chapter 4 in order to study the role of stochastic birth-death processes on competition outcomes, and applied this framework to the problem of adaptation during metastasis formation.

In our modelling approach, the birth and proliferation of cells in a given environment are defined via a fitness function. Fitness curves, or adaptive landscapes, are a common tool used by ecologists to define the reproductive success of an individual with different phenotypes in a given range of environments. Throughout Chapters 2–4 we used the definition of fitness as follows

$$R(x, S(t), \rho(t)) = \underbrace{\gamma \frac{S(t)}{\kappa + S(t)}(1 - x^2) + \zeta \left(1 - \frac{S(t)}{\kappa + S(t)}\right)(1 - (1 - x)^2)}_{\text{net proliferation rate } p(x, S(t))} - \underbrace{d\rho(t)}_{\text{competition}} , \quad (5.1)$$

where x is the phenotype, $S(t)$ is the level of nutrient, the parameters γ and ζ model, respectively, the maximum proliferation rate of the fully oxidative and fully glycolytic phenotypic variants, and parameter κ represents nutrient concentration at which the reaction rate is half of the maximal value. This fitness function can be split into two terms, representing the net growth rate, $p(S(t), x)$ (Equation (2.6)), and a non-local term modelling competition, $d\rho(t)$. In particular, we assumed that there exist two fitness peaks – one at $x = 0$, which is the fittest when the nutrient level is high, and one at $x = 1$, which is largest when the nutrient is absent. The defined net growth rate has a polynomial form, consistent with the shape of fitness landscapes that can be inferred from experimental data [155]. Moreover, this definition increased the analytical tractability of the model.

The chosen shape of fitness function and underlying biological assumption are, of course, a simplification of cancer cell growth and metabolism. In reality, we expect the net growth rate of the population to depend on other factors, including other nutrients that are crucial not only for the generation of ATP, but also for production of nucleotides and other building blocks of the cell. Realistic adaptive landscapes are likely to be multidimensional and rugged, with multiple fitness peaks present for a given environment [230]. Furthermore, we expect the fitness peaks to vary in their shapes, such as width and steepness [230], which might affect the success of particular adaptive strategies. Therefore, it is crucial to test our modelling framework by using different forms of the net growth rate, $p(x, S(t))$, in order to identify the constraints that must be imposed on the shape of the adaptive landscape when looking at risk-spreading strategies.

In this short chapter, we present preliminary results exploring the impact of the shape of the fitness function on competition outcomes between two phenotype-structured populations. We study a system of non-local PDEs evolving in prescribed environments, as presented in Chapter 2. We formulate the fitness function as a sum of Gaussian functions, which are often used in ecological models to construct adaptive landscapes along the environmental gradients [63]. By varying the shape of fitness peaks (i.e. the width), we identify qualitative characteristics of the fitness landscape that favour populations with higher rates of spontaneous phenotypic variation.

We begin this chapter by introducing the model and the new definition for the net growth rate, $p(x, S(t))$, in Section 5.2. In Section 5.3 we solve the model equations numerically and study how the shape of the fitness peaks affects the competition outcomes in constant and periodically fluctuating environments. We finish this chapter with a discussion of the results in Section 5.4.

5.2 Model set-up

We inherit the modelling framework presented in Chapter 2, where we study competition between two phenotype-structured populations in prescribed environments. In particular, we assume the population dynamics are governed by the system of nonlocal PDEs (2.3):

$$\begin{cases} \dfrac{\partial n_H}{\partial t} = \beta_H \dfrac{\partial^2 n_H}{\partial x^2} \; + \; \big(p(x, S(t) - d\rho(t)\big)\, n_H, \\ \dfrac{\partial n_L}{\partial t} = \beta_L \dfrac{\partial^2 n_L}{\partial x^2} \quad + \; \big(p(x, S(t) - d\rho(t)\big)\, n_L, \\ \rho_H(t) = \displaystyle\int_0^1 n_H(x,t)\, \mathrm{d}x, \quad \rho_L(t) = \int_0^1 n_L(x,t)\, \mathrm{d}x, \\ \rho(t) = \rho_H(t) + \rho_L(t), \end{cases} \tag{5.2}$$

for $x \in [0,1]$ and $t \in \mathbb{R} \times (0, \infty)$. We assume that oxygen level is prescribed and is non-dimensionalised as follows

$$\tilde{S}(t) = \frac{S(t)}{S_{max}}, \tag{5.3}$$

where S_{max} is the maximal concentration of oxygen, e.g. in the blood vessel. This non-dimensionalisation ensures that $\tilde{S}(t) \in [0,1]$. The tilde notation for the oxygen concentration will now be dropped for notational simplicity.

We use the assumptions introduced in Chapter 3 regarding the definition of the phenotypic states. In particular, we assume that cells in the phenotypic state $x = 0$ are adapted to oxygen-rich conditions, i.e. are fully oxidative. Cells in the phenotypic state $x = 1$, on the other hand, are adapted to oxygen-low environments, i.e. are fully glycolytic. Thus, we assume the phenotype space to be limited with $x \in [0,1]$.

We define the net proliferation rate, $p(x, S(t))$, in Equation (2.5) as a sum of Gaussian functions [63] which are centred at phenotypic state, ϕ_i. This definition provides the flexibility to alter the shape of fitness peaks and potentially to add additional fitness peaks to create rugged landscapes. We suppose that the net growth function consists of two fitness peaks. We assume that the peak centred at $\phi_1 = 0$ represents the phenotype adapted to nutrient-rich conditions (i.e. oxidative phenotype), whereas the peak centred at $\phi_2 = 1$ represents the phenotype adapted to nutrient-scarce conditions (i.e. glycolytic phenotype):

$$p(x, S(t)) = \underbrace{\gamma S(t) \exp\left(-\frac{(x-\phi_1)^2}{q_1}\right)}_{\text{oxidative phenotype}} + \underbrace{\zeta(1 - S(t)) \exp\left(-\frac{(x-\phi_2)^2}{q_2}\right)}_{\text{glycolytic phenotype}}. \tag{5.4}$$

In Equation (5.4), the parameters ζ and γ represent maximal proliferation rates (i.e. the height of fitness peak) of cells in phenotypic state $x = 0$ and $x = 1$, respectively. We retain

our assumption that the glycolytic phenotype comes at a cost, i.e. $\zeta < \gamma$. Parameters q_1 and q_2 determine the width of the fitness peak. These two parameters act as a measure of a fitness valley, i.e. the cost of switching between two fitness peaks [231]. For simplicity, we assume that the widths of the two peaks are equal, i.e. $q_1 = q_2 = q_i$. Examples of typical of fitness landscapes given by Equation (5.4) for different values of q_i are shown in Figure 5.1.

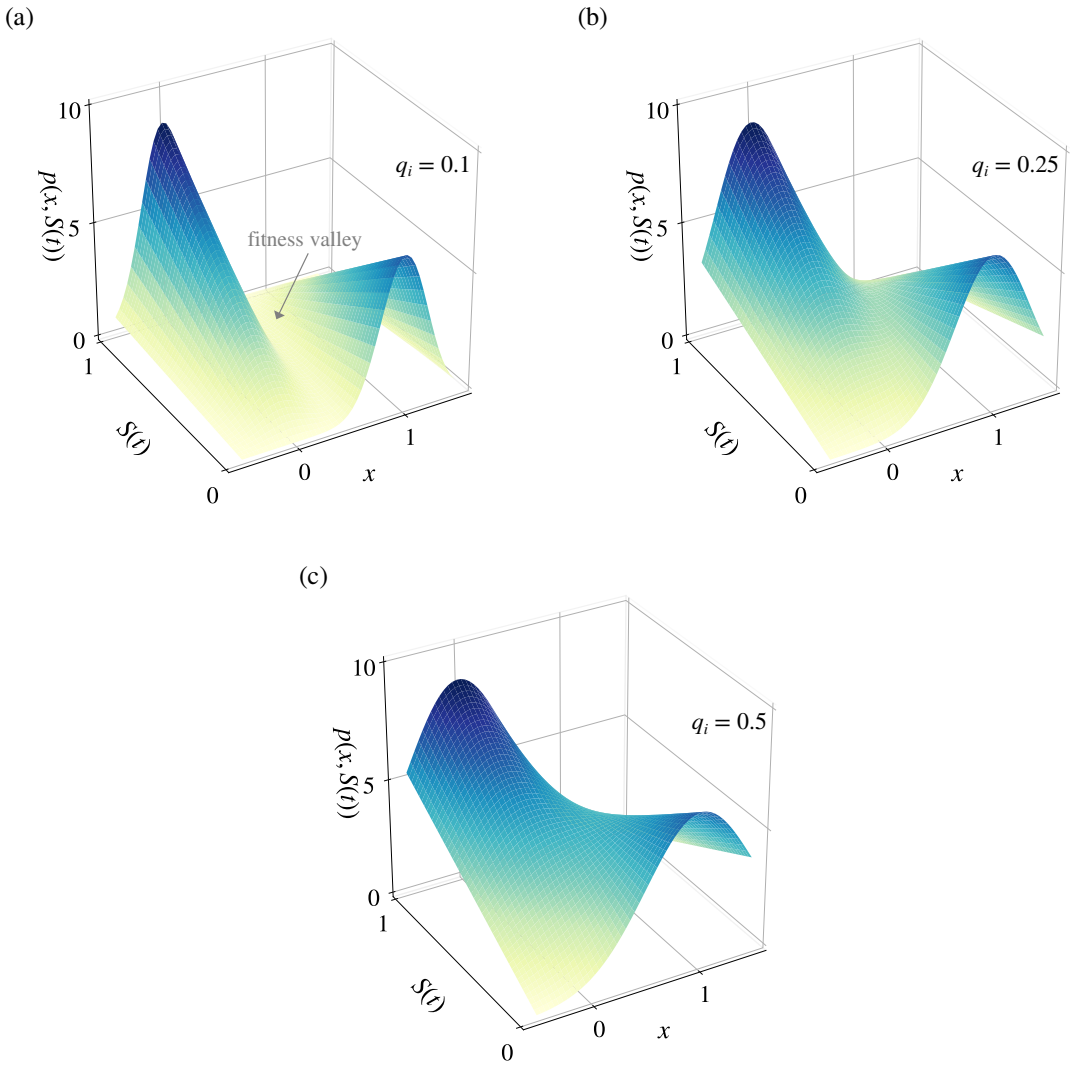

Figure 5.1: Fitness landscape given by Equation (5.4) plotted for different values of q_i. Parameters used here: $\gamma = 8.6$ day^{-1}, $\zeta = 6.5$ day^{-1}, $\phi_1 = 0$, and $\phi_2 = 1$. The arrow in **(a)** highlights the fitness valley.

We generate approximate solutions to the system of PDEs (5.2) using the numerical scheme described in Section 2.4.1. We select a uniform discretisation consisting of 200 points on the interval $[0, 1]$ as the computational domain of the independent variable x. We

discretise the interval $[0, t_f]$ with the uniform step $\Delta t = 0.0001$.

We use parameter values as given by Table 5.1. Consistent with the cell densities observed in tumours and previous models [180], we assume that the carrying capacity is about $\approx 10^8$ cells. We must note that structural identifiability analysis was not performed and remains as future work. The parameter values are chosen in order to demonstrate qualitative behaviour of the model.

Parameter	**Value**	**Unit**
β_H	0.01	day^{-1}
β_L	0.001	day^{-1}
γ	8.64	day^{-1}
ζ	6.57	day^{-1}
d	1.72×10^{-8}	$\text{cell}^{-1}\ \text{day}^{-1}$

Table 5.1: Parameter values used in numerical simulations.

In every simulation, the initial phenotype distribution is given by Equation (2.12) with $\rho_i^0 = 10^5$ cells, $\mu_i^0 = 0$ and $v_i^0 = 10$ for $i \in \{H, L\}$.

5.3 Main results

We start exploring the role of fitness landscapes on the competition between two populations undergoing spontaneous phenotypic variations by considering the net growth rate defined via Equation (5.4). First, we study the dynamics of the populations and resulting mean phenotypes in constant environments (Section 5.3.1). Then, in Section 5.3.2, we consider the case where the environment undergoes periodic oscillations.

5.3.1 Constant environment

First, we study the evolutionary dynamics in constant environments in order to verify that the analysis from Chapters 2 and 3 carries through when the net growth rate is defined according to Equation (5.4). We assume that oxygen level is constant, and is given by

$$S(t) \equiv \bar{S} \in [0, 1]. \tag{5.5}$$

When oxygen level is constant, as expected, the population with lower rate of phenotypic variation survives. By choosing different shapes of the fitness peaks (i.e. different values of $q_i \in \{0.1, 0.25, 0.5, 0.75\}$), we look at how the population size and the mean phenotype of the surviving population are affected under different level of oxygenation, $\bar{S}$. This is summarised in the bifurcation plots in Figure 5.2, where we run the simulations until $t_f = 360$ days and note the values of $\rho_L(t_f)$ and $\mu_L(t_f)$ at the end. The value of t_f is chosen such that all simulations reach steady state by that time.

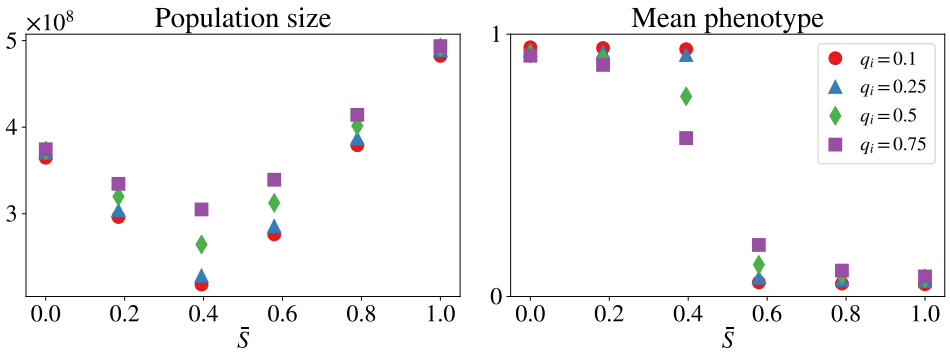

Figure 5.2: Values of the population size $\rho_L(t_f)$ (left) and the mean phenotype $\mu_L(t_f)$ (right) at $t_f = 360$ days (i.e. at the end of numerical simulations) obtained by solving numerically Equation (5.2) with $p(x, S(t))$ given by Equation (5.4) for different values of $\bar{S}$ in Equation (5.5) and q_i. The parameter values are defined in Table 5.1.

Consistent with our modelling assumptions, when the environment is well-oxygenated ($\bar{S} \to 1$), the selected population has oxidative phenotype and has the largest population size. On the other hand, when the oxygen level is low ($\bar{S} \to 0$), the glycolytic population is selected with lower population size compared to the oxidative population. This reflects the fact that there is a fitness cost associated with glycolysis ($\zeta < \gamma$). Furthermore, when the fitness peaks are narrow (smaller values of q_i), the transition between oxidative and glycolytic populations is very sharp. As the peaks get broader (larger values of q_i), the transition becomes more smooth and population with intermediate phenotypes (e.g. $x = 0.5$) can be selected.

5.3.2 Periodically fluctuating environment

We now investigate the evolutionary dynamics in periodically fluctuating environments. In particular, we consider the following definition for oxygen concentration, $S(t)$:

$$S(t) = \max\left(A_{min}, A_{max}\sin\left(\frac{2\pi t}{T}\right)\right), \tag{5.6}$$

with values of A_{min} and A_{max} chosen such that $S(t) \in [0, 1]$. Figure 5.3 demonstrates an example of oxygen dynamics.

We consider the environmental regime where cells experience periods of starvation followed by re-oxygenation. Figure 5.4 shows population dynamics in periodically fluctuating environments when different values of q_i are considered. When the fitness peaks are narrow (Figure 5.4(a)), population L out-competes population H. However, as the fitness peaks become broader, the population with higher rate of phenotypic variation is ultimately se-

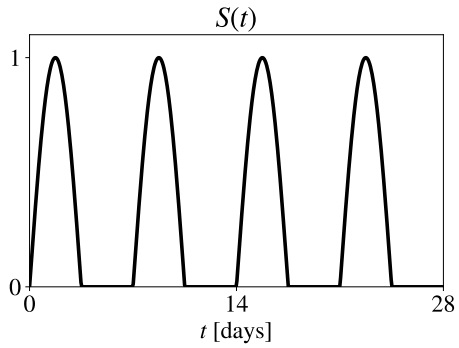

Figure 5.3: Dynamics of oxygen given by Equation (5.6) with $A_{min} = 0$, $A_{max} = 1$ and $T = 7$ days.

lected (Figure 5.4(c)). Thus, having wider fitness peaks seems to be advantageous for the population with higher rates of phenotypic variation.

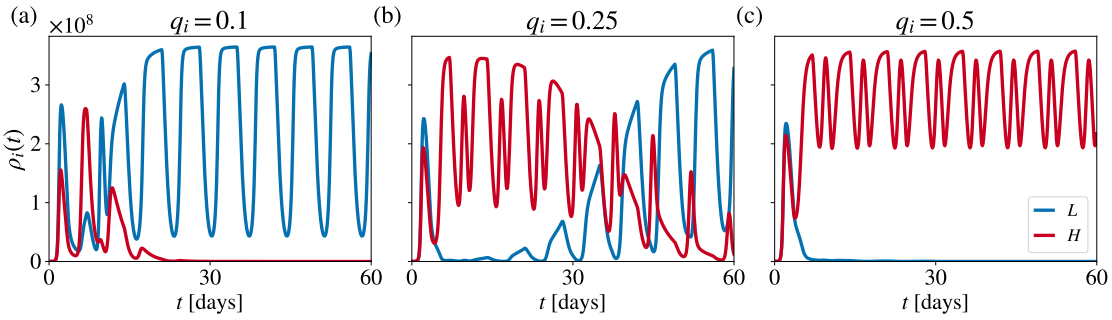

Figure 5.4: **(a)** Dynamics of population sizes obtained by solving numerically Equation (5.2) with $p(x, S(t))$ given by Equation (5.4) with $q_1 = q_2 = q_i = 0.1$. The oxygen concentration is given by Equation (5.6) with $T = 7$ days, $A_{min} = 0$, and $A_{max} = 1$. Other parameter values are as listed in Table 5.1. **(b)** – **(c)** Same as **(a)** but for $q_i = 0.25$ **(b)** and $q_i = 0.5$ **(c)**.

The parameters for the maximal proliferation rates of oxidative and phenotypic phenotypes, γ and ζ, used in Figure 5.4 are too large to be realistic for cancer cells. These values are, instead, more consistent for proliferation values in bacteria [219]. Therefore, since our model is general and remains applicable to other asexually reproducing individuals, we may expect to observe such behaviour in bacteria. Furthermore, we use the parameter values used in Chapter 2, given in Table 2.1, in order to demonstrate that such qualitative behaviour persists when considering other parameter regimes, as shown in Figure 5.5. Identification of other parameter regimes that would be applicable to cancer cell lines remains as future work.

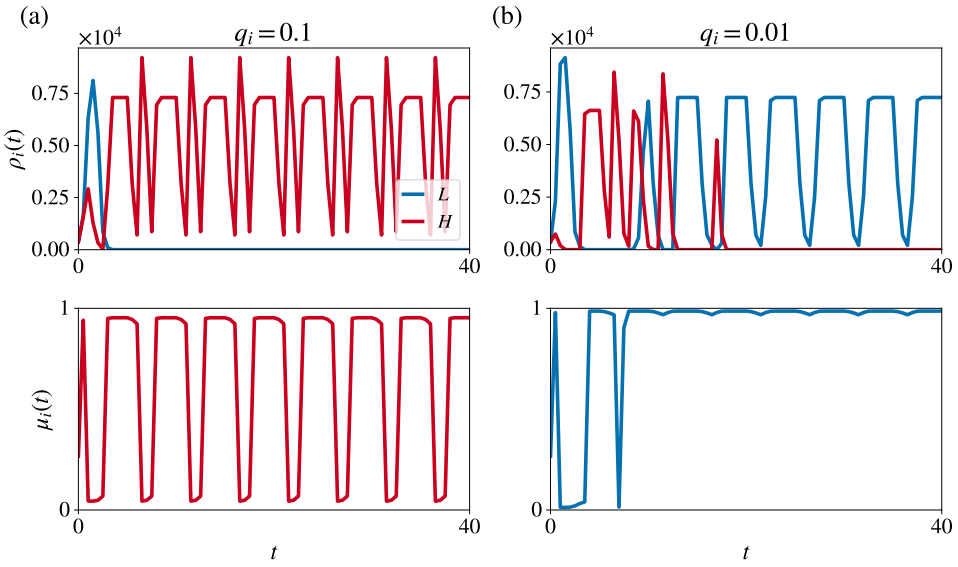

Figure 5.5: **(a)** Dynamics of population sizes (top) and mean phenotype of the surviving population (bottom) obtained by numerically solving Equation (5.2) with $p(x, S(t))$ given by Equation (5.4) with $q_1 = q_2 = q_i = 0.1$. The oxygen concentration is given by Equation (5.6) with $T = 7$ days, $A_{min} = 0$ and $A_{max} = 1$. Other parameter values are as listed in Table 2.1. **(b)** Same as **(a)** but for $q_i = 0.01$.

In order to understand the consequences of varying shape of fitness landscape, it is important to look at the dynamics of the mean phenotype. In Figure 5.6, we plot the change in the net growth rate for all phenotypic states when the environment oscillates periodically according to Equation (5.6) with $A_{min} = 0$, $A_{max} = 1$ and $T = 7$ days. The black dots in Figure 5.6 represent the dynamics of the mean phenotype of the surviving population (in (a) – population L, in (b) – population H). These plots correspond to population dynamics from Figures 5.4(a) and 5.4(c).

When the fitness peaks are narrow (Figure 5.6(a)), the surviving population, after a short initial period, acquires the glycolytic phenotype and remains glycolytic at all times, even when the environment becomes re-oxygenated. This can be explained by the fact that, when the peaks are narrow, the net growth rate of intermediate fitness states (i.e. fitness valley) is very low, as shown in Figure 5.1(a). Therefore, in order to switch, the population will 'pay a cost' by dramatically reducing in size during the process of switching. Therefore, the 'keep it safe' strategy, where the population remains in one particular phenotypic state, perhaps adapted to averaged conditions, is more advantageous.

When the fitness peaks are relatively wide and cells do not have to pay such a large cost in order to change their phenotype (Figure 5.1(c)), an adaptive strategy where the population has higher rate of phenotypic variation and is able to switch phenotype between

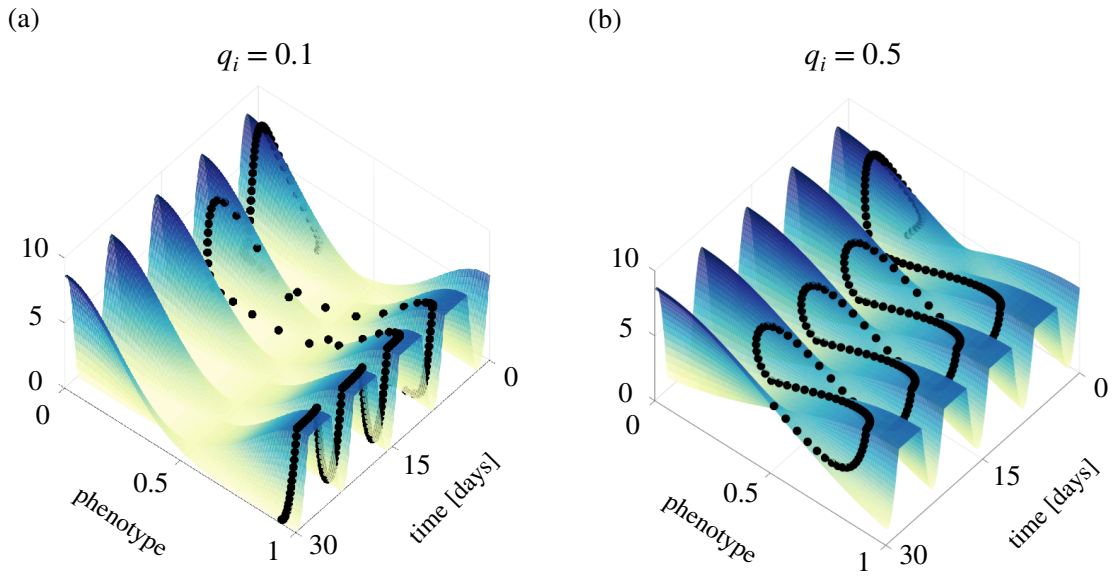

Figure 5.6: **(a)** Dynamics of net growth rate given by Equation (5.4) when the environment fluctuates according to Equation (5.6) with $A_{min} = 0$, $A_{max} = 1$ and $T = 7$ days. The black dots represent the mean phenotype of surviving population L (see Figure 5.4(a) for population dynamics). Here, the fitness peaks are narrow ($q_i = 0.1$). **(b)** Same as **(a)**, but for the wide fitness peaks, $q_i = 0.5$. The black dots represent the mean phenotype of surviving population H (see Figure 5.4(c)).

the more oxidative and more glycolytic states is preferred, as shown Figure 5.6(b).

Earlier we hypothesised that in the case where switching comes at a high cost (i.e. narrow fitness peaks), the population might acquire a phenotype adapted to averaged conditions. To test this idea, we consider two environmental regimes. In the first case, the oxygen level fluctuates between zero and a maximal value (Figure 5.7(a)), whereas in the second case, the oxygen level varies between two non-zero values (Figure 5.7(b)).

In Figure 5.7(a) the cells experience, on average, a lower concentration of oxygen, compared to cells in Figure 5.7(b). By plotting the net growth rate for averaged oxygen conditions, S_{avg}, one can then compare the heights of fitness peaks for averaged conditions. When oxygen availability is lower (Figure 5.7(a)), the fitness peak centred at $x = 1$ is higher. Therefore, the population with glycolytic phenotype is selected. On the other hand, when average oxygen level is higher (Figure 5.7(b)), the oxidative phenotype is selected.

These results highlight the idea that the adaptive strategy in dynamic environments depends crucially on the structure of the fitness landscape. In particular, when the fitness peaks are narrow and located far away from each other, there exists a significant cost that the population has to pay in order to switch the phenotype. In this case, a more safe strategy is to acquire a phenotype most adapted to the averaged conditions. However, when the fitness

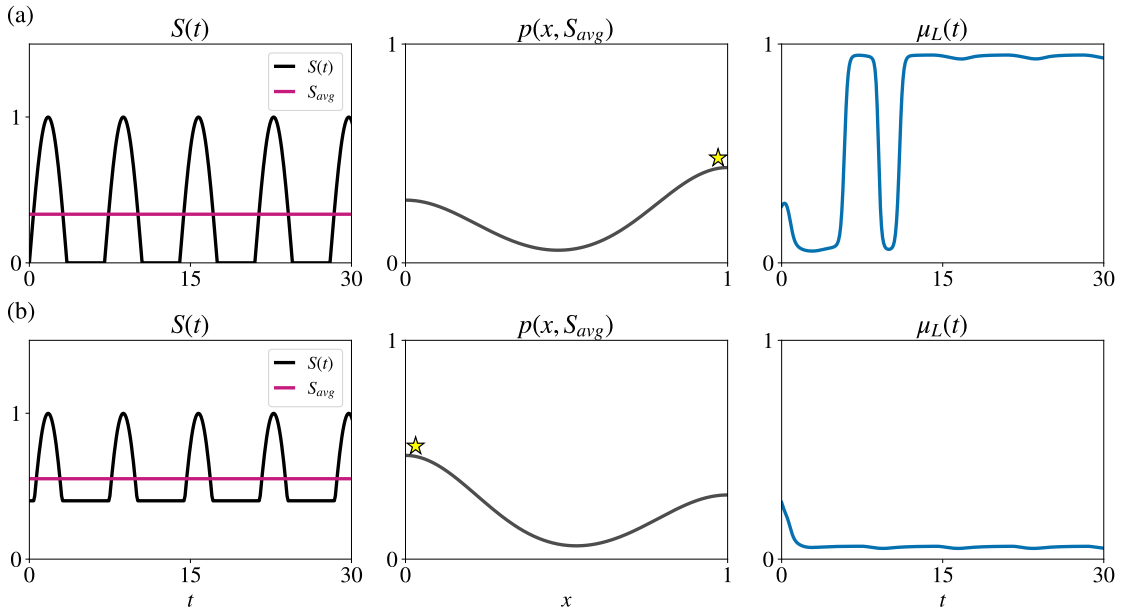

Figure 5.7: **(a)** Dynamics of oxygen and average oxygen level (left), fitness curve for average oxygen level (middle), and mean phenotype of the surviving population L (right) obtained by solving numerically Equations (2.3) with $p(x, S(t))$ given by Equation (5.4) with $q_1 = q_2 = q_i = 0.1$. The star in the middle column represents the fittest phenotypic state for a given environment. The oxygen concentration is given by Equation (5.6) with $T = 7$ days, $A_{min} = 0$, and $A_{max} = 1$. Other parameter values are as listed in Table 5.1. **(b)** Same as **(a)** but for $A_{min} = 0.4$.

peaks are wide and located close enough to each other, it is possible to switch phenotype without a great cost in order to deal with temporally varying environments. Therefore, in order to apply this modelling approach and study evolutionary dynamics in temporally varying environments, it is crucial to have detailed understanding of the underlying fitness landscape, preferably by inferring it from experimental data.

5.4 Discussion

In this chapter, we have presented preliminary results where we investigate the impact of the shape of fitness landscape on the success of a risk-spreading strategy. We have defined the fitness landscape as a sum of Gaussian functions, and by numerically approximating the system of nonlocal PDEs with prescribed oxygen levels, we have looked at the competition outcomes while varying the width of the fitness peaks.

We have demonstrated that in constant conditions, the population with lower phenotypic variation will survive, in agreement with previous results established in Chapter 2. Furthermore, we considered the environmental conditions where cells experience periods

of starvation followed by re-oxygenation. Previously, we noted that such environmental regimes under certain timescales select the population with the higher rate of phenotypic variation. However, as demonstrated in this chapter, the success of this strategy depends also on the width of the fitness peaks, as is schematically demonstrated in Figure 5.8.

When the fitness peaks are narrow, switching between two extreme phenotypes is too costly, and the surviving population acquires a phenotype adapted to averaged conditions. For example, if the environment is on average well oxygenated (left panel in top row of Figure 5.8), cells remain in the oxidative phenotype, whereas if the medium is poorly oxygenated (right panel in top row of Figure 5.8), then the cells become glycolytic. Furthermore, it is not advantageous to undergo spontaneous phenotypic variations at a higher rate. When the peaks are relatively wide and the cost to switch is low, higher rates of spontaneous phenotypic variation confer a competitive advantage. In this case, the surviving population switches its phenotype between the glycolytic and oxidative states (bottom row of Figure 5.8).

These preliminary results are a first step towards understanding the consequences of different geometries of fitness landscapes. Here, we considered the simplest shape tailored to our biological assumptions, and investigated the impact of only one parameter - the width of fitness peak. Furthermore, we assumed that the widths of both peaks are equal, i.e. $q_1 = q_2$. However, this assumption can be relaxed and asymmetric peaks can be further investigated.

Moreover, throughout this thesis we assumed an idealised scenario where the fitness curve is smooth and there are no ridges. However, in the fitness landscapes inferred from the experimental data, there might exist high-fitness ridges on both fitness peaks and fitness valleys [231]. Therefore, there might exist a rugged bridge via which cells could switch to another fitness peak even in the presence of the fitness valley.

Finally, it is important to stress that we assumed a very abstract simplification of tumour metabolism, considering two antithetical phenotypes, i.e. the two resources are substitutable. Incorporation of more biologically realistic scenarios would lead to a more accurate description of tumour metabolism. This would require construction of multi-dimensional fitness landscapes with several fitness peaks that would reflect different feedback mechanisms. Such development of the model would require extension of both analytical and numerical approaches used to study the dynamics of populations and adaptive strategies and is postponed for future work.

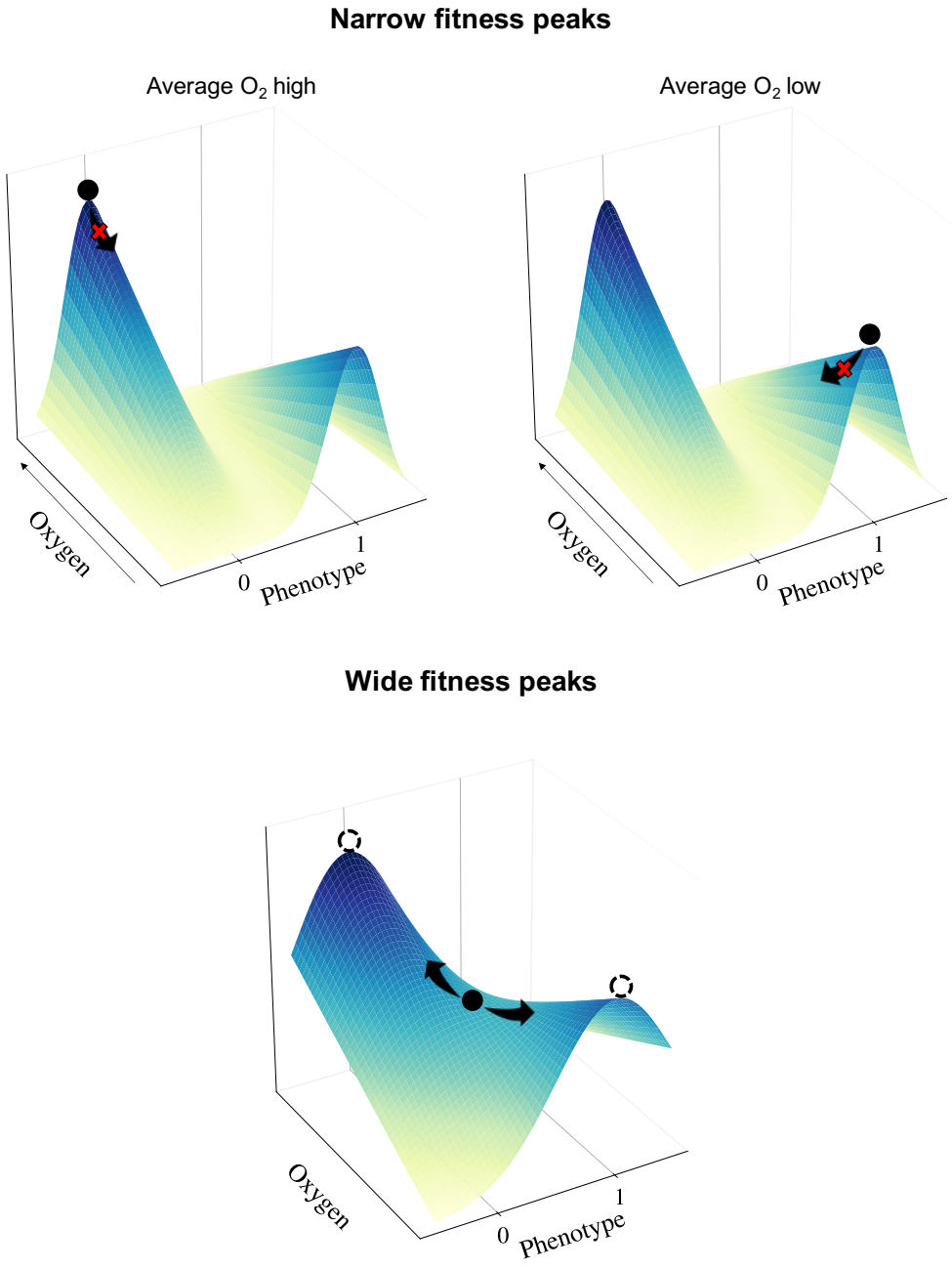

Figure 5.8: Schematic representation of adaptive strategies in different fitness landscape geometries and periodically fluctuating environmental conditions. When the fitness peaks are narrow (top row), the crossed arrows indicate that is is not advantageous to switch phenotype. Therefore, cells acquire phenotype most adapted to averaged conditions. When the fitness peaks are wide (bottom row), an adaptive strategy in which the population crosses the fitness valley and switches between two phenotypes, denoted by white circles, is preferred.

Chapter 6

Conclusions

6.1 Introduction

We conclude this thesis by summarising the results of Chapters 2 – 5 and outlining ideas for future work. The aim of this thesis was to investigate how cancer cells may adapt when dealing with temporal fluctuations in their microenvironment due to irregular blood flow. Varying gradients of nutrients allow us to draw an analogy with ecological problems where substantial progress has been made in understanding how different species coexist and/or adapt. In particular, we developed a suite of mathematical models of increasing biological complexity that evaluate the role of heritable, spontaneous phenotypic variation in dynamic environments. We identified the environmental regimes which are likely to select populations with higher rates of phenotypic variations and promote phenotypic heterogeneity. At the same time, these results suggest potential therapeutic strategies and provide a basis for future experimental investigation.

6.2 Summary of work

In this section, we summarise the key findings of each chapter.

6.2.1 Chapter 2

In Chapter 2, we developed a mathematical model for the evolutionary dynamics of two asexual populations, structured by phenotype and competing in periodically fluctuating environments. The population dynamics are governed by a system of nonlocal partial differential equations, where the linear diffusion term models the heritable, spontaneous phenotypic variation, and a non-local reaction term represents the effects of asexual reproduction and intra-population competition. The phenotypic state of each individual is represented by a continuous variable, and the phenotypic fitness landscape of the populations depends on

nutrient levels which may evolve over time. The two populations only differ in the rates at which the individuals undergo phenotypic variations, i.e. their diffusion coefficients.

Exploiting the analytical tractability of our model, we studied the long-time behaviour of the solutions in order to obtain a detailed mathematical depiction of the evolutionary dynamics. In particular, by assuming that the population distribution is Gaussian, we were able to derive a set of ordinary differential equations governing the dynamics of the variance, mean phenotype and size of each population. Our analytical results suggest that when nutrient levels experience small and slow periodic oscillations, the population with lower rate of phenotypic variation is selected. On the other hand, when the environment oscillates fast and with relatively large amplitude, leading to cycles of starvation followed by nutrient abundance, the population with higher rate of phenotypic variation is selected. Furthermore, in this case, we expected a higher level of phenotypic heterogeneity to be present. Finally, our results suggest that bet-hedging evolutionary strategies, whereby individuals switch between antithetical phenotypic states, can naturally emerge in the presence of relatively large and fast nutrient fluctuations leading to drastic environmental changes.

6.2.2 Chapter 3

While the model developed in Chapter 2 is abstract in nature, it provides valuable insight into understanding which adaptive strategies are most suitable for particular environmental conditions. In Chapter 3, we added several layers of biological complexity in order to apply the modelling framework to cancer dynamics. As before, we modelled the evolution of cells that are grouped into two populations. We linked the phenotypic state to the metabolic profile of each cell and assumed that cells in the phenotypic state $x = 0$ are fully oxidative (i.e. depend on oxidative phosphorylation only), whereas cells in the phenotypic state $x = 1$ are fully glycolytic (i.e. depend on glycolysis only). Thus, oxidative cells are selected when oxygen level is relatively high (normoxia) and glycolytic cells are favoured when oxygen level is low (hypoxia). We modelled oxygen dynamics via an ODE, assuming that oxygen is supplied via blood vessels, decays naturally and is consumed by the cells. The rate of consumption depends on the phenotype of the cells. Such coupling of population dynamics with the environment allowed us to study the feedback between cancer cells and their environment, and to investigate its implications on evolutionary dynamics. Furthermore, since glycolysis is less efficient than the aerobic pathway, we investigated the impact of fitness cost (i.e. reduced net growth rate of fully glycolytic phenotype) on the selection of particular adaptive strategies.

We started our exploration by considering a simplified, but analytically tractable, model. Here, the oxygen dynamics decoupled from the PDEs governing the population dynamics,

and nutrient consumption and natural decay were encapsulated in a linear term. Analysis of this simplified model, together with numerical simulations, showed that the results from the original model presented in Chapter 2 carry through.

We then studied the full model with a phenotype-dependent consumption term. Model simulations indicated that, depending on the rate at which oxygen is consumed by the cells, nonlinear interactions between cells and oxygen can stimulate chronic hypoxia and cycling hypoxia when the oxygen supply is varying temporally. Moreover, the model supports the idea that under chronic-hypoxic conditions lower rates of phenotypic variation lead to a competitive advantage, whereas higher rates of phenotypic variation can confer a competitive advantage under cycling-hypoxic conditions. In the latter case, the numerical results obtained show that bet-hedging evolutionary strategies, whereby cells switch between oxidative and glycolytic phenotypes, can spontaneously emerge.

Furthermore, considering a set of parameter values obtained from the literature, we estimated the timescales of fluctuations at which a risk spreading strategy might be advantageous. In particular, we observed that population with higher rates of phenotypic variation were selected when oxygen levels varied on the time scale of weeks, likely to be driven by angiogenesis and vascular remodelling. Finally, we explained how these results can shed light on the evolutionary process that may underpin the emergence of phenotypic heterogeneity in vascularised tumours. In particular, we expect to select more specialised populations with lower rates of phenotypic variations in high- and low-oxygenated regions, whereas regions with intermittent hypoxia would select populations with higher rates of phenotypic variation and, hence, with higher levels of phenotypic heterogeneity.

6.2.3 Chapter 4

Deterministic continuum models, such as those presented in Chapters 2 and 3, are based on population-scale phenomenological assumptions. While being amenable to mathematical analysis, such models usually fail to capture the adaptive dynamics of single individuals, which become important during population bottleneck events, i.e. when population size becomes very low. Although tumours are usually composed of large number of cells, the course of the disease and treatment success is often dictated by small populations. For instance, a small number of drug-resistant cancer cells can survive and expand when treatment ends and there is no competition from drug-sensitive cells. Additionally, metastases that occur during later stages of disease and lead to patients death, originate from a single cell or small cell cluster.

In order to accurately depict adaptation of cancer cells in dynamic environments, in Chapter 4, we developed a stochastic individual-based model for the coevolution of two

competing phenotype-structured cell populations that are exposed to time-varying nutrient levels and undergo spontaneous, heritable phenotypic variation with different probabilities. The evolution of every cell is described by a set of rules that result in a discrete-time branching random walk on the space of phenotypic states. First, we formally showed that the deterministic continuum counterpart of this model comprises a system of non-local partial differential equations for the cell population density functions coupled with an ordinary differential equation for the nutrient concentration (analogous to the model from Chapter 3). Then, we compared simulations from the individual-based model and its continuum analogue, focussing on scenarios whereby the predictions of the two models differ. Such scenarios were identified by looking at single realisations of IB model.

The results obtained via sensitivity analysis clarify the conditions under which significant differences between the two models can emerge due to bottleneck effects that bring about both lower regularity of the density functions of the two populations and more pronounced demographic stochasticity. In particular, bottleneck effects emerge in the presence of lower probabilities of phenotypic variation, and are more apparent when the two populations are characterised by lower fitness initial mean phenotypes and smaller initial levels of phenotypic heterogeneity. The emergence of these effects, and thus the agreement between the two modelling approaches, also depend on the initial proportions of the two populations.

Finally, as an illustrative example, we demonstrated the implications of our theoretical results for the early stage of metastatic colonisation of distant organs. We parametrised the model using values from the literature and studied the scenario where a small cluster of cancer cells invades a healthy tissue. We showed that higher probabilities of spontaneous phenotypic variations may be beneficial for cancer cells invading poorly-oxygenated distant organs, and that care should be taken when selecting a mathematical modelling approach, i.e. choosing between discrete and continuum approaches.

6.2.4 Chapter 5

In the modelling approach used in Chapters 2–4, the proliferation and death of cells in a given environment is governed by the fitness function. In particular, we assumed that the fitness function has polynomial form and consists of two fitness peaks, each adapted to an extreme environmental condition. In Chapter 5, we relax this assumption and investigate how the shape of the fitness peaks affects the competition outcomes.

Our preliminary results demonstrate that the competitive advantage of higher rates of spontaneous phenotypic variation in periodically fluctuating environments depends crucially on the width of the fitness peaks. In particular, narrow fitness peaks correspond to the situation where cells have to pay a high cost in order to switch. In this case, it is more

advantageous to acquire a specialised phenotype adapted to the averaged conditions. On the other hand, wide fitness peaks, where the cost of switching is not too high, promote the population with higher rate of phenotypic variation.

6.3 Future directions

There are several possibilities for extending the work in this thesis. In this section, we list several open questions that we believe are important to investigate to obtain a more complete understanding of the adaptive strategies that cancer cells might adopt in dynamic environments.

6.3.1 Tumour metabolism and data-driven fitness landscapes

In the model developed in this thesis, the behaviour of different phenotypic variants was based on idealised assumptions on tumour metabolism. We defined two extreme phenotypes – one dependent on oxygen and one dependent on glucose. In reality, however, both cancer and healthy cells rely on the OXPHOS and glycolytic metabolic pathways simultaneously in order to generate energy. Thus, the first natural extension of this work is incorporation of a more detailed description of tumour metabolism.

In this thesis, we assumed that glucose is always abundant and is not a limiting factor for glycolytic cells. This, however, might not be the case in real tumours where temporary interruptions in the blood flow could lead to decrease in glucose levels as well. Therefore, it is necessary to model the dynamics of glucose explicitly via ODE. Here, glucose would be supplied by the blood vessel and consumed by the cells with rates that depend on their phenotypes, as, for example, is implemented in [58]. Incorporation of glucose would further lead to modifications of the fitness landscape.

Furthermore, it is well known that the upregulated glycolysis in cancer cells leads to the increased production of lactic acid and subsequent acidification of the medium. Low environmental pH is toxic to healthy, non-acid resistant cells. This feedback can be incorporated into the model by modelling levels of lactate explicitly via an ODE, and modifying the fitness function accordingly. For example, higher levels of acid would lead to lower growth rate of phenotypic variants that are adapted to high-oxygen environments [19]. Furthermore, it is possible to introduce a second trait, e.g. acid resistance, to study whether the intermittent hypoxia contributes to selection of acid-resistant phenotypes.

Since in this model our focus was on the adaptive strategies, we assumed that the two cell populations H and L differ only in the rates at which they undergo spontaneous phenotypic variations. However, our modelling framework can be adjusted to study competition between populations of cells with different metabolic profiles, for example, breast cancer

cell lines MCF-7 and MDA-MB-231, which are commonly used in *in vitro* studies. MCF-7 cells demonstrate a normal, Pasteur-like metabolism, whereas MDA-MB-231 cells are more Warburg-like (glycolytic). Such differences in metabolism can be incorporated by assigning different fitness functions to each population. For instance, these two cell lines have already been grown *in vitro* in different concentrations of glucose, both in mono- and co-culture [232]. Data on competition outcomes and growth rates from these experiments can be used to construct accurate, experimentally-motivated fitness landscapes, and to capture the dynamics observed in experiments. The model can then be used to predict competition outcomes in periodically fluctuating environments and provide a theoretical basis for *in vitro* experimental protocols.

6.3.2 Other cell-environmental feedback mechanisms

In Chapter 3, we modelled oxygen dynamics explicitly and included consumption of oxygen by cells. This is an example of the negative feedback mechanisms that regulate population growth. An example of a positive feedback that promote the supply of nutrient is angiogenesis. This can be achieved by assuming that the cells in the glycolytic phenotype (i.e. hypoxic) release signals, such as VEGF, to promote formation of new blood vessels [233].

The simplest way to incorporate angiogenesis into the model is by making the blood supply term in Equation (2.3) phenotype-dependent, i.e. oxygen supply increases after significant exposure of cancer cells to hypoxia. Therefore, by considering appropriate timescales of the formation of new blood vessels, we expect the fluctuations in the environment that are driven by the angiogenesis process to emerge. Consideration of this feedback mechanism is expected to affect the advantages gained by each population, and therefore the phenotypic composition of the tumour, in a given environment.

In the same way, it would be interesting to extend the model to account for dynamics of reactive oxygen species that promote DNA damage and lead to mutagenesis [207]. For instance, this can be achieved by including an advection term for phenotypic variation with constant velocity.

6.3.3 Accelerating adaptation timescales

In our model, the heritable, spontaneous phenotypic variations are modelled using a diffusion term (PDE model) or discrete-time branching random walk (IB model). Such adaptations are relatively slow (on the timescale of cancer cell lifetime) and, thus, are appropriate to deal with slow fluctuations that occur on the timescale of weeks due to on-going formation of new blood vessels. However, fluctuations that are observed in tumours can also occur

on much faster timescales, ranging from minutes to days [22]. Therefore, in order to study adaptive strategies at faster timescales, it is necessary to adapt our modelling framework.

Adaptation at faster timescales can be achieved by incorporating guided phenotypic variation. In particular, we can assume that cancer cells can sense the environment and adapt accordingly, e.g. by up-regulating hypoxia inducible factors, which is a relatively fast process [113]. Guided phenotypic variation can be modelled via an advection term in PDE setup, where the velocity is the gradient of the fitness function. The equation modelling the evolution of cell population density will then take the following form:

$$\frac{\partial n_i}{\partial t} = \underbrace{\beta_i \frac{\partial^2 n_H}{\partial x^2}}_{\substack{\text{spontaneous} \\ \text{phenotypic} \\ \text{variation}}} \underbrace{- \alpha_i \frac{\partial}{\partial x}\left(\frac{\partial}{\partial x} R(x, S(t), \rho(t)) n_i\right)}_{\text{guided phenotypic variation}} + \underbrace{R(x, S(t), \rho(t)) n_i}_{\substack{\text{death and} \\ \text{proliferation}}}. \tag{6.1}$$

In other words, this mathematical formulation represents the idea that the cell will always move towards the fitness peak. Moreover, when using the fitness function defined by Equation (2.5) with growth rate given by Equation (2.6), this model is analytically tractable and it is possible to study the asymptotic behaviour of the solutions to obtain the competition dynamics in both constant and periodically-fluctuating environments, following the analysis approach presented in Chapter 2.

Furthermore, it is also important to derive such a model from a stochastic setting in order to validate our motivation to model guided phenotypic variations using the advection term in Equation (6.1). For instance, this can be done by following examples outlined in [234].

6.3.4 Spatial models

An additional development of our study would be to incorporate spatial structure into the PDE model (tractable for mathematical analysis), as done for instance by [170] and [179], and a corresponding stochastic model (e.g. hybrid agent-based model) [58].

First, it would be interesting to develop a spatial model with Krogh-cylinder geometry, modelling the phenotypic composition of perivascular tissue when the blood flow in the vessel undergoes periodic occlusions. The schematic 1D representation of the model is demonstrated in Figure 6.1(a). Here, oxygen and other molecules diffuse in space and are consumed by the cells. Such a model can be calibrated using experimentally measured values of oxygen and pH, for example, from [235]. Development of this model would provide a better understanding of spatial location of more aggressive phenotypes, and provide insights into potential therapeutic interventions.

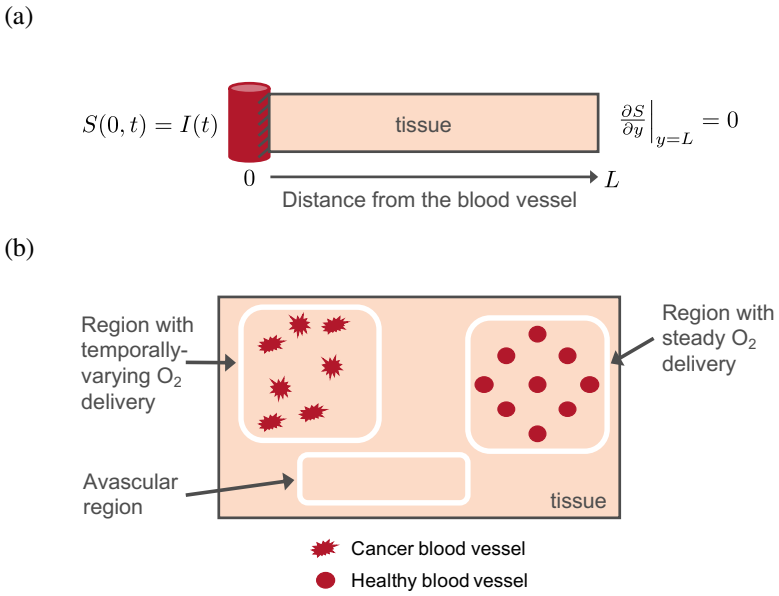

Figure 6.1: Schematic representation of **(a)** 1D Krogh-cylinder model and **(b)** spatial model with multiple blood vessels.

Another extension would be to follow the modelling approach in [180] and [58], where multiple blood vessels are distributed across the spatial domain (Figure 6.1(b)). This would enable a more detailed assessment of the way in which the interplay between spatial and temporal variability of oxygen levels may dictate the phenotypic composition and the level of phenotypic heterogeneity of vascularised tumours. In particular, spatial niche partitioning is known to have an important impact on interspecies competition, as it promotes the coexistence between species best adapted to different local environmental conditions [236, 237].

Moreover, since experimental results suggest that cycling hypoxia increases cell motility and promotes the formation of metastases [238, 47], when including spatial structure in the model it would also be interesting to explore the adaptive role of the trade-off between cell motility and cellular proliferation [239]. Cell movement can be incorporated via both diffusion and chemotactic advection terms. Such a model would have the potential to inform new treatment strategies aimed at minimising the pro-metastatic effect of cycling hypoxia.

6.4 Closing remarks

We have explored the risk spreading strategy where cells undergo heritable, spontaneous phenotypic variations, as a potential adaptive strategy for cancer cells existing in temporally varying environments. Building upon an abstract mathematical model of competition between two phenotype-structured populations, we considered more biologically realistic

scenarios where cells interact with their environment and considered fitness landscapes with different geometry. Furthermore, we applied the discrete version of the model to the problem of metastasis. The generality of the developed models makes them applicable to a broad range of asexual populations evolving in fluctuating environments. While the developed modelling framework can be extended to incorporate finer biological details, we believe it provides valuable insights into the evolutionary dynamics of cancer cell populations under temporally varying levels of oxygen, and will motivate further theoretical and experimental work in this direction.

Appendix A

Generalist-specialist model

Here we provide further exploration of the consumer-resource model that investigates competition between two specialists and a generalist for two resources. In particular, we outline the linear stability analysis in the cases where nutrient is supplied at constant rate for both non-adaptive and adaptive generalist. In this appendix, we also provide the details on the numerical setup of the model as well as numerical results that explore the dynamics of a non-adaptive generalist in a periodically fluctuating environment.

A.1 Non-dimensionalisation of the model

Consider the generalist-specialist model given by Equations (1.3)–(1.7). Let $t = T\tau$, $V = \tilde{v}v$, $U_1 = \tilde{u}_1 u_1$, and $U_2 = \tilde{u}_2 u_2$, where $\tilde{u}_1$, $\tilde{u}_2$, $\tilde{v}$ are to be determined. The equations becomes

$$\frac{\tilde{u}_1}{T}\frac{du_1}{d\tau} = a_1\tilde{u}_1 u_1 R_1 - d_1\tilde{u}_1 u_1, \tag{A.1}$$

$$\frac{\tilde{u}_2}{T}\frac{du_2}{d\tau} = a_2\tilde{u}_2 u_2 R_2 - d_2\tilde{u}_2 u_2, \tag{A.2}$$

$$\frac{dR_1}{d\tau} = TS_1 - a_1 b_1 R_1 T\tilde{u}_1 u_1 - g_1\theta_1(R_1, R_2)R_1\tilde{v}Tv, \tag{A.3}$$

$$\frac{dR_2}{d\tau} = TS_2 - a_2 b_2 R_2 T\tilde{u}_2 u_2 - g_2\theta_2(R_1, R_2)R_2\tilde{v}Tv, \tag{A.4}$$

$$\frac{\tilde{v}}{T}\frac{dv}{d\tau} = \theta(R_1, R_2)c_1 g_1\tilde{v}R_1 v + \theta(R_1, R_2)c_2 g_2\tilde{v}R_2 v - d_3\tilde{v}v. \tag{A.5}$$

Let $a_1 T = 1 \Rightarrow T = \frac{1}{a_1}$. Let $\frac{a_2}{a_1} = \alpha$ and $\frac{g_2}{g_1} = \gamma$. Additionally, let $\tilde{u}_1 = \frac{a_1}{b_1}$, $\tilde{u}_2 = \frac{a_1}{b_2}$, $\frac{b_1 \tilde{u}_1}{a_1} = 1$, $\frac{b_2 \tilde{u}_2}{a_1} = 1$, and $T g_1 \tilde{v} = 1 \Rightarrow v^* = \frac{a_1}{g_1}$. Hence:

$$\frac{du_1}{d\tau} = u_1 R_1 - \frac{d_1}{a_1} u_1, \tag{A.6}$$

$$\frac{du_2}{d\tau} = \alpha u_2 R_2 - \frac{d_2}{a_1} u_2, \tag{A.7}$$

$$\frac{dr_1}{d\tau} = \frac{S_1}{a_1} - R_1 u_1 - \theta_1(R_1, R_2) R_1 v, \tag{A.8}$$

$$\frac{dr_2}{d\tau} = \frac{S_2}{a_1} - \alpha R_2 u_2 - \gamma \theta_2(R_1, R_2) R_2 v, \tag{A.9}$$

$$\frac{dv}{d\tau} = \theta_1(R_1, R_2) R_1 v + \theta_2(R_1, R_2) \alpha R_2 v - \frac{d_3}{a_1} v. \tag{A.10}$$

Finally, let $\frac{S_1}{a_1} = I_1$, $\frac{S_2}{a_1} = I_2$, $\frac{d_i}{a_i} = \delta_i$, $r_i = R_i$:

$$\frac{du_1}{d\tau} = u_1 r_1 - \delta_1 u_1, \tag{A.11}$$

$$\frac{du_2}{d\tau} = \alpha u_2 r_2 - \delta_2 u_2, \tag{A.12}$$

$$\frac{dr_1}{d\tau} = I_1(\tau) - r_1 u_1 - \theta_1(r_1, r_2) r_1 v, \tag{A.13}$$

$$\frac{dr_2}{d\tau} = I_2(\tau) - \alpha r_2 u_2 - \theta_2(r_1, r_2) \gamma r_2 v, \tag{A.14}$$

$$\frac{dv}{d\tau} = \theta_1(r_1, r_2) c_1 r_1 v + \theta_2(r_1, r_2) c_2 r_2 v - \delta_3 v. \tag{A.15}$$

A.2 Linear stability analysis

Let us consider a case where both resources are supplied at a constant rate:

$$I_1(t) \equiv \bar{I}_1 \geq 0 \quad \text{and} \quad I_2(t) \equiv \bar{I}_2 \geq 0. \tag{A.16}$$

A.2.1 Non-adaptive generalist

The simplicity of the non-adaptive generalist model allows us to determine the steady states when the environment is constant. Here we consider the non-dimensionalised model (Equations (A.11)–(A.15)) with resource supplies given by Equation (A.16) and the uptake of each resource by the generalist given by

$$\theta_i(r_1, r_2) \equiv \bar{\theta} \geq 0 \quad \text{for} \quad i \in \{1, 2\}. \tag{A.17}$$

Setting $\frac{d}{dt} = 0$ in Equations (A.11)–(A.15) we deduce that are five non-trivial steady states and we characterise their local linear stability. We do not consider steady states for which resources are absent, since we assume that $\bar{I}_1, \bar{I}_2 > 0$.

i) Coexistence of three populations ($u_1 \neq 0$, $u_2 \neq 0$, $v \neq 0$). We find the following steady state values:

$$r_1^* = \delta_1, \tag{A.18}$$

$$r_2^* = \frac{\delta_2}{\alpha}, \tag{A.19}$$

$$\bar{I}_1 = r_1^*(u_1^* + \bar{\theta}_1 v^*), \tag{A.20}$$

$$\bar{I}_2 = r_2^*(\alpha u_2^* + \bar{\theta}_2 \gamma v^*), \tag{A.21}$$

$$\bar{\theta}_1 c_1 r_1 + \bar{\theta}_2 \gamma c_2 r_2 - \delta_3 = 0. \tag{A.22}$$

Equations (A.18), (A.19) and (A.22) are three equations for the two unknowns, r_1^* and r_2^*. Hence, we have a solvability condition:

$$\bar{\theta}_1 c_1 \delta_1 + \bar{\theta}_2 c_2 \alpha \delta_2 - \delta_3 = 0.$$

When this holds, the system reduces to two equations (Equations (A.20) and (A.21)) for three unknowns (u_1^*, u_2^* and v^*). Hence, we have an infinite number of solutions:

$$u_1^* = \frac{\bar{I}_1}{r_1} - \bar{\theta}_1 v^*, \tag{A.23}$$

$$u_2^* = \frac{\bar{I}_2}{r_2} - \bar{\theta}_2 \gamma v^*, \tag{A.24}$$

$$v^* \in (0, v_{max}), \tag{A.25}$$

where

$$v_{max} = \min\left(\frac{\bar{I}_1}{\bar{\theta}_1 r_1}, \frac{\bar{I}_2}{\bar{\theta}_2 r_2}\right). \tag{A.26}$$

This degenerate case, while mathematically possible, is biologically very unrealistic. Therefore, we do not consider it further.

ii) Specialists win ($u_1 \neq 0$, $u_2 \neq 0$, $v = 0$). In this case,

$$r_1^* = \delta_1, \qquad r_2^* = \frac{\delta_2}{\alpha}, \tag{A.27}$$

$$u_1^* = \frac{\bar{I}_1}{\delta_1}, \qquad u_2^* = \frac{\bar{I}_2}{\delta_2}. \tag{A.28}$$

The Jacobian is

$$\mathbf{J_{1ii}} = \begin{pmatrix} r_1^* - \delta_1 & 0 & u_1^* & 0 & 0 \\ 0 & \alpha r_2^* - \delta_2 & 0 & \alpha u_2^* & 0 \\ -r_1^* & 0 & -u_1^* & 0 & -\bar{\theta}_1 r_1^* \\ 0 & -r_2^* & 0 & -u_2^* & -\bar{\theta}_2 \gamma r_2^* \\ 0 & 0 & 0 & 0* & \bar{\theta}_1 c_1 r_1^* + \bar{\theta}_2 \gamma c_2 r_2 - \delta_3 \end{pmatrix}, \tag{A.29}$$

which has eigenvalues:

$$\lambda_{1,2} = \frac{-\bar{I}_1 \pm \sqrt{\bar{I}_1^2 - 4\delta_1^2 \bar{I}_1}}{2\delta_1}, \tag{A.30}$$

$$\lambda_{3,4} = \frac{-\alpha\bar{I}_2 \pm \sqrt{\alpha\bar{I}_2(\alpha\bar{I}_2 - 4\delta_2^2)}}{2\delta_2}, \tag{A.31}$$

$$\lambda_5 = \frac{-\alpha\delta_3 + \alpha c_1\delta_1\bar{\theta}_1 + c_2\delta_2\gamma\bar{\theta}_2}{\alpha}. \tag{A.32}$$

The real parts of $\lambda_{1,2,3,4}$ are all less than zero. Therefore, for this steady state to be stable, λ_5 has to be negative, hence the following condition must be satisfied:

$$\bar{\theta}_1 < \frac{\alpha\delta_3 - \bar{\theta}_2\gamma c_2\delta_2}{\alpha c_1\delta_1}. \tag{A.33}$$

iii) Generalist wins ($u_1 = 0$, $u_2 = 0$, $v \neq 0$). For this case, the steady states are:

$$r_1^* = \frac{\delta_3\bar{I}_1}{\bar{\theta}_1(c_1\bar{I}_1 + c_2\bar{I}_2)}, \tag{A.34}$$

$$r_2^* = \frac{\delta_3\bar{I}_2}{\bar{\theta}_2\gamma(c_1\bar{I}_1 + c_2\bar{I}_2)}, \tag{A.35}$$

$$v^* = \frac{c_1\bar{I}_1 + c_2\bar{I}_2}{\delta_3}. \tag{A.36}$$

The Jacobian can be simplified to

$$\mathbf{J_{1iii}} = \begin{pmatrix} r_1^* - \delta_1 & 0 & 0 & 0 & 0 \\ 0 & \alpha r_2^* - \delta_2 & 0 & 0 & 0 \\ -r_1^* & 0 & -\bar{\theta}_1 v^* & 0 & -\frac{\bar{I}_1}{v^*} \\ 0 & -r_2^* & 0 & -\bar{\theta}_2\gamma v^* & -\frac{\bar{I}_2}{v^*} \\ 0 & 0 & \bar{\theta}_1 c_1 v^* & \bar{\theta}_2\gamma c_2 v^* & 0 \end{pmatrix}, \tag{A.37}$$

and the eigenvalue problem yields

$$\lambda_1 = r_1^* - \delta_1, \tag{A.38}$$

$$\lambda_2 = \alpha r_2^* - \delta_2, \tag{A.39}$$

$$\lambda^3 + \lambda^2 v^* \left(\bar{\theta}_1 + \bar{\theta}_2\gamma\right) + \lambda\left(\bar{\theta}_1\bar{\theta}_2\gamma v^{*2} + \bar{I}_2\bar{\theta}_2\gamma c_2 + \bar{I}_1\bar{\theta}_1 c_1\right) + \bar{\theta}_1\bar{\theta}_2\gamma v^*\left(\bar{I}_1 c_1 + \bar{I}_2 c_2\right) = 0. \tag{A.40}$$

All the parameters are positive numbers and hence the steady states are positive. Since the number of positive roots in a polynomial is equal to the number of changes in the sign of the coefficients, Equation (A.40) can have only negative eigenvalues. Therefore, from Equations (A.38), (A.39) and (A.34), (A.35), this steady state is stable only when the following conditions are satisfied:

$$\theta_1 > \frac{\alpha\delta_3\bar{I}_1}{\delta_1(c_1\bar{I}_1 + c_2\bar{I}_2)}, \tag{A.41}$$

$$\theta_2 > \frac{\alpha\delta_3\bar{I}_2}{\gamma\delta_2(c_1\bar{I}_1 + c_2\bar{I}_2)}. \tag{A.42}$$

Thus,

$$\bar{\theta}_1 + \bar{\theta}_2 > \frac{\alpha\delta_3}{c_1\bar{I}_1 + c_2\bar{I}_2}\left[\frac{\bar{I}_1}{\delta_1} + \frac{\bar{I}_2}{\gamma\delta_2}\right]. \tag{A.43}$$

If we assume for simplicity that $\delta_1 = \delta_2 = \delta_3 = \delta$ and $c_1 = c_2 = 1$, $\alpha = \gamma = 1$, then we have the condition

$$\bar{\theta}_1 + \bar{\theta}_2 > \frac{\bar{I}_1 + \bar{I}_2}{\bar{I}_1 + \bar{I}_2} > 1, \tag{A.44}$$

which violates our restriction that $\bar{\theta}_1 + \bar{\theta}_2 < 1$. Thus, the competitive exclusion of specialists by a generalist cannot occur in this case.

iv) Coexistence of specialist u_1 and the generalist ($u_1 \neq 0$, $u_2 = 0$, $v \neq 0$). In this case, the steady state is

$$r_1^* = \delta_1, \tag{A.45}$$

$$r_2^* = \frac{\delta_3 - c_1\delta_1\bar{\theta}_1}{c_2\gamma\bar{\theta}_2}, \tag{A.46}$$

$$u_1^* = \frac{\delta_3\bar{I}_1 - c_1\delta_1\bar{I}_1\bar{\theta}_1 - c_2, \delta_1\bar{I}_2\bar{\theta}_1}{\delta_1\gamma(\delta_3 - c_1\delta_1\bar{\theta}_1)}, \tag{A.47}$$

$$v^* = \frac{c_2\bar{I}_2}{\delta_3 - c_1\delta_1\bar{\theta}_1}. \tag{A.48}$$

For non-negative initial conditions, due to the invariance of the positive quadrant, the steady state values must be non-negative. Therefore, the following condition must be satisfied:

$$\bar{\theta}_1 < \frac{\delta_3}{\delta_1}\frac{\bar{I}_1}{c_1\bar{I}_1 + c_2\bar{I}_2}. \tag{A.49}$$

The Jacobian simplifies to

$$\mathbf{J_{1iv}} = \begin{pmatrix} 0 & 0 & u_1^* & 0 & 0 \\ 0 & \alpha r_2^* - \delta_2 & 0 & 0 & 0 \\ -\delta_1 & 0 & -\frac{\bar{I}_1}{\delta_1} & 0 & -\bar{\theta}_1\delta_1 \\ 0 & -r_2^* & 0 & -\bar{\theta}_2\gamma v^* & -\frac{\bar{I}_2}{v^*} \\ 0 & 0 & \bar{\theta}_1 c_1 v^* & \bar{\theta}_2\gamma c_2 v^* & 0 \end{pmatrix}, \tag{A.50}$$

and the eigenvalues satisfy

$$\begin{aligned} \det|\mathbf{J_{1iv}} - \lambda\mathbf{I}| = (\alpha r_2^* - \delta_2 - \lambda)(\lambda^4 + \lambda^3\left(\frac{\bar{I}_1 + \delta_1\gamma\bar{\theta}_2 v^*}{\delta_1}\right) + \\ \lambda^2\left(\frac{c_2\delta_1\gamma\bar{I}_2\bar{\theta}_2 + \delta_1^2 u_1^* + c_1\delta_1^2\bar{\theta}_1^2 v^* + \gamma\bar{I}_1\bar{\theta}_2 v^*}{\delta_1}\right) + \\ \lambda\left(\frac{c_2\gamma\bar{I}_1\bar{I}_2\bar{\theta}_2 + \delta_1^2\gamma\bar{\theta}_2 u_1^* v^* + c_1\delta_1^2\gamma\bar{\theta}_1^2\bar{\theta}_2 v^{*2}}{\alpha\delta_2}\right) + c_2\delta_1\gamma\bar{I}_2\bar{\theta}_2 u_1^*). \end{aligned}$$

The first eigenvalue is:

$$\lambda_1 = \frac{\alpha\delta_3 - \alpha c_1\delta_1\bar{\theta}_1 - c_2\delta_2\gamma\bar{\theta}_2}{c_2\gamma\bar{\theta}_2}, \tag{A.51}$$

which is negative under the following condition:

$$\bar{\theta}_1 < \frac{\alpha\delta_3 - \bar{\theta}_2 c_2 \gamma \delta_2}{\alpha c_1 \delta_1}. \tag{A.52}$$

The remaining eigenvalues are negative.

v) Coexistence of specialist u_2 and the generalist ($u_1 = 0$, $u_2 \neq 0$, $v \neq 0$). In this case the steady states are:

$$r_1^* = \frac{\alpha\delta_3 - c_2\delta_2\gamma\bar{\theta}_2}{ac_1\bar{\theta}_1}, \tag{A.53}$$

$$r_2^* = \frac{\delta_2}{\alpha}, \tag{A.54}$$

$$u_2^* = \frac{\alpha\delta_3\bar{I}_2 - c_1\delta_2\gamma\bar{I}_1\bar{\theta}_2 - c_2\delta_2\gamma\bar{I}_2\bar{\theta}_2}{\delta_2(\alpha\delta_3 - c_2\delta_2\gamma\bar{\theta}_2)}, \tag{A.55}$$

$$v^* = \frac{\alpha c_1 \bar{I}_1}{\alpha\delta_3 - c_2\delta_2\gamma\bar{\theta}_2}. \tag{A.56}$$

Arguing as above, we have

$$\bar{\theta}_2 < \frac{\alpha\delta_3\bar{I}_2}{\delta_2\gamma(c_1\bar{I}_1 + c_2\bar{I}_2)}. \tag{A.57}$$

The Jacobian can be simplified to take the form

$$\mathbf{J_{1v}} = \begin{pmatrix} r_1^* - \delta_1 & 0 & 0 & 0 & 0 \\ 0 & 0 & 0 & \alpha u_2^* & 0 \\ -r_1^* & 0 & -\bar{\theta}_1 v^* & 0 & -\frac{\bar{I}_1}{v^*} \\ 0 & -\frac{\delta_2}{\alpha} & 0 & -\frac{\alpha\bar{I}_2}{\delta_2} & -\frac{\bar{\theta}_2\gamma\delta_2}{\alpha} \\ 0 & 0 & \bar{\theta}_1 c_1 v^* & \bar{\theta}_2\gamma c_2 v^* & 0 \end{pmatrix}, \tag{A.58}$$

and the eigenvalues satisfy

$$\begin{aligned} \det|\mathbf{J_{1v}} - \lambda\mathbf{I}| = (r_1^* - \delta_1 - \lambda)(\lambda^4 + \lambda^3 &\left(\frac{\alpha\bar{I}_2 + \delta_2\bar{\theta}_1 v^*}{\delta_2}\right) + \\ \lambda^2 &\left(\frac{\alpha c_1\delta_2\bar{I}_1\bar{\theta}_1 + \alpha\delta_2^2 u_2^* + \alpha^2\bar{I}_2\bar{\theta}_1 v^* + c_2\delta_2^2\gamma^2\bar{\theta}_2^2 v^*}{\alpha\delta_2}\right) + \\ \lambda &\left(\frac{\alpha^2 c_1\bar{I}_1\bar{I}_2 + \alpha\delta_2^2\bar{\theta}_1 u_2^* v^* + c_2\delta_2^2\gamma^2\bar{\theta}_1\bar{\theta}_2^2 v^{*2}}{\alpha\delta_2}\right) + c_1\delta_2\bar{I}_2\bar{\theta}_1 u_2^*. \end{aligned}$$

The first eigenvalue is:

$$\lambda_1 = \frac{\alpha\delta_3 - \alpha c_1\delta_1\bar{\theta}_1 - c_2\delta_2\bar{\theta}_2}{\alpha c_1\bar{\theta}_1}. \tag{A.59}$$

The other eigenvalues are negative. Thus, the steady state is stable if $\lambda_1 < 0$. This is the same condition as in Equation A.57 (case iv).

A.2.2 Adaptive generalist

Here, we assume that

$$\theta_1(r_1, r_2) = \Theta_1 \frac{r_1}{r_1 + r_2} \quad \text{and} \quad \theta_2(r_1, r_2) = \Theta_2 \frac{r_2}{r_1 + r_2}, \tag{A.60}$$

where Θ_1 and Θ_2 are positive constant values.

There are 5 non-trivial steady states. Here, however, we consider only two [(i) coexistence and ii) exclusion of generalist] analytically because the other three are not analytically tractable or occur outside the parameter range considered (i.e. $\Theta_1 + \Theta_2 < 1$). For Equations (A.11) – (A.15) with Equation (A.60) and nutrient supply given by Equation (A.16), it is straightforward to show that the Jacobian matrix is:

$$\mathbf{J_2} = \begin{pmatrix} r_1 - \delta_1 & 0 & u_1 & 0 & 0 \\ 0 & \alpha r_2 - \delta_2 & 0 & \alpha u_2 & 0 \\ -r_1 & 0 & -u_1 - \frac{\Theta_1 r_1 (2r_2 + r_1) v}{(r_1 + r_2)^2} & \frac{\Theta_1 r_1^2 v}{(r_1 + r_2)^2} & -\frac{\Theta_1 r_1^2}{r_1 + r_2} \\ 0 & -r_2 & \frac{\Theta_2 \gamma r_2^2 v}{r_1 + r_2} & -\alpha u_2 - \frac{\Theta_2 \gamma r_2 (2r_1 + r_2) v}{(r_1 + r_2)^2} & -\frac{\Theta_2 \gamma r_2^2}{r_1 + r_2} \\ 0 & 0 & \frac{c_1 \Theta_1 r_1 (2r_2 + r_1) v - \Theta_2 c_2 \gamma r_2^2 v}{(r_1 + r_2)^2} & \frac{c_2 \Theta_2 \gamma r_2 (2r_1 + r_2) v - \Theta_1 c_1 r_1^2}{(r_1 + r_2)^2} & \frac{c_1 \Theta_1 r_1^2 + c_2 \Theta_2 \gamma r_2^2}{r_1 + r_2} - \delta_3 \end{pmatrix}. \tag{A.61}$$

i) Coexistence of all three cell populations ($u_1 \neq 0$, $u_2 \neq 0$, $v \neq 0$) In this case, the steady states satisfy

$$r_1^* = \delta_1, \tag{A.62}$$

$$r_2^* = \alpha \delta_2, \tag{A.63}$$

$$\bar{I}_1 = r_1^* u_1^* + \frac{\Theta_1 r_1^{*2}}{r_1^* + r_2^*} v^*, \tag{A.64}$$

$$\bar{I}_2 = r_2^* \alpha u_2^* + \frac{\Theta_2 \gamma r_2^{*2}}{r_1^* + r_2^*} v^*, \tag{A.65}$$

$$\frac{\Theta_1 c_1 r_1^{*2}}{r_1^* + r_2^*} + \frac{\Theta_2 \gamma c_2 r_2^{*2}}{r_1^* + r_2^*} - \delta_3 = 0. \tag{A.66}$$

As before, we see that Equations (A.62), (A.63) and (A.66) are 3 equations for the 2 unknowns, r_1^* and r_2^*, leading to the solvability condition:

$$\Theta_1 = \frac{\alpha \delta_3 (\alpha \delta_1 + \delta_2) - c_2 \Theta_2 \gamma \delta_2^2}{\alpha^2 c_1 \delta_1^2}. \tag{A.67}$$

When this condition holds, Eqs. (A.64) and (A.65) imply an infinite number of solutions. As for the non-adaptive generalist model (i), we do not investigate this case any further.

ii) Specialists win ($u_1 \neq 0$, $u_2 \neq 0$, $v = 0$) In this case, the steady state is

$$r_1^* = \delta_1, \qquad r_2^* = \frac{\delta_2}{\alpha}, \tag{A.68}$$

$$u_1^* = \frac{\bar{I}_1}{\delta_1}, \qquad u_2^* = \frac{\bar{I}_2}{\delta_2}, \tag{A.69}$$

and linear stability analysis yields the following expressions for the five eigenvalues:

$$\lambda_1 = \frac{\alpha^2\Theta_1 c_1\delta_1^2 + \Theta_2\gamma c_2\delta_2^2 - \alpha^2\delta_1\delta_3 - \alpha\delta_2\delta_3}{\alpha(\alpha\delta_1 + \delta_2)}, \tag{A.70}$$

$$\lambda_{2,3} = \frac{-\bar{I}_1 \pm\sqrt{\bar{I}_1^2 - 4\delta_1^2}}{2\delta_1}, \tag{A.71}$$

$$\lambda_{4,5} = \frac{-\alpha\bar{I}_2 \pm\sqrt{\alpha^2\bar{I}_2^2 - 4\delta_2^2\bar{I}_2}}{2\delta_2}. \tag{A.72}$$

Eigenvalues $\lambda_{2,3}$ and $\lambda_{4,5}$ always have negative real part since all parameters are positive. For λ_1 to be negative, the following inequality must hold:

$$\Theta_1 < \frac{\alpha\delta_3(\alpha\delta_1 + \delta_2) - c_2\Theta_2\gamma\delta_2^2}{\alpha^2 c_1\delta_1^2}. \tag{A.73}$$

If we assume that the generalist and specialist have equal death terms, $\delta_1 = \delta_2 = \delta_3 = \delta$, and set the remaining parameters equal to 1, then Equation (A.73) becomes:

$$\Theta_1 + \Theta_2 < 2. \tag{A.74}$$

From the definition of the generalist, $a + b < 1$, therefore, if the death rates of the generalist and specialists are equal and the other parameters are equal to 1, the specialist will always exclude the generalist.

A.3 Setup of numerical simulations

To numerically solve the system of Equations (1.3)–(1.7), we use the `ode15s` function in MATLAB. In addition, we set a requirement that none of the populations or resource levels can go below zero, since it is biologically unrealistic. To do so, we set the `'Non-negative'` option. The simulation is run for t_{max} with the following initial conditions:

$$U_1(0) = U_2(0) = V(0) = 1 \quad \text{and} \quad R_1(0) = R_2(0) = 0.1. \tag{A.75}$$

To double check that the solutions are correct, we compared the final values of population sizes and resource levels at the end of simulation with steady state values obtained from the analysis.

A.4 Non-adaptive generalist in a fluctuating environment

We split $\bar{\theta}_i$, $i \in \{1, 2\}$, into equally split 25 values and for each combination of ($\bar{\theta}_1$, $\bar{\theta}_2$) we solve numerically Equations (1.3)–(1.7) and note the average populations size over the last period. By comparing the averages, we obtain the competition outcome. If one of the population sizes is below 0.001, then this population is considered extinct. Each simulation runs until $t = t_{max} = 5000$. Moreover, we consider different fluctuation regimes by choosing different values of the half-amplitude, ΔI, and period of fluctuations, T, while keeping $I_{mean} = 1$. Figure A.1 summarises the outcomes of the non-adaptive generalist model when the nutrient supply fluctuates sinusoidally as given by Equation (1.11).

The outcomes of competition were not affected by the choice of I_{mean} considered. When the environment varies on relatively faster timescales ($T \in [1, 10, 100]$), the outcomes do not differ from the analytical predictions of competition in a steady environment (see Figure 1.7(a)). Additionally, the amplitude of the fluctuations does not affect the outcome. Slower ($T = 500$) fluctuations do not affect the outcomes for a generalist that is inferior to the specialists, i.e. when $\bar{\theta}_1 + \bar{\theta}_2 < 1$. Slow, high-amplitude ($\Delta I = 0.9$) fluctuations select for a strong generalist and prevent the coexistence of one specialist and the generalist if $\bar{\theta}_1 + \bar{\theta}_2 > 1$.

Figure A.2 demonstrates the population dynamics in fluctuating environment in the case where both specialists survive (a), and all three populations coexist (b).

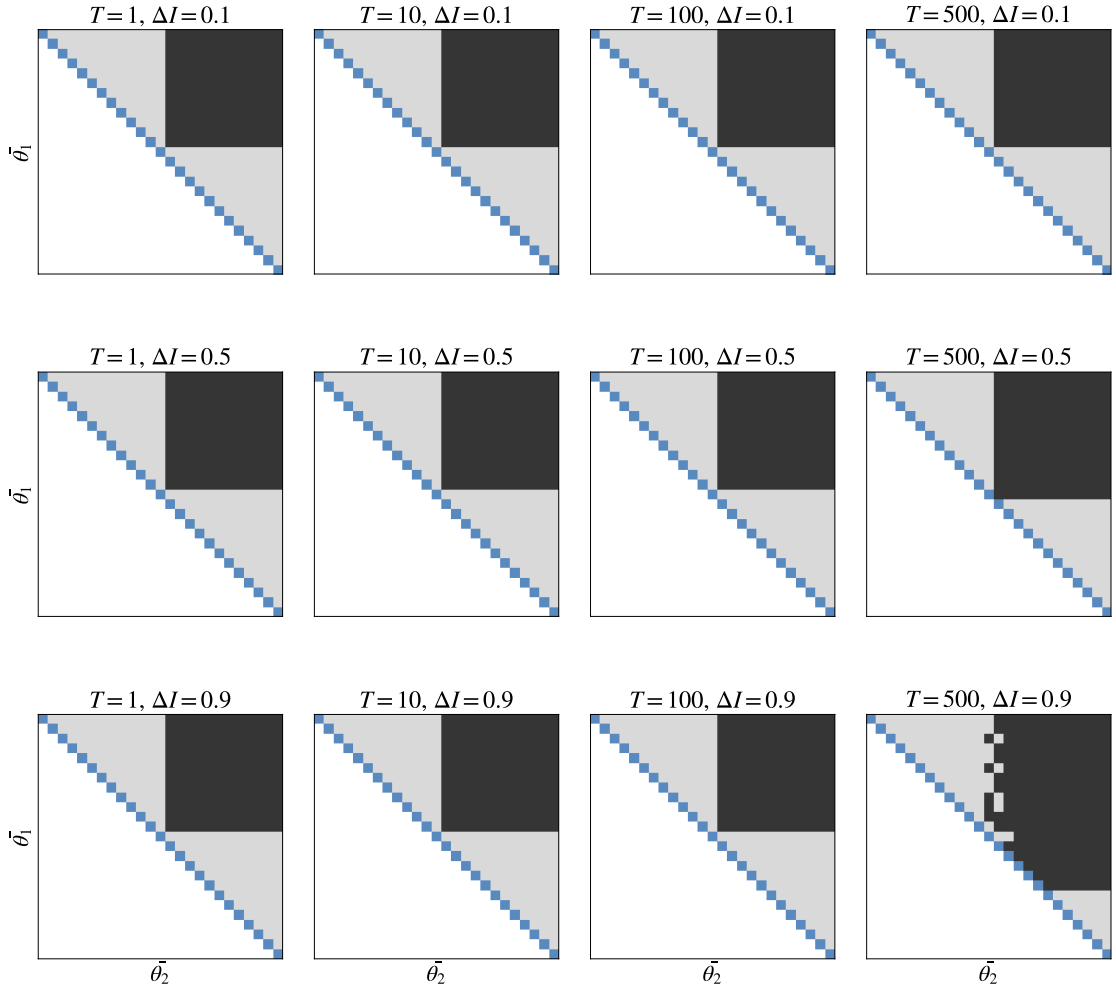

Figure A.1: Outcomes of the non-adaptive generalist model obtained by solving numerically Equations (1.3)–(1.7) with Equation (1.8) when the nutrient supply is defined by Equation (1.11). The simulations were run until $t_{max} = 5000$. Colours represent competition outcomes: black – survival of the generalist; white – survival of both specialists; grey – survival of one specialist and the generalist; blue – coexistence of all three populations. Parameter values used here: $d = 0.1$, $I_{mean} = 1$, $\alpha = 1$, $\gamma = 1$, $c_1 = c_2 = 1$,$g_1 = g_2 = 1$, $b_1 = b_2 = 1$.

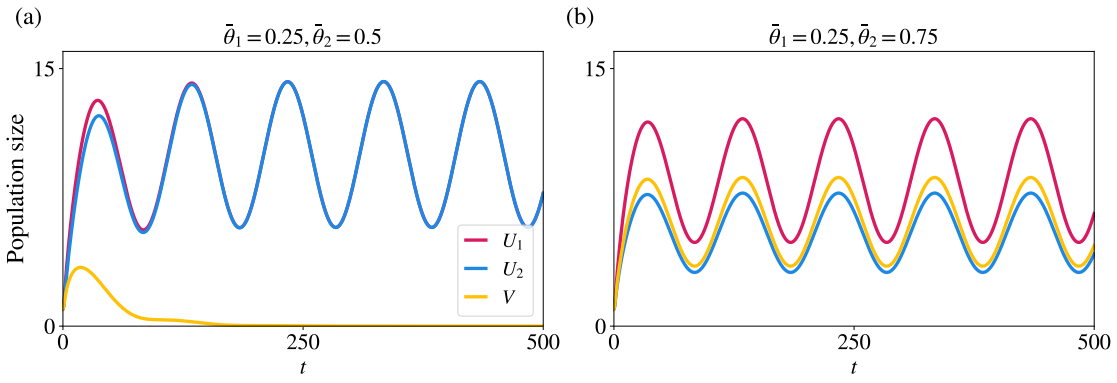

Figure A.2: Sample of population dynamics obtained by solving numerically Equations (1.3)–(1.7) with Equation (1.8) when the nutrient supply is defined by Equation (1.11). **(a)** Both specialists out-compete the generalist ($\bar{\theta}_1 = 0.25, \bar{\theta}_2 = 0.5$). **(b)** The three populations coexist ($\bar{\theta}_1 = 0.25, \bar{\theta}_2 = 0.75$). Parameter values used here: $d = 0.1$, $T = 100$, $I_{mean} = 1$, $\Delta I = 0.5$, $\alpha = 1$, $\gamma = 1$, $c_1 = c_2 = 1$, $g_1 = g_2 = 1$, $b_1 = b_2 = 1$.

Appendix B

Asymptotic analysis of simplified model

Here we provide proofs to the Theorems 6 and 7 presented in Chapter 3.

B.1 Proof of Theorem 6: Evolutionary dynamics with constant oxygen supply

Proof. Using the fact that, as established by Proposition 1, the population density function $n_i(x,t)$ is of the Gaussian form (2.13), we divide the proof of Theorem 2 into five steps which build on the method of proof that we developed in Chapter 3.

Step 1: asymptotic behaviour of $S(t)$ for $t \to \infty$. Since $S(t)$ solves the Cauchy problem (3.9), we have that

$$\lim_{t\to\infty} S(t) = \overline{S}, \tag{B.1}$$

with $\overline{S}$ given by Equation (3.11). This implies that

$$\lim_{t\to\infty} g(S(t)) = \overline{g}, \quad \lim_{t\to\infty} \varphi(S(t)) = \overline{\varphi} \quad \text{and} \quad \lim_{t\to\infty} h(S(t)) = \overline{h} \tag{B.2}$$

with $\overline{g}$, $\overline{\varphi}$ and $\overline{h}$ given by Equation (3.11).

Step 2: asymptotic behaviour of $v_i(t)$, $\mu_i(t)$ and $F_i(S(t), v_i(t), \mu_i(t))$ for $t \to \infty$. The ODE $(2.22)_1$ for v_i gives

$$\frac{\mathrm{d}}{\mathrm{d}t}\left(v_i(t) - \sqrt{\frac{\overline{h}}{\beta_i}}\right)^2 = 4\beta_i \left(v_i(t) - \sqrt{\frac{\overline{h}}{\beta_i}}\right)\left(\sqrt{\frac{h(t)}{\beta_i}} - v_i(t)^2\right).$$

Estimating from above the right-hand side of the latter ODE, using the fact that $0 < v_i(t) < \infty$ for all $t \geq 0$, $0 < h(S) < \infty$ for all $S \geq 0$ and $h(S(t)) \to \overline{h}$ as $t \to \infty$, one can easily

show that

$$\lim_{t\to\infty}\left(v_i(t)-\sqrt{\frac{\overline{h}}{\beta_i}}\right)^2=0 \quad\Longrightarrow\quad \lim_{t\to\infty} v_i(t)=\sqrt{\frac{\overline{h}}{\beta_i}}. \tag{B.3}$$

Moreover, the ODE $(2.22)_2$ for μ_i gives

$$\frac{\mathrm{d}}{\mathrm{d}t}\left(\mu_i(t)-\overline{\varphi}\right)^2=\frac{4h(t)}{v_i(t)}\left(\mu_i(t)-\overline{\varphi}\right)\left(\varphi(t)-\mu_i(t)\right).$$

Estimating from above the right-hand side of the latter ODE, using the fact that $0<v_i(t)<\infty$ for all $t\geq 0$, $0<h(S)<\infty$ for all $S\geq 0$ and $\varphi(S(t))\to\overline{\varphi}$ as $t\to\infty$, one can easily show that

$$\lim_{t\to\infty}\left(\mu_i(t)-\overline{\varphi}\right)^2=0 \quad\Longrightarrow\quad \lim_{t\to\infty}\mu_i(t)=\overline{\varphi}. \tag{B.4}$$

Lastly, the asymptotic results (B.2)–(B.4) ensure that the the following asymptotic result holds for the function F_i defined according to Equation (2.23)

$$\lim_{t\to\infty} F_i(S(t),v_i(t),\mu_i(t))=\gamma\,\overline{g}-\sqrt{\overline{h}\,\beta_i}. \tag{B.5}$$

Step 3: non-negativity and boundedness of $\rho_i(t)$. Solving the ODE $(2.22)_3$ for ρ_i and imposing the initial condition $(2.22)_4$ yields

$$\rho_i(t)=\rho_i^0\exp\left[\int_0^t\left(F_i(S(z),v_i(z),\mu_i(z))-d\rho(z)\right)\mathrm{d}z\right]. \tag{B.6}$$

This result, along with the positivity of ρ_i^0, implies that

$$\rho_i(t)\geq 0 \quad \text{for all } t\geq 0. \tag{B.7}$$

Moreover, substituting Equation (2.23) into the ODE $(2.22)_3$ for ρ_i yields

$$\frac{\mathrm{d}\rho_i}{\mathrm{d}t}=\left[\gamma\,g(S)-\frac{h(S)}{v_i}-h(S)\left(\mu_i-\varphi(S)\right)^2\right]\rho_i-d\left(\rho_i+\rho_j\right)\rho_i,$$

with $j=L$ if $i=H$ and $j=H$ if $i=L$. Using the non-negativity of $\rho_j(t)$, the positivity of $h(t)$ and $v_i(t)$, and the fact that under assumption (3.6) the following estimate holds

$$g(S)=\frac{1}{1+S}\left(S+\frac{\zeta}{\gamma}\frac{\zeta}{\zeta+\gamma S}\right)<2,$$

we estimate from above the right-hand side of the latter ODE for ρ_i and obtain

$$\frac{\mathrm{d}\rho_i}{\mathrm{d}t}\leq\left(2\gamma-d\,\rho_i\right)\rho_i,$$

which gives the uniform upper bound

$$\rho_i(t)\leq\max\left\{\rho_i^0,\frac{2\,\gamma}{d}\right\} \quad \text{for all } t\geq 0. \tag{B.8}$$

Step 4: proof of claim (3.12)**.** Combining the asymptotic result (B.5) with the expression (B.6) for ρ_i we find that

$$\rho_i(t) \sim C\rho_i^0 \exp\left[\left(\gamma\overline{g} - \sqrt{\overline{h}\,\beta_i}\right)t - d\int_0^t \rho(s)\,\mathrm{d}s\right] \quad \text{as} \;\; t \to \infty, \tag{B.9}$$

for some positive constant C. Since the function $\rho(t)$ is non-negative [*cf.* the uniform lower bound (B.7)], the asymptotic relation (B.9) ensures that

$$\text{if} \quad \sqrt{\overline{h}\,\beta_i} \geq \gamma\,\overline{g} \quad \text{then} \quad \lim_{t\to\infty} \rho_i(t) = 0. \tag{B.10}$$

Under assumption (2.4) and the additional assumption (2.26), claim (2.27) follows from the asymptotic result (B.10).

Step 5: proof of claims (2.29) **and** (2.30)**.** As long as $\rho_H(t) > 0$, we can compute the quotient of $\rho_L(t)$ and $\rho_H(t)$ using Equation (B.6). In so doing we find

$$\frac{\rho_L(t)}{\rho_H(t)} = \frac{\rho_L^0}{\rho_H^0} \exp\left[\int_0^t \left(F_L(S(z), v_L(z), \mu_L(z)) - F_H(S(z), v_H(z), \mu_H(z))\right)\mathrm{d}z\right]. \tag{B.11}$$

Using the limit (B.5) for F_i, we then have

$$\frac{\rho_L(t)}{\rho_H(t)} \sim C\exp\left[\sqrt{\overline{h}}\left(\sqrt{\beta_H} - \sqrt{\beta_L}\right)t\right] \quad \text{as} \;\; t \to \infty, \tag{B.12}$$

for some positive constant C. Under assumption (2.4), the asymptotic relation (B.12) gives

$$\lim_{t\to\infty} \frac{\rho_L(t)}{\rho_H(t)} = \infty$$

and, since ρ_L is uniformly bounded from above [*cf.* the uniform upper bound (B.8)], we conclude that

$$\lim_{t\to\infty} \rho_H(t) = 0. \tag{B.13}$$

We can rewrite the ODE $(2.22)_3$ for ρ_L as

$$\frac{\mathrm{d}\rho_L}{\mathrm{d}t} = \left[\left(\gamma\overline{g} - \sqrt{\overline{h}\,\beta_L} + \eta(t)\right) - d\rho_L\right]\rho_L(t), \tag{B.14}$$

where the function $\eta(t)$ is defined as

$$\eta(t) = \gamma\left(g(S) - \overline{g}\right) + \left(\sqrt{\overline{h}\,\beta_L} - \frac{h(S)}{v_i(t)}\right) - h(S)\left(\mu_L(t) - \overline{\varphi}\right)^2 - d\rho_H(t).$$

Using the asymptotic results (B.2)–(B.4) and (B.13), we see that

$$\eta(t) \longrightarrow 0 \quad \text{as} \quad t \to \infty.$$

Solving the ODE (B.14) subject to the initial condition $\rho_L(0) = \rho_L^0$ yields [190]

$$\rho_L(t) = \frac{\rho_L^0 \exp\left[\int_0^t \left(\gamma\overline{g} - \sqrt{\overline{h}\,\beta_L} + \eta(\tau)\right) \mathrm{d}\tau\right]}{1 + d\,\rho_L^0 \int_0^t \exp\left[\int_0^\tau \left(\gamma\overline{g} - \sqrt{\overline{h}\,\beta_L} + \eta(z)\right) \mathrm{d}z\right] \mathrm{d}\tau}. \tag{B.15}$$

Since $\eta(t) \to 0$ as $t \to \infty$, in the asymptotic regime $t \to \infty$ we have

$$\exp\left[\int_0^t \left(\gamma\overline{g} - \sqrt{\overline{h}\,\beta_L} + \eta(\tau)\right) \mathrm{d}\tau\right] \sim C \exp\left[\left(\gamma\overline{g} - \sqrt{\overline{h}\,\beta_L}\right) t\right]$$

and, under the additional assumption (2.28), we also have

$$\int_0^t \exp\left[\int_0^\tau \left(\gamma\overline{g} - \sqrt{\overline{h}\,\beta_L} + \eta(z)\right) \mathrm{d}z\right] \mathrm{d}\tau \sim C\, \frac{\exp\left[\left(\gamma\overline{g} - \sqrt{\overline{h}\,\beta_L}\right) t\right]}{\gamma\overline{g} - \sqrt{\overline{h}\,\beta_L}},$$

for some positive constant C. These asymptotic relations, along with the expression (B.15) for ρ_L, allow us to conclude that

$$\lim_{t\to\infty} \rho_L(t) = \frac{\gamma\overline{g} - \sqrt{\overline{h}\,\beta_L}}{d}. \tag{B.16}$$

Claims (3.13) follow from the asymptotic results (B.13) and (B.16), and the asymptotic results (B.4) and (B.3) with $i = L$, respectively. □ □

B.2 Proof of Theorem 7: Evolutionary dynamics with periodically fluctuating oxygen supply

Proof. Using the fact that, as established by Proposition 1, the population density function $n_i(x,t)$ is of the Gaussian form (2.13), we divide the proof of Theorem 2 into five steps which build up on the method of proof that we developed in [190, 182] and Chapter 2.

Step 1: asymptotic behaviour of $S(t)$ for $t \to \infty$. Massera's Convergence Theorem [199, 200] ensures that, under assumptions (3.29), the solution $S(t)$ of the Cauchy problem (3.9) is such that

$$S(t) \to \hat{S}(t) \quad \text{as } t \to \infty. \tag{B.17}$$

This implies that

$$\lim_{t\to\infty} g(S(t)) = \hat{g}(t), \quad \lim_{t\to\infty} \varphi(S(t)) = \hat{\varphi}(t) \tag{B.18}$$

and

$$\lim_{t\to\infty} h(S(t)) = \hat{h}(t), \tag{B.19}$$

where $\hat{g}$, $\hat{h}$ and $\hat{\varphi}$ are Lipschitz continuous and T-periodic functions of t.

Step 2: asymptotic behaviour of $v_i(t)$, $\mu_i(t)$ and $F_i(S(t), v_i(t), \mu_i(t))$ for $t \to \infty$. Using the asymptotic result (B.19), from the ODE $(2.22)_1$ for $v_i(t)$ we deduce that $v_i(t) \to \tilde{v}_i(t)$ as $t \to \infty$ where $\tilde{v}_i(t)$ solves the ODE

$$\frac{\mathrm{d}\tilde{v}_i}{\mathrm{d}t} = 2\left(\hat{h}(t) - \beta_i \tilde{v}_i^2\right) \tag{B.20}$$

subject to the initial condition $\tilde{v}_i(0) \in \mathbb{R}_{>0}$. Massera's Convergence Theorem [199, 200] ensures that $\tilde{v}_i(t) \to \hat{v}_i(t)$ as $t \to \infty$, where $\hat{v}_i(t)$ is the unique T-periodic solution of the ODE (B.20) subject to the initial condition $\hat{v}_i(0) \in \mathbb{R}_{>0}$. Hence,

$$v_i(t) \to \hat{v}_i(t) \quad \text{as } t \to \infty. \tag{B.21}$$

Moreover, using the asymptotic results (B.18), (B.19) and (B.21), from the ODE $(2.22)_2$ for $\mu_i(t)$ we deduce that $\mu_i(t) \to \tilde{\mu}_i(t)$ as $t \to \infty$ where $\tilde{\mu}_i(t)$ solves the ODE

$$\frac{\mathrm{d}\tilde{\mu}_i}{\mathrm{d}t} = \frac{2\hat{h}(t)}{\hat{v}_i(t)}\left(\hat{\varphi}(t) - \tilde{\mu}_i\right) \tag{B.22}$$

subject to the initial condition $\tilde{\mu}_i(0) \in \mathbb{R}$. Massera's Convergence Theorem [199, 200] ensures that $\tilde{\mu}_i(t) \to \hat{\mu}_i(t)$ as $t \to \infty$, where $\hat{\mu}_i(t)$ is the unique T-periodic solution of the ODE (B.22) subject to the initial condition $\hat{\mu}_i(0) \in \mathbb{R}$. Hence,

$$\mu_i(t) \to \hat{\mu}_i(t) \quad \text{as } t \to \infty. \tag{B.23}$$

Lastly, the asymptotic results (B.18), (B.19), (B.21) and (B.23) ensure that the the following asymptotic result holds for the function F_i defined according to Equation (2.23)

$$\lim_{t\to\infty} F_i(S(t), v_i(t), \mu_i(t)) = \gamma\,\hat{g}(t) - \frac{\hat{h}(t)}{\hat{v}_i} - \hat{h}\left(\hat{\mu}_i - \hat{\varphi}(t)\right)^2. \tag{B.24}$$

Step 2: non-negativity and boundedness of $\rho_i(t)$. Proceeding in a similar way as in the proof of Theorem 2 (*cf.* Step 2 in the proof of Theorem 2), one can prove that

$$0 \leq \rho_i(t) \leq \max\left\{\rho_i^0, \frac{2\,\gamma}{d}\right\} \quad \text{for all } t \geq 0. \tag{B.25}$$

Step 3: proof of claim (3.21)**.** Solving the ODE $(2.22)_3$ for ρ_i and imposing the initial condition $(2.22)_4$ yields

$$\rho_i(t) = \rho_i^0 \exp\left[\int_0^t \left(F_i(S(z), v_i(z), \mu_i(z)) - d\rho(z)\right)\mathrm{d}z\right]. \tag{B.26}$$

Combining Equations (B.24) with (B.26) gives

$$\begin{aligned}\rho_i(t) \quad \sim \quad C\,\rho_i^0 \exp\Bigg[&\gamma\int_0^t \hat{g}(z)\,\mathrm{d}z - \int_0^t \frac{\hat{h}(z)}{\hat{v}_i(z)}\,\mathrm{d}z - \int_0^t \left(\hat{\mu}_i(z) - \hat{\varphi}(z)\right)^2 \hat{h}(z)\,\mathrm{d}z \\ &-d\int_0^t \rho(z)\,\mathrm{d}z\Bigg] \quad \text{as } t \to \infty,\end{aligned} \tag{B.27}$$

for some positive constant C. Hence using the fact that the functions $\hat{g}(t)$, $\hat{\varphi}(t)$, $\hat{h}_i(t)$, $\hat{v}_i(t)$ and $\hat{\mu}_i(t)$ are T-periodic and considering $\mathrm{m} \to \infty$ we find

$$\rho_i(t) \sim C \exp\left[\gamma\,\mathrm{m}\int_0^T \hat{g}(z)\,\mathrm{d}z - \mathrm{m}\int_0^T \frac{\hat{h}(z)}{\hat{v}_i(z)}\,\mathrm{d}z - \mathrm{m}\int_0^T (\hat{\mu}_i(z)-\hat{\varphi}(z))^2\,\hat{h}(z)\,\mathrm{d}z - d\int_0^t \rho(z)\,\mathrm{d}z\right] \quad \text{as } t\to\infty, \tag{B.28}$$

for some positive constant C. Since the function $\rho(t)$ is non-negative [*cf.* the uniform lower bound (B.25)], the asymptotic relation (B.28) ensures that if

$$\int_0^T \frac{\hat{h}(z)}{\hat{v}_i(z)}\,\mathrm{d}z + \int_0^T (\hat{\mu}_i(z)-\hat{\varphi}(z))^2\,\hat{h}(z)\,\mathrm{d}z > \gamma\int_0^T \hat{g}(z)\,\mathrm{d}z$$

then

$$\lim_{t\to\infty} \rho_i(t) = 0. \tag{B.29}$$

This proves that if assumption (3.21) is satisfied then claim (3.22) is verified.

Step 4: proof of claims (3.23), (3.24) and (3.25). Let $j = L$ if $i = H$, and $j = H$ if $i = L$. As long as $\rho_j(t) > 0$, we can compute the quotient of $\rho_i(t)$ and $\rho_j(t)$ through Equation (B.26). In so doing, and using the asymptotic relation (B.27) for $\rho_i(t)$ and $\rho_j(t)$, we find that

$$\frac{\rho_i(t)}{\rho_j(t)} \sim C\exp\left[\mathrm{m}\,T\left(\Lambda_j - \Lambda_i\right)\right] \quad \text{as } t\to\infty, \tag{B.30}$$

for some positive constant C, with $\mathrm{m}\to\infty$ and Λ_i and Λ_j being defined according to (2.55). Choosing

$$j = \arg\max_{k\in\{H,L\}} \Lambda_k \quad \text{and} \quad i = \arg\min_{k\in\{H,L\}} \Lambda_k, \tag{B.31}$$

the asymptotic relation (B.30) allows us to conclude that

$$\lim_{t\to\infty} \frac{\rho_i(t)}{\rho_j(t)} = \infty, \quad \text{for } j = \arg\max_{k\in\{H,L\}} \Lambda_k \text{ and } i = \arg\min_{k\in\{H,L\}} \Lambda_k. \tag{B.32}$$

Since ρ_i is uniformly bounded from above [*cf.* the uniform upper bound (B.25)], the asymptotic result (B.32) implies that

$$\lim_{t\to\infty} \rho_j(t) = 0 \quad \text{for } j = \arg\max_{k\in\{H,L\}} \Lambda_k. \tag{B.33}$$

Therefore, if $\Lambda_H > \Lambda_L$, then

$$\arg\max_{k\in\{H,L\}} \Lambda_k = H \quad \text{and} \quad \arg\min_{k\in\{H,L\}} \Lambda_k = L,$$

and the asymptotic result (B.33) gives

$$\lim_{t\to\infty} \rho_H(t) = 0.$$

Similarly, if $\Lambda_H < \Lambda_L$, then

$$\arg\max_{k\in\{H,L\}} \Lambda_k = L \quad \text{and} \quad \arg\min_{k\in\{H,L\}} \Lambda_k = H,$$

and the asymptotic result (B.33) gives

$$\lim_{t\to\infty} \rho_L(t) = 0.$$

We can rewrite the ODE $(2.22)_3$ for ρ_i with $i = \arg\min_{k\in\{H,L\}} \Lambda_k$ as

$$\frac{\mathrm{d}\rho_i}{\mathrm{d}t} = \left[\gamma\hat{g}(t) - \frac{\hat{h}(t)}{\hat{v}_i(t)} - \hat{h}(t)\left(\hat{\mu}_i(t) - \hat{\varphi}(t)\right)^2 + \eta(t) - d\rho_i\right]\rho_i, \tag{B.34}$$

where the function $\eta(t)$ is defined as

$$\begin{aligned}\eta(t) = \gamma\big[\hat{g}(t) - g(S(t))\big] &+ \left(\frac{\hat{h}(t)}{\hat{v}_i(t)} - \frac{h(S(t))}{v_i(t)}\right) \\ &+ \Big[\hat{h}(t)\left(\hat{\mu}_i(t) - \hat{\varphi}(t)\right)^2 - h(t)\left(\mu_i(t) - \varphi(S(t))\right)^2\Big] - d\rho_j(t),\end{aligned}$$

with $j = \arg\max_{k\in\{H,L\}} \Lambda_k$. Using the asymptotic results (B.18), (B.19), (B.21), (B.23) and (B.33) we see that $\eta(t) \longrightarrow 0$ as $t \to \infty$. Hence $\rho_i(t) \to \tilde{\rho}_i(t)$ as $t \to \infty$, with $\tilde{\rho}_i(t)$ being the solution of the ODE

$$\frac{\mathrm{d}i\tilde{\rho}_i}{\mathrm{d}t} = \left[\gamma\hat{g}(t) - \frac{\hat{h}(t)}{\hat{v}_i} - \hat{h}(t)\left(\hat{\mu}_i - \hat{\varphi}(t)\right)^2 + \eta(t) - d\tilde{\rho}_i\right]\tilde{\rho}_i, \tag{B.35}$$

subject to the initial condition $\tilde{\rho}_i(0) \in \mathbb{R}_{>0}$. Massera's Convergence Theorem [199, 200] ensures that $\tilde{\rho}_i(t) \to \hat{\rho}_i(t)$ as $t \to \infty$, where $\hat{\rho}_i(t)$ is the unique T-periodic solution of the ODE (B.35) subject to the initial condition $\hat{\rho}_i(0) \in \mathbb{R}_{>0}$. Hence,

$$\tilde{\rho}_i(t) \longrightarrow \hat{\rho}_i(t) \quad \text{as } t \to \infty. \tag{B.36}$$

Claims (3.23), (3.24) and (3.25), follow from the asymptotic results (B.33) and (B.36), the asymptotic result (B.23) and the result (B.21) with $i = \arg\min_{k\in\{H,L\}} \Lambda_k$, respectively.

□

Bibliography

[1] Kritika Saxena and Mohit Kumar Jolly. Acute vs. chronic vs. cyclic hypoxia: their differential dynamics, molecular mechanisms, and effects on tumor progression. *Biomolecules*, 9(8):339, 2019.

[2] Freddie Bray, Jacques Ferlay, Isabelle Soerjomataram, Rebecca L Siegel, Lindsey A Torre, and Ahmedin Jemal. Global cancer statistics 2018: Globocan estimates of incidence and mortality worldwide for 36 cancers in 185 countries. *CA: A Cancer Journal for Clinicians*, 68(6):394–424, 2018.

[3] Mel Greaves and Carlo C Maley. Clonal evolution in cancer. *Nature*, 481(7381):306–313, 2012.

[4] Mikala Egeblad, Elizabeth S Nakasone, and Zena Werb. Tumors as organs: complex tissues that interface with the entire organism. *Developmental Cell*, 18(6):884–901, 2010.

[5] Philippe L Bedard, Aaron R Hansen, Mark J Ratain, and Lillian L Siu. Tumour heterogeneity in the clinic. *Nature*, 501(7467):355–364, 2013.

[6] Andriy Marusyk, Vanessa Almendro, and Kornelia Polyak. Intra-tumour heterogeneity: a looking glass for cancer? *Nature Reviews Cancer*, 12(5):323–334, 2012.

[7] Robert J Gillies, Joel S Brown, Alexander RA Anderson, and Robert A Gatenby. Eco-evolutionary causes and consequences of temporal changes in intratumoural blood flow. *Nature Reviews Cancer*, 18(9):576–585, 2018.

[8] Werner Risau. Mechanisms of angiogenesis. *Nature*, 386(6626):671–674, 1997.

[9] Haymo Kurz, Peter H Burri, and Valentin G Djonov. Angiogenesis and vascular remodeling by intussusception: from form to function. *Physiology*, 18(2):65–70, 2003.

[10] Gabriele Bergers and Laura E Benjamin. Tumorigenesis and the angiogenic switch. *Nature Reviews Cancer*, 3(6):401–410, 2003.

[11] Peter Carmeliet and Rakesh K Jain. Angiogenesis in cancer and other diseases. *Nature*, 407(6801):249–257, 2000.

[12] Peter Carmeliet and Rakesh K Jain. Molecular mechanisms and clinical applications of angiogenesis. *Nature*, 473(7347):298–307, 2011.

[13] Yong S Chang, Emmanuelle di Tomaso, Donald M McDonald, Rosemary Jones, Rakesh K Jain, and Lance L Munn. Mosaic blood vessels in tumors: frequency of cancer cells in contact with flowing blood. *Proceedings of the National Academy of Sciences*, 97(26).

[14] Domenico Ribatti, Beatrice Nico, Enrico Crivellato, and Angelo Vacca. The structure of the vascular network of tumors. *Cancer Letters*, 248(1):18–23, 2007.

[15] Vincent Pautu, Adélie Mellinger, Pauline Resnier, Elise Lepeltier, Ludovic Martin, Lise Boussemart, Franck Letournel, Catherine Passirani, and Nicolas Clere. Melanoma tumour vasculature heterogeneity: From mice models to human. *Journal of Cancer Research and Clinical Oncology*, 145(3):589–597, 2019.

[16] Rakesh K Jain and Triantafyllos Stylianopoulos. Delivering nanomedicine to solid tumors. *Nature Reviews Clinical Oncology*, 7(11):653, 2010.

[17] Janice Nagy, Shou H Chang, Ann M Dvorak, and Harold F Dvorak. Why are tumour blood vessels abnormal and why is it important to know? *British Journal of Cancer*, 100(6):865–869, 2009.

[18] Timothy P Padera, Brian R Stoll, Jessica B Tooredman, Diane Capen, Emmanuelle di Tomaso, and Rakesh K Jain. Cancer cells compress intratumour vessels. *Nature*, 427(6976):695–695, 2004.

[19] Joseph J Casciari, Stratis V Sotirchos, and Robert M Sutherland. Variations in tumor cell growth rates and metabolism with oxygen concentration, glucose concentration, and extracellular ph. *Journal of Cellular Physiology*, 151(2):386–394, 1992.

[20] Weibo Luo and Yingfei Wang. Hypoxia mediates tumor malignancy and therapy resistance. In Daniele M. Gilkes, editor, *Hypoxia and Cancer Metastasis*, chapter 1, pages 1–18. Springer, 2019.

[21] Raymond H Thomlinson and Louis H Gray. The histological structure of some human lung cancers and the possible implications for radiotherapy. *British Journal of Cancer*, 9(4):539, 1955.

[22] Mark W Dewhirst. Relationships between cycling hypoxia, hif-1, angiogenesis and oxidative stress. *Radiation Research*, 172(6):653–665, 2009.

[23] Jennifer Lanzen, Rod D Braun, Bruce Klitzman, David Brizel, Timothy W Secomb, and Mark W Dewhirst. Direct demonstration of instabilities in oxygen concentrations within the extravascular compartment of an experimental tumor. *Cancer Research*, 66(4):2219–2223, 2006.

[24] Hiroyuki Kimura, Rod D Braun, Edgardo T Ong, Richard Hsu, Timothy W Secomb, Demetrios Papahadjopoulos, Keelung Hong, and Mark W Dewhirst. Fluctuations in red cell flux in tumor microvessels can lead to transient hypoxia and reoxygenation in tumor parenchyma. *Cancer Research*, 56(23):5522–5528, 1996.

[25] David J Chaplin and Sally A Hill. Temporal heterogeneity in microregional erythrocyte flux in experimental solid tumours. *British Journal of Cancer*, 71(6):1210–1213, 1995.

[26] Katharine H Pigott, Sally A Hill, David J Chaplin, and Michele I Saunders. Microregional fluctuations in perfusion within human tumours detected using laser doppler flowmetry. *Radiotherapy and Oncology*, 40(1):45–50, 1996.

[27] Mark W Dewhirst, Hiroyuki Kimura, SW Rehmus, Rod D Braun, Demetrios Papahadjopoulos, Keelung Hong, and Timothy W Secomb. Microvascular studies on the origins of perfusion-limited hypoxia. *The British Journal of Cancer. Supplement*, 27:S247, 1996.

[28] Shingo Matsumoto, Hironobu Yasui, James B Mitchell, and Murali C Krishna. Imaging cycling tumor hypoxia. *Cancer Research*, 70(24):10019–10023, 2010.

[29] Christine Baudelet, Réginald Ansiaux, Bénédicte F Jordan, Xavier Havaux, Benoit Macq, and Bernard Gallez. Physiological noise in murine solid tumours using t2*-weighted gradient-echo imaging: a marker of tumour acute hypoxia? *Physics in Medicine & Biology*, 49(15):3389, 2004.

[30] Avihai Ron, Xosé Luís Deán-Ben, Sven Gottschalk, and Daniel Razansky. Volumetric optoacoustic imaging unveils high-resolution patterns of acute and cyclic hypoxia in a murine model of breast cancer. *Cancer Research*, 79(18):4767–4775, 2019.

[31] Hironobu Yasui, Shingo Matsumoto, Nallathamby Devasahayam, Jeeva P Munasinghe, Rajani Choudhuri, Keita Saito, Sankaran Subramanian, James B Mitchell,

and Murali C Krishna. Low-field magnetic resonance imaging to visualize chronic and cycling hypoxia in tumor-bearing mice. *Cancer Research*, 70(16):6427–6436, 2010.

[32] Ashlyn G Rickard, Gregory M Palmer, and Mark W Dewhirst. Clinical and pre-clinical methods for quantifying tumor hypoxia. In Daniele M. Gilkes, editor, *Hypoxia and Cancer Metastasis*, chapter 2, pages 19–41. Springer, 2019.

[33] Gillian M Tozer, Simon M Ameer-Beg, Jennifer Baker, Paul R Barber, Sally A Hill, Richard J Hodgkiss, Rosalind Locke, Vivien E Prise, Ian Wilson, and Borivoj Vojnovic. Intravital imaging of tumour vascular networks using multi-photon fluorescence microscopy. *Advanced Drug Delivery Reviews*, 57(1):135–152, 2005.

[34] Carine Michiels, Céline Tellier, and Olivier Feron. Cycling hypoxia: A key feature of the tumor microenvironment. *Biochimica et Biophysica Acta (BBA)-Reviews on Cancer*, 1866(1):76–86, 2016.

[35] Mohit Kumar Jolly, Prakash Kulkarni, Keith Weninger, John Orban, and Herbert Levine. Phenotypic plasticity, bet-hedging, and androgen independence in prostate cancer: Role of non-genetic heterogeneity. *Frontiers in Oncology*, 8:50, 2018.

[36] Marco Gerlinger, Andrew J Rowan, Stuart Horswell, James Larkin, David Endesfelder, Eva Gronroos, Pierre Martinez, Nicholas Matthews, Aengus Stewart, Patrick Tarpey, et al. Intratumor heterogeneity and branched evolution revealed by multiregion sequencing. *New England Journal of Medicine*, 366:883–892, 2012.

[37] Gregg L Semenza. Hypoxia and cancer. *Cancer and Metastasis Reviews*, 26(2):223, 2007.

[38] Daniel Verduzco, Mark Lloyd, Liping Xu, Arig Ibrahim-Hashim, Yoganand Balagurunathan, Robert A Gatenby, and Robert J Gillies. Intermittent hypoxia selects for genotypes and phenotypes that increase survival, invasion, and therapy resistance. *PloS One*, 10(3):e0120958, 2015.

[39] Jon-Vidar Gaustad, Trude Golimo Simonsen, Ana Maria Acosta Roa, and Einar K Rofstad. Tumors exposed to acute cyclic hypoxia show increased vessel density and delayed blood supply. *Microvascular Research*, 85:10–15, 2013.

[40] Elizabeth Louie, Sara Nik, Juei-suei Chen, Marlies Schmidt, Bo Song, Christine Pacson, Xiu Fang Chen, Seonhye Park, Jingfang Ju, and Emily I Chen. Identification of a stem-like cell population by exposing metastatic breast cancer cell lines to repetitive cycles of hypoxia and reoxygenation. *Breast Cancer Research*, 12(6):1–14, 2010.

[41] Vasantha Kumar Bhaskara, Indra Mohanam, Jasti S Rao, and Sanjeeva Mohanam. Intermittent hypoxia regulates stem-like characteristics and differentiation of neuroblastoma cells. *PloS One*, 7(2):e30905, 2012.

[42] Céline Tellier, Déborah Desmet, Laurenne Petit, Laure Finet, Carlos Graux, Martine Raes, Olivier Feron, and Carine Michiels. Cycling hypoxia induces a specific amplified inflammatory phenotype in endothelial cells and enhances tumor-promoting inflammation in vivo. *Neoplasia*, 17(1):66–78, 2015.

[43] Victor Delprat, Céline Tellier, Catherine Demazy, Martine Raes, Olivier Feron, and Carine Michiels. Cycling hypoxia promotes a pro-inflammatory phenotype in macrophages via jnk/p65 signaling pathway. *Scientific Reports*, 10(1):1–13, 2020.

[44] Wei-Ling Chen, Chi-Chung Wang, Yu-Jung Lin, Chung-Pu Wu, and Chia-Hung Hsieh. Cycling hypoxia induces chemoresistance through the activation of reactive oxygen species-mediated b-cell lymphoma extra-long pathway in glioblastoma multiforme. *Journal of Translational Medicine*, 13(1):1–13, 2015.

[45] Rob A Cairns, Tuula Kalliomaki, and Richard P Hill. Acute (cyclic) hypoxia enhances spontaneous metastasis of kht murine tumors. *Cancer Research*, 61(24):8903–8908, 2001.

[46] Mahmoud Ali, Sandeep Kowkuntla, Derick J Delloro, Csaba Galambos, Deep Hathi, Siegfried Janz, Monica Shokeen, Chakrapani Tripathi, Hongwei Xu, Jisung Yuk, et al. Chronic intermittent hypoxia enhances disease progression in myeloma-resistant mice. *American Journal of Physiology-Regulatory, Integrative and Comparative Physiology*, 316(5):R678–R686, 2019.

[47] Anna Chen, Jaclyn Sceneay, Nathan Gödde, Tanja Kinwel, Sunyoung Ham, Erik W Thompson, Patrick O Humbert, and Andreas Möller. Intermittent hypoxia induces a metastatic phenotype in breast cancer. *Oncogene*, 37(31):4214–4225, 2018.

[48] Rakesh K Jain. Normalization of tumor vasculature: an emerging concept in antiangiogenic therapy. *Science*, 307(5706):58–62, 2005.

[49] Peter C Nowell. The clonal evolution of tumor cell populations. *Science*, 194(4260):23–28, 1976.

[50] Jessica J Cunningham, Joel S Brown, Thomas L Vincent, and Robert A Gatenby. Divergent and convergent evolution in metastases suggest treatment strategies based

on specific metastatic sites. *Evolution, Medicine, and Public Health*, 2015(1):76–87, 2015.

[51] Kenneth J Pienta, Emma U Hammarlund, Robert Axelrod, Sarah R Amend, and Joel S Brown. Convergent evolution, evolving evolvability, and the origins of lethal cancer. *Molecular Cancer Research*, 18(6):801–810, 2020.

[52] Douglas Hanahan and Robert A Weinberg. The hallmarks of cancer. *Cell*, 100(1):57–70, 2000.

[53] Douglas Hanahan and Robert A Weinberg. Hallmarks of cancer: the next generation. *Cell*, 144(5):646–674, 2011.

[54] Robert A Gatenby. Population ecology issues in tumor growth. *Cancer Research*, 51(10):2542–2547, 1991.

[55] Mark C Lloyd, Jessica J Cunningham, Marilyn M Bui, Robert J Gillies, Joel S Brown, and Robert A Gatenby. Darwinian dynamics of intratumoral heterogeneity: not solely random mutations but also variable environmental selection forces. *Cancer Research*, 76(11):3136–3144, 2016.

[56] Arig Ibrahim-Hashim, Mark Robertson-Tessi, Pedro M Enriquez-Navas, Mehdi Damaghi, Yoganand Balagurunathan, Jonathan W Wojtkowiak, Shonagh Russell, Kam Yoonseok, Mark C Lloyd, Marilyn M Bui, et al. Defining cancer subpopulations by adaptive strategies rather than molecular properties provides novel insights into intratumoral evolution. *Cancer Research*, 77(9):2242–2254, 2017.

[57] Robert A Gatenby, Edward T Gawlinski, Arthur F Gmitro, Brant Kaylor, and Robert J Gillies. Acid-mediated tumor invasion: a multidisciplinary study. *Cancer Research*, 66(10):5216–5223, 2006.

[58] Mark Robertson-Tessi, Robert J Gillies, Robert A Gatenby, and Alexander RA Anderson. Impact of metabolic heterogeneity on tumor growth, invasion, and treatment outcomes. *Cancer Research*, 75(8):1567–1579, 2015.

[59] Gregory P Brown, Cathy Shilton, Benjamin L Phillips, and Richard Shine. Invasion, stress, and spinal arthritis in cane toads. *Proceedings of the National Academy of Sciences*, 104(45):17698–17700, 2007.

[60] Khalid O Alfarouk, Muntaser E Ibrahim, Robert A Gatenby, and Joel S Brown. Riparian ecosystems in human cancers. *Evolutionary Applications*, 6(1):46–53, 2013.

[61] H Allen Orr. Fitness and its role in evolutionary genetics. *Nature Reviews Genetics*, 10(8):531–539, 2009.

[62] Marjolein E Lof, Thomas E Reed, John M McNamara, and Marcel E Visser. Timing in a fluctuating environment: environmental variability and asymmetric fitness curves can lead to adaptively mismatched avian reproduction. *Proceedings of the Royal Society B: Biological Sciences*, 279(1741):3161–3169, 2012.

[63] Daniel C Laughlin and Julie Messier. Fitness of multidimensional phenotypes in dynamic adaptive landscapes. *Trends in Ecology & Evolution*, 30(8):487–496, 2015.

[64] Russell Lande. Adaptation to an extraordinary environment by evolution of phenotypic plasticity and genetic assimilation. *Journal of Evolutionary Biology*, 22(7):1435–1446, 2009.

[65] Edo Kussell and Stanislas Leibler. Phenotypic diversity, population growth, and information in fluctuating environments. *Science*, 309(5743):2075–2078, 2005.

[66] BingKan Xue and Stanislas Leibler. Benefits of phenotypic plasticity for population growth in varying environments. *Proceedings of the National Academy of Sciences*, 115(50):12745–12750, 2018.

[67] Thomas J DeWitt, Andrew Sih, and David Sloan Wilson. Costs and limits of phenotypic plasticity. *Trends in Ecology & Evolution*, 13(2):77–81, 1998.

[68] Andrew P Hendry. Key questions on the role of phenotypic plasticity in eco-evolutionary dynamics. *Journal of Heredity*, 107(1):25–41, 2016.

[69] Jaime Ashander, Luis-Miguel Chevin, and Marissa L Baskett. Predicting evolutionary rescue via evolving plasticity in stochastic environments. *Proceedings of the Royal Society B: Biological Sciences*, 283(1839):20161690, 2016.

[70] Sigurd Einum and Ian A Fleming. Environmental unpredictability and offspring size: conservative versus diversified bet-hedging. *Evolutionary Ecology Research*, 6(3):443–455, 2004.

[71] Sheng Pei Wang and David M Althoff. Phenotypic plasticity facilitates initial colonization of a novel environment. *Evolution*, 73(2):303–316, 2019.

[72] BingKan Xue, Pablo Sartori, and Stanislas Leibler. Environment-to-phenotype mapping and adaptation strategies in varying environments. *Proceedings of the National Academy of Sciences*, 116(28):13847–13855, 2019.

[73] Piyush B Gupta, Ievgenia Pastushenko, Adam Skibinski, Cedric Blanpain, and Charlotte Kuperwasser. Phenotypic plasticity: driver of cancer initiation, progression, and therapy resistance. *Cell Stem Cell*, 24(1):65–78, 2019.

[74] Isabella S Kim, Silja Heilmann, Emily R Kansler, Yan Zhang, Milena Zimmer, Kajan Ratnakumar, Robert L Bowman, Theresa Simon-Vermot, Myles Fennell, Ralph Garippa, et al. Microenvironment-derived factors driving metastatic plasticity in melanoma. *Nature Communications*, 8(1):1–11, 2017.

[75] Nikolas K Haass, Kimberley A Beaumont, David S Hill, Andrea Anfosso, Paulus Mrass, Marcia A Munoz, Ichiko Kinjyo, and Wolfgang Weninger. Real-time cell cycle imaging during melanoma growth, invasion, and drug response. *Pigment Cell & Melanoma Research*, 27(5):764–776, 2014.

[76] Farzana Ahmed and Nikolas K Haass. Microenvironment-driven dynamic heterogeneity and phenotypic plasticity as a mechanism of melanoma therapy resistance. *Frontiers in Oncology*, 8:173, 2018.

[77] Dan Cohen. Optimizing reproduction in a randomly varying environment. *Journal of Theoretical Biology*, 12(1):119–129, 1966.

[78] Montgomery Slatkin. Hedging one's evolutionary bets. *Nature*, 250(5469):704–705, 1974.

[79] Tom Philippi and Jon Seger. Hedging one's evolutionary bets, revisited. *Trends in Ecology & Evolution*, 4(2):41–44, 1989.

[80] Keith R Hopper. Risk-spreading and bet-hedging in insect population biology. *Annual Review of Entomology*, 44(1):535–560, 1999.

[81] Dylan Z Childs, CJE Metcalf, and Mark Rees. Evolutionary bet-hedging in the real world: empirical evidence and challenges revealed by plants. *Proceedings of the Royal Society B: Biological Sciences*, 277(1697):3055–3064, 2010.

[82] Curtis A Gravenmier, Miriam Siddique, and Robert A Gatenby. Adaptation to stochastic temporal variations in intratumoral blood flow: the warburg effect as a bet hedging strategy. *Bulletin of Mathematical Biology*, 80(5):954–970, 2018.

[83] Bernadett Gaál, Jonathan W Pitchford, and A Jamie Wood. Exact results for the evolution of stochastic switching in variable asymmetric environments. *Genetics*, 184(4):1113–1119, 2010.

[84] Chen Jia, Minping Qian, Yu Kang, and Daquan Jiang. Modeling stochastic phenotype switching and bet-hedging in bacteria: stochastic nonlinear dynamics and critical state identification. *Quantitative Biology*, 2(3):110–125, 2014.

[85] Karl Wienand, Erwin Frey, and Mauro Mobilia. Evolution of a fluctuating population in a randomly switching environment. *Physical Review Letters*, 119(15):158301, 2017.

[86] Peter G Hufton, Yen Ting Lin, and Tobias Galla. Phenotypic switching of populations of cells in a stochastic environment. *Journal of Statistical Mechanics: Theory and Experiment*, 2018(2):023501, 2018.

[87] Einar Bjarki Gunnarsson, Subhajyoti De, Kevin Leder, and Jasmine Foo. Understanding the role of phenotypic switching in cancer drug resistance. *Journal of Theoretical Biology*, 490:110162, 2020.

[88] Ami Taitelbaum, Robert West, Michael Assaf, and Mauro Mobilia. Population dynamics in a changing environment: Random versus periodic switching. *Physical Review Letters*, 125:048105, 2020.

[89] Johannes Müller, Burkhard A Hense, Thilo M Fuchs, Margarete Utz, and Christian Pötzsche. Bet-hedging in stochastically switching environments. *Journal of Theoretical Biology*, 336:144–157, 2013.

[90] Marcel Salathé, Jeremy Van Cleve, and Marcus W Feldman. Evolution of stochastic switching rates in asymmetric fitness landscapes. *Genetics*, 182(4):1159–1164, 2009.

[91] Paula Villa Martín, Miguel A Muñoz, and Simone Pigolotti. Bet-hedging strategies in expanding populations. *PLoS Computational Biology*, 15(4):e1006529, 2019.

[92] Wiep Klaas Smits, Oscar P Kuipers, and Jan-Willem Veening. Phenotypic variation in bacteria: the role of feedback regulation. *Nature Reviews Microbiology*, 4(4):259–271, 2006.

[93] Jan-Willem Veening, Wiep Klaas Smits, and Oscar P Kuipers. Bistability, epigenetics, and bet-hedging in bacteria. *Annual Reviews Microbiology*, 62:193–210, 2008.

[94] Murat Acar, Jerome T Mettetal, and Alexander Van Oudenaarden. Stochastic switching as a survival strategy in fluctuating environments. *Nature Genetics*, 40(4):471–475, 2008.

[95] Hubertus JE Beaumont, Jenna Gallie, Christian Kost, Gayle C Ferguson, and Paul B Rainey. Experimental evolution of bet hedging. *Nature*, 462(7269):90–93, 2009.

[96] Pintu Patra and Stefan Klumpp. Population dynamics of bacterial persistence. *PLoS One*, 8(5):e62814, 2013.

[97] Alexander P Browning, Jesse A Sharp, Tarunendu Mapder, Christopher M Baker, Kevin Burrage, and Matthew J Simpson. Persistence is an optimal hedging strategy for bacteria in volatile environments. *bioRxiv*, 2019.12.19.883645, 2019.

[98] Nathalie Q Balaban, Jack Merrin, Remy Chait, Lukasz Kowalik, and Stanislas Leibler. Bacterial persistence as a phenotypic switch. *Science*, 305(5690):1622–1625, 2004.

[99] Frank Schreiber, Sten Littmann, Gaute Lavik, Stéphane Escrig, Anders Meibom, Marcel MM Kuypers, and Martin Ackermann. Phenotypic heterogeneity driven by nutrient limitation promotes growth in fluctuating environments. *Nature Microbiology*, 1(6):16055, 2016.

[100] Daniel Nichol, Mark Robertson-Tessi, Peter Jeavons, and Alexander RA Anderson. Stochasticity in the genotype-phenotype map: implications for the robustness and persistence of bet-hedging. *Genetics*, 204(4):1523–1539, 2016.

[101] Takayasu Kurata, K Tamura, H Kaneda, T Nogami, H Uejima, G o Asai, K Nakagawa, and M Fukuoka. Effect of re-treatment with gefitinib ('iressa', zd1839) after acquisition of resistance. *Annals of Oncology*, 15(1):173–174, 2004.

[102] Sreenath V Sharma, Diana Y Lee, Bihua Li, Margaret P Quinlan, Fumiyuki Takahashi, Shyamala Maheswaran, Ultan McDermott, Nancy Azizian, Lee Zou, Michael A Fischbach, et al. A chromatin-mediated reversible drug-tolerant state in cancer cell subpopulations. *Cell*, 141(1):69–80, 2010.

[103] Natalya N Pavlova and Craig B Thompson. The emerging hallmarks of cancer metabolism. *Cell Metabolism*, 23(1):27–47, 2016.

[104] Nicholas C Denko. Hypoxia, hif1 and glucose metabolism in the solid tumour. *Nature Reviews Cancer*, 8(9):705–713, 2008.

[105] Matthew G Vander Heiden, Lewis C Cantley, and Craig B Thompson. Understanding the warburg effect: the metabolic requirements of cell proliferation. *Science*, 324(5930):1029–1033, 2009.

[106] Tamir Epstein, Liping Xu, Robert J Gillies, and Robert A Gatenby. Separation of metabolic supply and demand: aerobic glycolysis as a normal physiological response to fluctuating energetic demands in the membrane. *Cancer & Metabolism*, 2(1):1–9, 2014.

[107] Louis Pasteur. *Mémoire sur la fermentation alcoolique*. Mallet-Bachelier, 1860.

[108] Otto Warburg. The metabolism of carcinoma cells. *The Journal of Cancer Research*, 9(1):148–163, 1925.

[109] Ahmad Almuhaideb, Nikolaos Papathanasiou, and Jamshed Bomanji. 18f-fdg pet/ct imaging in oncology. *Annals of Saudi Medicine*, 31(1):3–13, 2011.

[110] Robert A Gatenby and Robert J Gillies. Why do cancers have high aerobic glycolysis? *Nature Reviews Cancer*, 4(11):891–899, 2004.

[111] Tamir Epstein, Robert A Gatenby, and Joel S Brown. The warburg effect as an adaptation of cancer cells to rapid fluctuations in energy demand. *PloS One*, 12(9):e0185085, 2017.

[112] Valentina Palacio-Castañeda, Lucas Kooijman, Bastien Venzac, Wouter PR Verdurmen, and Séverine Le Gac. Metabolic switching of tumor cells under hypoxic conditions in a tumor-on-a-chip model. *Micromachines*, 11(4):382, 2020.

[113] Marc U Baumann, Stacy Zamudio, and Nicholas P Illsley. Hypoxic upregulation of glucose transporters in bewo choriocarcinoma cells is mediated by hypoxia-inducible factor-1. *American Journal of Physiology – Cell Physiology*, 293(1):C477–C485, 2007.

[114] Katherine L Eales, Kate ER Hollinshead, and Daniel A Tennant. Hypoxia and metabolic adaptation of cancer cells. *Oncogenesis*, 5(1):e190–e190, 2016.

[115] Bryce Ordway, Pawel Swietach, Robert J Gillies, and Mehdi Damaghi. Causes and consequences of variable tumor cell metabolism on heritable modifications and tumor evolution. *Frontiers in Oncology*, 10:373, 2020.

[116] Niko Beerenwinkel, Tibor Antal, David Dingli, Arne Traulsen, Kenneth W Kinzler, Victor E Velculescu, Bert Vogelstein, and Martin A Nowak. Genetic progression and the waiting time to cancer. *PLoS Computational Biology*, 3(11):e225, 2007.

[117] Alexander RA Anderson and Philip K Maini. Mathematical oncology. *Bulletin of Mathematical Biology*, 80(5):945–953, 2018.

[118] Alexander RA Anderson and Vito Quaranta. Integrative mathematical oncology. *Nature Reviews Cancer*, 8(3):227–234, 2008.

[119] Joseph J Casciari, Stratis V Sotirchos, and Robert M Sutherland. Mathematical modelling of microenvironment and growth in emt6/ro multicellular tumour spheroids. *Cell Proliferation*, 25(1):1–22, 1992.

[120] John P Ward and JR King. Mathematical modelling of avascular-tumour growth. *Mathematical Medicine and Biology: A Journal of the IMA*, 14(1):39–69, 1997.

[121] John P Kirkpatrick, David M Brizel, and Mark W Dewhirst. A mathematical model of tumor oxygen and glucose mass transport and metabolism with complex reaction kinetics. *Radiation Research*, 159(3):336–344, 2003.

[122] Raja Venkatasubramanian, Michael A Henson, and Neil S Forbes. Incorporating energy metabolism into a growth model of multicellular tumor spheroids. *Journal of Theoretical Biology*, 242(2):440–453, 2006.

[123] Kieran Smallbone, Robert A Gatenby, and Philip K Maini. Mathematical modelling of tumour acidity. *Journal of Theoretical Biology*, 255(1):106–112, 2008.

[124] Aalpen A Patel, Edward T Gawlinski, Susan K Lemieux, and Robert A Gatenby. A cellular automaton model of early tumor growth and invasion: the effects of native tissue vascularity and increased anaerobic tumor metabolism. *Journal of Theoretical Biology*, 213(3):315–331, 2001.

[125] Milad Shamsi, Mohsen Saghafian, Morteza Dejam, and Amir Sanati-Nezhad. Mathematical modeling of the function of warburg effect in tumor microenvironment. *Scientific Reports*, 8(1):1–13, 2018.

[126] August Krogh. The number and distribution of capillaries in muscles with calculations of the oxygen pressure head necessary for supplying the tissue. *The Journal of Physiology*, 52(6):409, 1919.

[127] Alessandro Bertuzzi and Alberto Gandolfi. Cell kinetics in a tumour cord. *Journal of Theoretical Biology*, 204(4):587–599, 2000.

[128] Alessandro Bertuzzi, Antonio Fasano, Alberto Gandolfi, and Doriana Marangi. Cell kinetics in tumour cords studied by a model with variable cell cycle length. *Mathematical Biosciences*, 177:103–125, 2002.

[129] James V Moore, Philip S Hasleton, and C Hilary Buckley. Tumour cords in 52 human bronchial and cervical squamous cell carcinomas: inferences for their cellular kinetics and radiobiology. *British Journal of Cancer*, 51(3):407–413, 1985.

[130] Sergey Astanin and Andrea Tosin. Mathematical model of tumour cord growth along the source of nutrient. *Mathematical Modelling of Natural Phenomena*, 2(3):153–177, 2007.

[131] Sergey Astanin and Luigi Preziosi. Mathematical modelling of the warburg effect in tumour cords. *Journal of Theoretical Biology*, 258(4):578–590, 2009.

[132] Alessandro Bertuzzi, Antonio Fasano, Alberto Gandolfi, and Carmela Sinisgalli. Atp production and necrosis formation in a tumour spheroid model. *Mathematical Modelling of Natural Phenomena*, 2(3):30–46, 2007.

[133] Philip Gerlee and Alexander RA Anderson. A hybrid cellular automaton model of clonal evolution in cancer: the emergence of the glycolytic phenotype. *Journal of Theoretical Biology*, 250(4):705–722, 2008.

[134] James D Murray. *Mathematical biology: I. An introduction. Interdisciplinary Applied Mathematics*. Springer, 2002.

[135] Jim M Cushing. Two species competition in a periodic environment. *Journal of Mathematical Biology*, 10(4):385–400, 1980.

[136] Piero De Mottoni and Andrea Schiaffino. Competition systems with periodic coefficients: a geometric approach. *Journal of Mathematical Biology*, 11(3):319–335, 1981.

[137] Jim M Cushing. Oscillatory population growth in periodic environments. *Theoretical Population Biology*, 30(3):289–308, 1986.

[138] Arthur L Koch. Coexistence resulting from an alternation of density dependent and density independent growth. *Journal of Theoretical Biology*, 44(2):373–386, 1974.

[139] Jim M Cushing. Periodic time-dependent predator-prey systems. *SIAM Journal on Applied Mathematics*, 32(1):82–95, 1977.

[140] Toshiyuki Namba. Competitive co-existence in a seasonally fluctuating environment. *Journal of Theoretical Biology*, 111(2):369–386, 1984.

[141] Robert M May and Robert H Mac Arthur. Niche overlap as a function of environmental variability. *Proceedings of the National Academy of Sciences*, 69(5):1109–1113, 1972.

[142] G Evelyn Hutchinson. The paradox of the plankton. *The American Naturalist*, 95(882):137–145, 1961.

[143] Peter Abrams. Variability in resource consumption rates and the coexistence of competing species. *Theoretical Population Biology*, 25(1):106–124, 1984.

[144] Tania LS Vincent, David Scheel, Joel S Brown, and Thomas L Vincent. Trade-offs and coexistence in consumer-resource models: it all depends on what and where you eat. *The American Naturalist*, 148(6):1038–1058, 1996.

[145] David Tilman. Resources: a graphical-mechanistic approach to competition and predation. *The American Naturalist*, 116(3):362–393, 1980.

[146] James P Grover. Resource competition in a variable environment: phytoplankton growing according to the variable-internal-stores model. *The American Naturalist*, 138(4):811–835, 1991.

[147] Peter A Abrams. The prerequisites for and likelihood of generalist-specialist coexistence. *The American Naturalist*, 167(3):329–342, 2006.

[148] William G Wilson and Peter A Abrams. Coexistence of cycling and dispersing consumer species: Armstrong and mcgehee in space. *The American Naturalist*, 165(2):193–205, 2005.

[149] David S Wilson and Jin Yoshimura. On the coexistence of specialists and generalists. *The American Naturalist*, 144(4):692–707, 1994.

[150] Shenshen Wang and Lei Dai. Evolving generalists in switching rugged landscapes. *PLoS Computational Biology*, 15(10):e1007320, 2019.

[151] Vedant Sachdeva, Kabir Husain, Jiming Sheng, Shenshen Wang, and Arvind Murugan. Tuning environmental timescales to evolve and maintain generalists. *Proceedings of the National Academy of Sciences*, 117(23):12693–12699, 2020.

[152] Benoît Perthame. *Transport equations in biology*. Springer Science & Business Media, 2006.

[153] Jean Clairambault and Camille Pouchol. A survey of adaptive cell population dynamics models of emergence of drug resistance in cancer, and open questions about evolution and cancer. *Biomath*, 8(1):23, 2019.

[154] Rebecca H Chisholm, Tommaso Lorenzi, and Jean Clairambault. Cell population heterogeneity and evolution towards drug resistance in cancer: biological and mathematical assessment, theoretical treatment optimisation. *Biochimica et Biophysica Acta (BBA)-General Subjects*, 1860(11):2627–2645, 2016.

[155] Jakub Otwinowski and Joshua B Plotkin. Inferring fitness landscapes by regression produces biased estimates of epistasis. *Proceedings of the National Academy of Sciences*, 111(22):E2301–E2309, 2014.

[156] Guillaume Martin, Santiago F Elena, and Thomas Lenormand. Distributions of epistasis in microbes fit predictions from a fitness landscape model. *Nature Genetics*, 39(4):555–560, 2007.

[157] Tommaso Lorenzi and Camille Pouchol. Asymptotic analysis of selection-mutation models in the presence of multiple fitness peaks. *Nonlinearity*, 33(11):5791–5816, 2020.

[158] Sílvia Cuadrado. Equilibria of a predator prey model of phenotype evolution. *Journal of Mathematical Analysis and Applications*, 354(1):286–294, 2009.

[159] Marcello Delitala and Tommaso Lorenzi. Asymptotic dynamics in continuous structured populations with mutations, competition and mutualism. *Journal of Mathematical Analysis and Applications*, 389(1):439–451, 2012.

[160] Xiaoqing He, King-Yeung Lam, Yuan Lou, and Wei-Ming Ni. Dynamics of a consumer–resource reaction–diffusion model. *Journal of Mathematical Biology*, 78(6):1605–1636, 2019.

[161] Matthieu Alfaro, Jérôme Coville, and Gaël Raoul. Travelling waves in a nonlocal reaction-diffusion equation as a model for a population structured by a space variable and a phenotypic trait. *Communications in Partial Differential Equations*, 38(12):2126–2154, 2013.

[162] Matthieu Alfaro, Henri Berestycki, and Gaël Raoul. The effect of climate shift on a species submitted to dispersion, evolution, growth, and nonlocal competition. *SIAM Journal on Mathematical Analysis*, 49(1):562–596, 2017.

[163] King-Yeung Lam and Yuan Lou. Evolution of conditional dispersal: evolutionarily stable strategies in spatial models. *Journal of Mathematical Biology*, 68(4):851–877, 2014.

[164] King-Yeung Lam. Stability of dirac concentrations in an integro-pde model for evolution of dispersal. *Calculus of Variations and Partial Differential Equations*, 56(3):79, 2017.

[165] King-Yeung Lam and Yuan Lou. An integro-pde model for evolution of random dispersal. *Journal of Functional Analysis*, 272(5):1755–1790, 2017.

[166] Emeric Bouin and Vincent Calvez. Travelling waves for the cane toads equation with bounded traits. *Nonlinearity*, 27(9):2233, 2014.

[167] Emeric Bouin, Vincent Calvez, Nicolas Meunier, Sepideh Mirrahimi, Benoît Perthame, Gaël Raoul, and Raphaël Voituriez. Invasion fronts with variable motility: phenotype selection, spatial sorting and wave acceleration. *Comptes Rendus Mathematique*, 350(15-16):761–766, 2012.

[168] Olga Turanova. On a model of a population with variable motility. *Mathematical Models and Methods in Applied Sciences*, 25(10):1961–2014, 2015.

[169] Alexander Lorz, Tommaso Lorenzi, Michael E Hochberg, Jean Clairambault, and Benoît Perthame. Populational adaptive evolution, chemotherapeutic resistance and multiple anti-cancer therapies. *ESAIM: Mathematical Modelling and Numerical Analysis*, 47(2):377–399, 2013.

[170] Alexander Lorz, Tommaso Lorenzi, Jean Clairambault, Alexandre Escargueil, and Benoît Perthame. Modeling the effects of space structure and combination therapies on phenotypic heterogeneity and drug resistance in solid tumors. *Bulletin of Mathematical Biology*, 77(1):1–22, 2015.

[171] Tommaso Lorenzi, Rebecca H Chisholm, and Jean Clairambault. Tracking the evolution of cancer cell populations through the mathematical lens of phenotype-structured equations. *Biology Direct*, 11(1):1–17, 2016.

[172] Rebecca H Chisholm, Tommaso Lorenzi, Alexander Lorz, Annette K Larsen, Luís Neves de Almeida, Alexandre Escargueil, and Jean Clairambault. Emergence of drug tolerance in cancer cell populations: an evolutionary outcome of selection, nongenetic instability, and stress-induced adaptation. *Cancer Research*, 75(6):930–939, 2015.

[173] Chiara Villa, Mark AJ Chaplain, and Tommaso Lorenzi. Evolutionary dynamics in vascularised tumours under chemotherapy: Mathematical modelling, asymptotic analysis and numerical simulations. *Vietnam Journal of Mathematics*, In press, 2020.

[174] Gabriel Dimitriu, Tommaso Lorenzi, and Răzvan Ştefănescu. Evolutionary dynamics of cancer cell populations under immune selection pressure and optimal control of chemotherapy. *Mathematical Modelling of Natural Phenomena*, 9(4):88–104, 2014.

[175] Luís Almeida, Patrizia Bagnerini, Giulia Fabrini, Barry D Hughes, and Tommaso Lorenzi. Evolution of cancer cell populations under cytotoxic therapy and treatment optimisation: insight from a phenotype-structured model. *ESAIM: Mathematical Modelling and Numerical Analysis*, 53(4):1157–1190, 2019.

[176] Camille Pouchol, Jean Clairambault, Alexander Lorz, and Emmanuel Trélat. Asymptotic analysis and optimal control of an integro-differential system modelling healthy and cancer cells exposed to chemotherapy. *Journal de Mathématiques Pures et Appliquées*, 116:268–308, 2018.

[177] J-E Busse, Piotr Gwiazda, and Anna Marciniak-Czochra. Mass concentration in a nonlocal model of clonal selection. *Journal of Mathematical Biology*, 73(4):1001–1033, 2016.

[178] Tommaso Lorenzi, Anna Marciniak-Czochra, and Thomas Stiehl. A structured population model of clonal selection in acute leukemias with multiple maturation stages. *Journal of Mathematical Biology*, 79(5):1587–1621, 2019.

[179] Tommaso Lorenzi, Chandrasekhar Venkataraman, Alexander Lorz, and Mark AJ Chaplain. The role of spatial variations of abiotic factors in mediating intratumour phenotypic heterogeneity. *Journal of Theoretical Biology*, 451:101–110, 2018.

[180] Chiara Villa, Mark AJ Chaplain, and Tommaso Lorenzi. Modelling the emergence of phenotypic heterogeneity in vascularised tumours. *arXiv preprint arXiv:1910.08566*, 2019.

[181] Sepideh Mirrahimi, Benoît Perthame, and Panagiotis E Souganidis. Time fluctuations in a population model of adaptive dynamics. In *Annales de l'Institut Henri Poincare (C) Non Linear Analysis*, volume 32, pages 41–58. Elsevier, 2015.

[182] Tommaso Lorenzi, Rebecca H Chisholm, Laurent Desvillettes, and Barry D Hughes. Dissecting the dynamics of epigenetic changes in phenotype-structured populations exposed to fluctuating environments. *Journal of Theoretical Biology*, 386:166–176, 2015.

[183] Susely Figueroa Iglesias and Sepideh Mirrahimi. Long time evolutionary dynamics of phenotypically structured populations in time-periodic environments. *SIAM Journal on Mathematical Analysis*, 50(5):5537–5568, 2018.

[184] Cécile Carrère and Grégoire Nadin. Influence of mutations in phenotypically-structured populations in time periodic environment. *Discrete & Continuous Dynamical Systems-B*, 22(11):0, 2020.

[185] Robert Stephen Cantrell, Chris Cosner, and King-Yeung Lam. Ideal free dispersal under general spatial heterogeneity and time periodicity. *arXiv preprint arXiv:2007.01341*, 2020.

[186] Lionel Roques, Florian Patout, Olivier Bonnefon, and Guillaume Martin. Adaptation in general temporally changing environments. *arXiv preprint arXiv:2002.09542*, 2020.

[187] Manon Costa, Christèle Etchegaray, and Sepideh Mirrahimi. Survival criterion for a population subject to selection and mutations; application to temporally piecewise constant environments. *arXiv preprint arXiv:2003.05498*, 2020.

[188] Nicolas Champagnat, R Ferričre, and G Ben Arous4. The canonical equation of adaptive dynamics: a mathematical view. *Selection*, 2(1-2):73–83, 2002.

[189] Nicolas Champagnat, Régis Ferrière, and Sylvie Méléard. Unifying evolutionary dynamics: from individual stochastic processes to macroscopic models. *Theoretical Population Biology*, 69(3):297–321, 2006.

[190] Rebecca H Chisholm, Tommaso Lorenzi, Laurent Desvillettes, and Barry D Hughes. Evolutionary dynamics of phenotype-structured populations: from individual-level mechanisms to population-level consequences. *Zeitschrift für angewandte Mathematik und Physik*, 67(4):100, 2016.

[191] Rebecca EA Stace, Thomas Stiehl, Mark AJ Chaplain, Anna Marciniak-Czochra, and Tommaso Lorenzi. Discrete and continuum phenotype-structured models for the evolution of cancer cell populations under chemotherapy. *Mathematical Modelling of Natural Phenomena*, 15:14, 2020.

[192] Barry D Hughes et al. *Random walks and random environments: random walks*, volume 1. Oxford University Press, 1995.

[193] Rafael R Bravo, Etienne Baratchart, Jeffrey West, Ryan O Schenck, Anna K Miller, Jill Gallaher, Chandler D Gatenbee, David Basanta, Mark Robertson-Tessi, and Alexander RA Anderson. Hybrid automata library: A flexible platform for hybrid modeling with real-time visualization. *PLoS Computational Biology*, 16(3):e1007635, 2020.

[194] Gary R Mirams, Christopher J Arthurs, Miguel O Bernabeu, Rafel Bordas, Jonathan Cooper, Alberto Corrias, Yohan Davit, Sara-Jane Dunn, Alexander G Fletcher, Daniel G Harvey, et al. Chaste: an open source c++ library for computational physiology and biology. *PLoS Computational Biology*, 9(3):e1002970, 2013.

[195] Ahmadreza Ghaffarizadeh, Randy Heiland, Samuel H Friedman, Shannon M Mumenthaler, and Paul Macklin. Physicell: an open source physics-based cell simulator for 3-d multicellular systems. *PLoS Computational Biology*, 14(2):e1005991, 2018.

[196] Sean H Rice. *Evolutionary theory: mathematical and conceptual foundations*. Sinauer Associates Sunderland, MA, 2004.

[197] Wilfried Gabriel, Michael Lynch, and Reinhard Bürger. Muller's ratchet and mutational meltdowns. *Evolution*, 47(6):1744–1757, 1993.

[198] Sarah R Amend, Robert A Gatenby, Kenneth J Pienta, and Joel S Brown. Cancer foraging ecology: Diet choice, patch use, and habitat selection of cancer cells. *Current Pathobiology Reports*, 6(4):209–218, 2018.

[199] José L Massera. The existence of periodic solutions of systems of differential equations. *Duke Mathematical Journal*, 17(4):457–475, 1950.

[200] Russell A Smith. Massera's convergence theorem for periodic nonlinear differential equations. *Journal of Mathematical Analysis and Applications*, 120(2):679–708, 1986.

[201] Randall J LeVeque. *Finite difference methods for ordinary and partial differential equations: steady-state and time-dependent problems*. Society for Industrial and Applied Mathematics (SIAM), Philadelphia, 2007.

[202] Ror Bellman and Karl Johan Åström. On structural identifiability. *Mathematical Biosciences*, 7(3-4):329–339, 1970.

[203] Michael J Chappell, Keith R Godfrey, and Sandor Vajda. Global identifiability of the parameters of nonlinear systems with specified inputs: a comparison of methods. *Mathematical Biosciences*, 102(1):41–73, 1990.

[204] Oana-Teodora Chis, Julio R Banga, and Eva Balsa-Canto. Structural identifiability of systems biology models: a critical comparison of methods. *PloS One*, 6(11):e27755, 2011.

[205] Johan Vande Voorde, Tobias Ackermann, Nadja Pfetzer, David Sumpton, Gillian Mackay, Gabriela Kalna, Colin Nixon, Karen Blyth, Eyal Gottlieb, and Saverio Tardito. Improving the metabolic fidelity of cancer models with a physiological cell culture medium. *Science Advances*, 5(1):eaau7314, 2019.

[206] Toshinori Okuyama. Demographic stochasticity alters the outcome of exploitation competition. *Journal of Theoretical Biology*, 365:347–351, 2015.

[207] Geou-Yarh Liou and Peter Storz. Reactive oxygen species in cancer. *Free Radical Research*, 44(5):479–496, 2010.

[208] Johan AJ Metz and Odo Diekmann. A gentle introduction to structured population models: three worked examples. In *The dynamics of physiologically structured populations*, pages 3–45. Springer, 1986.

[209] Odo Diekmann, Philipp Getto, and Mats Gyllenberg. Stability and bifurcation analysis of volterra functional equations in the light of suns and stars. *SIAM Journal on Mathematical Analysis*, 39(4):1023–1069, 2008.

[210] AM De Roos, O Diekmann, Ph Getto, and MA Kirkilionis. Numerical equilibrium analysis for structured consumer resource models. *Bulletin of Mathematical Biology*, 72(2):259–297, 2010.

[211] Odo Diekmann, Mats Gyllenberg, and Johan AJ Metz. On models of physiologically structured populations and their reduction to ordinary differential equations. *Journal of Mathematical Biology*, 80(1):189–204, 2020.

[212] F Van den Bosch, AM De Roos, and Wilfried Gabriel. Cannibalism as a life boat mechanism. *Journal of Mathematical Biology*, 26(6):619–633, 1988.

[213] Odo Diekmann. Modeling and analysing physiologically structured populations. In *Mathematics Inspired by Biology*, pages 1–37. Springer, 1999.

[214] Odo Diekmann, Mats Gyllenberg, Johan AJ Metz, Shinji Nakaoka, and Andre M de Roos. Daphnia revisited: local stability and bifurcation theory for physiologically structured population models explained by way of an example. *Journal of Mathematical Biology*, 61(2):277–318, 2010.

[215] David Basanta, Matthias Simon, Haralambos Hatzikirou, and Andreas Deutsch. Evolutionary game theory elucidates the role of glycolysis in glioma progression and invasion. *Cell Proliferation*, 41(6):980–987, 2008.

[216] Paul Macklin, Steven McDougall, Alexander RA Anderson, Mark AJ Chaplain, Vittorio Cristini, and John Lowengrub. Multiscale modelling and nonlinear simulation of vascular tumour growth. *Journal of Mathematical Biology*, 58(4-5):765–798, 2009.

[217] Amy G Tsai, Barbara Friesenecker, Michelle C Mazzoni, Heinz Kerger, Donald G Buerk, Paul C Johnson, and Marcos Intaglietta. Microvascular and tissue oxygen gradients in the rat mesentery. *Proceedings of the National Academy of Sciences*, 95(12):6590–6595, 1998.

[218] Patricio Cumsille, Aníbal Coronel, Carlos Conca, Cristóbal Quiñinao, and Carlos Escudero. Proposal of a hybrid approach for tumor progression and tumor-induced angiogenesis. *Theoretical Biology and Medical Modelling*, 12(1):13, 2015.

[219] Anne Goelzer and Vincent Fromion. Bacterial growth rate reflects a bottleneck in resource allocation. *Biochimica et Biophysica Acta (BBA)-General Subjects*, 1810(10):978–988, 2011.

[220] Alan Hastings. Transients: the key to long-term ecological understanding? *Trends in Ecology & Evolution*, 19(1):39–45, 2004.

[221] Caitriona Holohan, Sandra Van Schaeybroeck, Daniel B Longley, and Patrick G Johnston. Cancer drug resistance: an evolving paradigm. *Nature Reviews Cancer*, 13(10):714–726, 2013.

[222] Gaorav P Gupta and Joan Massagué. Cancer metastasis: building a framework. *Cell*, 127(4):679–695, 2006.

[223] Sui Huang. Genetic and non-genetic instability in tumor progression: link between the fitness landscape and the epigenetic landscape of cancer cells. *Cancer and Metastasis Reviews*, 32(3-4):423–448, 2013.

[224] Joan Massagué and Anna C Obenauf. Metastatic colonization by circulating tumour cells. *Nature*, 529(7586):298–306, 2016.

[225] Anna C Obenauf and Joan Massagué. Surviving at a distance: organ-specific metastasis. *Trends in Cancer*, 1(1):76–91, 2015.

[226] Nilay Sethi and Yibin Kang. Unravelling the complexity of metastasis?molecular understanding and targeted therapies. *Nature Reviews Cancer*, 11(10):735–748, 2011.

[227] Piyush B Gupta, Christine M Fillmore, Guozhi Jiang, Sagi D Shapira, Kai Tao, Charlotte Kuperwasser, and Eric S Lander. Stochastic state transitions give rise to phenotypic equilibrium in populations of cancer cells. *Cell*, 146(4):633–644, 2011.

[228] Aude Carreau, Bouchra El Hafny-Rahbi, Agata Matejuk, Catherine Grillon, and Claudine Kieda. Why is the partial oxygen pressure of human tissues a crucial parameter? small molecules and hypoxia. *Journal of Cellular and Molecular Medicine*, 15(6):1239–1253, 2011.

[229] Wilfried Thuiller, Jasper A Slingsby, Sean DJ Privett, and Richard M Cowling. Stochastic species turnover and stable coexistence in a species-rich, fire-prone plant community. *PLoS One*, 2(9):e938, 2007.

[230] Jon F Wilkins and Peter Godfrey-Smith. Adaptationism and the adaptive landscape. *Biology & Philosophy*, 24(2):199–214, 2009.

[231] Inês Fragata, Alexandre Blanckaert, Marco António Dias Louro, David A Liberles, and Claudia Bank. Evolution in the light of fitness landscape theory. *Trends in Ecology &Evolution*, 34(1):69–82, 2019.

[232] Audrey R Freischel, Mehdi Damaghi, Jessica J Cunningham, Arig Ibrahim-Hashim, Robert J Gillies, Robert A Gatenby, and Joel S Brown. Frequency-dependent interactions determine outcome of competition between two breast cancer cell lines. *bioRxiv*, 2020.03.06.979518, 2020.

[233] Gang Dong, Xia-Hui Lin, Hua-Hua Liu, Dong-Mei Gao, Jie-Feng Cui, Zheng-Gang Ren, and Rong-Xin Chen. Intermittent hypoxia alleviates increased vegf and pro-angiogenic potential in liver cancer cells. *Oncology Letters*, 18(2):1831–1839, 2019.

[234] Angela Stevens and Hans G Othmer. Aggregation, blowup, and collapse: the abc's of taxis in reinforced random walks. *SIAM Journal on Applied Mathematics*, 57(4):1044–1081, 1997.

[235] Gabriel Helmlinger, Fan Yuan, Marc Dellian, and Rakesh K Jain. Interstitial ph and po 2 gradients in solid tumors in vivo: high-resolution measurements reveal a lack of correlation. *Nature Medicine*, 3(2):177–182, 1997.

[236] Michael P Hassell, Hugh N Comins, and Robert M May. Species coexistence and self-organizing spatial dynamics. *Nature*, 370(6487):290–292, 1994.

[237] Jamie M Kneitel and Jonathan M Chase. Trade-offs in community ecology: linking spatial scales and species coexistence. *Ecology Letters*, 7(1):69–80, 2004.

[238] Litao Liu, Wenlan Liu, Lili Wang, Ting Zhu, Jianhua Zhong, and Ni Xie. Hypoxia-inducible factor 1 mediates intermittent hypoxia-induced migration of human breast cancer mda-mb-231 cells. *Oncology Letters*, 14(6):7715–7722, 2017.

[239] Jill A Gallaher, Joel S Brown, and Alexander RA Anderson. The impact of proliferation-migration tradeoffs on phenotypic evolution in cancer. *Scientific Reports*, 9(1):1–10, 2019.